Radiative Transfer Galaxy Models with Quiescent Clumps

Christopher J. Inman

A thesis submitted in partial fulfilment
of the requirements for the degree of
Doctor of Philosophy

Jeremiah Horrocks Institute for Mathematics, Physics and Astronomy
University of Lancashire

November 2025

Declaration

Type of Award: Doctor of Philosophy

School: Engineering and Computing

I declare that while registered as a candidate for the research degree, I have not been a registered candidate or enrolled student for another award of the University or other academic or professional institution.

I declare that no material contained in the thesis has been used in any other submission for an academic award and is solely my own work.

No proof-reading service was used in the compilation of this thesis.

Christopher J. Inman

November 2025

Abstract

Interstellar dust plays a major role in the transfer of radiation in galaxies, both through its microscopic optical properties and its macroscopic spatial distribution. Dust absorbs and scatters the stellar light, and re-emits it in the far-infrared (FIR) and sub-millimetre (submm) wavelength range, redistributing both the direction of the propagating photons, and their energy. The complexity of these processes is best described by radiative transfer (RT) models. In particular these models have been used to derive the intrinsic distributions of stars and dust in galaxies by decoding the panchromatic imaging observations of galaxies.

While RT models have been remarkably successful to date in performing this task, they have also encountered an energy balance problem between direct stellar light and dust re-emission, particularly in edge-on galaxies. This work attempts to resolve this long-standing issue by incorporating a treatment for the clumpy structure of the interstellar medium (ISM). Because the scale of individual clumps ($\sim 1\,\mathrm{pc}$) lies below the resolution of galaxy-scale models, a subgrid approach is adopted, treating the quiescent dust clouds as *pseudo-dust grains*, with equivalent optical and thermal emission properties. Dedicated RT calculations are performed to derive key quantities such as the absorption, scattering and extinction cross-sections. This enables the virtualisation of the macroscopic clump into a microscopic pseudo-grain that can be included alongside the existing dust model constituents. The addition of the pseudo-grain results in a flatter extinction curve. A library of clump emission

spectral energy distributions (SEDs) is constructed for radiation fields of various colours and intensities.

With the full incorporation of the extinction and emission properties of clumps into the RT models, this new clumpy model is applied to the edge-on galaxy NGC 891. For the first time, the clumpy model is able to achieve a good energy balance, simultaneously fitting both the submm and Near Infrared (NIR) data.

The clumpy model is further applied to a small sample of eight galaxies, and the results are compared with those from the purely diffuse models. Overall the clumpy models produced improved fits and provide a consistent solution for both face-on and edge-on galaxies.

The clumpy models are characterised by a reduction in dust opacity—and therefore attenuation—compared to their purely diffuse counterparts. Thus, the maximum face-on optical depth in the B-band, $\max(\tau_{\rm B}^{\rm f})$, derived from the clumpy models is found to be lower by factors ranging from 1.3 to 2.8. Of the eight galaxies, two are found to be optically thick in their centres, two are found to be moderately optically thick, and four are found to be optically thin. As a consequence of the decreased attenuation, the clumpy models also predict lower star-formation rates (SFRs), reduced by factors between 1.2 and 2.0.

Contents

List of Tables

List of Figures

Acknowledgements

Perhaps more daunting a task than writing a PhD thesis is attempting to adequately express the gratitude that is owed to a great many people.

First, and foremost, I would like to extend my deepest gratitude to Professor Cristina C. Popescu, who has provided not only guidance and support throughout the many years, but also the pattern of a truly great scientist. Her mentorship has been invaluable to my development as a researcher.

I would like to extend my thanks to Dr. Jordan Thirlwall, Dr. Mark Rushton, and Dr. David Murphy for many enlightening discussions. Particularly Jordan, whose patience was tested and proven in many a troubleshooting session in the early days. I am also grateful to my colleagues from whom I learned a great deal. It would be remiss of me not to thank the Science and Technology Facilities Council for their generous financial support, without which this research would not have been possible.

More personally, I would like to thank my wife Beth, whose patience, support, and companionship have truly been a gift. The depth of my gratitude for my family and friends cannot be overstated. Their encouragement during the challenging moments and celebration of the victories have meant everything to me. At every point, you have shaped who I am.

No man is an island.

John Donne

Chapter 1

Introduction

Our understanding of the Universe arises exclusively through our interaction with it. In astrophysics, this interaction is necessarily limited to passive observation; thus, progress is inherently driven by the interplay between theory and observation. Theoretical frameworks are developed to explain the physical processes taking place in the Universe and are continuously tested against observations of increasing precision and scope. This iterative process often dictates the direction of inquiry, as emerging inconsistencies prompt refinement or re-evaluation of existing models, spawning entirely new research domains and sometimes revolutionary paradigm shifts. A notable example of this is the discovery and subsequent understanding of interstellar dust (Trumpler, 1930; Greenberg, 1963; Galliano, Galametz & Jones, 2018). For a time the effect, and even existence, of interstellar dust was uncertain (Herschel, 1785). It was Trumpler (1930) who later confirmed that interstellar dust not only exists, but diminishes and reddens the light passing through it. Correctly identifying the influence dust has on observed stellar light led to the vital development of extinction laws (Trumpler, 1930; Savage & Mathis, 1979; Mathis, 1990). This early focus on extinction effects was just the beginning of our understanding of dust's multifaceted role in galaxies.

CHAPTER 1

Beyond the dimming and reddening of Milky Way (MW) stars, we now understand that dust plays an important role in the thermodynamic and chemical balance of star-forming galaxies (Greenberg, 1963; Calzetti, 2001; Sauvage, Tuffs & Popescu, 2005; Popescu & Tuffs, 2010). Even outside of galaxies, dust plays an important role in regulating the temperature of both the Intergalactic Medium (IGM) and Intracluster Medium (ICM). At high temperatures ($T > 10^7$ K) and for sufficiently high dust densities relative to the gas, dust is the dominant cooling mechanism in the ICM (Montier & Giard, 2004), bridging the gap between lower temperatures where atomic processes dominate ($T < 10^5$ K), and higher temperatures where bremsstrahlung dominates ($T > 10^8$ K). In the IGM dust becomes a strong heating mechanism in lower temperature environments ($T < 10^5$ K) with a strong enough UV background (Montier & Giard, 2004). Within galaxies, dust grains both heat the Interstellar Medium (ISM) via the photoelectric effect, and cool it via far-infrared (FIR) cooling lines through inelastic collisions, such as [C II] line emission (Draine, 1978; Juvela, Padoan & Jimenez, 2003). When the UV radiation fields weaken, this balance shifts: while photoelectric heating of the gas abates, the cooling via FIR emission lines continues leading to the condensation of gas into dense molecular clouds, which can eventually collapse to form stars. Beyond thermodynamic effects, dust also plays a role in the chemistry of galaxies. The surfaces of dust grains can act as a catalyst for numerous chemical reactions, including the formation of H_2 (Gould & Salpeter, 1963; Gould, Gold & Salpeter, 1963; Hollenbach & Salpeter, 1971; Tielens et al., 1991). As gas and dust are typically well-mixed, the dust traces the total gas mass in galaxies, including the cold molecular hydrogen, which due it its lack of a permanent dipole moment has no viable direct emission signature (Bohlin, Savage & Drake, 1978; Leroy et al., 2011). Furthermore, the reprocessing of high-energy photons to lower-energy photons provides vital 'seed' photons that are up-scattered to γ rays via inverse-Compton scattering (Jones, 1968).

CHAPTER 1

Within our current paradigm cosmological framework (the concordance model), the cosmological simulations have successfully accounted for the effects of gravity due to dark and ordinary matter in shaping the evolution of structure and formation of galaxies, as seen throughout the universe. Our biggest challenge in this field remains to understand the detailed baryonic physics that are equally critical for galaxy evolution. Already the largest cosmological computer simulations (e.g. MilleniumTNG - Hernández-Aguayo et al. (2023), FLAMINGO - Schaye et al. (2023)) include ever more realistic physics, like neutrino, cosmic rays, and interstellar gas and dust physics. But even if explicit calculations could be self-consistently performed throughout all the components of the ISM in galaxy simulations, the result would still be a statistical realisation of the galaxy populations. Thus, no specific individual galaxy could be obtained, even not the Milky Way.

An alternative approach (that can be applied to individual galaxies) is to decode the panchromatic imaging information, also through modelling, and derive an intrinsic representation of all galaxy components, stars, gas, dust, and cosmic rays, and their interplay, that can account for the formation and evolution of that specific galaxy. From a mathematical point of view, this is solving the inverse problem for a galaxy. In turn, this could better inform the cosmological simulations and improve the input baryonic physics, in addition to directly allowing advances in our knowledge of fundamental processes, like that of star formation in galaxies. Radiative transfer models that self-consistently account for all these processes are the most powerful tools, and, with the continuing increase in computational capacity, a reality in every aspect.

From an observational perspective, the James Webb Space Telescope is revealing amazing detail of the stellar structures and ISM in local Universe galaxies (e.g. Williams et al. (2024) for the PHANGS-JWST sample), and identified the first forming galaxies in the Universe (Carniani et al., 2024). Despite all these advances,

both in modelling and observations, when trying to decode galaxy messenger information with self-consistent models, even in the nearby Universe, a big problem has remained unsolved until now. Perhaps brushed under the carpet due to the recent developments, there is a left-over, but fundamental energy balance problem between direct stellar light and dust emission for galaxies seen under a specific orientation (Popescu et al., 2000; Baes et al., 2010). The story behind this is as follows:

When the first radiative transfer models of the surface brightness distribution of star forming galaxies were developed (Kylafis & Bahcall, 1987), they were first applied to edge-on galaxies, since images obtained under this orientation reveal the vertical stratification of stars and dust, allowing for additional model constraints, through the determination of the scale heights of the different galaxy components. Usually three advantages were invoked for using this view of galaxies: i) easy to separate the stellar disc, the bulge and the dust; ii) a lot of details are smeared out allowing for a simpler model; iii) the dust is prominently seen in the form of dust lanes (Xilouris et al., 1997). Whether advantage ii) may still be seen as such, or more as a curse recently, this may be a matter of debate.

The RT modelling in the optical bands of the prototype nearby edge-on spiral NGC 891, together with a few other edge-on galaxies, allowed Xilouris et al. (1997, 1998, 1999) to derive the spatial distribution of stars (mainly older stellar populations) and associated dust. They found that spirals are optically thin in the optical bands, with a central face-on B-band optical depth of around 1 ($\tau_0^{\rm f}(B) \approx 1$), so just becoming optically thick towards shorter UV wavelengths. This would have been seen as solving the long debate of whether spiral galaxies are optically thin or thick (Disney, Davies & Phillipps, 1989). However, when Popescu et al. (2000) developed the first panchromatic radiative transfer modelling of spiral galaxies, whereby the dust emission was self-consistently calculated with the dust attenuation, they found that the solution obtained in the optical bands for NGC 891 by Xilouris et al.

(1999), was underestimating the FIR and sub-millimetre (submm) emission by a factor of approximately 3. This was later called the energy balance problem (Baes et al., 2010). To solve the problem Popescu et al. (2000) proposed several scenarios, including the existence of additional large-scale diffuse or clumpy components and of modified dust grain properties, and adopted a solution with an additional disc of diffuse dust, with the dust opacity constrained to fit the submm data. This solution, with $\tau_0^{\rm f}(B) \sim 4$ provided a good fit to all FIR/submm images available at that time, including the optical images. It was clear that the solution derived for the optical images alone is degenerate. In other words, the appearance of the dust lane in the optical can be accommodated with both a face-on optically thin or thick solution. The degeneracy is though lifted in the NIR J and K bands, where edge-on lines of sight make the transition between optically thin and thick at these wavelengths. It was shown by Dasyra et al. (2005) that the model of NGC 891 with $\tau_0^{\rm f}(B) \sim 4$ produces too prominent dust lanes in the NIR, not observed in the then-new 2MASS (Two Micron All Sky Survey; Jarrett et al., 2003) images. The energy balance problem in edge-on galaxies was confirmed by all later studies of edge-on galaxies, including Bianchi (2008), Baes et al. (2010), De Geyter et al. (2015), Mosenkov et al. (2016), and Mosenkov et al. (2018).

One other scenario proposed in Popescu et al. (2000) was to take into account the clumpy nature of the ISM. Clumps are known to reduce the overall attenuation of the stellar light (e.g. Witt & Gordon, 1996,Városi & Dwek, 1999). Popescu et al. (2000) included a clumpy component associated with the star forming regions (see also Popescu et al. (2011, hereafter PT11) for further developments), although this was not enough to solve the issue. Models with quiescent clumps have been also used (Bianchi, Davies & Alton, 2000; Bianchi, 2008), but they could not account for the energy balance problem either.

Saftly et al. (2015) argued that using galaxy simulations, whereby the input distribution of stars and dust is known, does not result in an energy balance problem, and that therefore the solution to the problem could be to take into account the complex distribution of stars and dust, as seen in face-on galaxies, departing from the azimuthal symmetry involved in modelling the edge-on galaxies. The focus shifted towards face-on galaxies then. Using the SKIRT code and non-axi symmetric models, De Looze et al. (2014), Viaene et al. (2014), and Verstocken et al. (2020) fitted the panchromatic images of the face-on spirals M51, M31, and M81, with no signs of an energy balance problem. However, the axi-symmetric models of PT11 were also used to model face-on galaxies Thirlwall et al. (2020, hereafter TP20) for M33, Rushton et al. (2022) for NGC 628, Inman et al. (2023) for M51, Pricopi et al. (2025) for M101 and NGC 3938), with no sign of an energy balance problem, either. It became obvious that the use of axi-symmetric versus non-axi-symmetric models was not at the root of the problem. Dust with modified optical properties cannot provide the solution either, since the properties of dust should not vary with the viewing angle. Thus, the energy balance problem remained unsolved: RT models can account for the panchromatic surface brightness distributions of face-on spiral galaxies, but not for their edge-on counterparts. In edge-on systems either an optically thin solution is derived from the optical data, but this underestimates the FIR/submm data by factors between 2–4 (Popescu et al., 2000; Mosenkov et al., 2018), or an optically thick solution is derived from the submm data (Popescu et al., 2000, 2011), but this overestimates the strength of the dust lane in the NIR.

In this thesis it is shown that the clumpy nature of the ISM on scales of around 1 parsec provides the resolution to the energy balance problem. A subgrid approach is introduced, in the form of a novel concept, that of the so called "pseudo-grain". It is shown that this provides a consistent solution for both face-on and edge-on galaxies, thus solving the long standing debate in the literature.

This thesis is organised as follows. Chapter 2 presents a discussion of the physical properties of interstellar dust grains, and provides an overview of radiative transfer. Chapter 3 provides a description of the radiative transfer models used in this work, as well as the fitting procedure used for face-on and edge-on galaxies. Chapter 4 introduces the concept of the "pseudo-grain" and how its optical properties and infrared emissivity are derived, and how they are incorporated into the full radiative transfer models of galaxies. Chapter 5 applies the new clumpy model to the prototypical galaxy NGC 891 and is compared with its pure diffuse counterpart. Chapter 6 applies the clumpy model to the edge-on spiral galaxy, NGC 5907, which, while demonstrating no energy-balance problem, previous studies have been unable to fit its optical data. Chapter 7 presents the results of the clumpy model as applied to the sample of eight local galaxies, and contrasts the results with those found using the pure diffuse model. The summary and conclusions are provided in Chapter 8.

Chapter 2

Modelling Dust Attenuation and Emission through Radiative Transfer

Studying the panchromatic emission of galaxies is the primary method with which to gain insight into their structure and composition. The complex interactions between a galaxy's constituents, such as stars and dust, provide critical insights into their physical properties. To extract meaningful information from these data, it is essential to accurately characterise these interactions. This requires constructing models that account for both the microscopic interaction of stellar photons with interstellar dust grains—such as scattering, absorption and re-emission—and the macroscopic effect of these interactions across the spatial distribution of stars and dust within the galaxy.

CHAPTER 2

2.1 Dust Physics in the Context of Galaxy Formation

Following the Big Bang, the Universe underwent a period of rapid expansion and cooling during which quantum fluctuations gave rise to density inhomogeneities. This allowed matter to condense under gravity into the first dark matter haloes (White & Rees, 1978). As the Universe entered the matter dominated era, baryonic matter (mostly neutral hydrogen) accreted into these potential wells. The gas was heated to the virial temperature via shocks and subsequently cooled via radiative processes, leading to the formation of the first stars and protogalaxies (Rees & Ostriker, 1977). Through hierarchical merging and continuous accretion, these smaller assemblies grew into the larger galaxies observed today (Springel et al., 2005). As stellar evolution progressed, successive generations of stars enriched the ISM with heavy elements and dust formed in the stellar winds of AGB stars and potentially in supernova ejecta. (Dwek & Werner, 1981; Galliano, Galametz & Jones, 2018). Over cosmic time, this recycling of material has played a fundamental role in regulating star formation and galaxy evolution. Consequently, studying the ISM of galaxies provides crucial insight into their evolutionary histories and future pathways (Conroy, 2013).

In the context of spiral galaxies, dust profoundly influences both their physical evolution and their observed appearance. Dust grains absorb and scatter the UV and optical light from stars and re-emit this energy in the IR. Beyond its radiative effects, dust also plays an important role in the formation of structure. Through the inelastic collisions of dust grains with electrons and ions, dust can become the dominant cooling mechanism in the IGM for temperatures $T > 10^6\,\mathrm{K}$, even for low dust-to-gas mass ratios, $Z_d \approx 10^{-4}$ (Montier & Giard, 2004). Provided the presence of dust grains, this efficient cooling mechanism may help to explain the cooling of

the hot virialised galactic haloes, allowing gas to cool and accrete into the disc. Numerical simulations of galaxy formation done by Pointecouteau et al. (2009) found that the models including dust cooling resulted in a higher concentration of gas in the cool and high-density phase. Inside galaxies, dust grains maintain a thermodynamic balance by both heating the ISM through the photoelectric effect, and cooling it through FIR cooling lines powered by inelastic collisions with gas particles. A lack of UV photons to power the photoelectric heating will unbalance this equilibrium allowing the dust to further cool and condense into denser structures, leading to the formation of dense molecular clouds. Due to increasing optical thickness, thermal pressure can be reduced in these clouds which in turn allows them to become denser, therefore increasing the propensity of gas to condense into stars. Lastly, dust plays a vital role in the final stages of gravitational collapse in star-forming regions by efficiently cooling the gas via inelastic collisions, reducing the thermal pressure allowing further collapse.

Dust physics therefore plays a crucial role across cosmic scales, from the condensation of gas from the IGM into galaxies, to its structuring within the ISM, and ultimately to the formation of stars. Understanding dust is essential for reconstructing the star formation history of the Universe, as it regulates gas cooling and the formation of molecular clouds. Furthermore, dust strongly affects the light we observe from galaxies, meaning that interpreting astronomical observations accurately requires accounting for its effects.

2.2 Modelling the Extinction and Attenuation of Stellar Light in Galaxies

Within star-forming galaxies stellar photons propagate throughout the ISM interacting with the interstellar dust. These interactions alter both the energy and the

direction of propagation of the photons via the processes of absorption and scattering. Thus, what would otherwise be an isotropic process becomes highly anisotropic. Two important observables in studying these effects are the extinction and attenuation. Extinction refers to the loss of light along a line of sight due to absorption and scattering through a dusty medium. Attenuation concerns these effects while also considering the relative distribution of stars and dust. Therefore, to build a model of attenuation one must consider the optical properties of the microscopic dust grains and their macroscopic distribution among the stars.

2.2.1 The Interaction of Stellar Light with Dust Grains

Interstellar dust consists of various different compounds including silicates (Si), graphite (Gra) and polycyclic aromatic hydrocarbons (PAHs). These grains are described by a grain size distribution with grain sizes ranging form a few Angstroms (Å) to a few microns (μm) (Draine & Lee, 1984; Draine, 2003). Stellar photons incident on the interstellar dust are absorbed and reradiated as thermal radiation, primarily in the FIR. Thermal radiation is the radiation emitted by a black-body, which absorbs all radiation incident upon it, or more quantitatively a black-body has absorption efficiency $Q_{\rm abs} = 1$. However, a black-body is an idealised material, so real physical objects such as dust grains have absorption efficiencies $Q_{\rm abs} < 1$. From Kirchhoff's law of thermal radiation, $Q_{\rm abs} = Q_{\rm em}$ (where $Q_{\rm em}$ is the emission efficiency or the emissivity of a grain), it also follows that a real body has an emissivity $Q_{\rm em} < 1$. The value of $Q_{\rm abs}$ is dependent on the size of the real body and also on the wavelength of the radiation incident upon it. Because real bodies do not absorb all incident radiation, incident photons that are not absorbed will be scattered or will pass through without any interaction. Similarly, a scattering efficiency $Q_{\rm sca}$ can be defined. This scattering is anisotropic, so for each different direction the photons would have a different probability for scattering. This probability is the anisotropy

efficiency $Q_{\rm phase}$ and is calculated similarly to $Q_{\rm abs}$ and $Q_{\rm sca}$.

In order to derive the dust efficiencies for absorption and scattering the size of dust grains must be known as well as the wavelengths of the incident photons. For the size of the dust grains and wavelength of stellar photons, it is appropriate to use Mie theory to describe the interaction of stellar photons with dust grains, as $a \sim \lambda$, where a is the grain size. Mie theory involves solving Maxwell's equations within the dust grains, giving a microscopic description of the interaction of the dust grains with photons. This is used to obtain $Q_{\rm abs}$, $Q_{\rm sca}$, and $Q_{\rm phase}$ for each grain type as a function of grain size a and wavelength λ. The dust models of Weingartner & Draine (2001); Draine & Li (2007) consist of silicate and carbonaceous grains each with different properties. The carbonaceous material comprises graphite grains and large Polycyclic Aromatic Hydrocarbon (PAH) molecules. The PAHs are further subcategorised as $\rm PAH^0$ (neutral) and $\rm PAH^+$ (cationic). The silicates are assumed to be composed of Forsterite ($\rm Mg_2SiO_4$), Fayalite ($\rm Fe_2SiO_4$), and Olivine $\left(\rm (MgFe)_2SiO_4\right)$. In Fig. 2.1 an example is given of $Q_{\rm abs}$ as a function of wavelength for spherical silicates and neutral PAHs of different sizes, as given in the model of Draine & Lee (1984) and Draine & Li (2007).

The grain size distribution for each grain composition derived in Weingartner & Draine (2001) is as follows.

$$\frac{1}{n_{\rm H}}\frac{{\rm d}n_{\rm PAH}}{{\rm d}a} \equiv D(a) = \sum_{i=1}^{2}\frac{B_i}{a}\exp\left\{-\frac{1}{2}\left[\frac{\ln(a/a_{0,i})}{\sigma}\right]^2\right\},\ a > 3.5\text{Å}, \tag{2.1}$$

$$B_i = \frac{3}{(2\pi)^{3/2}}\frac{\exp(-4.5\sigma^2)}{\rho a_{0,i}^3\sigma}\frac{b_{{\rm C},i}m_{\rm C}}{1+{\rm erf}[3\sigma/\sqrt{2}+\ln(a_{0,i}/3.5\text{Å})/\sigma\sqrt{2}]}, \tag{2.2}$$

where $D(a)$ is the size distribution of PAH molecules, $n_{\rm PAH}$ and $n_{\rm H}$ is the number density of PAH molecules and hydrogen respectively, ρ is the density of graphite, $m_{\rm C}$ is the mass of a C atom, $b_{\rm C}$ is the total C abundance per H nucleus where

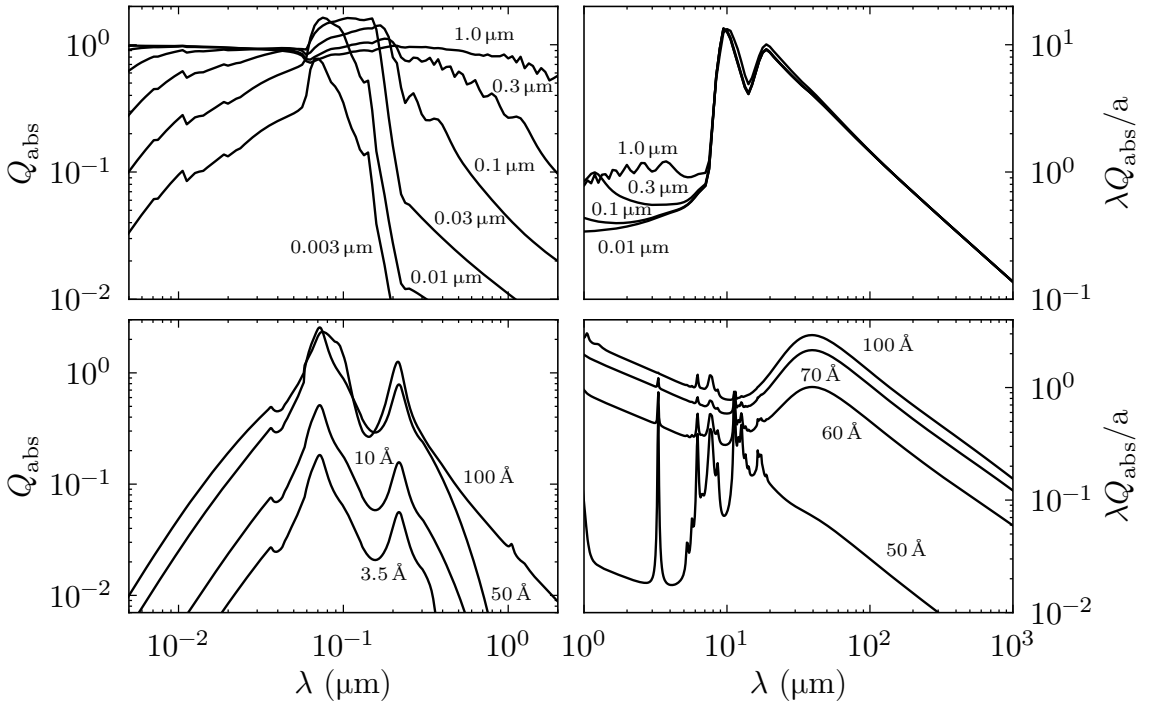

Figure 2.1: Absorption efficiencies $Q_{\rm abs}$ as a function of wavelength λ for silicates and PAH grains of varying sizes, where a is the grain size. The panels on the top row show the absorption efficiencies for the Si grains in the UV/optical regime (left) and the IR regime (right). The panels on the bottom row show the absorption efficiencies for the PAH^0 grains in the UV/optical regime (left) and IR regime (right). These efficiencies were taken from the model of Draine & Lee (1984) and Draine & Li (2007).

$b_{\rm C,1} = 0.75\,b_{\rm C}$ and $b_{\rm C,2} = 0.25\,b_{\rm C}$. $a_{0,1} = 3.5\,\text{Å}$, $a_{0,2} = 30\,\text{Å}$, and $\sigma = 0.4$. The grain size distributions for all carbonaceous and silicate grains are as follows.

$$\frac{1}{n_{\rm H}}\frac{{\rm d}n_{\rm g}}{{\rm d}a} = D(a) + \frac{C_{\rm g}}{a}\left(\frac{a}{a_{\rm t,g}}\right)^{\alpha_{\rm g}} F(a;\beta_{\rm g},a_{\rm t,g}) \times \begin{cases} 1, & 3.5\,\text{Å} < a < a_{\rm t,g} \\ \exp\left\{-\left[\frac{a-a_{\rm t,g}}{a_{\rm c,g}}\right]^3\right\}, & a < a_{\rm t,g} \end{cases} \tag{2.3}$$

$$\frac{1}{n_{\rm H}}\frac{{\rm d}n_{\rm s}}{{\rm d}a} = \frac{C_{\rm s}}{a}\left(\frac{a}{a_{\rm t,s}}\right)^{\alpha_{\rm s}} F(a;\beta_{\rm s},a_{\rm t,s}) \times \begin{cases} 1, & 3.5\,\text{Å} < a < a_{\rm t,s} \\ \exp\left\{-\left[\frac{a-a_{\rm t,s}}{a_{\rm c,s}}\right]^3\right\}, & a < a_{\rm t,s} \end{cases} \tag{2.4}$$

where $F(a;\beta,a_{\rm t})$ is given by:

$$F(a;\beta,a_{\rm t}) \equiv \begin{cases} 1+\beta a/a_{\rm t}\,, & \beta \geq 0 \\ \left(1-\beta a/a_{\rm t}\right)^{-1}\,, & \beta < 0, \end{cases} \tag{2.5}$$

where $n_{\rm g}$ and $n_{\rm s}$ are the number density of carbonaceous and silicate grains respectively, the absorption cross-section of the carbonaceous/silicate grains are given by $C_{\rm g/s}$. $a_{\rm t,g/s}$ is the grain size where the functional form transitions, $a_{\rm c,g/s}$ is the upper limit for the grain size distribution. $\alpha_{\rm g/s}$ are constants and $\beta_{\rm g/s}$ are parameters to provide curvature in order to best-fit the extinction. The values of these parameters for various conditions are given in Table 1 of Weingartner & Draine (2001).

For a population of grains of various chemical composition and sizes one can define a cross-section $C_{\rm abs}$ that describes the interaction of photons with dust grains. Thus, if it is assumed the composition of grains is made of silicates, graphites and polycyclic aromatic hydrocarbons, i ={Si, Gra, $\rm PAH^0$, $\rm PAH^+$}, the absorption cross-section $C_{{\rm abs},i}$, is calculated by integrating the absorption efficiencies of the grains $Q_{{\rm abs},i}$ over the grain size distribution $n(a)$:

$$C_{{\rm abs},i}(\lambda) = \int_{a_{\rm min}}^{a_{\rm max}} \pi a^2 n(a) Q_{{\rm abs},i}(a,\lambda) da \tag{2.6}$$

where $C_{{\rm abs},i}$ is given in units of $[{\rm cm^2\,H^{-1}}]$, and $a_{\rm min}$ and $a_{\rm max}$ are the minimum and maximum grain size respectively. The scattering cross-section is obtained similarly,

using the scattering efficiencies $Q_{\mathrm{sca},i}$:

$$C_{\mathrm{sca},i}(\lambda) = \int_{a_{\mathrm{min}}}^{a_{\mathrm{max}}} \pi a^2 n(a) Q_{\mathrm{sca},i}(a,\lambda) da \tag{2.7}$$

then the total absorption and scattering cross-sections, C_{abs} and C_{sca} are obtained by summing the cross-sections of the grain composition i:

$$C_{\mathrm{abs}}(\lambda) = \sum_i C_{\mathrm{abs},i}(\lambda) \tag{2.8}$$

$$C_{\mathrm{sca}}(\lambda) = \sum_i C_{\mathrm{sca},i}(\lambda) \tag{2.9}$$

Then the extinction cross-section C_{ext} is the sum of the absorption and scattering cross-sections:

$$C_{\mathrm{ext}}(\lambda) = C_{\mathrm{abs}}(\lambda) + C_{\mathrm{sca}}(\lambda) \tag{2.10}$$

The dimensions of C_{ext} are $[\mathrm{cm^2\,H^{-1}}]$. While expressing C_{ext} in units per unit hydrogen is useful when modelling gas, in the context of modelling dust it is more direct to express C_{ext} per unit dust mass. This is done by considering the density and volume of the grain material, and the number density of grains per unit hydrogen. This is written as

$$\mu_{\mathrm{d}} = \int_{a_{\mathrm{min}}}^{a_{\mathrm{max}}} \frac{4\pi a^3}{3}\, n(a)\, \rho_{\mathrm{g}}\, da \tag{2.11}$$

where $4\pi a^3/3$ is the volume of dust grains with radius a, $n(a)$ is the number density of grains with radius a per unit hydrogen atom, and ρ_{g} is the volume density by mass of the grain species. Hence, μ_{d} is the total mass of dust per unit hydrogen with units $[\mathrm{g\,H^{-1}}]$. Then the extinction cross-section per unit dust mass is denoted as $C^{\mathrm{m}}_{\mathrm{ext}}$:

$$C^{\mathrm{m}}_{\mathrm{ext}}(\lambda) = \frac{C_{\mathrm{ext}}(\lambda)}{\mu_{\mathrm{d}}} \tag{2.12}$$

where $C^{\mathrm{m}}_{\mathrm{ext}}$ is in units $[\mathrm{cm^2\,g^{-1}}]$. Fig. 2.2 shows as an example a model of the extinction curve of the Milky Way as a function of wavelength, derived using the

dust efficiencies from Draine & Lee (1984) and Draine & Li (2007), and the grain size distribution from Weingartner & Draine (2001). The figure also shows a comparison with the observed extinction curve of the Milky Way (Fitzpatrick, 1999).

In a spiral galaxy, where dust grains are distributed throughout the disc, axi-symmetry can be assumed, in which case the dust mass density is a function of radial position R and height z, $\rho_{\rm dust} = \rho_{\rm dust}(R, z)$. In this case an extinction coefficient $\kappa_{\rm ext}(\lambda, R, z)$ can be defined as the product of $C^{\rm m}_{\rm ext}$ and $\rho_{\rm dust}(R, z)$:

$$\kappa_{\rm ext}(\lambda, R, z) = \rho_{\rm dust}(R, z) \times C^{\rm m}_{\rm ext} \tag{2.13}$$

where $\rho_{\rm dust}(R, z)$ has units of $[\mathrm{g\,cm^{-3}}]$ so $\kappa_{\rm ext}(\lambda, R, z)$ has units of $[\mathrm{cm^{-1}}]$.

When a photon interacts with dust there is a chance that it is scattered from its original propagation direction $\hat{\boldsymbol{n}}$ to some different direction $\hat{\boldsymbol{n}}'$. The scattering phase function describes the probability that a photon travelling along $\hat{\boldsymbol{n}}$ will be scattered onto the new direction $\hat{\boldsymbol{n}}'$. In this work, the Henyey-Greenstein scattering phase function (Henyey & Greenstein, 1941) is used, and is given by Equation 2.14:

$$\Phi\left(\hat{\boldsymbol{n}}', \hat{\boldsymbol{n}}, \lambda\right) = \frac{1 - g(\lambda)^2}{\left(1 + g(\lambda)^2 - 2g(\lambda)\hat{\boldsymbol{n}}' \cdot \hat{\boldsymbol{n}}\right)^{3/2}} \tag{2.14}$$

where g is the anisotropy factor and $g \in [-1, 1]$. $g = -1$ corresponds to purely backwards scattering, $g = 1$ corresponds to purely forward scattering, and $g = 0$ corresponds to isotropic scattering, i.e., there is no preferred direction for scattering.

The averaged anisotropy of the scattering phase function g is found in a similar manner as shown in Equations. 2.6 – 2.9,

$$g_i(\lambda) = \int_{a_{\rm min}}^{a_{\rm max}} \pi a^2 n(a) Q_{{\rm sca},\,i}(a, \lambda) Q_{{\rm phase},\,i}(a, \lambda) {\rm d}a \tag{2.15}$$

$$g(\lambda) = \sum_i g_i(\lambda) \tag{2.16}$$

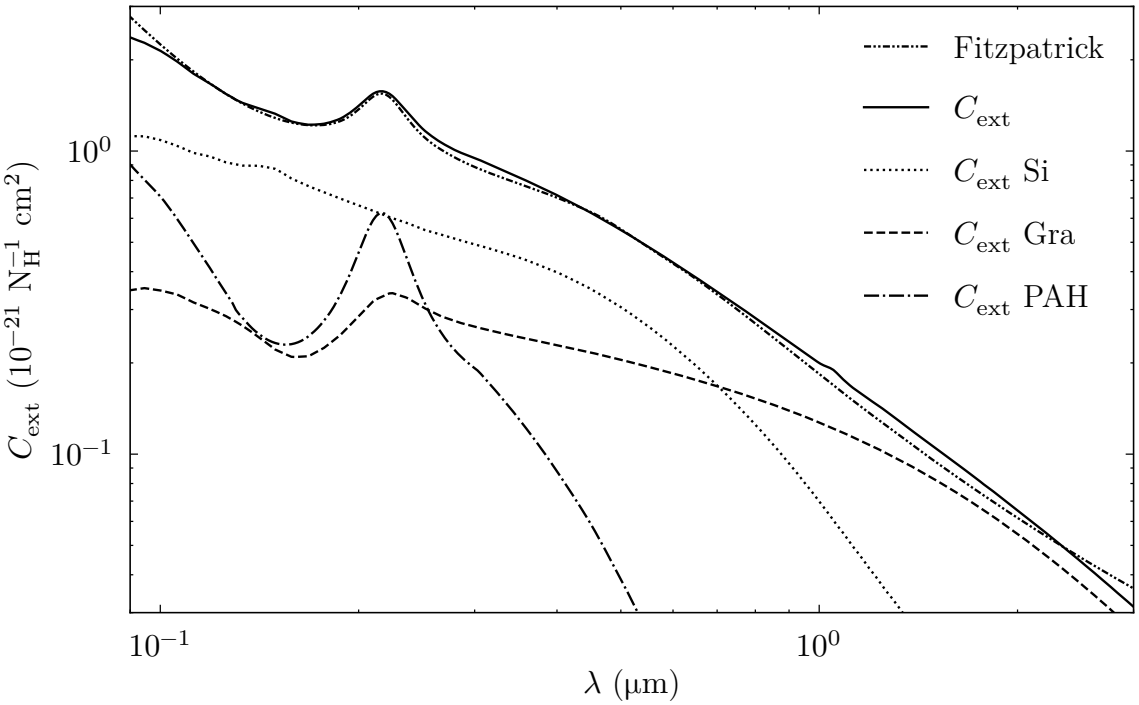

Figure 2.2: The extinction curve for the dust model of Weingartner & Draine (2001); Draine & Li (2007) (solid line) together with the individual contributions to the extinction from the different dust compositions: Si (dotted line), Gra (dashed line), PAH (dashed-three-dotted line). The dashed-dotted line represents the observed mean extinction curve for the Milky Way (Fitzpatrick, 1999).

2.2.2 The Extinction and Attenuation of a Galaxy

The extinction coefficient $\kappa_{\rm ext}(\lambda, R, z)$ is defined in§ 2.2.1 and is used to characterise the amount of photons being absorbed and scattered by dust. In galaxies, a useful quantity that is related to extinction is the dust opacity, which is the product of the extinction coefficient and the length of the column along the line of sight. For a disc galaxy where axi-symmetry is assumed, the face-on dust opacity is simply

$$\tau(\lambda, R, z) = 2\kappa_{\rm ext}(\lambda, R, z)\, z \tag{2.17}$$

where z is the scale height of the dust. In a galaxy, there is not merely a single column of dust in front of a stellar source, but a complex three-dimensional distribution

of emitters (stellar sources) and absorbers (dust grains). This means that stellar photons are not only scattered out of the line of sight, but photons can also come into the line of sight through scattering from other directions. The cumulative effect of all absorptions and scatterings of a distribution of sources and dust grains is called dust attenuation. It is important to distinguish between extinction and attenuation, with extinction being proportional to the column density of dust and its wavelength dependence being decided by the optical properties of the dust grains, whereas attenuation depends on the distribution of dust and stars, the variation of the dust properties throughout the distribution and the galaxy orientation. In a galaxy the total attenuation (of the galaxy as a whole) at a given wavelength (A_λ) is given by,

$$A_\lambda = \frac{L^0_\lambda}{L_\lambda} \tag{2.18}$$

where L^0_λ is the intrinsic luminosity density of the galaxy (as seen in the absence of dust), and L_λ is the apparent luminosity density (the observed luminosity). Usually the attenuation is given in magnitudes, and is then defined as,

$$A_\lambda = -2.5 \log \left(\frac{L_\lambda}{L^0_\lambda} \right) \tag{2.19}$$

2.3 Modelling Dust Emission in Galaxies

2.3.1 Emission Laws of a Black-Body

As discussed in § 2.2.1, dust grains are heated by their interaction with stellar photons and emit as modified black-bodies. To model the dust emission for dust grains of varying sizes and compositions the Planck function can be used to describe the spectral radiance of a black-body at a specific wavelength,

$$B_\lambda(T) = \frac{2hc^2}{\lambda^5} \frac{1}{e^{\frac{hc}{\lambda k_\mathrm{B} T}} - 1} \tag{2.20}$$

where $B_\lambda(T)$ is the spectral intensity as a function of temperature (T), k_B is the Boltzmann constant, h is the Planck constant, and c is the speed of light. The

peak temperature can be found by differentiating the Planck function with respect to λ and finding the stationary point. Wien's displacement law results from this method and states that the predominant wavelength of light emitted from a black-body is inversely proportional to its temperature. This can be used to determine the wavelength of light emitted by the dust grains. On average the dust grains have a temperature $T \sim 18\,\mathrm{K}$, so it is expected that the dust emission peaks at

$$\lambda = \frac{b}{T} \approx \frac{2898\,[\mu\mathrm{m\,K}]}{18\,[\mathrm{K}]} \approx 161\,\mu\mathrm{m} \tag{2.21}$$

;thus the dust grains emit in the FIR.

Planck's law (Equation 2.20) gives the spectral radiance of dust grains, with units $[B_\lambda] = [\mathrm{W\,m^{-2}\,sr^{-1}\,m^{-1}}]$. This can be integrated over the solid angle Ω of the hemisphere on the point of the emitting surface to give the spectral flux density, and integrated over wavelength to give the total flux

$$\begin{aligned} F &= \int_\Omega \mathrm{d}\Omega \int_{\lambda=0}^{\infty} B(\lambda, T)\,\mathrm{d}\lambda \\ &= \int_{\phi=0}^{2\pi} \mathrm{d}\phi \int_{\theta=0}^{\pi/2} \cos\theta \sin\theta\,\mathrm{d}\theta \int_{\lambda=0}^{\infty} B(\lambda, T)\,\mathrm{d}\lambda \\ &= \pi \int_{\lambda=0}^{\infty} B(\lambda, T)\,\mathrm{d}\lambda. \end{aligned} \tag{2.22}$$

To solve this integral, use the following substitutions:

$$x = \frac{hc}{\lambda k_\mathrm{B} T} \implies \lambda = \frac{hc}{x k_\mathrm{B} T} \tag{2.23}$$

$$\mathrm{d}\lambda = -\frac{hc}{k_\mathrm{B} T}\frac{1}{x^2}\,\mathrm{d}x. \tag{2.24}$$

When $\lambda \to 0$, $x \to \infty$ and $\lambda \to \infty$, $x \to 0$, hence Equation 2.22 can be written as:

$$F = 2\pi hc^2 \int_{x=\infty}^{0} \left(\frac{k_\mathrm{B} T x}{hc}\right)^5 \frac{1}{e^x - 1}\left(-\frac{hc}{x^2 k_\mathrm{B} T}\right)\mathrm{d}x, \tag{2.25}$$

simplifying and taking the constants out of the integral gives the Stefan-Boltzmann

equation

$$\begin{aligned} F &= \frac{2\pi k_{\mathrm{B}}^4 T^4}{h^3 c^2} \int_{x=0}^{\infty} \frac{x^3}{e^x - 1} \mathrm{d}x \\ &= \frac{2\pi k_{\mathrm{B}}^4 T^4}{h^3 c^2} \frac{\pi^4}{15} \\ &= \frac{2\pi^5 k_{\mathrm{B}}^4 T^4}{15 h^3 c^2} \\ &= \sigma T^4 \end{aligned} \tag{2.26}$$

where σ is the Stefan-Boltzmann constant and is equal to $\sigma = 5.67{\times}10^{-8}\,\mathrm{W\,m^{-2}\,K^{-4}}$. Equations 2.20, 2.21, and 2.26 are useful in calculating the equilibrium temperature of dust grains and their radiant flux. Given that the dust grains emit as modified black-bodies, a modulating factor Q_{abs} must be introduced into the Planck function. Since the dust emission is dependent on the temperature of the dust grains, it is important to derive the temperature of the dust grains for each size and composition.

2.3.2 Dust Temperature

Dust grains in the ISM are heated by the interstellar radiation fields and they can reach equilibrium temperature with the radiation in which they are embedded. The equilibrium temperature is derived by equating the rate of energy absorbed by the grain with the rate of energy emitted.

$$\int_0^{\infty} Q_{\mathrm{abs}}(\lambda, a) u_\lambda \,\mathrm{d}\lambda = \frac{4\pi}{c} \int_0^{\infty} Q_{\mathrm{abs}}(\lambda, a) \,\mathrm{d}\lambda \, B_\lambda(T_{\mathrm{eq}}) \tag{2.27}$$

where u_λ is the energy density of the radiation field and $B_\lambda(T_{\mathrm{eq}})$ is the Planck function, where T_{eq} is the equilibrium temperature of the grains. This gives the equilibrium temperature for a given grain size and composition. Although some grains are heated at equilibrium temperature, a large majority of grains that are embedded in the low energy density radiation fields present in the interstellar medium never reach equilibrium temperature, but are heated stochastically. This happens when

grains cool faster than the average time interval between the impacts of UV photons, leading to grains experiencing large temperature fluctuations. Such grains are referrred to as stochastically heated grains or flickering grains. The stochasticity of a grain heating depends on the grain size and the energy density of the radiation fields. For a given energy density of the radiation fields, smaller grains emit more stochastically than larger grains. By the same token, if the same grain (of a fixed size) is embedded in a weak radiation field it would emit more stochastically than if it were embedded in a stronger radiation field.

Due to this stochastic heating the temperature of the grains fluctuate so they do not emit at a single temperature, rather they emit according to a temperature distribution $P_i(a, T)$. The temperature at which the grains emit can be found by modifying Equation 2.27 to include an integration over all temperatures of the Planck function with its associated probability:

$$\int_0^\infty Q_{\rm abs}(\lambda, a) u_\lambda \, {\rm d}\lambda = \frac{4\pi}{c} \int_0^\infty Q_{\rm abs}(\lambda, a) \, {\rm d}\lambda \int_0^\infty B_\lambda(T) \, P_i(a, T) \, {\rm d}T \qquad (2.28)$$

Fig. 2.3 gives an example of a probability distribution of temperature for dust grains for various sizes and compositions heated by the interstellar radiation fields in M51 and calculated using the dust model of Draine & Lee (1984) and Draine & Li (2007). One can see from Fig. 2.3 that PAH molecules have much wider temperature distribution compared to that of the graphite grains. This is because in the model of Weingartner & Draine (2001) PAHs are considered to be all the carbonaceous grains with sizes smaller than 0.01 µm, while graphite grains are considered to be all carbonaceous grains with sizes larger than 0.01 µm. As such, in this example PAHs are heated stochastically, while graphites are closer to equilibrium temperature. Fig. 2.3 also shows that silicate grains exhibit both larger and narrower temperature distributions, since they have a continuous distribution of sizes in this model.

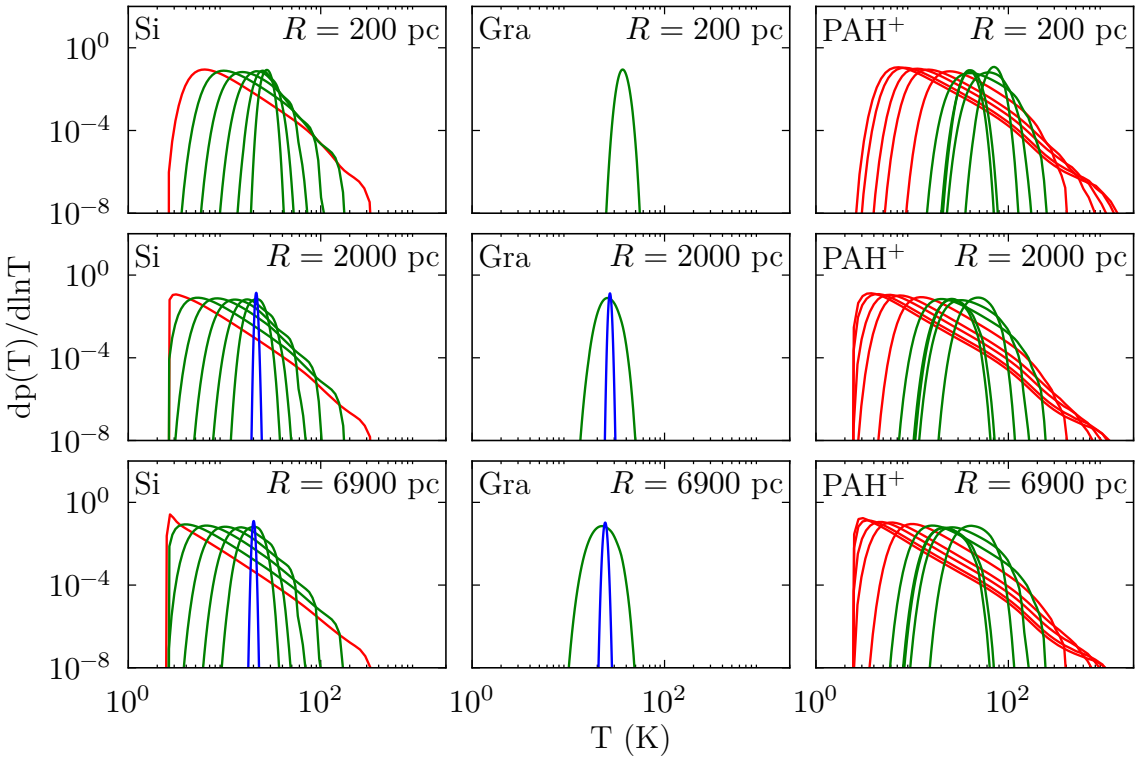

Figure 2.3: Temperature distributions of grains of various sizes and compositions from the model of Draine & Li (2007) heated by the interstellar radiation fields in M51. The panels show from left to right the temperature distributions of silicate, graphite and PAH^+ grains respectively, and from top to bottom the temperature distributions at a galactocentric radius of $R = 200\,\mathrm{pc}$, $R = 2000\,\mathrm{pc}$ and $R = 6900\,\mathrm{pc}$ respectively. The blue lines indicate grains with size $0.1\,\mu\mathrm{m} \geq \mathrm{a} > 0.01\,\mu\mathrm{m}$, the green lines indicate grains with size $0.01\,\mu\mathrm{m} \geq \mathrm{a} > 0.001\,\mu\mathrm{m}$ and the red lines indicate grains with size $a \leq 0.001\,\mu\mathrm{m}$.

2.3.3 Infrared Emissivity

Once the distribution of temperatures for a grain is known, the infrared brightness $I_{\lambda,i}$ of grain of size a and composition i is given by

$$I_{\lambda,i}(a) = Q_{\mathrm{abs},i}(a,\lambda) \int B_\lambda(a,T) P_i(a,T)\,\mathrm{d}T, \tag{2.29}$$

where $I_{\lambda,i}$ is in units of [$\mathrm{W\,m^{-2}\,sr^{-1}\,\AA^{-1}}$]. Once the infrared brightness has been calculated for each grain size and composition, integrating over the grain size distribution $n(a)$ gives the infrared emissivity per H atom of grains of composition i

$$j^{\mathrm{H}}_{\lambda,i} = \int_{a_{\min}}^{a_{\max}} \pi a^2 n(a) I_{\lambda,i}(a)\,\mathrm{d}a \tag{2.30}$$

where $j^{\mathrm{H}}_{\lambda,i}$ has units [$\mathrm{W\,sr^{-1}\,\AA^{-1}\,H^{-1}}$]. The total infrared emissivity per H atom j^{H}_{λ} is then given by the sum of $j^{\mathrm{H}}_{\lambda,i}$ over all the grain compositions,

$$j^{\mathrm{H}}_{\lambda} = \sum_i j^{\mathrm{H}}_{\lambda,i} \tag{2.31}$$

j^{H}_{λ} is given per unit solid angle, so to find the total luminosity of dust per H atom, we must integrate over all directions, which is equivalent to multiplying by a factor of 4π sr. The total luminosity then has units of [$\mathrm{W\,\AA^{-1}\,H^{-1}}$], so to express the total luminosity per unit volume we multiply by the number density of hydrogen n^{H} to obtain

$$L_{\lambda} = 4\pi j^{\mathrm{H}}_{\lambda} n^{\mathrm{H}} \tag{2.32}$$

where L_{λ} has units [$\mathrm{W\,\AA^{-1}\,cm^{-3}}$]. The dust is mixed with the interstellar hydrogen gas, and since the density of hydrogen n^{H} is not usually known, we can use the number density of dust particles n^{dust} to express n^{H}, assuming that the ratio of dust-to-gas is constant ($n^{\mathrm{H}} = n^{\mathrm{dust}} \cdot \mathrm{const}$).

It is more useful to define the distribution of dust in terms of the dust opacity τ,

$$\tau = 2\kappa_{\mathrm{ext}} z \tag{2.33}$$

where κ_{ext} is the extinction coefficient and can be written as

$$\kappa_{\mathrm{ext}} = \rho_{\mathrm{dust}} C^{\mathrm{m}}_{\mathrm{ext}} \tag{2.34}$$

with units of [$\mathrm{cm^{-1}}$] or as

$$\kappa_{\mathrm{ext}} = n^{\mathrm{dust}} C_{\mathrm{ext}} \tag{2.35}$$

From Equation 2.35 and Equation 2.33 we can express $n^{\rm dust}$ as

$$n^{\rm dust} = \frac{\kappa_{\rm ext}}{C_{\rm ext}} = \frac{\tau}{2\,C^{\rm m}_{\rm ext}\,z} \tag{2.36}$$

By substituting Equation 2.36 into Equation 2.32 we obtain

$$L_\lambda = 4\pi \frac{\tau}{2\,C^{\rm m}_{\rm ext}\,z} j^{\rm H}_\lambda \tag{2.37}$$

As discussed in § 2.2.1, with the assumption of axi-symmetry, then the total luminosity per unit volume as a function of radial position R and height z can be expressed as

$$L_\lambda(R,z) = 4\pi \frac{\tau}{2\,C^{\rm m}_{\rm ext}\,z} j^{\rm H}_\lambda(R,z) \times \exp\Big(-\frac{R}{h_{\rm d}} - \frac{|z|}{z_{\rm d}}\Big) \tag{2.38}$$

By integrating over the volume of the galaxy we can then obtain the total luminosity of the galaxy at the wavelength λ, which then can be used to obtain the SED.

2.4 Radiative Transfer

The existence of dust within galaxies makes it necessary to have sophisticated radiation transfer models (Kylafis & Xilouris, 2005) to gain insight into the mechanisms within spiral galaxies. Currently, four methods have been used to model radiative transfer: 'ray-tracing' (RayT), 'Monte Carlo' (MC), 'solution of the radiative transfer equation by discretization', and 'spherical harmonics' (Kylafis & Xilouris, 2005; Steinacker, Baes & Gordon, 2013). The models used in this work adopt the RayT radiative transfer method (Kylafis & Bahcall, 1987), with the addition of an elegant treatment of scattered light, based on the approximation of "scattered intensities" . The RayT code DART-Ray was also used, which explicitly takes into account all higher order scattered light above a threshold intensity (Natale et al., 2014, 2015, 2017). In particular DART-Ray was used to cross-check calculations done using the method of scattered intensities, and to produce the surface-brightness maps for the dust emission and the radiation fields in the dust emission.

Both of the codes used in this work utilise RayT which solves the Radiative Transfer Equation (RTE) along a finite set of paths considering the relevant interactions. The RTE calculates the intensity of radiation along a line of sight, considering the contributions of sources and sinks. Consider some stationary radiation field with specific intensity $I(\boldsymbol{r}, \hat{\boldsymbol{n}}, \lambda)$, where $\boldsymbol{r}$ is the position in space, $\hat{\boldsymbol{n}}$ is a unit vector in the direction of the propagation of radiation, and λ is the wavelength and some source of radiation (e.g. stars) with emission $j_\star(\boldsymbol{r}, \hat{\boldsymbol{n}}, \lambda)$, then the change in intensity along some path is

$$\boldsymbol{n} \cdot \nabla I(\boldsymbol{r}, \hat{\boldsymbol{n}}, \lambda) = j_\star(\boldsymbol{r}, \hat{\boldsymbol{n}}, \lambda). \tag{2.39}$$

In reality, the sources are embedded in a dusty medium that reduces the intensity by absorption and scattering, thus Equation 2.39 becomes:

$$\begin{aligned} \boldsymbol{n} \cdot \nabla I(\boldsymbol{r}, \hat{\boldsymbol{n}}, \lambda) &= j_\star(\boldsymbol{r}, \hat{\boldsymbol{n}}, \lambda) - \left(\kappa_{\text{abs}}(\boldsymbol{n}, \lambda) + \kappa_{\text{sca}}(\boldsymbol{n}, \lambda)\right) I(\boldsymbol{r}, \hat{\boldsymbol{n}}, \lambda) \\ &= j_\star(\boldsymbol{r}, \hat{\boldsymbol{n}}, \lambda) - \kappa_{\text{ext}}(\boldsymbol{n}, \lambda) I(\boldsymbol{r}, \hat{\boldsymbol{n}}, \lambda) \end{aligned} \tag{2.40}$$

where $\kappa_{\text{abs}}(\boldsymbol{n}, \lambda)$ is the absorption coefficient, $\kappa_{\text{sca}}(\boldsymbol{n}, \lambda)$ is the scattering coefficient, and $\kappa_{\text{ext}}(\boldsymbol{n}, \lambda)$ is the extinction coefficient. This is specifically for the direct stellar light. To account for the radiation propagating in in directions other than along the line of sight $\hat{\boldsymbol{n}}$, that is subsequently scattered into the line of sight $\hat{\boldsymbol{n}}$, a scattering source term is added:

$$\boldsymbol{n} \cdot \nabla I(\boldsymbol{r}, \hat{\boldsymbol{n}}, \lambda) = -\kappa_{\text{ext}}(\boldsymbol{n}, \lambda) I(\boldsymbol{r}, \hat{\boldsymbol{n}}, \lambda) + j_\star(\boldsymbol{r}, \hat{\boldsymbol{n}}, \lambda) + j_{\text{sca}}(\boldsymbol{r}, \hat{\boldsymbol{n}}, \lambda) \tag{2.41}$$

If the scattering is coherent, that is, the scattering event is elastic, then the scattering source term can be written as (Kylafis & Bahcall, 1987):

$$j_{\text{sca}}(\boldsymbol{r}, \hat{\boldsymbol{n}}, \lambda) = \kappa_{\text{sca}}(\boldsymbol{n}, \lambda) \int I(\boldsymbol{r}, \hat{\boldsymbol{n}}, \lambda) \Phi(\hat{\boldsymbol{n}}', \hat{\boldsymbol{n}}, \lambda) \frac{\mathrm{d}\Omega}{4\pi} \tag{2.42}$$

where $\Phi(\hat{\boldsymbol{n}}', \hat{\boldsymbol{n}}, \lambda)$ is the scattering phase function. In this work, the Henyey-Greenstein scattering phase function (Equation 2.14) is used. Thus, substituting

Equation 2.42 into Equation 2.41 gives:

$$\begin{aligned}\boldsymbol{n}\cdot\nabla I(\boldsymbol{r},\hat{\boldsymbol{n}},\lambda) =& -\kappa_{\rm ext}(\boldsymbol{n},\lambda)I(\boldsymbol{r},\hat{\boldsymbol{n}},\lambda) + j_\star(\boldsymbol{r},\hat{\boldsymbol{n}},\lambda)\\ &+\kappa_{\rm sca}(\boldsymbol{n},\lambda)\frac{1}{4\pi}\int I(\boldsymbol{r},\hat{\boldsymbol{n}},\lambda)\Phi(\hat{\boldsymbol{n}}',\hat{\boldsymbol{n}},\lambda){\rm d}\Omega. \end{aligned} \tag{2.43}$$

Using the albedo, $\omega(\boldsymbol{n},\lambda)\equiv\kappa_{\rm sca}(\boldsymbol{n},\lambda)/\kappa_{\rm ext}(\boldsymbol{n},\lambda)$, Equation 2.43 can be written as:

$$\begin{aligned}\boldsymbol{n}\cdot\nabla I(\boldsymbol{r},\hat{\boldsymbol{n}},\lambda) =& -\kappa_{\rm ext}(\boldsymbol{n},\lambda)\left[I(\boldsymbol{r},\hat{\boldsymbol{n}},\lambda) - \frac{\omega(\boldsymbol{n},\lambda)}{4\pi}\int I(\boldsymbol{r},\hat{\boldsymbol{n}},\lambda)\Phi(\hat{\boldsymbol{n}}',\hat{\boldsymbol{n}},\lambda){\rm d}\Omega\right]\\ &+ j_\star(\boldsymbol{r},\hat{\boldsymbol{n}},\lambda). \end{aligned} \tag{2.44}$$

Alternatively, one can define a distance s along the path defined the propagation along direction $\boldsymbol{n}$ at a position $\boldsymbol{r}$, i.e., $\boldsymbol{n}\cdot\nabla = {\rm d}/{\rm d}s$, then Equation 2.44 can be simplified:

$$\frac{{\rm d}I}{{\rm d}s}(s,\lambda) = j_\star(s,\lambda) - \kappa_{\rm ext}(s,\lambda)\left[I(s,\lambda) - \frac{\omega(s,\lambda)}{4\pi}\int I(s,\hat{\boldsymbol{n}}',\lambda)\Phi(\hat{\boldsymbol{n}}',\hat{\boldsymbol{n}},\lambda)\,{\rm d}\Omega\right] \tag{2.45}$$

Letting I_0 be the direct stellar emission, I_1 be the once scattered light, and I_n be the $n^{\rm th}$ scattered light, then total intensity is simply the sum of these contributions.

$$I(s) = \sum_{n=0}^{\infty} I_n(s). \tag{2.46}$$

I_0 and I_n can be written as

$$\frac{{\rm d}I_0}{{\rm d}s}(s) = -\kappa(s)I_0(s) + j_\star(s), \tag{2.47}$$

$$\frac{{\rm d}I_n}{{\rm d}s}(s) = -\kappa(s)\left[I_n(s) - \frac{\omega}{4\pi}\int I_{n-1}(s,\hat{\boldsymbol{n}}')\Phi(\hat{\boldsymbol{n}}',\hat{\boldsymbol{n}}){\rm d}\Omega'\right] \tag{2.48}$$

which have the solutions

$$I_0(s) = \int_0^s {\rm d}s' j_\star(s') e^{-\int_{s'}^s \kappa(s''){\rm d}s''} \tag{2.49}$$

$$I_n(s) = \omega\int_0^s {\rm d}s' e^{-\int_{s'}^s \kappa(s''){\rm d}s''} \times \frac{\kappa(s')}{4\pi}\int I_{n-1}(s',\hat{\boldsymbol{n}}')\Phi(\hat{\boldsymbol{n}}',\hat{\boldsymbol{n}}){\rm d}\Omega'. \tag{2.50}$$

Because of the computational impossibility of computing Equation 2.50 for all $n \in \mathbb{Z}$, a sufficient number of scattering events must be calculated such that

$$\frac{|I_{n+1}|}{\sum_{k=0}^{n}|I_k|} < \epsilon \tag{2.51}$$

which can be computationally expensive. In this work, an approximation from Kylafis & Bahcall (1987) is used. Equation 2.46 can be written as

$$I = I_0 \left(1 + \frac{I_1}{I_0} + \frac{I_2}{I_1}\frac{I_1}{I_0} + \cdots\right). \tag{2.52}$$

Making the approximation

$$\frac{I_{n+1}}{I_n} \approx \frac{I_1}{I_0}, \tag{2.53}$$

Equation 2.53 can be substituted into Equation 2.52 to give

$$I \approx I_0 \left(1 + \frac{I_1}{I_0} + \left[\frac{I_1}{I_0}\right]^2 + \cdots\right). \tag{2.54}$$

This approximation requires evaluation of only I_0 and I_1 to compute the total intensity, dramatically decreasing computation time.

Chapter 3

The Axisymmetric Model

The models in this work follow the axisymmetric RT models of PT11 which describe the dust opacity and stellar emissivity for spiral galaxies from the UV to submm wavelengths using parameterised analytic functions. The model considers the absorption and anisotropic scattering of stellar photons with dust grains of various size and chemical composition as discussed in § 2. Following TP20, the model of PT11 is adapted to allow for additional morphological components. Each morphological component comprises the generic stellar and dust components from PT11: the stellar disc, the thin stellar disc, the dust disc and thin dust disc. These are described in detail in § 3.1 and 3.2. The stellar volume emissivity and the dust density distribution for each disc component j are described by the following generic formula:

$$w_j(R,z) = \begin{cases} 0, & R < R_{\mathrm{tin},j} \\ A_{0,j}\left[\frac{R}{R_{\mathrm{in},j}}\left(1-\chi_j\right)+\chi_j\right]\exp\left(-\frac{R_{\mathrm{in},j}}{h_j}-\frac{z}{z_j}\right), & R_{\mathrm{tin},j} \le R < R_{\mathrm{in},j} \\ A_{0,j}\exp\left(-\frac{R}{h_j}\right)\exp\left(-\frac{z}{z_j}\right), & R_{\mathrm{in},j} \le R \le R_{\mathrm{t},j} \end{cases} \tag{3.1}$$

with:

$$\chi_j = \frac{w_j(0,z)}{w_j(R_{\mathrm{in},j},z)} \tag{3.2}$$

where R and z are the radial and vertical coordinates, h_j and z_j are the scale-length and scale-height respectively, $A_{0,j}$ is a constant scaling the amplitude, χ_j describes a linear slope of the radial distributions from the inner radius, R_{in}, to the centre of the galaxy. R_{tin} and R_{t} are the inner and outer truncation radii, respectively.

Equations 3.1 and 3.2 are wavelength dependent and describe the distribution of stars and dust. The spatial integration of these formulae (see Appendix C) between R_{tin} and R_{t} provides the intrinsic stellar luminosity L_ν if j represents a stellar disc component, or the dust mass M_{d} if j represents a dust disc component.

3.1 Stellar Components

3.1.1 The Stellar Disc

The stellar disc is made up of the old stellar populations and primarily emits in the optical and NIR wavelengths. As the stellar disc comprises the longer-lived, lower-mass stars they manage to migrate further from the plane of the galaxy over the course of their lives and thus this component typically has larger scale-heights. It is described by the four geometrical parameters: $h_{\mathrm{s}}^{\mathrm{disc}}$, $z_{\mathrm{s}}^{\mathrm{disc}}$, $R_{\mathrm{in,s}}^{\mathrm{disc}}$ and $\chi_{\mathrm{s}}^{\mathrm{disc}}$, and one amplitude parameter: $L^{\mathrm{disc}}(\lambda)$. $L^{\mathrm{disc}}(\lambda)$ is allowed to be a free parameter for each wavelength corresponding to U, B, V, I, J, K, $I1$, $I2$, $I3$. h_{s} is also allowed to be wavelength dependent, hence the scale-lengths in the U, B, V, I, J, K, $I1$, $I2$, $I3$ bands are treated as free parameters. If the galaxy being modelled is edge-on the vertical distribution can be fit, thus z_{s} is allowed to be wavelength dependent and fit the scale-lengths for the previously mentioned optical and NIR bands.

3.1.2 The Bulge

Among the stellar disc, the old stellar population also features a bulge component. The ellipsoidal bulge is described by the Sérsic distribution (Sérsic, 1963; Sersic, 1968). Since there is no exact analytic solution for the deprojection of this distribution, several approximations have been proposed in the literature. In these calculations the volume emissivity as derived in Natale et al. (2022) is used:

$$w_{\rm bulge}(\lambda, R, z) = w(\lambda, 0, 0)\sqrt{\frac{b_{\rm s}}{2\pi}}\frac{(a/b)}{R_{\rm e}}\eta^{(1/2n_{\rm s})-1}\exp\left(-b_{\rm s}\,\eta^{1/n_{\rm s}}\right) \tag{3.3}$$

with:

$$\eta(\lambda, R, z) = \frac{\sqrt{R^2 + z^2(a/b)^2}}{R_{\rm e}} \tag{3.4}$$

where $\eta^{\rm bulge}(\lambda, 0, 0)$ is the stellar emissivity at the centre of the bulge, $R_{\rm e}$ is the effective radius of the bulge, a and b are the semi-major and semi-minor axes of the bulge, respectively, and $b_{\rm s}$ is a constant which depends on the value of the Sérsic index $n_{\rm s}$, given by the approximation (Ciotti & Bertin, 1999):

$$b_{\rm s} \approx 2n_{\rm s} - \frac{1}{3} + \frac{4}{405n_{\rm s}} - \frac{46}{25515n_{\rm s}^2}. \tag{3.5}$$

In principle $R_{\rm e}$ and $\frac{a}{b}$ are allowed to be wavelength dependent, however typically they do not vary significantly for a given galaxy.

3.1.3 The Thin Stellar Disc

The thin stellar disc hosts the young stellar population. Primarily emitting in the UV regime, the young stellar disc contributes the majority of the UV output of the galaxy. In the model of PT11 the thin stellar disc has a smaller scale-height than that of the stellar disc, since, from physical considerations, the young stars are expected to still be associated with the molecular layer from where the stars form. Unlike older stars, the shorter-lived young stars did not have time to evolve and form a thicker configuration. Thicker discs are usually due to the multiple interactions of stars

with spiral density waves or molecular clouds during their lifetime. Thus, the young stars are expected to reside in a thin disc configuration, as adopted in this work. The thin stellar disc is described by the four geometrical parameters: $h_{\rm s}^{\rm tdisc}$, $z_{\rm s}^{\rm tdisc}$, $R_{\rm in,s}^{\rm tdisc}$ and $\chi_{\rm s}^{\rm tdisc}$, and one amplitude parameter: $L^{\rm tdisc}(\lambda)$. The spectral integrated luminosity $L^{\rm tdisc}$ is related to the star-formation rate $\mathrm{SFR}^{\rm tdisc}$ using Equations 16, 17, 18 from PT11. Following previous modelling, the use of SFR as the amplitude parameter is preferred. Nonetheless, there is a difference between PT11 and in this approach. The model of PT11 includes a fixed template SED (fixed wavelength dependence), because its purpose was to create a large library of model SEDs to fit galaxies from statistical samples, and thus it had to limit the number of free parameters. In addition, the model was first established for edge-on galaxies, where the UV emission is almost entirely obscured by the dust, with no possibility to constrain the shape of the UV SED from observations. However, for non edge-on galaxies with inclinations up to 80° the UV emission is not completely obscured by dust and there are meaningful data available. Because of this the approach is to derive the shape of the SED and thus to adopt as free parameters the wavelength dependent amplitude parameters $L^{\rm tdisc}(\lambda)$.

3.2 Dust Components

3.2.1 The Dust Disc

The dust disc describes the large scale diffuse distribution of dust associated with the stellar population in the stellar disc and the H I gas. The dust disc is usually more radially extended than the old stellar disc (Xilouris et al., 1999), while having a scale-height $z_{\rm d}^{\rm disc}$ larger than that of the young stellar disc $z_{\rm s}^{\rm tdisc}$, and smaller than the scale-height of the old stellar disc $z_{\rm s}^{\rm disc}$. The dust disc is described by the geometrical parameters $h_{\rm d}^{\rm disc}$, $z_{\rm d}^{\rm disc}$, $R_{\rm in,d}^{\rm disc}$ and $\chi_{\rm d}^{\rm disc}$ and the amplitude parameter, the

face-on optical depth of the B-band at the inner radius $\tau_{\rm B}^{\rm f,disc}\left(R_{\rm in,d}^{\rm disc}\right)$.

3.2.2 The Thin Dust Disc

The thin dust disc represents the diffuse dust distribution associated with the young stellar population and the molecular layer. The thin dust disc is described by the geometrical parameters $h_{\rm d}^{\rm tdisc}$, $z_{\rm d}^{\rm tdisc}$, $R_{\rm in,d}^{\rm tdisc}$ and $\chi_{\rm d}^{\rm tdisc}$ and the amplitude parameter, the face-on optical depth of the B-band at the inner radius $\tau_{\rm B}^{\rm f,tdisc}\left(R_{\rm in,d}^{\rm tdisc}\right)$. In principle these are all free parameters, however, following PT11 the scale-height and the scale-length of the thin dust disc are fixed to that of the young stellar disc. This is because a physical correspondence is expected between the distribution of young stars and the dust associated with the molecular layer from where the stars form.

3.2.3 The Active Clumpy Component

The active clumpy component represents the small dense localised dust clouds associated with star forming regions that are illuminated by the strong, UV-dominated radiation fields produced by the photons emitted from the young stars inside the clouds. The dust in these regions reaches thermal equilibrium with the intense radiation fields and emits dominantly in the 24 µm to 70 µm region, and can surpass the emission due to the diffuse component at these wavelengths. PT11 define a "clumpiness factor" F, which is the amplitude parameter of the active clumpy component, and represents the fraction of the total luminosity of massive stars that is locally absorbed by the dust in these star-forming clouds. The diffuse component is then illuminated by the escape fraction $1-F$. The F factor has a wavelength dependence that is not determined by the optical properties of the dust grains, but by the evolutionary stage of the birth clouds. This is because in this model the dust cloud is very opaque, thus completely blocking any radiation from inside the cloud. The only way

photons escape is through holes in the cloud, produced by the fragmentation in the cloud. Thus the radiation is either completely blocked by the opaque dust or freely escapes without being absorbed. As a star-forming cloud becomes older, it tends to become increasingly fragmented, while stars inside the cloud start to migrate and disperse away from the cloud. This will produce an increased escape of radiation from the cloud. The wavelength dependence of the escaping radiation thus arises because lower mass and less blue stars spend a higher proportion of their lifetime radiating when they are further away from their birth-clouds, and because of the progressive fragmentation of the clouds.

3.2.4 The Quiescent Clumpy Component

The quiescent clumpy component represents the cirrus-like clouds that are optically thin to optical photons but are optically thick in the UV. Due to being optically thin in the optical and NIR regime historically these clumps have not been included in the RT models, as they were thought to negligibly affect the transfer of radiation. However, being optically thick in the UV means that dust, particularly in the core, is shielded from UV radiation. Allocating some of the total dust mass into these clumps can lead to a significant reduction in dust heating when compared to a purely diffuse dust configuration. This component is described in detail in § 4.

3.3 Fitting Procedures

3.3.1 Face-On Fitting Procedure

To directly compare the model to the data, azimuthally averaged surface brightness profiles of both are produced. The observed surface brightness profiles were obtained by segmenting the data images into a series of annuli each corresponding to a fixed galactocentric radius and plotting the average flux through the annulus as a function

of radius. A similar procedure was performed to produce the surface brightness profiles of the model. Examples of these profiles can be seen in Fig. G.1. To fully capture the details seen in the surface brightness profiles the galaxies were segmented into distinct morphological components where necessary, following TP20. A detailed description of these components can be found in § 3.

The fitting procedure described in TP20 was followed in this work. This method involves an intelligent searching algorithm of the parameter space, taking into account the fact that different parameters do not equally affect the emission at all wavelengths. This allows one to identify pairs of parameters that predominantly shape the emission at key wavelengths and use this to fit one pair (usually made of a geometric parameter and an amplitude parameter) of parameters at a time.

Modelling begins by identifying the morphological components seen in the observed surface brightness profiles. These are demarcated by breaks in the exponential profile, constraining the parameters: $R_{\rm tin}$, $R_{\rm in}$, and $R_{\rm t}$ for each morphological component identified. While these parameters are fitted at the start of modelling, they may undergo some minor optimisations as the model develops. The entire wavelength range of the data set is considered when determining the morphological components.

With the morphological components set, the first RT calculations are performed with some initial 'guess' parameters. First, the NUV profile is optimised. This is equivalent to constraining the spatial distribution of the young stellar population residing in the thin stellar disc. Although the thin stellar disc is highly attenuated in the UV, an estimate can be derived for the corresponding geometrical and amplitude parameters for an initial guess of dust opacity. In this step the scale length $h_{\rm s}^{\rm tdisc}$ and luminosity density $L^{\rm tdisc}$ are derived in the NUV filter. If the disc has $R_{\rm in} > 0$, $\chi_{\rm s}^{\rm disc}$ is also fitted at this stage (see Equations 3.1–3.2 for details). It is important to note that for a galaxy with multiple morphological disc components, the optimisation procedure is identical for each, as the discs are similarly parameterised.

Once a good fit has been achieved in the NUV (for the trial dust opacity), an attempt to fit the dust distribution is made. This is done by re-running the RT calculation using the present parameters used to fit the NUV profile, and calculating the dust emission at all IR wavelengths. The spatial distribution of dust is then constrained by fitting the 500 μm profiles, since at this wavelength the dust emission primarily traces dust column density rather than heating sources. This results in a fit for the scale length of the dust disc $h_{\rm d}^{\rm disc}$ and the dust opacity (plus the parameter $\chi_{\rm d}^{\rm disc}$). Altering the parameters of the dust disc necessarily affects the fits in the NUV. Therefore, a few iterations are required between the NUV and 500 μm profiles, until a good fit is achieved simultaneously. During these more detailed iterations, the luminosity of the FUV is also adjusted to best fit the FUV profiles.

Once the parameters related to the thin stellar disc and dust disc are constrained, the RT is recalculated to derive the distribution of the stellar disc and bulge by fitting the optical and NIR profiles for the available data. Since in a face-on galaxy the optical and NIR emission is reasonably optically thin to the dust, the final fits at these wavelengths do not significantly impact the solution for the dust disc and thin stellar disc obtained in previous iterations. Finally, an active clumpy component is fitted to account for any dearth in emission at 24- and 70- μm.

Overall, a solution for whole spectral range is arrived at with only a small number of iterations. Notably, the 70- to 350- μm emission is not directly used in the fit, but is instead predicted. To conclude, the fit mainly consists in fitting only a pair of parameters (a scale length and an amplitude) at any given time, for each morphological component at a given wavelength. The goodness of fit was evaluated using the residuals D between the surface brightness profiles of the observed data and the model, as well as a reduced chi-squared $\mathrm{chi}_{\rm r}^2$ statistic[1], which becomes more relevant when finalising the model solution. The $\mathrm{chi}_{\rm r}^2$ is calculated for each wavelength by

[1]The notation chi^2 is used rather than χ^2, as the latter notation is reserved in this work for the geometrical parameter.

the following formulae:

$$\mathrm{chi}^2_{\lambda} = \sum_{n=1}^{N} \frac{(M_n - O_n)^2}{\epsilon^2_{\mathrm{SB},n}} \tag{3.6}$$

$$\mathrm{chi}^2_{\mathrm{r},\lambda} = \frac{\mathrm{chi}^2_{\lambda}}{N - m} \approx \frac{\mathrm{chi}^2_{\lambda}}{N} \tag{3.7}$$

where N is the total number of annuli n, m is the number of free parameters at wavelength λ, O_n is the azimuthally averaged flux through annuli n, M_n is the model flux through annuli n, and $\epsilon^2_{\mathrm{SB},n}$ is the total error of the azimuthally averaged surface brightness profile corresponding to annuli n. For each wavelength N is determined by:

$$N = \frac{R}{2 \times r} \tag{3.8}$$

where R is the radius of the galaxy, and r is the physical pixel scale of the data. The coefficient of 2 was determined to balance the level of detail resolved while minimising oversampling. While this was adequate for the majority of the data, for some data sets this coefficient was altered to avoid artefacts due to oversampling. Generally $N \gg m$, hence m is neglected in Equation 3.7. The residuals D are calculated as:

$$D = \frac{M_n - O_n}{O_n} \tag{3.9}$$

3.3.2 Edge-On Fitting Procedure

The fitting procedure from Natale et al. (2022), which was used to fit the Milky Way, is adopted in this work. This is similar to the procedure used to fit face-on galaxies (TP20; Rushton et al., 2022; Inman et al., 2023; Pricopi et al., 2025), as described in § 3.3.1, but has a few differences. Firstly, for edge-on galaxies the vertical profiles can be used to derive the scale-heights of stars and dust, which is not possible for face-on galaxies. In addition, because large optical depth due to

the edge-on orientation, the UV emission from the thin UV emitting stellar disc is completely obscured by dust, and, as in the Milky Way, the UV emission is derived to best fit the FIR emission, in particular at the peak of the dust emission SED (Natale et al., 2022). The lack of direct constraints in the UV and the use of FIR data is well documented in the previous modelling of NGC 891 in PT11.

For edge-on galaxies horizontal and vertical surface brightness profiles are produced using aperture photometry. The vertical profiles are calculated by averaging the flux within the rectangular region $|R| \leq R_{\rm gal}$ and $z_i < |z| \leq z_{i+1}$, where $|R|$ is the absolute horizontal distance from the centre of the galaxy, $R_{\rm gal}$ is the radius of the galaxy, $|z|$ is the absolute height above or below the plane of the disc, z_i and z_{i+1} are the lower and upper bounds respectively of the strip probing a given z. This is repeated by incrementing z and plotting these averaged surface brightnesses as a function of vertical distance z. The horizontal profiles are produced similarly, with $|z| \leq z_{\rm gal}$ and $R_i < |R| \leq R_{i+1}$. The average flux through these slits is then plotted against horizontal or vertical distance from the centre, depending on the orientation of the strips.

In the horizontal profiles, at all horizontal distances from the centre, the vertical extent of the disc/bulge reasonably fills the region $|z| \leq z_{\rm gal}$ without exception. However, this is not always true in the vertical profiles. For example, in NGC 891, the bulge has an effective radius of $R_{\rm e} = 1.44\,$kpc while the truncation radius of the disc is $R_{\rm t} = 14\,$kpc. So, the surface brightness of the bulge would be significantly underestimated if averaged over the radius of the galaxy. For this reason, multiple vertical plots were made, probing different regions of the disc. It was found that two regions of interest were necessary for fitting; the bulge region, and the disc region. For example, for NGC 891, these regions lie between $|R| \leq 2\,$kpc (probing the bulge), and $2\,$kpc $\leq |{\rm R}| \leq 5\,$kpc (probing the disc). Thus one horizontal and two vertical profiles are produced at each wavelength where data are available.

Modelling begins by identifying the morphological components seen in the horizontal observed surface brightness profiles. These are demarcated by breaks in the exponential profile, constraining the parameters: $R_{\rm tin}$, $R_{\rm in}$, and $R_{\rm t}$ for each morphological component identified.

The young stellar distribution cannot be constrained directly as the UV data are obscured by dust, so the optical and NIR data are fit first to constrain the stellar distribution of the disc and bulge. This is done with some 'guess' parameters for the dust distribution. For each wavelength where data are available, the model is optimised simultaneously using the horizontal, bulge-vertical profiles, and disc-vertical profiles. The parameters derived in this step are the effective radius of the bulge $R_{\rm e}$, Sérsic index $n_{\rm s}$, bulge ellipticity $\frac{b}{a}$, and the scale length and scale height of the stellar disc $h_{\rm s}$ and $z_{\rm s}$ respectively.

Once a fit for the bulge and stellar disc is made, another RT calculation is done to produce the dust emission. As for face-on galaxies, the 500 µm data are used as a proxy for the cold dust distribution. Fitting the 500 µm constrains the dust opacity and the dust scale length $h_{\rm d}$. In principle, the scale height of the dust $z_{\rm d}$ could also be constrained at this step, however the spatial resolution of the SPIRE 500 instrument is insufficient to resolve the detailed vertical distribution of the dust as it it dominated by the instrument's PSF (Bianchi & Xilouris, 2011).

Once a satisfactory fit has been simultaneously achieved for both the stellar and dust discs, the 160 µm data can be used to provide insight into the thin stellar and dust discs. Since the dust emission SED typically peaks near 160 µm, the luminosity of the thin stellar disc is adjusted to match the peak of the dust emission. While these data can also offer some insight into the distribution of young stars, such information is limited due to the relatively low spatial resolution of the PACS 160 µm observations, which, like the submm data, cannot resolve the vertical structure of the disc. In this step the scale length $h_{\rm s}^{\rm tdisc}$ and luminosity $L^{\rm tdisc}$ of the thin stellar

disc are constrained.

Because of the high dust column density, even minor adjustments to the dust distribution can have a substantial impact on the fits to the optical and NIR data. It is an iterative process between fitting the optical and NIR data, and the submm data until a solution is converged upon.

Visual comparison between the surface brightness maps of the data and the model were also used as fitting metric. These comparisons are valuable as a verification tool to ensure that each component of the galaxy is being correctly modelled. Otherwise, for example, an under-estimation of the bulge might be compensated by an over-estimation in the disc. These images allow identification of such an error. Examples of these images can be seen in Fig. 5.7.

The goodness-of-fit is quantified in a similar way to the face-on galaxies, described in § 3.3.1, with the difference being that three $\mathrm{chi}^2_\mathrm{r}$ statistics are being optimised per wavelength. In addition to the residuals of the surface brightness profiles, the residuals between the surface brightness maps are also considered. These residuals are calculated in the same way as for the profiles, and examples can be seen in the right-most panels of Fig. 5.7.

Chapter 4

The Pseudo-Grain Concept

The diffuse dust, pervading the interstellar medium of star forming galaxies, is a fundamental component of any dusty radiative transfer model, including the one used in this work (PT11). A significant fraction of "diffuse dust" is distributed in cirrus-like clouds; however, since these structures are optically thin in the optical range of the electromagnetic spectrum, they yield radiative transfer solutions equivalent to those of a purely diffuse medium. Thus, for all practical purposes, optically thin clumps have not been explicitly incorporated into RT models until now. However, while this assumption holds very well in the optical bands, it will progressively break at shorter UV wavelengths, in particular within the clump cores on scales of approximately one parsec or smaller, where clouds become optically thick. As a result, a fraction of the dust is more effectively shielded from UV radiation than would be expected in a purely diffuse medium.

Sampling galactic discs on tens-of-kiloparsec scales with parsec-scale resolution exceeds the computational capabilities of existing radiative transfer codes. To address this limitation, a novel subgrid approach is introduced, based on the concept of

pseudo-grains. In this approach, a macroscopic, parsec sized dust cloud can be analysed in terms of its attenuation properties of the interstellar radiation fields, as well as of its dust emission properties (dust emission SED) in the same way a dust particle can be characterised by its optical properties when interacting with a planar wave. By performing dedicated radiative transfer calculations of a single dust cloud illuminated externally by stellar radiation fields, one can determine the amount of absorption and scattering produced by the clump, and thus define an efficiency for absorption and scattering of the cloud, $Q_{\rm abs}$ and $Q_{\rm sca}$. Based on these efficiencies, the corresponding absorption and scattering cross-sections, $C_{\rm abs}$ and $C_{\rm sca}$, can also be calculated. Furthermore, for given incident radiation fields, the temperature of the dust within the cloud can be calculated using the radiative transfer codes, and a dust emission SED derived, analogous to the infrared emissivity of an individual dust grain. Because of all these similarities in methodology, the cloud can be replaced in the model with a virtual particle of dust—referred to as a pseudo-grain—that carries the same photon interaction efficiencies and corresponding emissivities defined by the above macroscopic calculation. As such, the resulting effect is as if the dust model would have a new component of dust, supplementing the existing species present in the dust model such as silicates, graphites and PAHs.

4.1 Pseudo-Grain Parametrisation

As introduced above, each pseudo-grain is a single macroscopic dust cloud (associated with a gas cloud). The volume density (by mass) of dust in the cloud can be defined by a spherically symmetric King profile (Lane, 1870; Emden, 1907; King, 1962) with

$$\rho^{\rm c,s}(r) = \begin{cases} \frac{\rho_0^{\rm c,s}}{[1+(r/r_{\rm c})^2]^{3/2}} & r < r_{\rm t} \\ 0 & \text{otherwise,} \end{cases} \tag{4.1}$$

where the abbreviation "c,s" stands for a "single cloud", $\rho_0^{\mathrm{c,s}}$ is the volume density of dust in the cloud at $r = 0$, and r_c is a scale factor (core radius) given by

$$r_\mathrm{c} = \sqrt{\frac{k_\mathrm{B} T}{4\pi G \rho_{\mathrm{gas},0}\, \mu\, m_\mathrm{H}}}\,, \tag{4.2}$$

where $\rho_{\mathrm{gas},0}$ is the volume density by mass of gas at the cloud centre, T is the gas temperature at the centre, k_B is the Boltzmann constant, G is the gravitational constant, m_H is the mass of the hydrogen atom, and μ is the mean mass per gas particle in units of m_H.

For $r \lesssim r_\mathrm{c}$, Equation 4.1 is a good representation of an isothermal pressure-supported gas cloud. It should be noted that this is valid only if μ is not a function of r; that is, that the gas does not undergo a phase transition from H I to H_2. Moreover, $r_\mathrm{t}/r_\mathrm{c}$ is required to be a reasonably small multiple. These assumptions are reasonably satisfied in diffuse H I-dominated clouds observed in the solar neighbourhood with central H densities of a few hundred cm^{-3} or less and T on the order of 50–100 K. In such clouds, the H I emission is also observed to be tightly linked to the dust column, justifying the further implicit assumption that both dust and gas distributions follow Equation 4.1.

For a typical diffuse H I cloud, Equation 4.2 yields:

$$\frac{r_\mathrm{c}}{\mathrm{pc}} = 2.22 \left(\frac{T}{100\,\mathrm{K}}\right)^{\frac{1}{2}} \left(\frac{n_{\mathrm{H},0}}{100\,\mathrm{cm}^{-3}}\right)^{-\frac{1}{2}}, \tag{4.3}$$

where $n_{\mathrm{H},0}$ is the neutral hydrogen density at the cloud centre.

If κ_ν^tot is the total mass extinction coefficient of the microscopic grains, in units of area per mass, due to scattering and absorption from all sizes and composition of grains, then the opacity τ_ν along any ray $\underline{l}$ is defined by

$$\frac{\mathrm{d}\tau_\nu^{\mathrm{c,s}}}{\mathrm{d}l}(r) = \kappa_\nu^\mathrm{tot} \rho^{\mathrm{c,s}}(r), \tag{4.4}$$

with $\rho^{\mathrm{c,s}}(r)$ given by Equation 4.1. Then, the parameter $\tau_\nu^{\mathrm{c,s}}$ is the total opacity at

frequency ν along a line-of-sight through the cloud centre:

$$\begin{aligned}\tau_\nu^{\rm c,s} &= 2\kappa_\nu^{\rm tot}\int_0^{r_{\rm t}}\rho^{\rm c,s}(r){\rm d}r \\ &= 2\kappa_\nu^{\rm tot}\rho_0^{\rm c,s}\int_0^{r_{\rm t}}\frac{{\rm d}r}{\left(1+(r/r_{\rm c})^2\right)^{3/2}} \\ &= 2\kappa_\nu^{\rm tot}\rho_0^{\rm c,s}r_{\rm c}\,I_1, \text{ with} \\ I_1 &= \int_0^{r_{\rm t}/r_{\rm c}}\frac{dx}{(1+x^2)^{3/2}}.\end{aligned} \tag{4.5}$$

Solving for I_1, gives:

$$\tau_\nu^{\rm c,s} = 2\kappa_\nu^{\rm tot}\rho_0^{\rm c,s}r_{\rm c}\xi \tag{4.6}$$

with

$$\xi = \sin\left(\arctan(r_{\rm t}/r_{\rm c})\right) = \frac{x}{\sqrt{x^2+1}}.$$

It is also useful to derive the total mass of dust in each cloud, i.e. each pseudo-grain, as this will be later needed to derive the volume number density of pseudo-grains in the galaxies being modelled:

$$\begin{aligned}M^{\rm c,s} &= \int_0^{r_{\rm t}}\rho^{\rm c,s}(r)\cdot 4\pi r^2{\rm d}r \\ &= 4\pi\rho_0^{\rm c,s}\int_0^{r_{\rm t}}\frac{r^2{\rm d}r}{\left(1+(r/r_{\rm c})^2\right)^{3/2}} \\ &= 4\pi\rho_0^{\rm c,s}r_{\rm c}^3\cdot I_2, \text{ with} \\ I_2 &= \int_0^{r_{\rm t}/r_{\rm c}}\frac{x^2dx}{(1+x^2)^{3/2}}.\end{aligned} \tag{4.7}$$

Solving for I_2, gives:

$$M^{\rm c,s} = 4\pi\rho_0^{\rm c,s}r_{\rm c}^3\left(\ln\sqrt{\frac{1+\xi}{1-\xi}}-\xi\right), \text{ with} \tag{4.8}$$

$$\xi = \sin\left(\arctan(r_{\rm t}/r_{\rm c})\right).$$

Note that as $r_{\rm t} \to \infty$, $\xi \to 1$, and $\tau_\nu^{\rm c,s} \to 2\kappa_\nu^{\rm tot}\rho_0^{\rm c,s} r_{\rm c}$, but $M^{\rm c,s}$ does not converge. The unbounded nature of $M^{\rm c,s}$ is also found in the fully self-consistent solution for $\rho^{\rm c,s}(r)$ of a pressure-supported cloud with the boundary condition $\rho^{\rm c,s} \to 0$ as $r \to \infty$.

Equation. 4.6 can be rearranged to solve for the density by mass at the centre of the clump, $\rho_0^{\rm c,s}$, and the dust opacity in the B-band:

$$\rho_0^{\rm c,s} = \frac{\tau_{\rm B}^{\rm c,s}}{2r_{\rm c}\xi\kappa_{\rm B}} \tag{4.9}$$

where $\tau_{\rm B}^{\rm c,s}$ is the opacity in the B-band of a single clump and $\kappa_{\rm B}$ is the mass extinction coefficient in the B-band with units $[{\rm pc^2\,M_\odot^{-1}}]$.

By substituting Equation. 4.9 into Equation. 4.8 the mass of the clump is

$$\begin{aligned} M^{\rm c,s} &= 4\pi\rho_0^{\rm c,s} r_{\rm c}^3 \left(\ln\left(\sqrt{\frac{1+\xi}{1-\xi}}\right) - \xi \right) \\ &= 4\pi \frac{\tau_{\rm B}^{\rm c,s}}{2r_{\rm c}\xi\kappa_{\rm B}} r_{\rm c}^3 \left(\ln\left(\sqrt{\frac{1+\xi}{1-\xi}}\right) - \xi \right) \\ &= 2\pi \frac{\tau_{\rm B}^{\rm c,s} r_{\rm c}^2}{\kappa_{\rm B}} \chi \end{aligned} \tag{4.10}$$

where

$$\chi = \frac{\ln\left(\sqrt{\frac{1+\xi}{1-\xi}}\right)}{\xi} - 1, \tag{4.11}$$

and ξ is a function of $r_{\rm t}$. Thus, the mass of a single dust clump is $M^{\rm c,s}(\tau^{\rm c,s}, r_{\rm c}, r_{\rm t})$. The average density of the clump within the clump volume V can then be defined as

$$\rho^{\rm c,av} = \frac{M^{\rm c,s}}{V}. \tag{4.12}$$

In this work clumps are considered with $r_{\rm c} = 1\,{\rm pc}$, $r_{\rm t} = 1\,{\rm pc}$, and dust opacity through the clump (from the centre to the truncation radius) of $\tau_{\rm B}^{\rm c,s} = 1$. The

dust model used has $\kappa_{\rm B} = 8.07$ pc^2 M$_\odot^{-1}$ which leads to a dust clump with mass $M^{\rm c,s} = 0.1919$ M$_\odot$. The choice to truncate the clump at one core radius is motivated by the desire to incorporate only the contribution of the optically thick core of the clump. From a conceptual point of view any dust outside the truncation radius of the clump would belong to the diffuse medium.

4.2 Extinction Efficiency and Cross-Section of the Pseudo-Grain

Having prescribed the dust density distribution of the cloud, the interaction with the interstellar radiation fields can be described. The RT codes from PT11 are used to determine the efficiencies of absorption, scattering and extinction of the cloud, denoted by $Q^{\rm c}_{\rm abs}$, $Q^{\rm c}_{\rm sca}$, and $Q^{\rm c}_{\rm ext}$, respectively.

4.2.1 $Q^{\rm c}_{\rm abs}$

The efficiency of absorption or absorptivity, $Q^{\rm c}_{\rm abs}$, relates the energy absorbed by the dust in the clump to the energy of the photons incident on the clump. Given this definition, a method is required for illuminating the clump and measuring the energy absorbed. In attempts to analogise the scenario where the clump is being heated by some ambient radiation field, the clump is placed at the centre of a spherical shell of stellar emissivity. Thus, the spherical dust cloud is uniformly illuminated from outside. The radiative transfer code (including scattering) is then applied for this specific configuration.

The $Q^{\rm c}_{\rm abs}$ of the clump is calculated as:

$$Q^{\rm c}_{\rm abs}(\lambda) = \frac{4\pi \int_0^{r_{\rm t}} e_{\rm abs}(\lambda, r)\, {\rm d}r}{L_{\rm inc}(\lambda)}, \tag{4.13}$$

where $e_{\rm abs}$ is the volume density of energy absorbed by dust in the clump, and

$L_{\rm inc}(\lambda)$ is the luminosity of the incident radiation at the surface of the clump, at $r = r_{\rm t}$. In these calculations the illuminating shell is considered to have a thickness of 1 pc and to lie at a distance of 9 pc from the surface of the clump, therefore the midpoint of the shell lies at $r = 9.5$ pc from the surface of the clump. This specific geometric configuration is also ideal for calculating the heating of the grains in the clump, and therefore it is used to derive the infrared emissivities of the clump, as detailed in § 4.3.

4.2.2 $Q^{\rm c}_{\rm sca}$

To measure the efficiency with which the clump scatters light, a different geometric configuration than the one used to derive the absorption efficiency in § 4.2.1 must be considered. This is because the spherical symmetry previously used to determine $Q^{\rm c}_{\rm abs}$ makes it difficult to disentangle the contribution of the scattered light. Instead, a clump is placed in front of an illuminating disc whose cross-sectional area is equal to that of the clump. RT calculations are performed to obtain the surface brightness maps of the illuminating disc, with and without the attenuating clump. The luminosities of the clump-attenuated and clump-free maps are $L^{\rm map}_{\rm att}$ and $L^{\rm map}_{0}$, respectively. Since there is no direct output to determine the luminosity of scattered light, $L_{\rm sca}$, from the RT calculations, the following formulation is used:

$$Q^{\rm c}_{\rm sca}(\lambda) = \frac{\left(L^{\rm map}_{0}(\lambda) - L^{\rm map}_{\rm att}(\lambda)\right) - 4\pi \int_0^{r_{\rm t}} e_{\rm abs}(\lambda, r)\, {\rm d}r}{L_{\rm inc}(\lambda)}, \tag{4.14}$$

where $e_{\rm abs}$ is the volume density of energy absorbed by dust in the clump and $L_{\rm inc}(\lambda)$ is the incident radiation at the surface of the clump $r = r_{\rm t}$, for this specific configuration. The difference between $L^{\rm map}_{0}$ and $L^{\rm map}_{\rm att}$ is the attenuation map (due to the combined effect of scattering and absorption), therefore the difference between this quantity and the energy absorbed isolates the luminosity of scattered light.

4.2.3 Q^{c}_{ext}

The extinction efficiency of the cloud is simply:

$$Q^{c}_{ext} \equiv Q^{c}_{abs} + Q^{c}_{sca}. \tag{4.15}$$

4.2.4 Cross-Sections of Interaction

Relating Q^{c}_{abs}, Q^{c}_{sca} and Q^{c}_{ext} to the geometric cross-section of the clump πr_t^2, and the mass of the dust within the cloud, $M^{c,s}$, gives the cross-sections of absorption C^{c}_{abs}, scattering C^{c}_{sca} and extinction C^{c}_{ext} per unit mass of dust:

$$C^{c}_{abs} = \frac{\pi\, r_t^2\, Q^{c}_{abs}}{M^{c,s}}, \tag{4.16}$$

$$C^{c}_{sca} = \frac{\pi\, r_t^2\, Q^{c}_{sca}}{M^{c,s}}, \tag{4.17}$$

$$C^{c}_{ext} = \frac{\pi\, r_t^2\, Q^{c}_{ext}}{M^{c,s}}, \tag{4.18}$$

where $M^{c,s}$ is defined in the previous subsection, by Equation. 4.10. C^{c}_{abs}, C^{c}_{sca} and C^{c}_{ext} have units of $[\mathrm{pc}^2\,\mathrm{M}_\odot^{-1}]$.

Fig. 4.1 shows the optical properties of the clump, as derived from the methods described above, plotted together with the extinction curve for the diffuse dust, which is a Milky-Way type dust with the optical properties from Weingartner & Draine (2001). It can be seen that the two extinction curves differ significantly at shorter wavelengths ($\lambda \lesssim 1\,\mu\mathrm{m}$), then begin to converge at longer wavelengths ($\lambda \gtrsim 1\,\mu\mathrm{m}$), as is expected for $\tau_B = 1$ clumps.

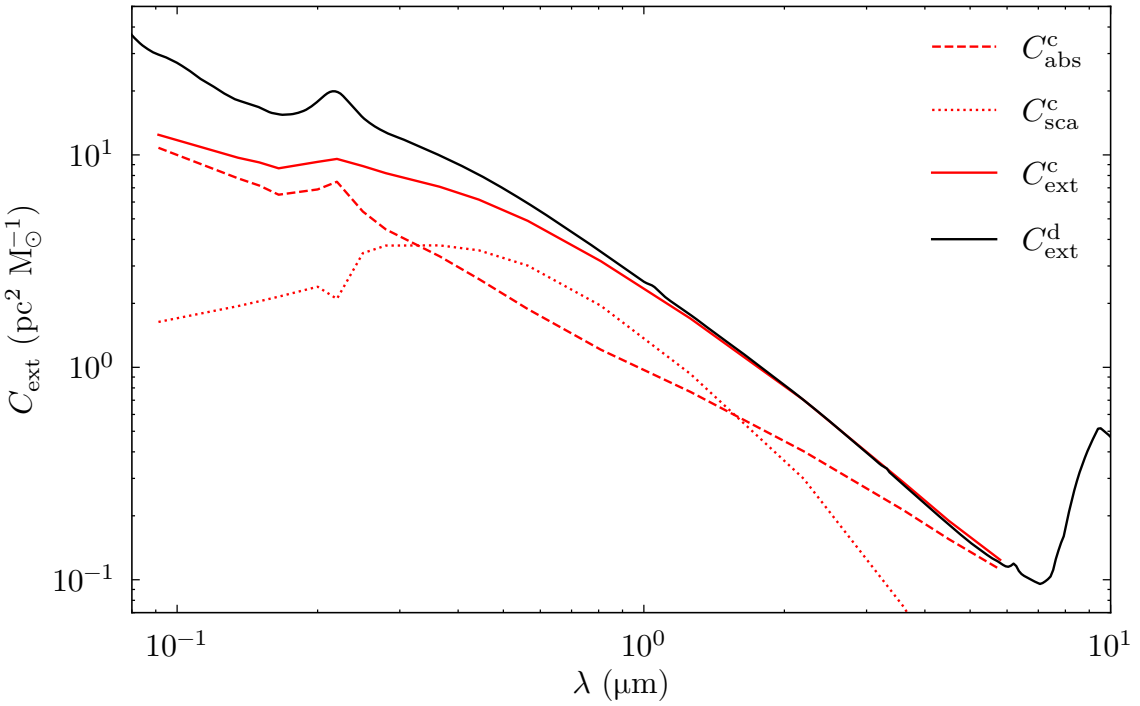

Figure 4.1: Absorption, scattering, and extinction cross sections of a single clump, $C^{\rm c}_{\rm abs}$, $C^{\rm c}_{\rm sca}$, and $C^{\rm c}_{\rm ext}$, plotted in red, with the dashed, dotted, and solid lines, respectively. Also plotted with a solid black line is the extinction cross-section $C^{\rm d}_{\rm ext}$ of the diffuse dust used in these models, which is a Milky Way-type dust, with the properties from Weingartner & Draine (2001).

4.3 The Infrared Emissivities of the Pseudo-Grain

In the previous § 4.2 the extinction properties of the pseudo-grain were derived. Here the emission properties of the clump are calculated, to obtain a complete characterisation of the pseudo-grain.

The infrared emissivity of the pseudo-grain (the clump SED) is calculated using the geometric configuration from § 4.2.1, with the clump being uniformly illuminated by a spherical shell of stellar emissivity that is concentric with the centre of the clump. However, unlike the derivation of the absorption efficiency, which only depends on the geometry and optical depth of the dust cloud (for dust grains with fixed optical properties), the calculation of the dust emission SED also depends on the intensity and colour of the radiation fields (RFs) heating the dust in which the clump is embedded. For a comprehensive characterisation, the SEDs are calculated for clumps placed in RFs with different strengths and colours to produce a corresponding library of dust emission SEDs for the clump.

The RFs used for these calculations are scaled from the RFs of the Milky Way derived at the solar position in Popescu et al. (2017), which are referred to as "unit" RFs. The RFs are divided into "UV" (0.0912−0.3650 μm) and "optical" (0.443−5.800 μm) spectral ranges. Two quantities are defined as

$$u_{\rm UV}^{\rm unit} = \int_{0.0912\,\mu{\rm m}}^{0.365\,\mu{\rm m}} u_{\lambda}^{\rm unit}\,{\rm d}\lambda \tag{4.19}$$

$$u_{\rm opt}^{\rm unit} = \int_{0.443\,\mu{\rm m}}^{5.800\,\mu{\rm m}} u_{\lambda}^{\rm unit}\,{\rm d}\lambda \tag{4.20}$$

where $u_{\lambda}^{\rm unit}$ is the RF energy density at the Solar position (Popescu et al., 2017) – "the unit RF energy density", $u_{\rm UV}^{\rm unit}$ is the spectral integration over the UV of the unit RF – "the unit UV RF energy", and $u_{\rm opt}^{\rm unit}$ is the spectral integration over the optical/NIR range of the unit RF – "the unit optical RF energy". The strengths of

the UV and optical/NIR RFs are then expressed in units of $u_{\rm UV}^{\rm unit}$ and $u_{\rm opt}^{\rm unit}$,

$$\mathrm{UV_{RF}} = \frac{\int_{0.0912\,\mu\mathrm{m}}^{0.365\,\mu\mathrm{m}} u_\lambda \,\mathrm{d}\lambda}{u_{\rm UV}^{\rm unit}} \tag{4.21}$$

$$\mathrm{OPT_{RF}} = \frac{\int_{0.443\,\mu\mathrm{m}}^{5.800\,\mu\mathrm{m}} u_\lambda \,\mathrm{d}\lambda}{u_{\rm opt}^{\rm unit}}. \tag{4.22}$$

These are the two parameters of the library of dust emission clump SEDs.

The clump SEDs were calculated for the following values of $\mathrm{UV_{RF}}$ and $\mathrm{OPT_{RF}}$: 0.001, 0.01, 0.1, 0.2, 0.6, 1, 2, 6, 10, 20, 60, 100, 160, 500, 800, 1000. The values were chosen to balance sampling density with computational efficiency. Fig. 4.2 shows the clump dust emission SED for various combinations of $\mathrm{UV_{RF}}$ and $\mathrm{OPT_{RF}}$. One can see that if the radiation fields have a small UV component (e.g. top left panel of Fig. 4.2), then an increase in $\mathrm{OPT_{RF}}$ will have a large effect in the dust emission SED: the peak of the dust emission will shift to shorter wavelengths, and the amplitude of the emission will strongly increase. On the contrary, if the radiation fields are UV dominated (bottom right panel of Fig. 4.2, then the same increase in $\mathrm{OPT_{RF}}$ will produce very small effects.

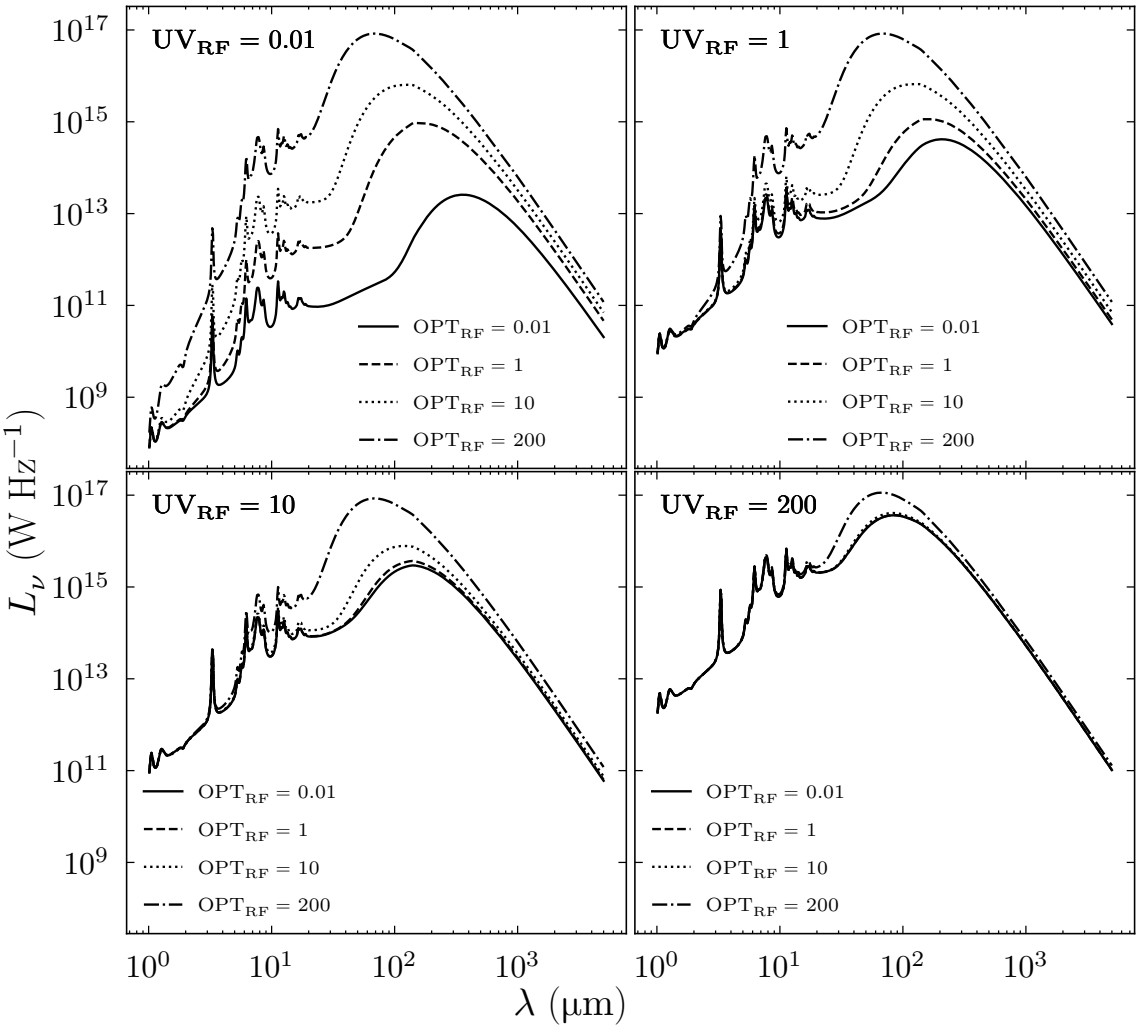

Figure 4.2: Clump dust emission SEDs, for clumps embedded in radiation fields with various values of the parameters $\mathrm{UV_{RF}}$ and $\mathrm{OPT_{RF}}$.

4.3.1 Optical and Emission Properties of Clumps with Various Optical Depths

To fully understand the optical and emission properties of quiescent clumps, extinction curves and dust emission SEDs were produced for clumps with various optical depths. Fig. 4.3 shows the absorption cross-section for quiescent clumps with opacities ranging from $\tau_{\mathrm{B}}^{\mathrm{c,s}} = 1$ to 8. Predictably, the dependence on wavelength of the absorption cross-section decreases with increasing $\tau_{\mathrm{B}}^{\mathrm{c,s}}$. As $\tau_{\mathrm{B}}^{\mathrm{c,s}}$ increases, a more

significant portion of the dust mass associated with the clump is shielded from radiation. Thus, a saturation limit is reached whereby photons of a given λ are fully absorbed and increasing $\tau_{\rm B}^{\rm c,s}$ (and therefore $\rm M^{c,s}$) does not result in more absorption.

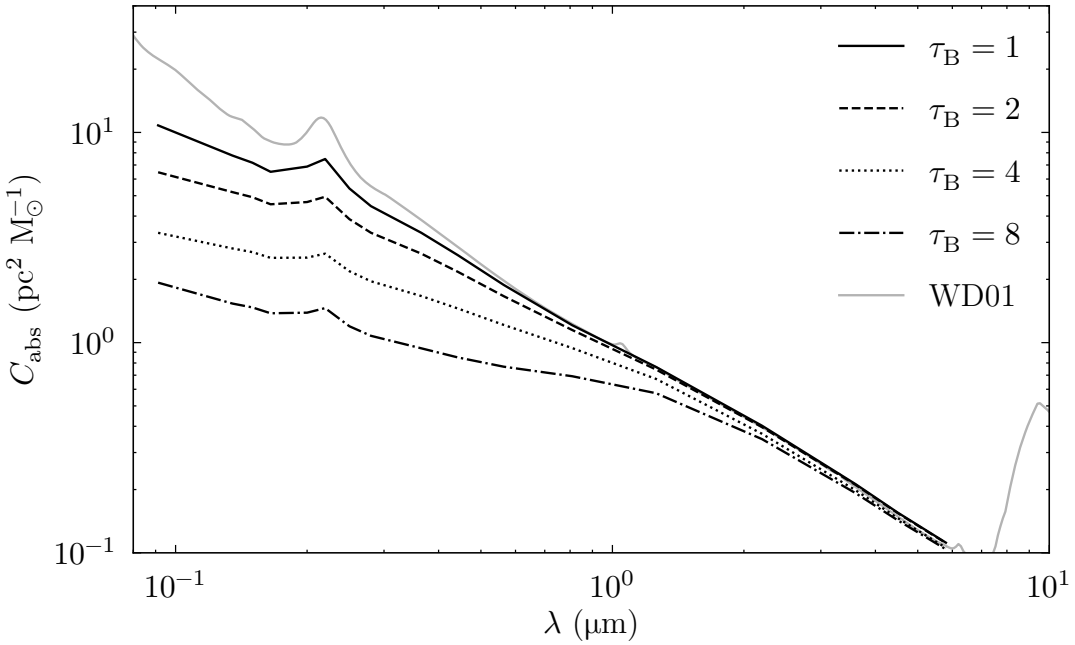

Figure 4.3: Cross-section of absorption for quiescent clumps $\tau_{\rm B}^{\rm c,s} = 1$ to 8. The absorption cross-section for the MW-type dust from Weingartner & Draine (2001) is also plotted to demonstrate the pure diffuse dust model.

Fig. 4.4 shows the dust emission SED calculated for quiescent clumps for opacities ranging from $\tau_{\rm B}^{\rm c,s} = 1$ to 8 as heated by the unit RFs (normalised at $\lambda = 5\,$mm). It can be seen that SEDs are consistently cooler for more opaque clumps, as a greater portion of the total dust mass is shielded from energetic UV photons, and effectively heated by redder RFs. From Equation 4.10, it can be seen that $M^{\rm c,s} \propto \tau_{\rm B}^{\rm c,s}$.

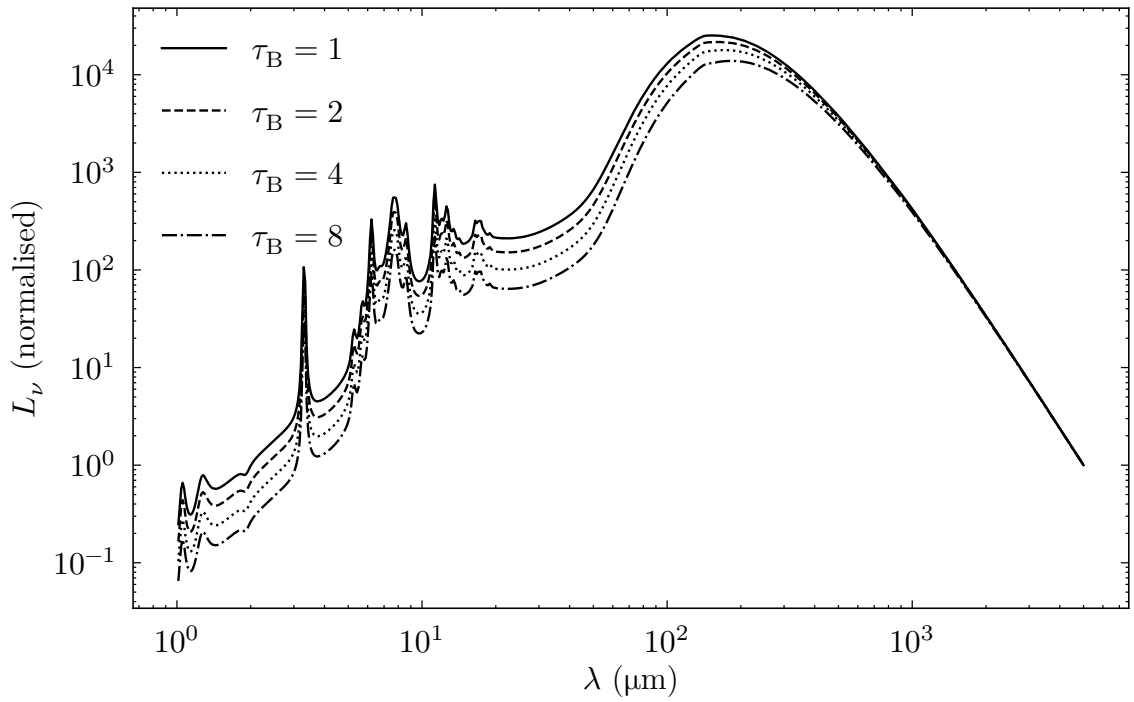

Figure 4.4: Dust emission SED of the quiescent clumps with $\tau_B^{c,s} = 1$ to 8, normalised to $\lambda = 5\,\mathrm{mm}$. Each SED was calculated with $\mathrm{UV_{RF}} = 1$ and $\mathrm{OPT_{RF}} = 1$ (see Equations 4.21 and 4.22).

4.4 Incorporation of the Pseudo-Grain Component into the Large-Scale, Galactic Calculation

The calculation of the absorption and scattering efficiencies of the clump, as well as of the infrared emissivities enables the replacement of the macroscopic clump with a pseudo-grain with equivalent extinction and emission characteristics. Accordingly, the dust grain mixture, originally composed of Si, Gra, PAH^0 and PAH^+, was supplemented with a fifth component: the pseudo-grain.

4.4.1 The Extinction Law of the New Dust Model

The radiative transfer code and the overall formalism remain unchanged from the previous (diffuse) version of the model, but, because the input albedo and extinction coefficients will be different, a different extinction law will be considered in the calculation, depending on the fraction of mass in clumps, $f^{\rm c}$, assumed in the model. Examples of extinction laws for a few values $f^{\rm c}$ are given in Fig. 4.5. One can see that the new dust model will produce less extinction in the UV with respect to a pure diffuse model.

4.4.2 The Central Face-On Optical Depth of a Galaxy Disc Due to Pseudo-Grains (Clumps)

The fraction of mass in clumps, $f^{\rm c}$, is usually kept constant throughout the galaxy disc. It can therefore be defined at any position in the disc. At the centre $f^{\rm c}$ will

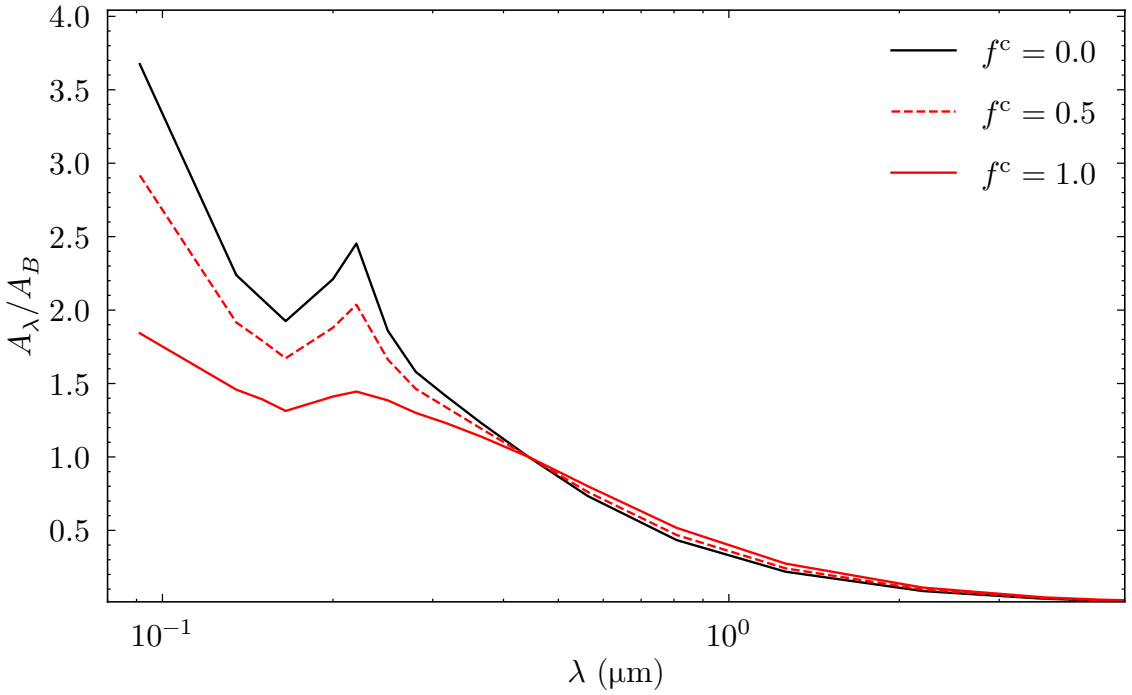

Figure 4.5: Extinction curves normalised in the B-band for three values of the fraction of mass in clumps: $f^{\rm c} = 0$ in solid black, $f^{\rm c} = 0.5$ in dashed red, and $f^{\rm c} = 1.0$ in solid red.

then be:

$$\begin{aligned} f^{\rm c} &= \frac{\rho_0^{\rm c}}{\rho_0^{\rm c} + \rho_0^{\rm d}} \\ &= \frac{n_0^{\rm c} M^{\rm c,s}}{n_0^{\rm c} M^{\rm c,s} + \rho_0^{\rm d}}, \end{aligned} \tag{4.23}$$

where $\rho_0^{\rm c}$ and $\rho_0^{\rm d}$ are the central volume density by mass of dust in the clumps and diffuse component, respectively, and $n_0^{\rm c}$ is the central number density of clumps. The fraction of mass in clumps can also be expressed as a percentage of the total dust mass, $c/d = 100 \times f^{\rm c}$. Using Equation 4.10 for the mass of a single clump, $M^{\rm c,s}$, and Equation C.5 for $\rho_0^{\rm d}$, and taking the inverse of $f^{\rm c}$ gives

$$\begin{aligned} \frac{1}{f^{\rm c}} &= 1 + \frac{\rho_0^{\rm d}}{n_0^{\rm c} M^{\rm c,s}} \\ &= 1 + \frac{\tau_{\rm B}^{d}}{2\kappa_{\rm B} z_{\rm d}} \frac{\kappa_{\rm B}}{n_0^{\rm c} 2\pi \tau_{\rm B}^{\rm c,s} r_{\rm c}^2 \chi} \end{aligned}$$

Then, the central number density of clumps is

$$n_0^{\rm c} = \frac{\tau_{\rm B}^{\rm d}}{\tau_{\rm B}^{\rm c,s}} \frac{1}{4\pi z_{\rm d} r_{\rm c}^2 \chi} \frac{f^{\rm c}}{1-f^{\rm c}}. \tag{4.24}$$

Assuming that galaxy discs have exponential dust distributions in the vertical direction (assumption used in most of the PT11 galaxy models, see also Equations 1–2 of TP20), then the total face-on central optical depth through the clumpy component, $\tau_{\rm B}^{\rm c}$, can be calculated by integrating over the vertical direction,

$$\tau_{\rm B}^{\rm c} = 2\left[\int_{z=0}^{\infty} n_0^{\rm c} e^{-\frac{z}{z_{\rm d}}}\, {\rm d}z\right] \cdot \pi r_{\rm t}^2 Q_{\rm ext,B}^{\rm c} \tag{4.25}$$

where $Q_{\rm ext,B}^{\rm c}$ is the extinction efficiency of a single clump in the B-band. Solving the integral gives:

$$\tau_{\rm B}^{c} = 2 n_0^{\rm c} z_{\rm d} \cdot \pi r_{\rm t}^2 Q_{\rm ext,B}^{c}.$$

Substituting $n_0^{\rm c}$ from Equation 4.24 into the above equation gives:

$$\tau_{\rm B}^{\rm c} = \frac{1}{2\chi}\left(\frac{r_{\rm t}}{r_{\rm c}}\right)^2 \left(\frac{\tau_{\rm B}^{\rm d}}{\tau_{\rm B}^{\rm c,s}}\right)\left(\frac{f^{\rm c}}{1-f^{\rm c}}\right) Q_{\rm ext,B}^{\rm c}.$$

If $f^{\rm c}$ and $\frac{r_{\rm t}}{r_{\rm c}}$ are allowed to be variables, and generalising to any wavelength λ gives

$$\tau_{\lambda}^{\rm c}\left(f^{\rm c}, \frac{r_{\rm t}}{r_{\rm c}}\right) = \frac{1}{2\chi}\left(\frac{r_{\rm t}}{r_{\rm c}}\right)^2 \left(\frac{\tau_{\rm B}^{\rm d}}{\tau_{\rm B}^{\rm c,s}}\right)\left(\frac{f^{\rm c}}{1-f^{\rm c}}\right) Q_{{\rm ext},\lambda}^{\rm c}\left(\tau_{\rm B}^{\rm c,s}\right). \tag{4.26}$$

As $f^{\rm c}$ is the fraction of dust mass in clumps, Equation 4.26 is only valid for $0 \leq f^{\rm c} < 1$.

4.4.3 The Dust Emission SED

As described in § 2.3, the present radiative transfer model explicitly calculates the heating of the dust grains, including the stochastic heating. Thus, for each grain size and composition, the probability distribution of dust temperature, and therefore the infrared emissivity, is calculated based on the radiation fields heating the dust at

each individual location in the galaxy. However, a similar calculation applied to the pseudo-grain would entail doing a separate calculation for the macroscopic clump heated by the radiation fields at each sampled position in the model galaxy. Taking into account that the modelling of an individual galaxy is an iterative process, whereby the radiation fields are recalculated for each iteration, the explicit calculation for the pseudo-grain would be prohibitive. Instead, the library of dust emission SEDs for the clump—derived in § 4.3—is used, taking the two parameters of the library and performing a double interpolation in $\mathrm{UV_{RF}}$ and $\mathrm{OPT_{RF}}$, see § D.1 for a detailed description, thus avoiding the heavy computational burden of explicitly calculating the clump SEDs based on the RFED at each position. The clump SEDs comprising the library are calculated for a single macroscopic quiescent clump, thus to apply them to a galaxy model, the SEDs must be scaled according to the dust density at each position in the galaxy. For more details see Appendix D.

Chapter 5

Application of the Clumpy Model to the Prototype Edge-On Spiral NGC 891

As discussed in § 1, the solution obtained for NGC 891 by Popescu et al. (2000, 2011) successfully matched the FIR data available at the time, but produced an overly prominent dust lane in the NIR J and K_s bands. In principle, this earlier model could be used for comparison with the new clumpy model. However, the previous model was fitted using the Infrared Space Observatory's (ISO, Kessler et al., 1996) ISOPHOT data (Lemke et al., 1996), which, at that time, were the only ones available to cover the peak of the dust emission SED in the FIR. With the advent of the Herschel Space Observatory (Pilbratt et al., 2010) data, it became apparent that there was a discrepancy between the fluxes measured by the two missions, with the Herschel flux densities exceeding the ISO measurements by a factor of approximately 1.5 (see Bianchi & Xilouris, 2011). This discrepancy does not seem to be confined to NGC 891 only, but also to other resolved galaxies. Given

that most of the recent work in the field has been calibrated on Herschel rather than on ISO data, including this work on modelling NGC 891 with clumps, it was decided to re-fit the previous model as well, using the updated Herschel data. This chapter presents both the updated diffuse model and the clumpy model of NGC 891.

First discovered by William Herschel in 1784, NGC 891 is an near perfectly edge-on spiral galaxy. It is classified morphologically as an Sb spiral by Sandage (1961), and as an SA(s)b by de Vaucouleurs (1991). NGC 891 is often referred to as a close analogue to the Milky Way due to its similar structure and stellar mass content (van der Kruit, 1984). However, its neutral and ionised gas content is significantly more vertically extended (Garcia-Burillo et al., 1992; Scoville et al., 1993; Seon et al., 2014; Katsioli et al., 2023). It also hosts an extended H I disc with coincident cold dust emission (Popescu & Tuffs, 2003). NGC 891 has a radio continuum halo (Allen, Baldwin & Sancisi, 1978; Hummel et al., 1991), and it hosts a significant H I halo (Swaters, Sancisi & van der Hulst, 1997; Oosterloo, Fraternali & Sancisi, 2007). High-energy observations have also unveiled the presence of a large hot gaseous halo around NGC 891, detected through X-ray emission using *Chandra* and *XMM-Newton* (Hodges-Kluck & Bregman, 2013; Hodges-Kluck, Bregman & Li, 2018). In addition, NGC 891 exhibits a larger global SFR (Shinn & Seon, 2015; Yoon et al., 2021) compared to similar spirals such as NGC 4565 ($0.74\,\mathrm{M_\odot yr^{-1}}$; Wiegert et al., 2015), M31 ($0.4\,\mathrm{M_\odot yr^{-1}}$; Rahmani, Lianou & Barmby, 2016), and the MW ($1.25\,\mathrm{M_\odot yr^{-1}}$; Natale et al., 2022). It is suggested that NGC 891 is a starburst galaxy in a quiescent state in the current epoch (Temple, Raychaudhury & Stevens, 2005).

NGC 891 lies at a distance of approximately 9.5 Mpc. Radburn-Smith et al. (2011) and Tikhonov & Galazutdinova (2005) derive a distance of $D = 9.1 \pm 0.4\,\mathrm{Mpc}$ and $D = 9.82 \pm 0.37\,\mathrm{Mpc}$ respectively, both using the tip of the red giant branch. van der Kruit & Searle (1981) find a distance of $D = 9.5\,\mathrm{Mpc}$. To be consistent with

the previous papers on NGC 891 (Popescu et al., 2000, 2011), a distance of 9.5 Mpc and an inclination of $i = 89.7°$ (Xilouris et al., 1998, 1999) is adopted in this work.

5.1 Observational Data

Following from previous work on NGC 891, all available panchromatic imaging data spanning from the optical to submm range were used, while UV imaging data was not used. This is because, in an almost perfectly edge-on galaxy like NGC 891, any UV emission from the disc is completely obscured by dust, thus making it impossible to rely on direct constraints from this wavelength range. In Table 5.1 (columns 1–3) the instruments and corresponding wavelengths of the data used in this work for modelling NGC 891 are listed.

Skinakas Observatory

The optical images in the B, V, and I bands obtained using the 1.3 m telescope at the Skinakas Observatory by Xilouris et al. (1998) were utilised in this work. The pixel scale of these data is 0.75 arcsec corresponding to 35 pc at the assumed distance.

2MASS

NGC 891 was imaged in the NIR bands J, H, and K_s as part of the The Two Micron All Sky Survey (2MASS; Skrutskie et al., 2006) Large Galaxy Atlas (LGA; Jarrett et al., 2003). These data have a pixel scale of 1.0 arcsec corresponding to 46 pc at the assumed distance. Only the J and K_s bands were utilised in this study as the effective wavelength of the H band is not included in this model.

Table 5.1: Summary of observational data used to model NGC 891. [a]Xilouris et al. (1998), [b]Skrutskie et al. (2006), [c]Fazio et al. (2004), [d]Poglitsch et al. (2010)

Telescope	Filter/ Instrument	Wavelength (μm)	Flux (Jy)	pixel scale (arcsec)	pixel scale (pc)	Calibration error (per cent)
Skinakas[a]	B	0.443	0.17 ± 0.02	0.75	35	
	V	0.564	0.29 ± 0.03	0.75	35	
	I	0.809	0.84 ± 0.08	0.75	35	
2MASS[b]	J	1.2	1.79 ± 0.05	1	46	3
	K_s	2.2	2.62 ± 0.08	1	46	3
Spitzer[c]	IRAC	3.6	1.84 ± 0.06	0.6	28	3
	IRAC	4.5	1.27 ± 0.04	0.6	28	3
	IRAC	5.8	3.21 ± 0.10	0.6	28	3
	MIPS	24	5.32 ± 0.06	1.5	69	1
Herschel[d]	PACS	70	106.7 ± 14.4	1.4	64	12
	PACS	100	227.7 ± 28.0	1.7	78	12
	PACS	160	294.1 ± 34.4	2.85	131	12
	SPIRE	250	158.7 ± 22.5	6	276	15
	SPIRE	350	66.6 ± 9.4	8	368	15
	SPIRE	500	23.5 ± 3.2	12	553	15

Spitzer

The Spitzer Space Telescope conducted imaging in the infrared with two instruments, the Infrared Array Camera (IRAC; Fazio et al., 2004) and the Multiband Imaging Photometer for Spitzer (MIPS; Rieke et al., 2004). IRAC was a four channel camera that simultaneously imaged the 3.6, 4.5, 5.8, and 8 μm bands. The pixel scale of the IRAC images are 0.6 arcsec corresponding to 28 pc. MIPS imaged from the MIR to FIR (24, 70, and 160 μm). In this study only the 24 μm images were utilised as higher quality images for the 70 and 160 μm bands are used instead. The

pixel scale of the 24 µm data are 1.5 arcsec (69 pc)

Herschel

The Herschel Space Observatory imaged NGC 891 in the FIR and submm. The Photodetecting Array Camera and Spectrometer (PACS; Poglitsch et al., 2010) provided image data at 70, 100, and 160 µm with pixel scales of 1.40, 1.70, and 2.85 arcsec, corresponding to 64, 78, and 131 pc, respectively. The Spectral and Photometric Imaging Receiver (SPIRE; Griffin et al., 2010) observed NGC 891 at the wavelengths 250, 350, and 500 µm with pixel scales of 6, 8, and 12 arcsec, corresponding to 276, 368, and 553 pc, respectively. Although these data are useful for the major axis of NGC 891 the emission above and below the plane of the galaxy is dominated by the PSF for all but the 70 µm data, hence the vertical surface brightness distribution is unresolved.

5.1.1 Data Post Processing

Data from 2MASS, MIPS and Herschel was found on NASA/IPAC Extragalactic Database (NED)[1]. The optical data were obtained by Xilouris et al. (1998). The IRAC data were downloaded from the Spitzer Heritage Archive[2]. While these data are calibrated from their raw form, further processing is required to make them useful for use in these models.

Background Removal

The cumulative sum of the averaged surface brightness of the data in the vertical direction was examined to determine the height above the disc at which the emission of the galaxy falls below the background level. A visual inspection of each map was done to ensure that the emission associated with NGC 891 does not extend beyond

[1] https://ned.ipac.caltech.edu

[2] https://irsa.ipac.caltech.edu/data/SPITZER/docs/spitzerdataarchives/

this point, which was found to be $|z| = 6\,\mathrm{kpc}$. The region $6 \leq |z| \leq 9$ was chosen to be the background sample. This ensured that a large, representative region of the sky was being sampled, while not extending beyond the dimensions of the image. The average background flux per pixel is then calculated by taking the mean surface brightness through 6 strips of equally spaced in the region $6 \leq |z| \leq 9$. Finally, the average background flux is subtracted from each pixel in the image.

Foreground Star Removal

Foreground stars are visible in the UV/optical/NIR wavelengths and can influence the measured values of emission within the galaxy. It is therefore important to mask these stars. An automatic masking routine used which first produces a median map where each pixel of the median map is equal to the median of the 3×3 pixels centred on the pixel. A bias map is also produced, that is principally the same as the median map, but takes the median of the 21×21 pixels. The bias map is used as an additional check to mitigate against false positives when masking noisy data. Pixels with values that exceed both the median and bias maps are then masked. After this initial pass, each mask is manually inspected for regions that may have been missed, or erroneously masked, such as H II regions. H II regions can appear as point sources (similarly to foreground stars) and thus are often falsely masked by this automated process. To help with identification of these H II regions additional colour information was used. As H II regions comprise localised hot dust they appear brightly in the MIR, thus the 24 µm data were examined to help identify the H II regions and unmask them in the optical/NIR data.

Extraplanar Emission

As shown in multiple studies (Pildis, Bregman & Schombert, 1994; Rand, 1996; Hoopes, Walterbos & Rand, 1999; Jo et al., 2018), NGC 891 exhibits extraplanar

stellar emission, which is not included in this model. Therefore, in order to compare model with observations, this emission needs to be subtracted from the available optical/NIR images used in this study. The level of the extraplanar emission was estimated from a region beyond the main vertical extent of the disc and bulge. Since the model stellar disc has a maximum scale height of $z_{\rm s} = 500\,{\rm pc}$, and the model bulge a projected effective radius (on the vertical direction) of $R_{\rm e} \times \frac{b}{a} = 1600 \times 0.47 = 752\,{\rm pc}$, it is reasonable to assume that beyond 2 kpc the emission from the main morphological components of NGC 891 becomes negligible. This assumption is also validated by a visual inspection of the observed vertical profiles of NGC 891. Thus, the emission in the region $2 < |z| < 3\,{\rm kpc}$ was taken to be dominated by extraplanar emission, and subtracted from images using a method similar to that used for the Milky Way in Popescu et al. (2017) and Natale et al. (2022). Since the surface brightness decreases with horizontal distance, the subtraction of the extraplanar emission was done separately for each bin in horizontal distance. Using the same horizontal binning described in § 3.3.2, the extraplanar emission was calculated to be the average of all the pixels with $2 < z < 3\,{\rm kpc}$ within each horizontal bin, and subtracted correspondingly from the image.

For wavelengths $\lambda \geq 70\,\mu{\rm m}$, no extraplanar emission was detected in available dust emission images (Bianchi & Xilouris, 2011). In any case, the PSF of the observing instrument is coarse enough that true emission from the plane of the galaxy would be seen contributing to any emission at high vertical distances. Because of this no attempt was made to extract extraplanar emission at these wavelengths.

5.2 An Updated Diffuse Model of NGC 891

As discussed at the beginning of this chapter, the main reason to re-fit the diffuse model of NGC 891 was justified by the need to calibrate it on the same (new)

data as the clumpy model. In addition, recent work on modelling face-on galaxies (Thirlwall et al., 2020; Rushton et al., 2022; Inman et al., 2023; Pricopi et al., 2025) and the Milky Way (Natale et al., 2022) has highlighted the need to incorporate a more detailed geometrical and morphological description. Because of all these reasons it was imperative to re-fit the diffuse model of NGC 891, to provide a more meaningful comparison with the clumpy model. The fits to the averaged surface brightness profiles can seen in Figs.5.1–5.2 and Figs.E.1–E.4.

Inspection of the averaged horizontal profiles of dust emission (Fig. 5.2 and E.3–E.4) shows that there is a local maximum at $R = 3\,\mathrm{kpc}$, suggesting a possible inner disc in the dust distribution, as well as an inner disc of young stars that could contribute to the dust heating in the inner regions. This was also investigated by Katsioli et al. (2023) who found similar emission enhancements at $\pm 3\,\mathrm{kpc}$. Using data spanning 24 µm–1.15 mm, they propose a scenario where the spiral arms lie on either side of the central bulge region when viewed through the line-of-sight. These locations at $\pm 3\,\mathrm{kpc}$ mark the interface between where the line-of-sight emission is dominated by the bulge region, and the spiral arms. Indeed, it was found that the profiles are better fitted when an inner disc of young stars and dust are added, and the main disc of both stars and dust has a linear decline towards the galaxy centre, within an inner radius $R_{\mathrm{in}} = 3\,\mathrm{kpc}$. In the optical and NIR bands there was no obvious need for an inner disc of stellar emissivity. Thus, the diffuse model of NGC 891 consists of three morphological components: a bulge, a main disc and an inner disc. The main disc morphological component has the typical vertical stratification of the PT11 model, with a stellar disc, a thin stellar disc, a dust disc and a thin dust disc. The inner disc morphological component has only a thin stellar disc, a dust disc and a thin dust disc. The fits of this updated diffuse model to the surface brightness profiles (from the best fitting solution) at selected wavelengths are shown in Figs. 5.1–5.2. The corresponding surface brightness maps of the data, model, and their residuals

are shown in Fig. 5.3. The fits and maps at all wavelengths used in this study can be found in Figs. E.1–E.5. The spatially integrated SED of the model is shown in Fig. 5.4. The geometric parameters of this fit are given in Table 5.2 (column 'd'), Table 5.3 and Table 5.4 (upper section 'd').

In comparison with the previous diffuse model of NGC 891, the more complex morphology allows for a somewhat better fit to the surface brightness profiles, although it still does not resolve the problem with the prominence of the dust lanes. Inspection of Fig. 5.1 shows that in the J band there is a very strong trough in the model vertical profiles, around the midplane. By contrast, the observed profiles show only a mild trough. In the K_s band the observed vertical profiles, in particular in the $2 < |R| < 5\,\mathrm{kpc}$ region, do not show any trough, yet the model predicts one.

Similarly, the J band model images from Fig. 5.3 show a more pronounced dust lane than observed, with the residual images exhibiting a strong residual dust lane. In the K_s the observed images do not exhibit a dust lane, except for a few dark dots around the midplane. Yet, the model predicts a distinct dust lane, also strongly visible in the residual maps. In fact at all wavelengths shorter than $3.6\,\mu\mathrm{m}$ the model fits show an overestimation of the dust lane (see Fig. E.1), and there are some midplane residuals at even longer wavelengths. It is clear that the updated diffuse model does not solve the energy balance problem.

it is noted that the best fitting solution for the diffuse model has 2/3 opacity in the thin dust disc and 1/3 in the dust disc. This is the original ratio used in Popescu et al. (2000) and Popescu et al. (2011). Solutions with different values of this ratio were also explored, but these resulted in poorer fits. In particular, solutions with 2/3 opacity in the dust disc and 1/3 in the thin dust disc cannot reproduce the shape of the vertical profiles, with the maximum SB being at too great a vertical distance from the midplane.

Coming back to the best fit solution, it is also apparent from the SB profiles in Fig. E.3 that in the 24–100 μm range the model overestimates the emission in the central regions.

On the other hand, the overall spatially integrated emission SED (Fig. 5.4), shows a good match between the data and model, with a slight overestimation in the MIR. Nonetheless, the dust-deattenuated SED predicts that even in K_s and IRAC 3.6 μm bands the line-of sight attenuation is severe, possibly indicating an overestimation of dust attenuation in the diffuse model.

Table 5.2: The free geometrical parameters of NGC 891, for the best fitting diffuse (middle column), and clumpy models (right column), denoted with 'd' and 'c', respectively. The superscripts 'i' and 'm' found in the notation for the different parameters denote the inner and main discs, respectively.

Parameter	d	c
$h_s^{\mathrm{disc-m}}(B)$	10 ± 1	10 ± 1
$h_s^{\mathrm{tdisc-(i,m)}}$	$(3.0 \pm 0.4,\ 5.0 \pm 0.3)$	$(3.0 \pm 0.4,\ 5.0 \pm 0.3)$
$h_d^{\mathrm{disc-(i,m)}}$	$(3.0 \pm 0.3,\ 10 \pm 1)$	$(3 \pm 0.3,\ 10 \pm 1)$
$\chi_s^{\mathrm{disc-m}}$	0.0 ± 0.1	0.0 ± 0.1
$\chi_s^{\mathrm{tdisc-(i,m)}}$	$(0,\ 1.0 \pm 0.2)$	$(0,\ 1.0 \pm 0.2)$
$\chi_d^{\mathrm{disc-(i,m)}}$	$(0,\ -0.9 \pm 0.2)$	$(0,\ -0.9 \pm 0.2)$
$z_s^{\mathrm{disc-m}}(B)$	0.42 ± 0.02	0.50 ± 0.02
$z_d^{\mathrm{disc-(i,m)}}$	$(0.28 \pm 0.03,\ 0.28 \pm 0.03)$	$(0.28 \pm 0.03,\ 0.28 \pm 0.03)$
$R_e(B)$	1.4 ± 0.2	1.4 ± 0.2
$\frac{b}{a}(B)$	0.43 ± 0.01	0.47 ± 0.01

Table 5.3: The geometrical parameters of NGC 891 fixed from data and theoretical considerations. The values are the same between the diffuse and clumpy models. The Sérsic index was fixed to the value considered in Xilouris et al. (1999). The superscripts 'i' and 'm' found in the notation for the different parameters denote the inner and main discs respectively. Where applicable, all values are given in kpc.

Parameter	value
$R_{\rm in,s}^{\rm tdisc-(i,m)}$	(0, 0)
$R_{\rm in,s}^{\rm disc-m}$	3
$R_{\rm in,d}^{\rm disc-(i,m)}$	(0, 3)
$R_{\rm tin,s}^{\rm tdisc-(i,m)}$	(0, 0)
$R_{\rm tin,s}^{\rm disc-m}$	0
$R_{\rm tin,d}^{\rm disc-(i,m)}$	(0, 0)
$R_{\rm t,s}^{\rm tdisc-(i,m)}$	(3, 14)
$R_{\rm t,s}^{\rm disc-m}$	14
$R_{\rm t,d}^{\rm disc-(i,m)}$	(3, 14)
$z_{\rm s}^{\rm tdisc-(i,m)}$	(0.09, 0.09)
$n_{\rm s}$	4

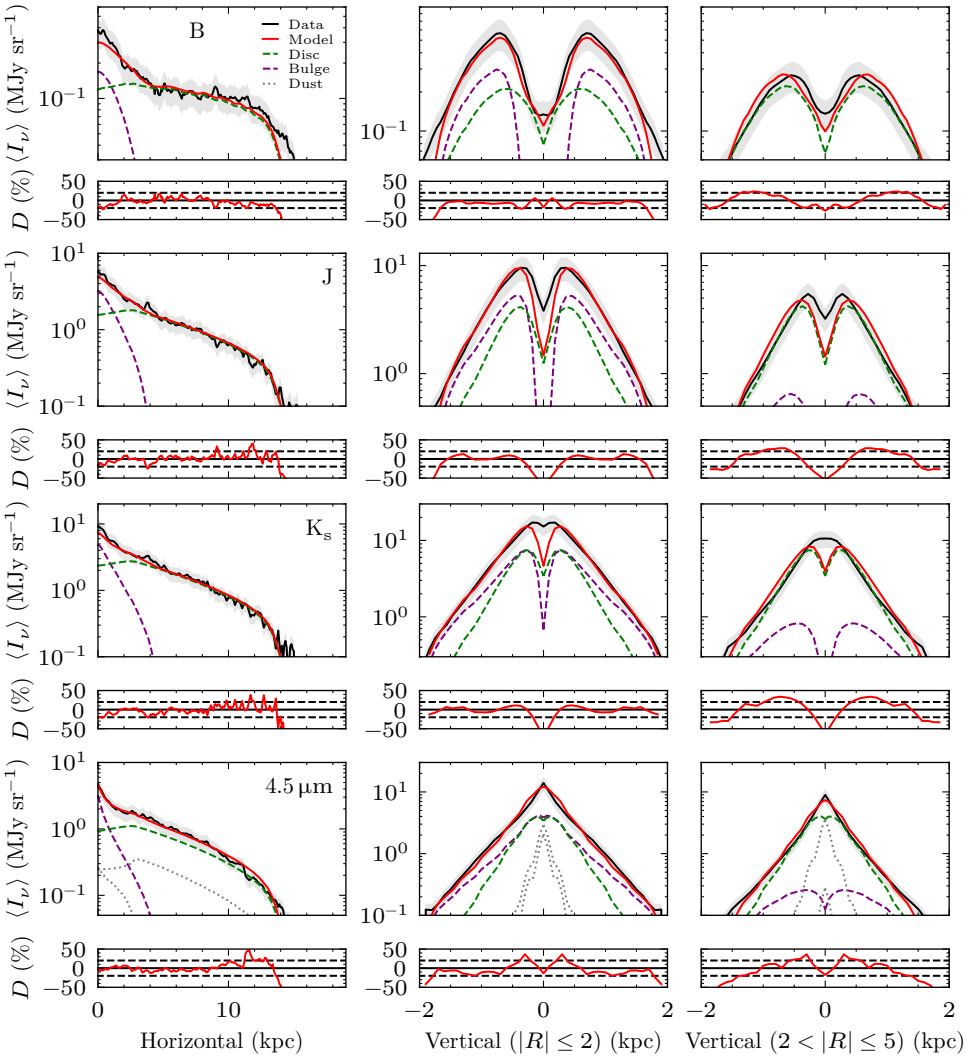

Figure 5.1: Averaged horizontal SB profiles (mirrored about the central vertical axis) (LH panels) and averaged vertical SB profiles (middle and RH panels) of the pure diffuse model of NGC 891 at selected wavelengths in the optical/NIR. The observed SB profiles are plotted with solid black line with the shaded banding indicating the uncertainty. The solid red line indicates the model total, with the individual component contributions plotted with the dashed and dotted lines. The percent differences between the model total and the observed profiles, $D\,[\%]$, are plotted in the panels below each profile, with the dashed horizontal lines indicating $\pm\,20\%$ deviation.

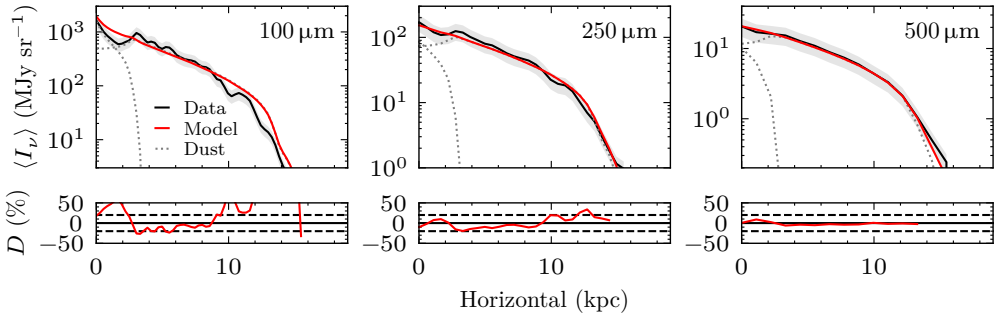

Figure 5.2: Averaged horizontal SB profiles (mirrored about a central vertical axis) of the pure diffuse model at selected wavelengths in the FIR/submm. The plotting details are as in Fig. 5.1.

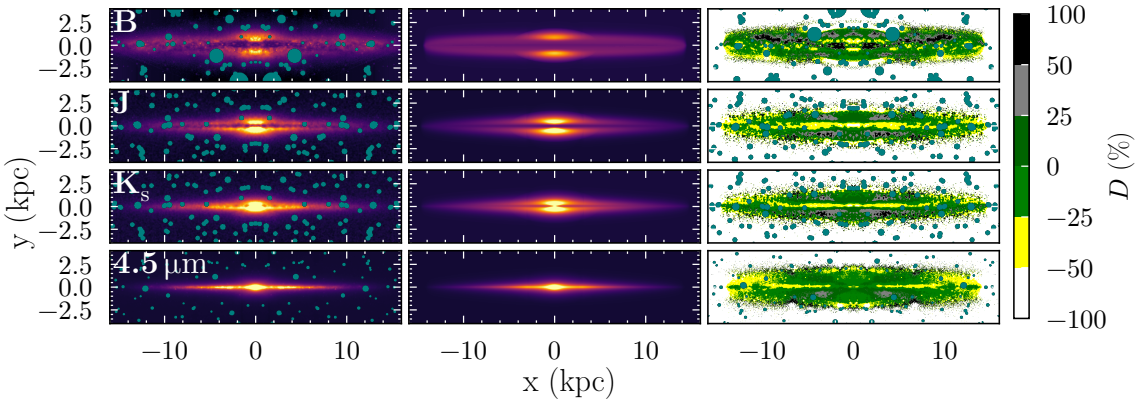

Figure 5.3: Left: surface brightness maps of NGC 891 at selected optical/NIR wavelengths, mirrored about their vertical central axis. Middle: surface brightness maps of the corresponding diffuse model images. Right: residuals between the data and model images calculated as $D = (M - O)/O$. Masked foreground stars are marked in teal.

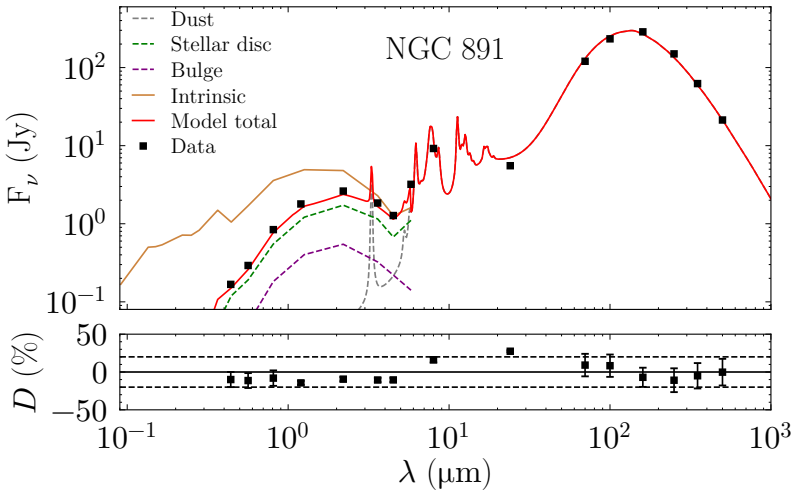

Figure 5.4: The spatially integrated model SED of the pure diffuse solution of NGC 891 plotted with the observed data (black squares) and the associated uncertainties (which are mainly contained in the black squares). Contributions from each of the galaxy components (dashed lines) and the intrinsic stellar SED (solid brown line) are also shown. The lower panel shows the per cent difference between the model SED and the observed data. To guide the eye dashed lines are plotted to show ±20% deviation.

Table 5.4: NGC 891: wavelength dependent model parameters for main disc and bulge, for the diffuse and clumpy models, denoted with 'd' and 'c', respectively. All length parameters are given in kpc.

Parameter	Filter							
	B	V	I	J	$K_{\rm s}$	3.6 μm	4.5 μm	5.8 μm
d								
$h_{\rm s}^{\rm disc-m}$	10 ± 1	6.5 ± 0.2	4.6 ± 0.1	3.8 ± 0.1	3.8 ± 0.1	4.0 ± 0.1	4.0 ± 0.1	3.6 ± 0.2
$z_{\rm s}^{\rm disc-m}$	0.42 ± 0.02	0.41 ± 0.02	0.40 ± 0.02	0.34 ± 0.01	0.31 ± 0.01	0.28 ± 0.01	0.28 ± 0.01	0.27 ± 0.01
$R_{\rm e}$	1.44 ± 0.05	1.44 ± 0.05	1.44 ± 0.05	1.44 ± 0.05	1.60 ± 0.05	1.60 ± 0.05	1.60 ± 0.05	1.44 ± 0.05
b/a	0.43 ± 0.02	0.43 ± 0.01	0.43 ± 0.01	0.43 ± 0.01	0.43 ± 0.01	0.43 ± 0.01	0.43 ± 0.01	0.43 ± 0.01
c								
$h_{\rm s}^{\rm disc-m}$	10 ± 1	7.0 ± 0.2	5.3 ± 0.1	4.4 ± 0.1	4.0 ± 0.1	4.2 ± 0.1	4.2 ± 0.1	3.6 ± 0.1
$z_{\rm s}^{\rm disc-m}$	0.50 ± 0.02	0.50 ± 0.02	0.46 ± 0.01	0.36 ± 0.01	0.31 ± 0.01	0.30 ± 0.01	0.31 ± 0.02	0.27 ± 0.02
$R_{\rm e}$	1.44 ± 0.04	1.44 ± 0.04	1.44 ± 0.04	1.44 ± 0.04	1.60 ± 0.04	1.60 ± 0.04	1.60 ± 0.04	1.44 ± 0.04
b/a	0.47 ± 0.01	0.47 ± 0.01	0.47 ± 0.01	0.47 ± 0.01	0.47 ± 0.01	0.47 ± 0.01	0.47 ± 0.01	0.47 ± 0.01

5.3 The Clumpy Model of NGC 891

Using the same morphological components and the same number of geometric parameters as in the diffuse model case, the new clumpy model was fitted to the data. This time an additional free parameter was needed, the fraction of mass in clumps $f^{\rm c}$. The best model fit was found for $f^{\rm c} = 0.5$. It was also found that most of the geometric and luminosity parameters changed in the new model, with various degree of variation, as discussed in Chapter 5.4.

The fits to the surface brightness profiles from the best fitting solution for the clumpy model are shown for a selection of wavelengths in Fig. 5.5, and for all wavelengths in Figs. E.6–E.9. The surface brightness maps of the data, model and their residuals are shown at a selection of wavelengths in Fig. 5.7, and for all optical/NIR wavelengths in Fig. E.10. The spatially integrated SED of the model is shown in Fig. 5.8. The geometric parameters of this fit are given in right-hand column of Table 5.2 and Table 5.3.

Inspection of the fits to the surface brightness profiles (Fig. 5.5 and Figs. E.6–E.9) shows very good agreement with the data. In particular, the J and $K_{\rm s}$ band vertical profiles are well fitted. This is also seen in the model images from Fig. 5.7, with the residual maps showing no prominent residual dust lanes. Overall, the fits to all wavelengths are improved and lie within 20% errors. This is the first model of NGC 891 that provides consistency with the panchromatic imaging data and solves the energy balance problem.

The spatially integrated model SED from Fig. 5.8 is well matched to the data. This is also the case for the diffuse model. However, unlike the diffuse model, the intrinsic stellar SED is more realistic, with a smaller difference between the intrinsic and dust attenuated stellar SED, predicting thus less attenuation.

Bianchi (2008) presented a model of NGC 891 using his own code TRADING, which

included an explicit treatment of clumps (both quiescent and active). Although his model was unable to fit the MIR emission of NGC 891, it is noteworthy that the best-fitting model in his study assigned the same 50% of the total dust mass to quiescent clumps, as was found in this work.

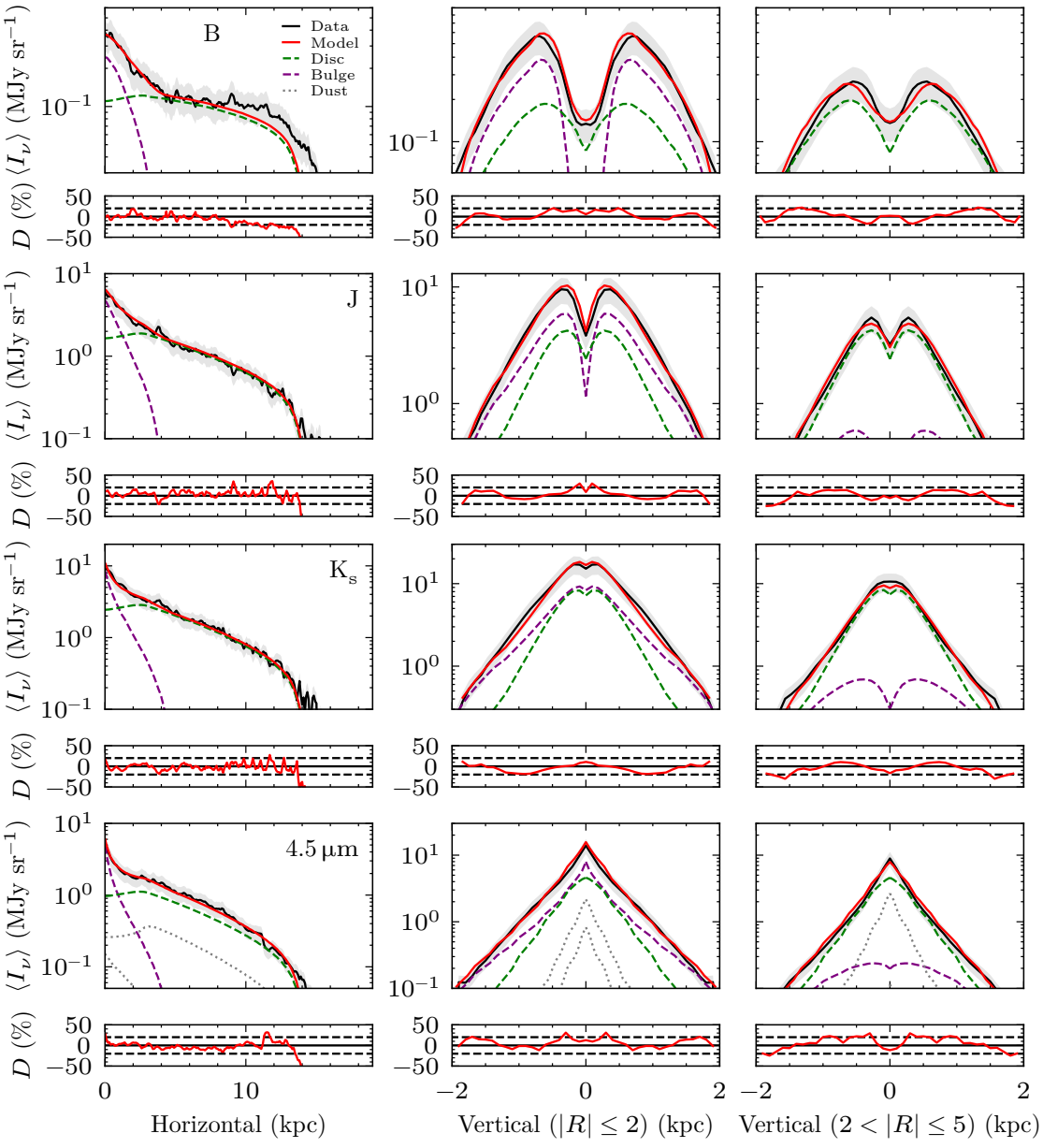

Figure 5.5: Same as Fig. 5.1, for the clumpy model of NGC 891.

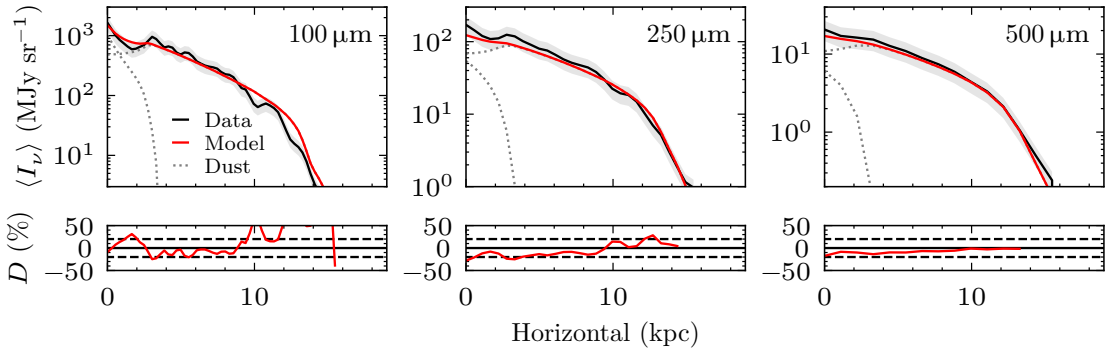

Figure 5.6: Same as Fig. 5.2, for the clumpy model of NGC 891.

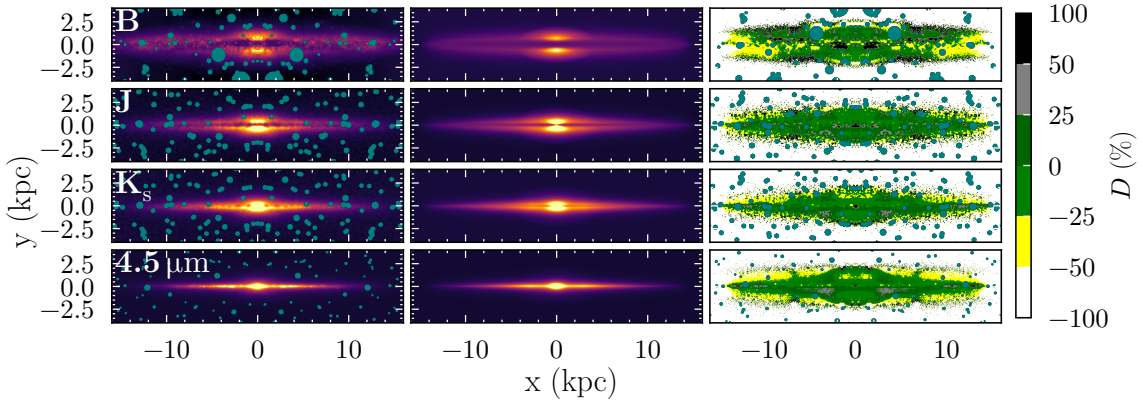

Figure 5.7: Same as Fig. 5.3, but for the clumpy model of NGC 891.

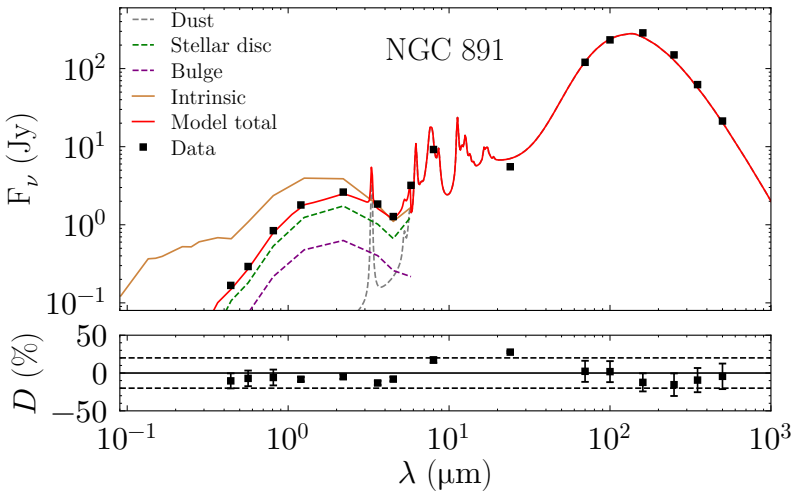

Figure 5.8: Same as Fig. 5.4, for the clumpy model of NGC 891.

5.4 Comparison Between the Diffuse and Clumpy Models of NGC 891

The key distinction between the diffuse and clumpy models is that, in the latter, a fixed fraction (50%) of the total dust mass is assigned to the clumpy component. As a result, the most notable difference between the best-fitting models is the optical depth of the diffuse component. With 50% of the dust mass in clumps ($f^{\rm c} = 0.5$), the optical depth of the diffuse component in the clumpy model is approximately half that of the purely diffuse model. The effects of this are a better fit to the data, in particularly at the critical NIR 2MASS J and $K_{\rm s}$ bands, essentially solving the energy balance problem in NGC 891. This is illustrated in Figs. 5.9 and 5.10, which directly compare the diffuse and the clumpy model fits at these wavelengths, both in the surface brightness profiles and in the maps.

5.4.1 Geometric Parameters

Since the dust opacity varies between the diffuse and the clumpy models, the fitted geometrical parameters are also expected to differ between models. Indeed, inspection of the values of these parameters, as listed in Table 5.2 and Table 5.4, shows the expected variation.

Both the diffuse and the clumpy models follow a similar stellar distribution to that of the MW (Natale et al., 2022), comprising a bulge and a disc that linearly declines in emissivity from the inner radius to the centre.

The radial distribution of stars in the main stellar disc is overall more extended in the clumpy model. This trend can be seen in Table 5.4, with the values starting to converge between models at longer NIR wavelengths. This difference can be attributed to attenuation effects. As the dust density declines exponentially with radius, its attenuation effect will also decrease with radius. In the outer regions of

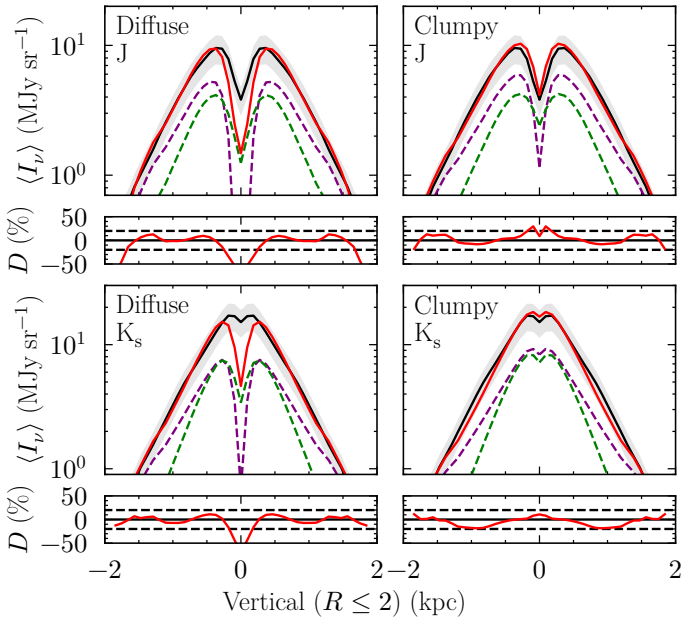

Figure 5.9: Comparison between the diffuse (left panels) and clumpy (right panels) models of NGC 891 in the 2MASS J and K_s bands. The plots follow the same format as Fig. 5.1.

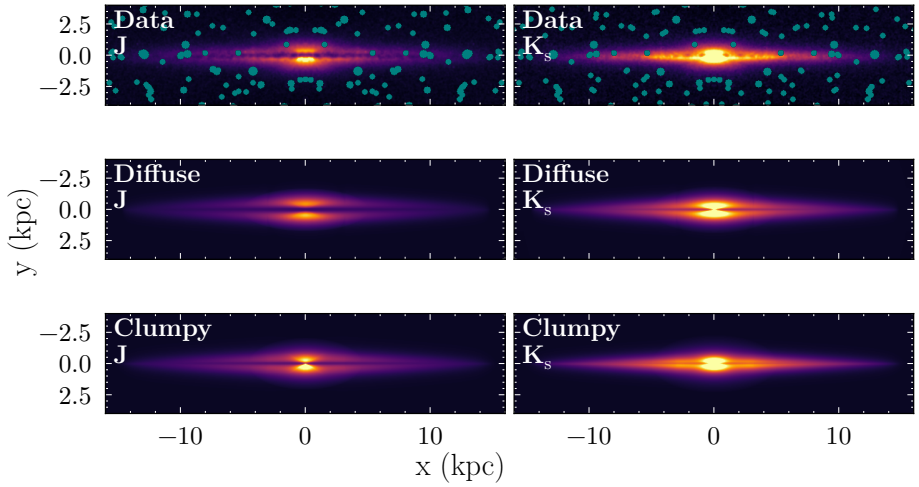

Figure 5.10: Surface brightness maps of NGC 891 in the 2MASS J and K_s bands. The top panels show the observed data reflected about the vertical axis passing through the galaxy's centre, the middle panels show the diffuse model, and the bottom panels show the clumpy model.

the galaxy, the disc becomes more optically thin, resulting in minimal attenuation of stellar emission. In contrast, the translucent regions at intermediate radii suppress stellar emission, making the surface brightness profile appear flatter than it would in the absence of dust. Greater attenuation leads to stronger suppression of emission, causing the diffuse model to favour a shorter stellar scale length.

For the same reason, the scale height of the main stellar disc, $z_{\rm s}^{\rm m-disc}$, differs significantly between the clumpy and diffuse models, with $z_{\rm s}^{\rm m-disc}(B) = 0.50\,{\rm pc}$ and $z_{\rm s}^{\rm m-disc}(B) = 0.42\,{\rm pc}$, respectively. Scale heights at all other wavelengths are listed in Table 5.4.

The radial distribution of stars (and consequently dust) in the main thin disc are found to be equivalent with a scale length of $h^{\rm m-tdisc} = 5\,{\rm kpc}$ derived in both the clumpy and diffuse models. Conversely, the scale length of the main dust disc is shorter in the clumpy model than in the diffuse model, with $h_{\rm d}^{\rm m-disc} = 10\,{\rm kpc}$ and $h_{\rm d}^{\rm m-disc} = 11\,{\rm kpc}$, respectively; however, these values are consistent within the uncertainties.

The increased attenuation in the diffuse model can account for the difference in the bulge parameters. The diffuse model has a considerably flatter bulge with respect to the clumpy model, with its emission more strongly confined to the midplane. This helps to compensate for the higher attenuation in the midplane. With a lower optical depth, such confinement is not necessary in the clumpy model. Interestingly, unlike the scale lengths and scale heights, the values determined for b/a for the two models do not seem to converge at longer wavelengths.

5.4.2 Global Properties

Dust Optical Depth and Dust Mass

The maximum face-on B-band optical depths are $\max\left(\tau_{\mathrm{B}}^{\mathrm{f}}\right) = 4.4 \pm 0.3$ for the diffuse model and $\max\left(\tau_{\mathrm{B}}^{\mathrm{f}}\right) = 1.6 \pm 0.1$ for the clumpy model. In both cases, these maxima occur at the galaxy's centre. The lower central optical depth in the clumpy model arises directly from its defining assumption: 50% of the total dust mass is placed in clumps, thereby reducing the opacity of the diffuse component. Because the fraction of dust that would otherwise reside in the diffuse component is redistributed to the clumpy component, the total dust mass between the two configurations is expected to be equivalent. The total dust masses are $M_{\mathrm{d}} = 8.0 \pm 0.5 \times 10^7\,\mathrm{M}_\odot$ for the diffuse model and $M_{\mathrm{d}} = 7.0 \pm 0.4 \times 10^7\,\mathrm{M}_\odot$ for the clumpy model. The small difference is likely due to the clumpy component contributing more efficiently to the submm emission, from which the dust mass is constrained.

When weighting the average dust opacity by the surface area, it was found that $\langle \tau_{\mathrm{B,area}}^{f} \rangle = 1.0 \pm 0.1$ for the diffuse model and 0.4 ± 0.1 for the clumpy model. The global view of dust opacity across the galaxy thus reveals that in the diffuse model the galaxy is roughly optically thick on average, whereas the clumpy model suggests the galaxy is optically thin.

Star Formation Rate

The global SFR of NGC 891 is found to be $\mathrm{SFR} = 7.2 \pm 0.6\,\mathrm{M}_\odot\,\mathrm{yr}^{-1}$ and $\mathrm{SFR} = 4.6 \pm 0.4\,\mathrm{M}_\odot\,\mathrm{yr}^{-1}$ for the diffuse and clumpy models, respectively. Since the clumpy model has a lower dust opacity in the diffuse medium, it produces less dust attenuation, which in turn leads to a solution with a lower intrinsic UV luminosity, and consequently, a lower SFR. This explains the differences in the derived solutions for NGC 891.

In the previous model by Popescu et al. (2004) a much smaller value for the SFR was obtained, with SFR $= 3.8\,\mathrm{M}_\odot\,\mathrm{yr}^{-1}$. This was solely due to the use of the ISOPHOT data in the 160 and 200 µm range, which, as discussed in the preamble of this chapter, provided flux densities that were approximately 1.5 times lower than those from the more recent Herschel observations, that were used in this work.

Shinn & Seon (2015) find a global star formation rate of SFR $= 2.4\,\mathrm{M}_\odot\,\mathrm{yr}^{-1}$ using the relation between SFR and IR luminosity (Kennicutt, 1998), however it should be noted that Hα is non-negligibly attenuated in NGC 891. Persic & Rephaeli (2007) obtain SFR $= 3.9\,\mathrm{M}_\odot\,\mathrm{yr}^{-1}$ and SFR $= 3.4\,\mathrm{M}_\odot\,\mathrm{yr}^{-1}$ when correcting for cirrus emission. Yoon et al. (2021) give an SFR $= 5.0\,\mathrm{M}_\odot\,\mathrm{yr}^{-1}$.

In the diffuse model, the main disc contributes 87.1% to the total SFR, with the remaining 12.9% provided by the inner disc. In the clumpy model however, the main disc contributes a higher percentage to the total, namely, 94.4% ($4.37\,\mathrm{M}_\odot\,\mathrm{yr}^{-1}$). The difference in the relative contributions of the main and inner disc to the total SFR can again be attributed to the higher dust attenuation of the diffuse model with respect to the clumpy one, with the attenuation having a larger effect in the inner regions of the galaxy.

5.4.3 Radial Trends

In addition to the global properties of NGC 891, their spatial variation within the galaxy is also examined. Fig. 5.11 shows the radial variation of surface density of SFR (Σ_{SFR}), specific SFR (sSFR), and surface density of stellar mass ($\Sigma_{M_\star}$). The stellar mass is calculated from the NIR flux following the method of Eskew, Zaritsky & Meidt (2012). The radial trends in Σ_{SFR} are similar between the clumpy and diffuse models. Given the larger global SFR, it is not surprising that the diffuse model shows higher values of Σ_{SFR} across the extent of the galaxy, particularly in the inner disc. Conversely, the values of $\Sigma_{M_\star}$ for the two models converge near the

centre. As a result, in the inner regions, the diffuse model has a higher sSFR until the interface between the morphological components is reached, beyond which the clumpy model consistently shows a higher sSFR.

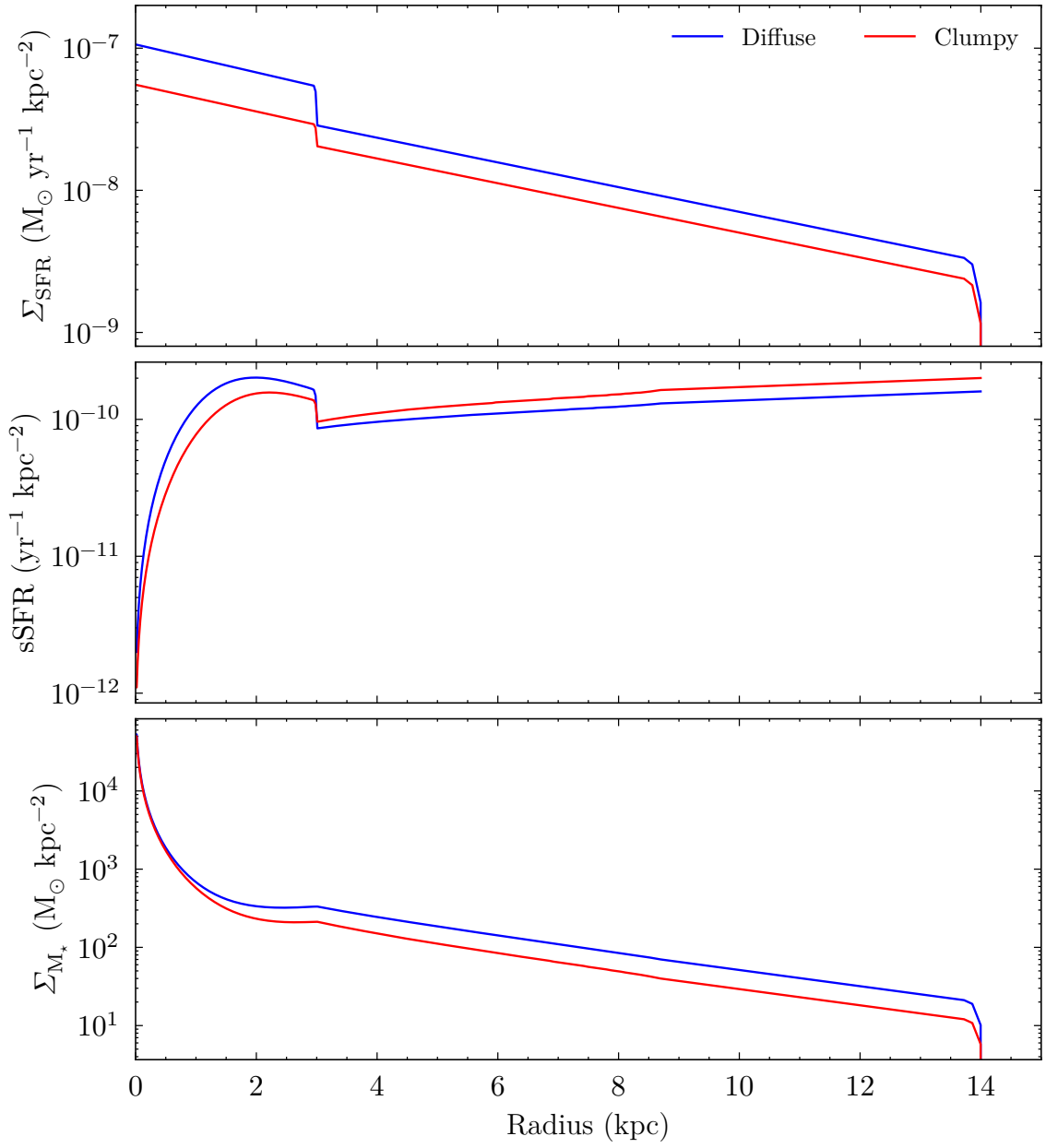

Figure 5.11: NGC 891 surface density of SFR ($\Sigma_{\rm SFR}$) (top), specific SFR (sSFR) (middle), and surface density of stellar mass ($\Sigma_{M_\star}$) (bottom). The diffuse and clumpy models are plotted with the blue, and red lines, respectively.

Chapter 6

Modelling the Edge-On Spiral Galaxy NGC 5907

With the success of the clumpy model in solving the energy balance problem in NGC 891, an attempt is made to see if it can also be applied to a peculiar edge-on spiral, that did not show an energy balance problem in previous studies, but for which no appropriate fits for the optical images could be found (Mosenkov et al., 2018).

NGC 5907 is one of the three galaxies comprising the NGC 5866 group, and is classified as an SA(s)c galaxy. It has a total stellar mass of $7.8 \times 10^{10}\,\mathrm{M}_{\odot}$ (Laine et al., 2016), and features a strongly warped H I disc (Sancisi, 1976) with a total H I mass of $M_{\mathrm{H\,I}} = 1.99 \times 10^{10}\,\mathrm{M}_{\odot}$ (Allaert et al., 2015). The warping can be attributed to its interaction with dwarf galaxy PGC 54419, which can be seen near the tip of the H I warp (Shang et al., 1998). Another feature likely arising from this interaction is a faint stellar stream, first discovered by Shang et al. (1998). However, the true structure of this stream remains debated, as several independent observations have yielded conflicting results (Zheng et al., 1999; Martínez-Delgado

et al., 2008; van Dokkum et al., 2019; Müller, Vudragović & Bílek, 2019). NGC 5907 is located at a distance of $D = 16.3\,\mathrm{Mpc}$ (Verstappen et al., 2013), and with a modest inclination of $i = 87.2°$ (Xilouris et al., 1999) it is noticeably more inclined than NGC 891. Nevertheless, NGC 5907 still exhibits a thin dust lane in the shorter optical wavelengths.

NGC 5907 was one of the galaxies previously modelled by Xilouris et al. (1999) in the optical range. NGC 5907 was subsequently modelled with the panchromatic diffuse model of Popescu et al. (2000) in Misiriotis et al. (2001), but at that time there were no observational data at the peak of the dust emission SED, therefore that model lacked enough observational constraints. Here the available panchromatic data are used to model NGC 5907, with both the diffuse and clumpy models.

Table 6.1: Summary of observational data used to model NGC 5907. [a]York et al. (2000), [b]Skrutskie et al. (2006), [c]Fazio et al. (2004), [d]Poglitsch et al. (2010)

Telescope	Filter/ Instrument	Wavelength (μm)	Flux (Jy)	pixel scale (arcsec)	pixel scale (pc)	Calibration error (per cent)
SDSS[a]	u	0.355	0.04 ± 0.003	0.5	40	2
	g	0.469	0.15 ± 0.003	0.5	40	2
	r	0.617	0.30 ± 0.01	0.5	40	2
	i	0.748	0.46 ± 0.01	0.5	40	2
2MASS[b]	J	1.2	1.02 ± 0.03	1	79	3
	K_s	2.2	1.30 ± 0.04	1	79	3
Spitzer[c]	IRAC	3.6	0.79 ± 0.02	0.6	47	3
	IRAC	4.5	0.52 ± 0.02	0.6	47	3
	IRAC	5.8	1.03 ± 0.03	0.6	47	3
	MIPS	24	1.57 ± 0.02	1.5	119	1
Herschel[d]	PACS	100	58.26 ± 3.50	1.7	134	12
	PACS	160	89.31 ± 5.36	2.85	225	12
	SPIRE	250	52.80 ± 3.96	6	474	15
	SPIRE	350	24.70 ± 1.85	8	632	15
	SPIRE	500	9.65 ± 0.72	12	948	15

6.1 Observational Data

Given the ubiquity of the imaging data, much of the panchromatic data used to model NGC 5907 were obtained by the instruments described in § 5.1. An exception is that optical data from the Sloan Digital Sky Survey (SDSS; York et al., 2000) was used, specifically the u, g, r, and i bands. The pixel size of these data are 0.5 arcsec, which at the distance of $D = 16.3$ Mpc, corresponds to a physical size of 40 pc per pixel. The full list of the data used to model NGC 5907 are given in Table 6.1. The same post-processing procedure was used for these data, as described in § 5.1.1.

As mentioned before, NGC 5907 shows some mild departure from the edge-on view, being less inclined that the previously studied NGC 891 (see left panels of Fig. F.4). This introduces a stronger asymmetry about its midplane than in NGC 891, in particular in the optical images, where a near side and a far side can be easily identified.

6.2 The Diffuse Model

Inspection of the averaged horizontal profiles of the data (Figs. 6.1–6.2 for selected wavelengths and Figs. F.1–F.3 for all available wavelengths) shows that NGC 5907 exhibits a prominent central peak in the optical/NIR wavelengths due to bulge emission. Outside the bulge-dominated region, there is a clear exponential decline in SB, a trend that is visible in both the optical/NIR and in the FIR/submm wavelengths. Usually bulge emission produces strong central peaks in the MIR/FIR when the dust distribution is exponential right to the centre (e.g. Popescu & Tuffs, 2013). However this is not seen in NGC 5907. This is taken as indicative of a reduction of dust towards the centre of the galaxy.

Thus, NGC 5907 was modelled with two main morphological components: a bulge and a disc. The disc consists of a stellar disc, a thin stellar disc, a dust disc, and a thin dust disc. The dust disc was taken to have an inner radius of $R_{\rm in} = 2\,{\rm kpc}$, with a linearly decreasing dust density towards the centre inwards of $R_{\rm in}$, and an exponential decrease outwards of $R_{\rm in}$. The full list of geometrical parameters for the diffuse model can be found in the left-column of Table 6.2, and Table 6.3. The fits to the surface brightness profiles are shown again in Figs. 6.1–6.2 for selected wavelengths and Figs. F.1–F.3 for all available wavelengths. The surface brightness maps of the data, best-fitting model, and their residuals are shown in Fig. 6.3 for selected wavelengths and in Fig. F.4 for all available wavelengths. The integrated

SED is shown in Fig. 6.4.

Overall, the diffuse model provides a reasonable fit to the horizontal and vertical SB profiles at most of the wavelengths, although there are still some residual features in the optical maps, and some deviations from the exact shape of the profiles, indicative of a more complex geometry. The poorest fits occur at 24 and 100 μm, where the emission is dominated by hot dust. The diffuse model predicts too warm a dust component, overestimating the emission in this region. This can also be seen in the fit to the integrated SED, plotted in Fig. 6.4.

Unlike in NGC 891, the diffuse model does not seem to suffer for an energy balance problem (between optical/NIR and submm), confirming thus the finding of Mosenkov et al. (2018). This difference can be attributed to NGC 5907's lower optical depth: while the diffuse model of NGC 891 has a maximum optical depth in the centre of $\max(\tau_{\rm B}^{f}) = 3.3$, NGC 5907 has approximately half this value with $\max(\tau_{\rm B}^{f}) = 1.6$. Additionally, NGC 5907's less inclined orientation further reduces the dust column density along the line-of-sight compared with a perfectly edge-on orientation. On the other hand the diffuse model overestimates the emission in the MIR/FIR. This can also be thought of as being part of an energy balance problem: the diffuse model predicts too hot a dust component, due to the overestimation of attenuation of energetic photons.

Table 6.2: The free geometrical parameters of NGC 5907, for the best fitting diffuse (middle column), and clumpy models (right column), denoted with 'd' and 'c' respectively. All length parameters are given in kpc.

Parameter	d	c
$h_{\rm s}^{\rm disc}(g)$	7.8 ± 0.4	8.2 ± 0.4
$h_{\rm s}^{\rm tdisc}$	5.5 ± 0.3	6.0 ± 0.3
$h_{\rm d}^{\rm disc}$	15 ± 1	14 ± 1
$\chi_{\rm d}^{\rm disc}$	-1.0 ± 0.2	-1.0 ± 0.2
$z_{\rm s}^{\rm disc}(g)$	0.44 ± 0.02	0.52 ± 0.02
$z_{\rm d}^{\rm disc}$	0.30 ± 0.03	0.30 ± 0.03
$R_{\rm e}(g)$	1.0 ± 0.2	1.0 ± 0.2
$\frac{b}{a}(g)$	0.40 ± 0.04	0.48 ± 0.04

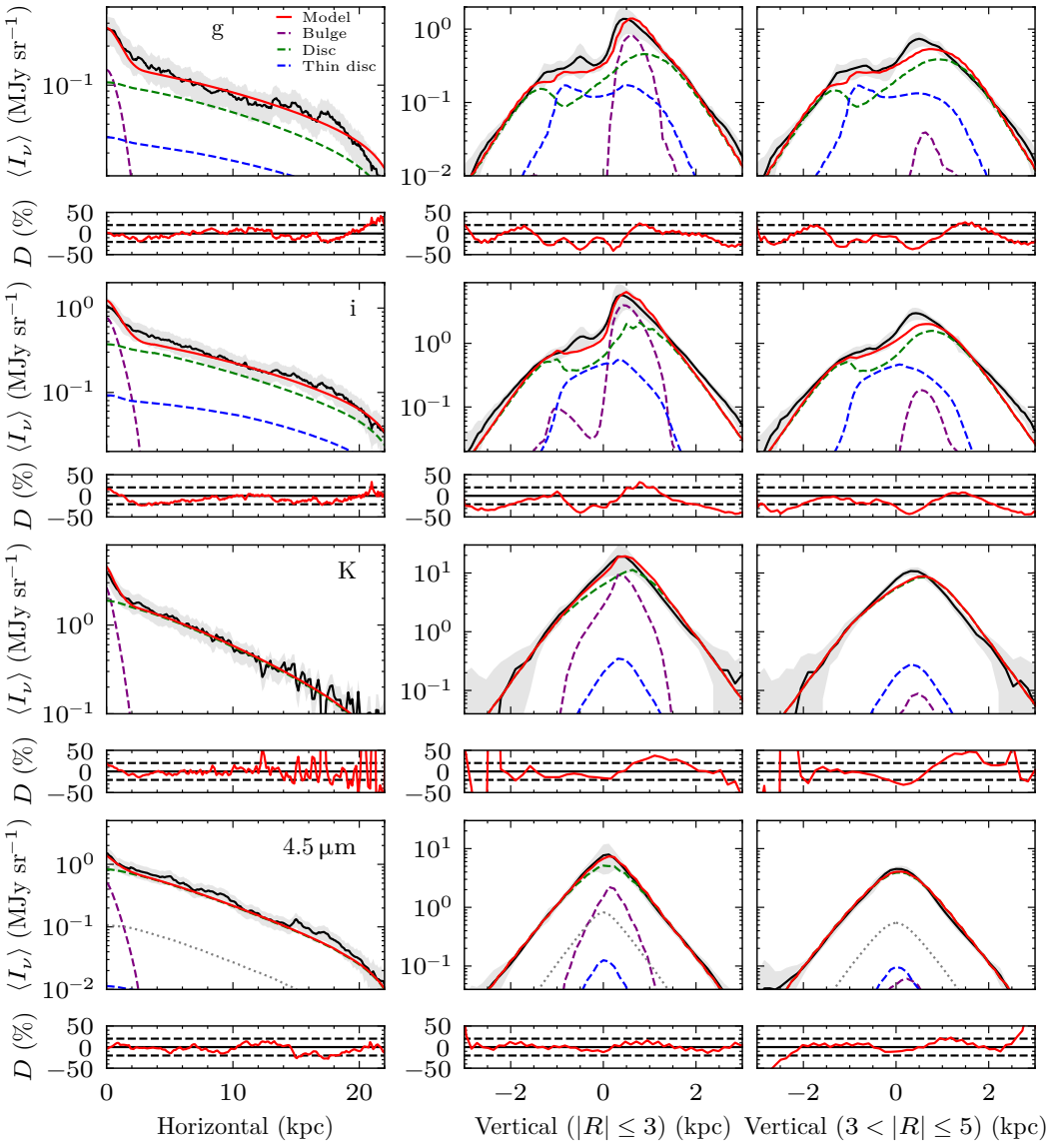

Figure 6.1: Averaged horizontal (mirrored about the central vertical axis)(LH panel) and averaged vertical (middle and RH panel) SB profiles of the pure diffuse model of NGC 5907 at selected wavelengths in the optical/NIR. The observed SB profiles are plotted with solid black line with the shaded banding indicating the uncertainty. The solid red line indicates the model total, with the individual component contributions plotted with the dashed and dotted lines. The percent differences between the model total and the observed profiles, $D\,[\%]$, are plotted in the panels below each profile, with the dashed horizontal lines indicating $\pm\,20\,\%$ deviation.

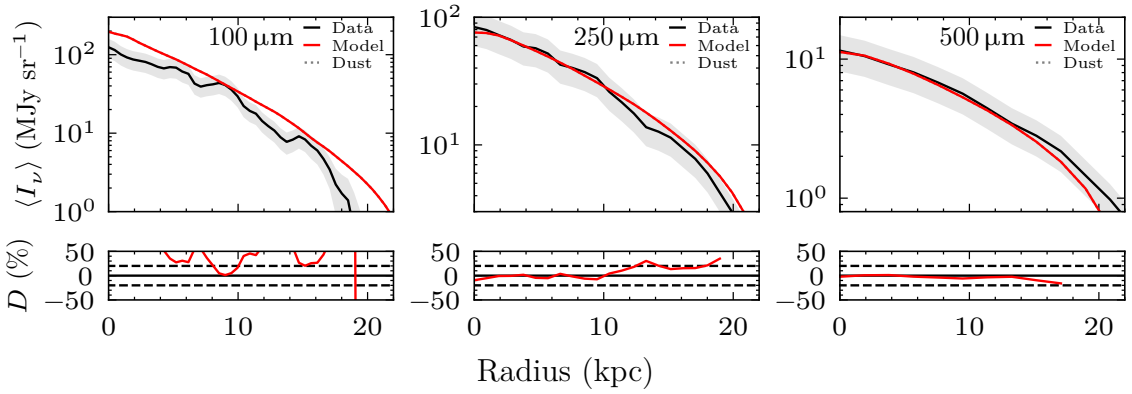

Figure 6.2: Averaged horizontal SB profiles of the pure diffuse model at selected wavelengths in the FIR/submm. The plotting details are the same as in Fig. 6.1

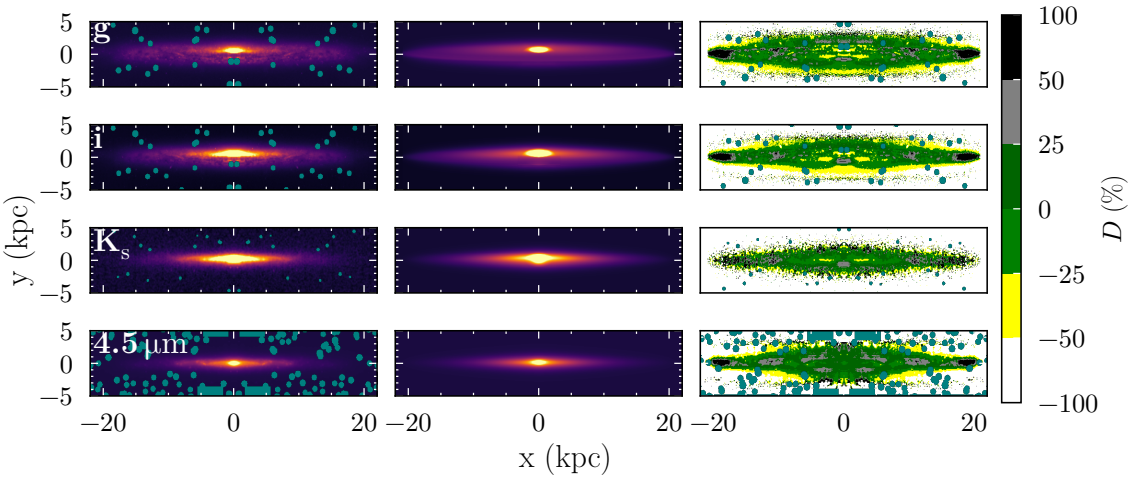

Figure 6.3: Left: surface brightness maps of NGC 5907 at selected optical/NIR wavelengths, mirrored about their vertical central axis. Middle: surface brightness maps of the corresponding diffuse model images. Right: residuals between the data and model images calculated as $D = (M - O)/O$. Masked foreground stars are marked in teal.

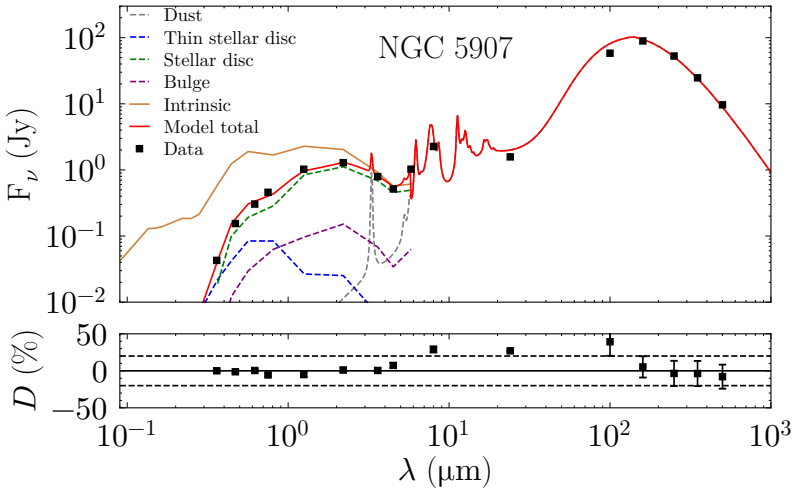

Figure 6.4: The spatially integrated model SED of the pure diffuse solution of NGC 5907 plotted with the observed data (black squares) and the associated uncertainties (which are mainly contained in the black squares). Contributions from each of the galaxy components (dashed lines) and the intrinsic stellar SED (solid brown line) are also shown. The lower panel shows the per cent difference between the model SED and the observed data. To guide the eye dashed lines are plotted to show ±20 % deviation.

Table 6.3: The geometrical parameters of NGC 5907 fixed from data and theoretical considerations. The values are the same between the diffuse and clumpy models. All length parameters are given in kpc.

Parameter	Value
$R_{\rm in,s}^{\rm tdisc}$	0
$R_{\rm in,s}^{\rm disc}$	0
$R_{\rm in,d}^{\rm disc}$	2
$R_{\rm tin,s}^{\rm tdisc}$	0
$R_{\rm tin,s}^{\rm disc}$	0
$R_{\rm tin,d}^{\rm disc}$	0
$R_{\rm t,s}^{\rm tdisc}$	23
$R_{\rm t,s}^{\rm disc}$	23
$R_{\rm t,d}^{\rm disc}$	23
$z_{\rm s}^{\rm tdisc}$	0.09
$n_{\rm s}$	1

Table 6.4: NGC 5907: wavelength dependent model parameters for main disc and bulge, for the diffuse and clumpy models, denoted with 'd' and 'c', respectively. All length parameters are given in kpc.

Parameter	Filter								
	u	g	r	i	J	$K_{\rm s}$	3.6 µm	4.5 µm	5.8 µm
d									
$h_{\rm s}^{\rm disc}$	7.8 ± 1	7.8 ± 1	6.3 ± 0.2	6.0 ± 0.1	4.7 ± 0.1	4.8 ± 0.1	4.8 ± 0.1	4.7 ± 0.1	4.5 ± 0.2
$z_{\rm s}^{\rm disc}$	0.44 ± 0.01	0.44 ± 0.01	0.43 ± 0.01	0.43 ± 0.01	0.42 ± 0.01	0.4 ± 0.01	0.44 ± 0.02	0.43 ± 0.02	0.42 ± 0.02
$R_{\rm e}$	1.0 ± 0.05	1.0 ± 0.05	1.0 ± 0.05	1.0 ± 0.05	1.0 ± 0.05	0.8 ± 0.05	1.0 ± 0.05	1.0 ± 0.05	1.0 ± 0.05
b/a	0.4 ± 0.01	0.4 ± 0.01	0.4 ± 0.01	0.44 ± 0.01	0.36 ± 0.01	0.5 ± 0.01	0.38 ± 0.01	0.38 ± 0.01	0.38 ± 0.01
c									
$h_{\rm s}^{\rm disc}$	8.2 ± 1	8.2 ± 1	6.7 ± 0.2	6.3 ± 0.1	5.0 ± 0.1	5.0 ± 0.1	4.8 ± 0.1	4.7 ± 0.1	4.5 ± 0.1
$z_{\rm s}^{\rm disc}$	0.52 ± 0.02	0.52 ± 0.02	0.50 ± 0.02	0.52 ± 0.01	0.45 ± 0.01	0.43 ± 0.01	0.44 ± 0.01	0.43 ± 0.02	0.42 ± 0.02
$R_{\rm e}$	1.0 ± 0.05	1.0 ± 0.05	1.0 ± 0.05	1.0 ± 0.05	1.0 ± 0.05	0.8 ± 0.05	1.0 ± 0.05	1.0 ± 0.05	1.0 ± 0.05
b/a	0.48 ± 0.01	0.48 ± 0.01	0.48 ± 0.01	0.44 ± 0.01	0.36 ± 0.01	0.50 ± 0.01	0.38 ± 0.01	0.38 ± 0.01	0.38 ± 0.01

6.3 The Clumpy Model

The best-fitting clumpy model derived for NGC 5907 has the same morphological components as its diffuse counterpart. Just as for NGC 891, the only additional parameter in the clumpy model is the fraction of mass in clumps f^{c}, which was found to be $f^{\mathrm{c}} = 0.5$. The fits to the surface brightness profiles are shown for a selection of wavelengths in Figs. 6.5–6.6, and for all wavelengths in Figs. F.5–F.7. The surface brightness maps of the data, model and residuals are shown for a selection of wavelengths in Fig. 6.7, and for all optical/NIR wavelengths in Fig. F.8. The spatially integrated SEDs of the model and data are shown in Fig. 6.8. The geometric parameters of the clumpy model are given in the right-hand column of Table 6.2 and Table 6.3.

The most notable improvement in the clumpy model over the diffuse model can be seen in the MIR/FIR, where the clumpy model is able to fit the data with deviations typically less than $\pm 20\,\%$. As characteristic of the clumpy model, this can be attributed to the reduction in attenuation and consequently the reduction in dust grain heating from the energetic photons emitted by young stars. Otherwise the quality of the fit achieved by the clumpy model in the optical/NIR is of similar quality.

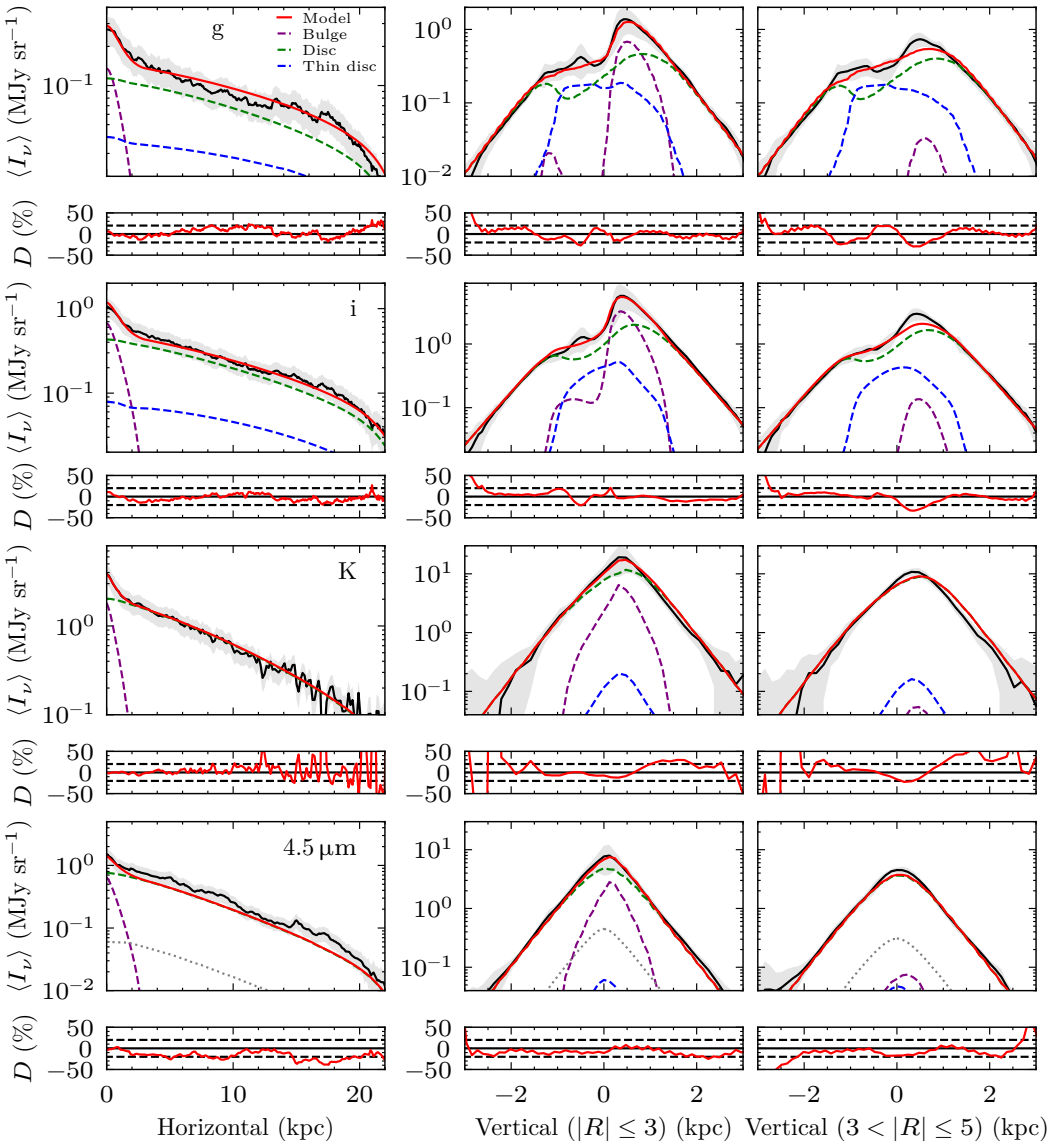

Figure 6.5: Same as Fig. 6.1, for the clumpy model of NGC 5907.

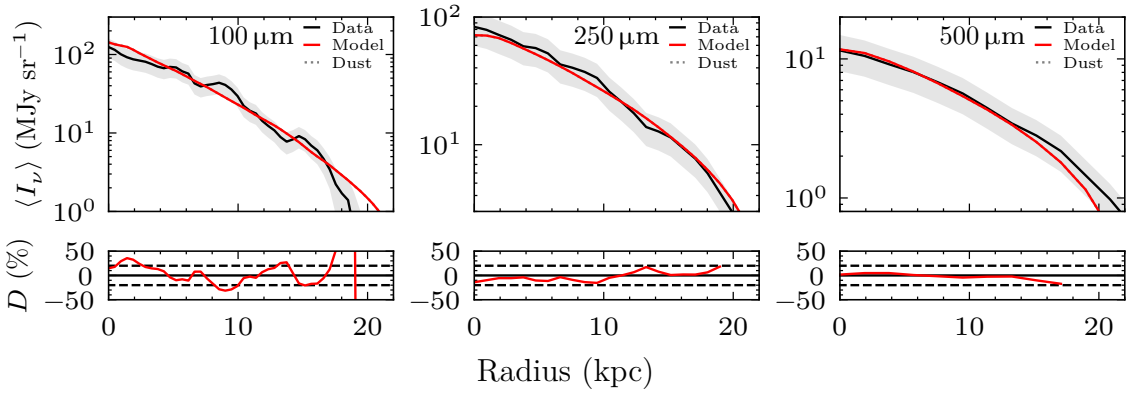

Figure 6.6: Same as Fig. 6.2, for the clumpy model of NGC 5907.

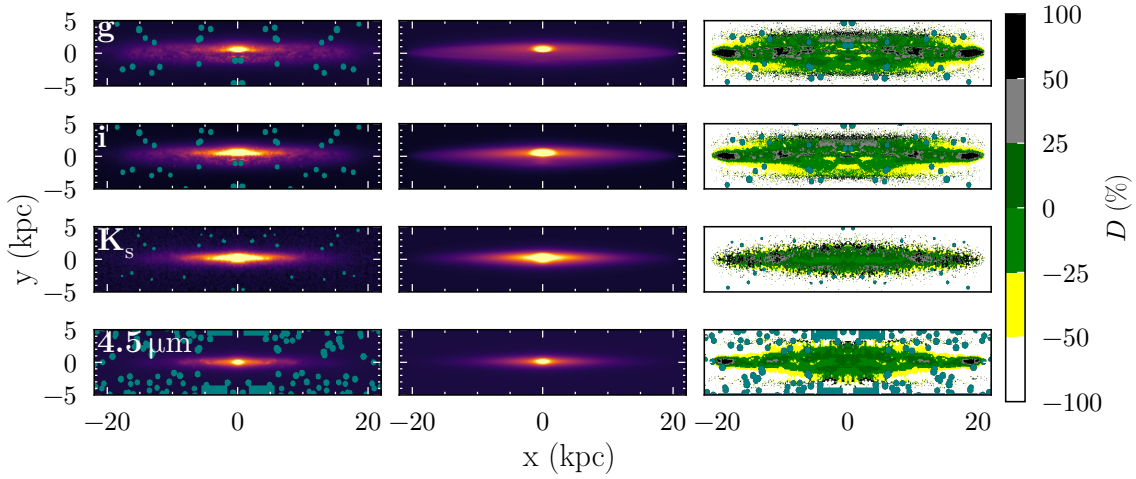

Figure 6.7: Same as Fig. 6.3, for the clumpy model of NGC 5907.

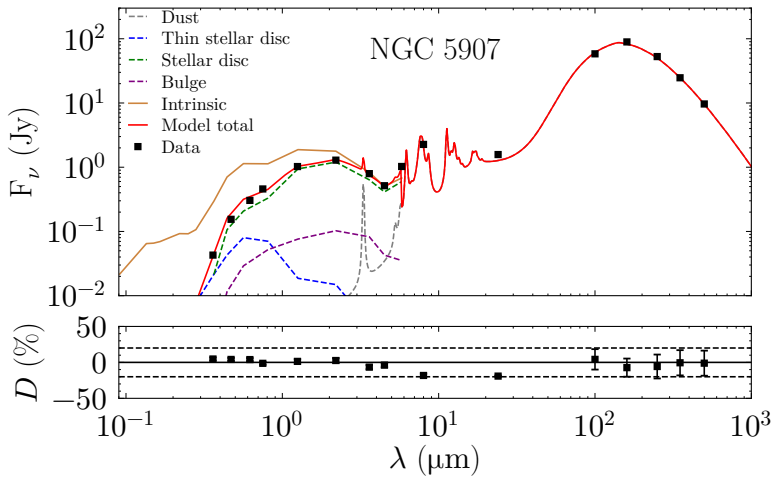

Figure 6.8: Same as Fig. 6.4, for the clumpy model of NGC 5907.

6.4 Comparison Between the Diffuse and Clumpy Models of NGC 5907

The defining difference between the diffuse and clumpy models is that, in the latter, 50% of the galaxy's total dust mass is assigned to the clumpy component. Consequently, the optical depth of the clumpy model is approximately half that of the diffuse model, and as a result, attenuation is significantly reduced. In NGC 5907, the consequence of this is most noticeable detected in the MIR/FIR, where the integrated model emission is reduced by up to 40% at 24 μm and 25% at 100 μm, thus providing a good fit to the data.

6.4.1 Geometrical Parameters

With the significant reduction in opacity in the clumpy model, the optimal parameters derived with the pure diffuse model will not necessarily be optimal in the clumpy model. Re-optimising these parameters for the clumpy model enables a direct comparison with those derived in the diffuse model. Table 6.2 lists the parameters for the diffuse and clumpy models in the left and right columns, respectively. The trends generally follow those found in NGC 891. The stellar disc of the clumpy model is more radially extended than in the diffuse model, with larger scale lengths particularly at shorter wavelengths. This can be seen in Table 6.4, with the values converging at longer wavelengths in the NIR. Table 6.4 also shows the wavelength-dependent values of scale height, for which a similar trend can be seen. The clumpy model shows a more vertically extended stellar disc, particularly at shorter wavelengths. Again, these values begin to converge at longer wavelengths. Both of these results can be explained with the difference in attenuation between the two models, which is explained in detail in § 5.4.1. No such trend can be detected in the bulge parameter b/a, as apart from the g and r bands, the diffuse and clumpy models

share the same values.

The clumpy model shows a more radially extended thin stellar disc with a scale length of $h^{\rm tdisc} = 6.0\,$kpc, compared with the scale length of $h^{\rm tdisc} = 5.5\,$kpc in the diffuse model. While it is true that the dust disc in the clumpy model is more radially concentrated with a scale length of $h_{\rm d}^{\rm disc} = 14\,$kpc compared to the scale length of $h_{\rm d}^{\rm disc} = 15\,$kpc found in the diffuse model, the difference is relatively small. Especially for such large scale lengths, this difference is attributable to noise introduced by fitting.

Table 6.5: Comparison of parameters derived for NGC 5907 in this work to the models of Xilouris et al. (1999) and Mosenkov et al. (2018). N.B., the stellar parameters derived by Mosenkov et al. (2018) were done so using IMFIT (Erwin, 2015), which differ slightly from the parameters derived in this work.

	$h_{\rm d}^{\rm disc}$ (kpc)	$z_{\rm d}^{\rm disc}$ (kpc)	$\tau_{\rm B}^{\rm f}$	$h_{\rm s}^{\rm disc}(g)$ (kpc)	$h_{\rm s}^{\rm tdisc}(g)$ (kpc)	i
This work (clumpy model)	14.0	0.30	0.88	8.20	6.00	87.2°
Xilouris et al. (1999)	5.30	0.13	0.55	5.02	-	87.2°
Mosenkov et al. (2018)	7.13	0.25	2.65[a]	5.59	4.75	85.1°

[a] $\tau_{\rm B}^{\rm f}$ is converted from $\tau_{\rm V}^{\rm f} = 2.01$

As previously mentioned, NGC 5907 was modelled by Mosenkov et al. (2018) as part of a study on seven edge-on spiral galaxies. A comparison of the scale length, scale height and optical depth derived from the clumpy model and that of Mosenkov et al. (2018) is given in Table 6.5. A notable difference is that Mosenkov et al. (2018) derive a lower inclination of 85.1°, which, at these extreme high inclinations, can significantly influence the fit. This is discussed more in § 6.5. Otherwise, the scale length of the stellar disc and thin stellar disc at 3.6 µm are remarkably similar, with $h_{\rm s}^{\rm disc}(3.6\,\mu{\rm m}) = 4.8\,$kpc derived with the clumpy model and $h_{\rm s}^{\rm disc}(3.6\,\mu{\rm m}) = 5.59\,$kpc

by Mosenkov et al. (2018). This is to be expected, since at this wavelength images are not so significantly affected by dust attenuation. At other wavelengths Mosenkov et al. (2018) fixed the scale lengths to be the same as at 3.6 µm, resulting in a large discrepancy to this model. In the clumpy model, a strong increase was found in the derived scale length of the stellar disc, $h_{\rm s}^{\rm disc}$, with decreasing wavelength, from 4.8 kpc at 3.6 µm to 8.2 kpc in the g band. This means that at shorter wavelengths, this model has a scale length that is almost twice the value fixed by Mosenkov et al. (2018). This would produce significant changes in the appearance of the predicted optical images.

Another significant difference is seen in the scale length of the dust disc, with this work deriving $h_{\rm d}^{\rm disc} = 14$ kpc, almost twice that of $h_{\rm d}^{\rm disc} = 7.13$ kpc found in Mosenkov et al. (2018). This is likely related to the difference in the scale length of the stellar disc, as well as to the derived optical depth.

The parameters derived by Xilouris et al. (1999) through fitting the optical images are also shown in Table 6.5. The difference in the dust scale length is even greater, with Xilouris et al. (1999) finding $h_{\rm d}^{\rm disc} = 5.30$ kpc. Xilouris et al. (1999) also derived the scale height of the dust disc to be $z_{\rm d}^{\rm disc} = 0.13$ kpc. While at first glance this seems to be significantly lower than the scale height derived with the clumpy model, the comparison is not straightforward, as the model of Xilouris et al. (1999) comprises a single dust disc, whereas the clumpy model has an additional thin disc.

6.4.2 Global Properties

Dust Optical Depth and Dust Mass

The clumpy model of NGC 5907 allocates 50 % of the galaxy's dust mass into clumps, hence, the maximum face-on optical depth in the B-band found for the clumpy model ($\max(\tau_{\rm B}^{\rm f}) = 0.9$) is significantly lower than in the diffuse model ($\max(\tau_{\rm B}^{\rm f}) = 1.4$).

Both maxima occur at the inner radius of the dust disc ($R_{\rm in,d}^{\rm disc} = 2\,{\rm kpc}$). Mosenkov et al. (2018) found $\max(\tau_{\rm B}^{\rm f}) = 2.7$[1], significantly larger than even the diffuse model finds. However, their results are derived using a single dust disc in conjunction with a smaller scale length for both the dust and the stellar disc and the authors comment that their solution is likely over-estimating the dust opacity.

The dust masses derived with both models are similar. The total dust mass of the clumpy model is $M_{\rm d} = 1.2 \pm 0.2 \times 10^8\,{\rm M}_\odot$, while the diffuse model has $M_{\rm d} = 1.0 \pm 0.2 \times 10^8\,{\rm M}_\odot$. Mosenkov et al. (2018) found the total dust mass of NGC 5907 to be $M_{\rm d} = 8.97 \pm 1.31 \times 10^7\,{\rm M}_\odot$, which is smaller than the values derived in this study, despite their higher dust opacity. This is due to their different dust model used for the optical constants of the grains (THEMIS model; Jones et al., 2017, as opposed to the Draine model; Weingartner & Draine, 2001; Draine & Li, 2007).

Star Formation Rate

The diffuse and clumpy models find global SFRs of ${\rm SFR} = 1.4 \pm 0.1\,{\rm M}_\odot{\rm yr}^{-1}$ and ${\rm SFR} = 0.9 \pm 0.1\,{\rm M}_\odot{\rm yr}^{-1}$, respectively. This reduction in SFR directly follows from the reduction in attenuation, allowing for a lower intrinsic UV luminosity, as described in § 5.4.2. Misiriotis et al. (2001) find ${\rm SFR} = 0.99\,{\rm M}_\odot{\rm yr}^{-1}$[2]. Leroy et al. (2019) find ${\rm SFR} = 2.4 \pm 1.8\,{\rm M}_\odot{\rm yr}^{-1}$[2] using the FUV and WISE W4 luminosities.

6.5 Dust Attenuation Effects in Highly Inclined Disc Galaxies

In a nearly edge-on galaxy, such as in NGC 891, there is typically a strong large scale symmetry above and below the disc, although one can still detect the asymmetry

[1] Converted from $\max(\tau_{\rm V}^{\rm f}) = 2.01$

[2] rescaled for the assumed distance $D = 16.3\,{\rm Mpc}$

due to the slight deviation from 90°. Larger deviations from this edge-on inclination can introduce complex projection effects into views of the stellar and dust discs, such as is seen in NGC 5907, with an inclination of $i = 87.2°$. Upon examination of the surface brightness maps (see Fig. 6.3) one can identify the near side (in the negative y region of Fig. 6.3) and a far side (in the positive y region of Fig. 6.3). For NGC 5907, it was found that the thin stellar disc and the stellar disc show different behaviour with respect to their asymmetry above and below the midplane. This effect is most readily seen in the vertical surface brightness profiles of NGC 5907 in the u-band (see Fig. F.1). The thin disc with a scale height of $z_{\rm s}^{\rm tdisc} = 90\,{\rm pc}$ peaks at $z \approx -1\,{\rm kpc}$, while the stellar disc, with $z_{\rm s}^{\rm disc} = 520\,{\rm pc}$ peaks at $z \approx 1\,{\rm kpc}$. The magnitude of this effect diminishes with increasing wavelength, due to the reduction in attenuation.

To better understand the interplay between the scale heights of stars and dust in modulating the appearance of highly inclined galaxies, simulations of a NGC 5907-like disc were produced (same inclination and geometry for the dust disc). However, in the simulations only one stellar disc with varying scale height was used. Thus the scale height of the dust disc was fixed to $z_{\rm d} = 300\,{\rm pc}$ and the scale height of the stellar disc was varied between values of $z_{\rm s} = 90 - 500\,{\rm pc}$. These simulations are shown in Fig. 6.9. It can be seen that with $z_{\rm s} = 90\,{\rm pc}$, the emission dominates in the near side of the disc. As $z_{\rm s}$ is incrementally increased, the peak of the emission shifts upwards from the near side until at $z_{\rm s} = 150\,{\rm pc}$ the entire disc appears uniformly bright. Increasing the $z_{\rm s}$ further shifts the peak of the emission to the far side of the disc, revealing extinction from the dust lane. At the largest $z_{\rm s}$, emission from the underside of the galaxy becomes visible.

These effects can be explained by the attenuation of the discs and their relative scale heights. At small scale heights, the stellar disc is fully engulfed by the dust disc. Viewing the backside of the galaxy, the line-of-sight optical depth is large,

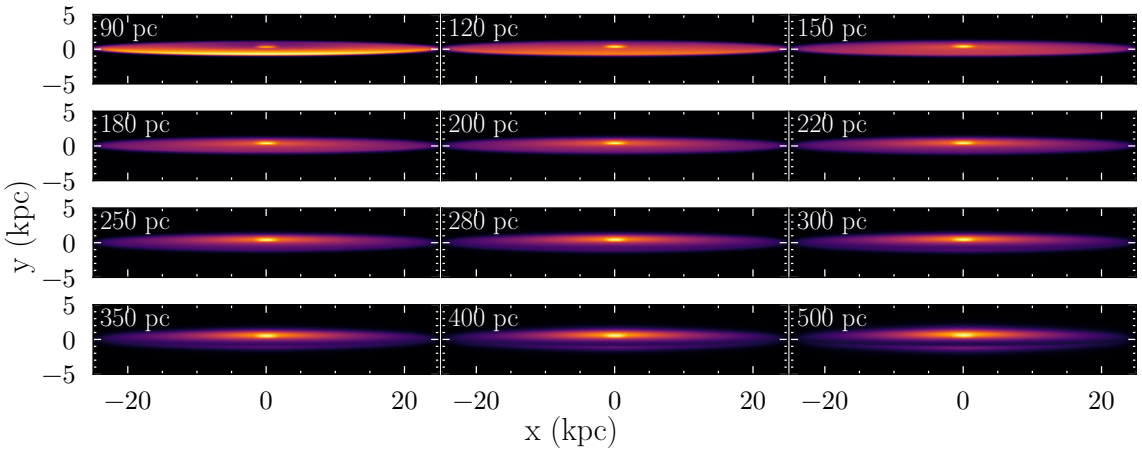

Figure 6.9: Surface brightness maps of a single stellar disc attenuated by dust. The viewing angle is at 87.2°. For the smallest scale height of $z = 90\,\mathrm{pc}$ the disc is brightest at the near edge of the disc. The scale height of the dust disc is kept constant at $z^{\mathrm{d}} = 300\,\mathrm{pc}$. As the scale height increases, the brightest region shifts upwards and lies at the top-side of the disc leaving a prominent dust lane.

suppressing the emission, however at the very front edge of the galaxy, the light is far less obscured. At the largest z_{s}, stars extend above and below the extent of the dust disc, thus their emission is unobscured. In this case, $z_{\mathrm{s}} = 150\,\mathrm{pc}$ is the inflexion point where these two effects are balanced.

Chapter 7

Application of the Clumpy Model to a Small Galaxy Sample

The success in the modelling of NGC 891 (§ 5) and NGC 5907 (§ 6) using the clumpy model and solving the energy balance problem raises the question of whether the clumpy model produces the right energy balance for other galaxies, and if it is generally applicable for galaxies of any inclination. To test this a small sample of galaxies was built spanning the whole inclination range. The sample includes the galaxies that have previously been modelled with the pure diffuse model, and were described in § 1: M33, TP20; NGC 628, Rushton et al., 2022; M51, Inman et al., 2023; M101 and NGC 3938, Pricopi et al., 2025. In addition, NGC 3521 was also included in this sample. NGC 3521 was chosen to include a galaxy with an intermediate inclination ($i = 73°$; Walter et al., 2008; Pilyugin, Tautvaišienė & Lara-López, 2023). The fitting procedure used for each face-on and edge-on galaxy is described in § 3.3.1, and § 3.3.2, respectively. For the intermediate inclination galaxy NGC 3521 the fitting procedure designed for face-on galaxies was used. The panchromatic data used to constrain the clumpy models are largely the same as those used in the original diffuse models, with the exception of NGC 5907 and NGC 891

for which, as discussed in § 5.1 and § 6.1, newer data have become available.

7.1 Global Properties of the Galaxy Sample

The galaxies contained in this small sample considered for modelling are tabulated with some of their basic properties in Table 7.1.

Table 7.1: Basic properties of galaxies in this sample. The distances and inclination are those used in modelling.

Galaxy	D (Mpc)	i (deg)	RA (J2000)	Dec (J2000)	Type
M33	0.859	56.0	$01^h33^m51^s$	$+30^d39^m37^s$	SA(s)cd
M51	8.58	20.3	$13^h29^m53^s$	$+47^d11^m43^s$	SA(s)bc pec
M101	6.71	18.0	$14^h03^m13^s$	$+54^d20^m56^s$	SAB(rs)cd
NGC 628	9.50	15.0	$01^h36^m42^s$	$+15^d47^m01^s$	SA(s)c
NGC 891	9.85	89.7	$02^h22^m33^s$	$+42^d20^m54^s$	SA(s)b
NGC 3521	10.7	72.7	$11^h05^m49^s$	$-00^d02^m09^s$	SAB(rs)bc
NGC 3938	17.9	14.0	$11^h52^m49^s$	$+44^d07^m15^s$	SA(s)c
NGC 5907	16.3	87.2	$15^h15^m53^s$	$+56^d19^m48^s$	SA(s)c

M33

Classified as an SA(s)cd galaxy by de Vaucouleurs (1991), M33 is a flocculant spiral, and is the third largest galaxy in the Local Group. M33 can be considered as a minor satellite, with a total stellar mass approximately 30 times smaller than that of the Milky Way and a dark matter halo mass roughly 60 times lower than that of the Local Group as a whole (Corbelli, 2003; Sawala, Teeriaho & Johansson, 2023). It is relatively metal-poor with $12 + \log(\mathrm{O/H}) = 8.36$ (Rosolowsky & Simon, 2008), and gas rich (Corbelli, 2003). The most proximate galaxy in this sample, M33 lies at a

distance of 0.859 Mpc and is moderately inclined with $i = 56°$ (TP20). The pure diffuse model of this galaxy was presented by TP20.

M51

M51 is a system of two closely interacting galaxies: the larger, grand-design spiral M51a (=NGC 5194), and the smaller lenticular galaxy M51b. M51a is classified as an SA(s)bc pec galaxy by de Vaucouleurs (1991). While the interaction between these galaxies is evident from the prominent bridge linking them, there remains debate as to whether they have experienced a single fly-by encounter (Toomre & Toomre, 1972; Durrell et al., 2003) or multiple close passages (Salo & Laurikainen, 2000; Dobbs et al., 2010). Despite this interaction, M51a maintains a high degree of axisymmetry, particularly in its inner regions. M51a is located at a distance of 8.58 Mpc and is nearly face-on, with an inclination of $i = 20.3°$. Hereafter, any reference to M51 pertains exclusively to M51a. The pure diffuse model of this galaxy was presented by Inman et al. (2023).

M101

M101 is the brightest member of its eponymous group and is classified as an SAB(rs)cd galaxy by de Vaucouleurs (1991). M101 has an H I disc that extends far beyond its optical disc. A faint 'plume' extending northward and 'spur' extending eastward can been seen in very deep optical images (Mihos et al., 2013). While the origin of these features is uncertain, Linden & Mihos (2022), show that NE plume and sharp western edge of the disc could be explained by a close passage of the companion galaxy NGC 5474. M101 lies at a distance of 6.71 Mpc and has an inclination of $i = 18°$. The pure diffuse model of this galaxy was presented by Pricopi et al. (2025).

CHAPTER 7

NGC 628

NGC 628 is a relatively isolated and largely unperturbed spiral, classified as an SA(s)c by de Vaucouleurs (1991). The galaxy features a faint Hα-emitting outer disc that reaches beyond twice the optical radius (Ferguson et al., 1998; Lelièvre & Roy, 2000), and it also hosts an extended H I disc (Briggs et al., 1980; Briggs, 1982). NGC 628 lies at a distance of 9.5 Mpc and has an inclination of $i = 15°$. The pure diffuse model of this galaxy was presented by Rushton et al. (2022).

NGC 891

The basic properties of NGC 891 can be found in the introduction to Chapter 5.

NGC 3521

NGC 3521 is classified as an SAB(rs)bc spiral by de Vaucouleurs (1991). It has a total stellar mass of $M_\star = 5 \times 10^{10}\,\mathrm{M}_\odot$ and a total gas mass of $M_\star = 8 \times 10^{9}\,\mathrm{M}_\odot$ (Leroy et al., 2008; Walter et al., 2008). It is moderately star-forming with an SFR $= 2.1\,\mathrm{M}_\odot\,\mathrm{yr}^{-1}$. NGC 3521 is a significantly inclined galaxy at $i = 72.7°$ (Walter et al., 2008; Pilyugin, Tautvaišienė & Lara-López, 2023) and is situated 10.7 Mpc away (de Blok et al., 2008).

NGC 3938

NGC 3938, classified as an SA(s)c galaxy by de Vaucouleurs (1991), is a member of the Ursa Major cluster and is relatively isolated. It is slightly metal-poor with $12 + \log(\mathrm{O/H}) = 8.42$ (Aniano et al., 2020). At a distance of 17.9 Mpc, NGC 3938 is both the most distant and the most face-on galaxy in the sample, with an inclination of $i = 14°$. The pure diffuse model of this galaxy was presented by Pricopi et al. (2025).

NGC 5907

The basic properties of NGC 5907 can be found in the introduction to Chapter 6.

7.2 Comparison between the Predictions of the Diffuse and Clumpy Models for the Surface Brightness Profiles

The new fits of the clumpy model to the surface brightness profiles for all the galaxies in the sample are shown in Appendix G. The fits are at the wavelengths corresponding to the available panchromatic data. The geometric parameters corresponding to these fits are also listed in the Appendix I. The corresponding fits produced by the diffuse model can be found in the original publications for the modelling of the face-on galaxies, as listed in the preamble of this section. For NGC 891 and NGC 5907 the re-evaluated fits using the diffuse model can be found in § 5.2 and § 6.2 and in the Appendix E and F. For ease of comparison some examples are shown here in Fig. 7.1 and 7.2.

Except for the (almost exactly) edge-on galaxy NGC 891, for which the diffuse model completely fails to account for the appearance of the dust lane in the optical/NIR bands, for all the galaxies at non-edge-on inclinations, both the diffuse and the clumpy models provide reasonable fits to the data. Nevertheless, the clumpy model tends to show slightly better fits than the diffuse model in some cases. In particular at 24 μm, the diffuse models tend to over-predict the data in some cases, and to under-predict the data at 500 μm, as shown in Figs. 7.1 and 7.2. For these specific cases the clumpy model tends to perform better. Thus, at 24 μm the clumpy models usually predict less emission, due to some small suppression of the PAH and warm dust emission in the clumps (with respect to the diffuse component). This is the

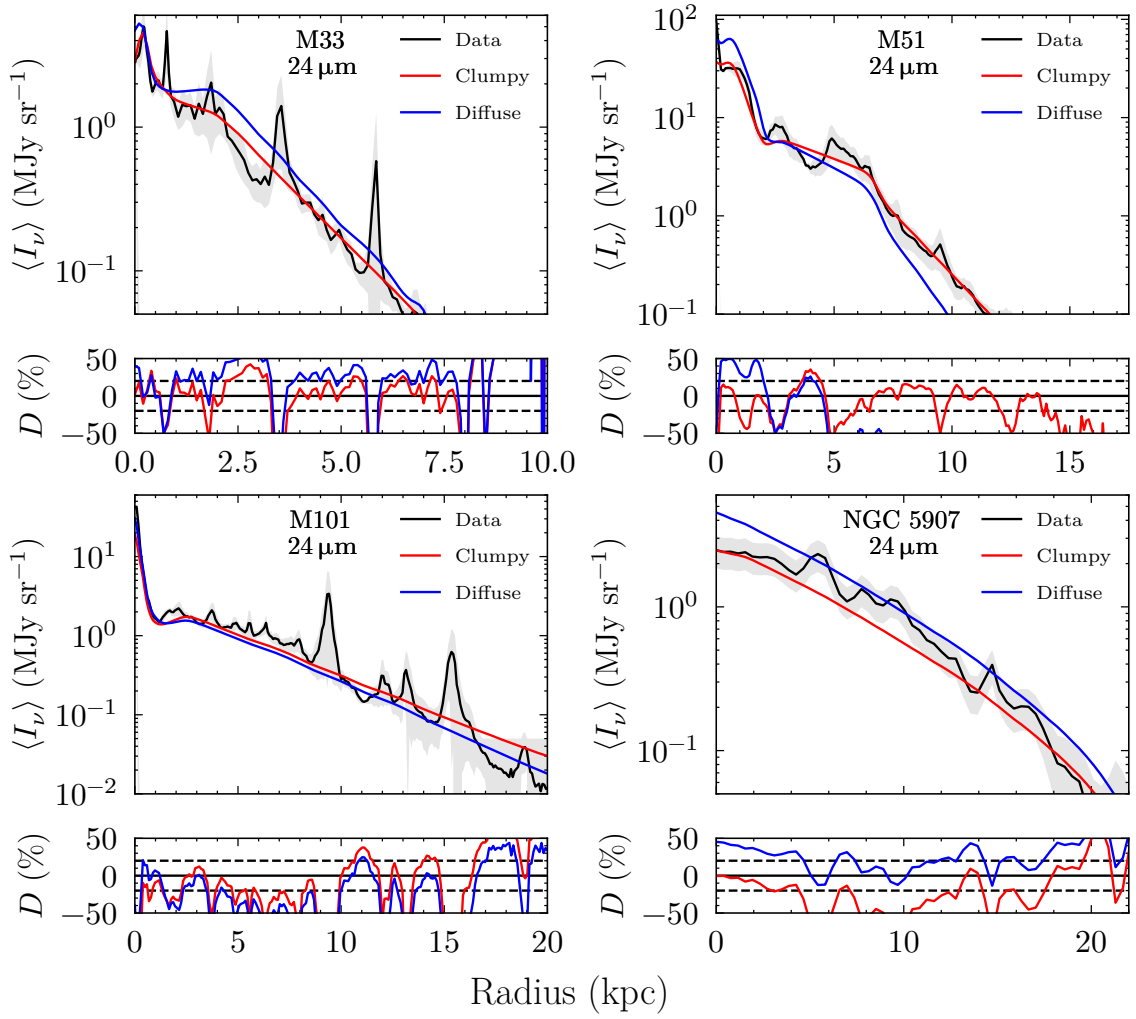

Figure 7.1: Comparison of the diffuse model (blue line) and clumpy model (red line) fits to 24 μm surface brightness profiles (black line) for selected galaxies in the sample. The shaded region indicates the errors associated with the data. The per cent differences between the model totals and the observed profiles D [%] are plotted in the lower panels in the colour corresponding to the main plot.

case for M33, the inner regions of M51, and NGC 5907 (Fig. 7.1). For M101 both models perform equally well at 24 μm. At 500 μm, the clumpy models continue to provide an improvement for M33 and the inner regions of M51 (Fig. 7.2).

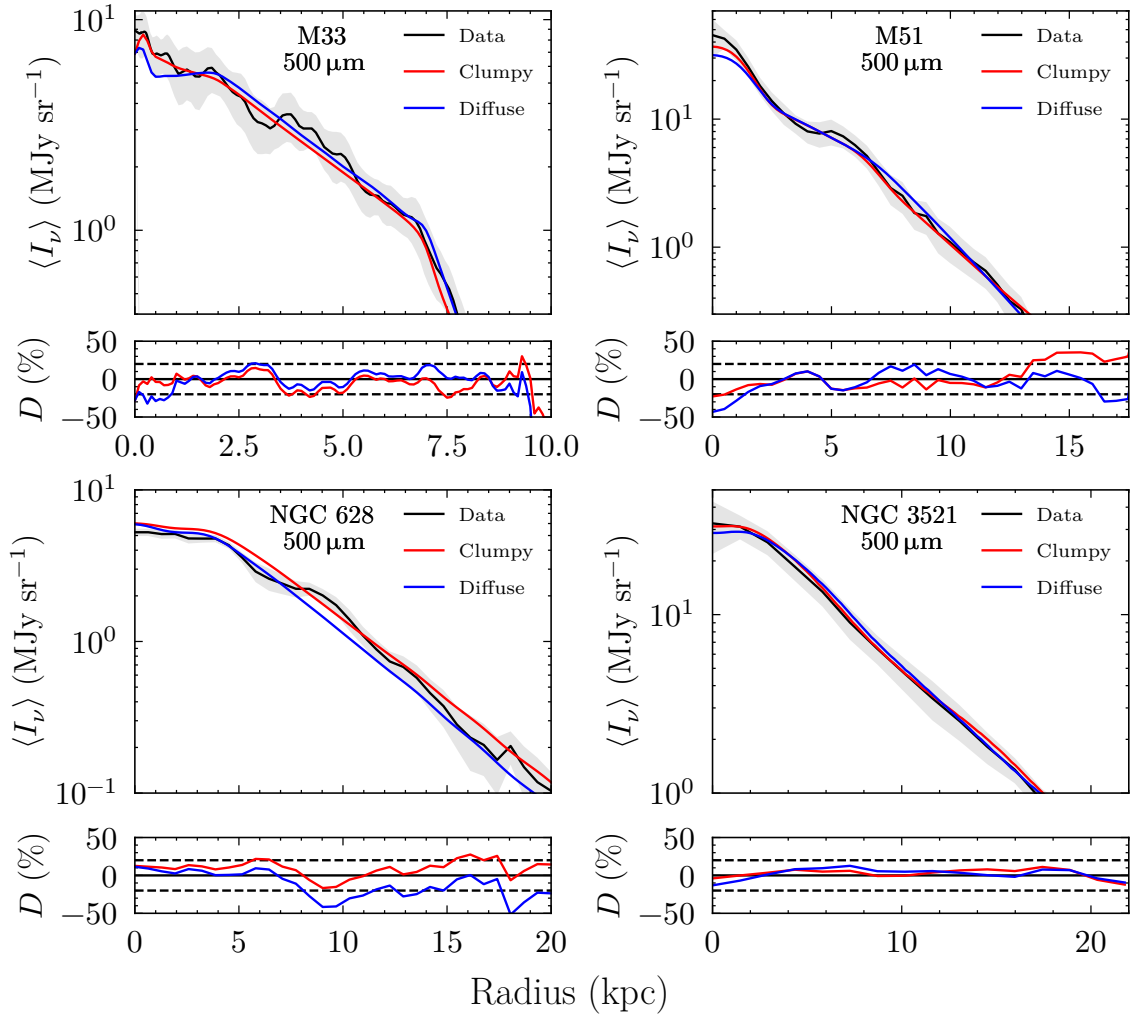

Figure 7.2: Same as Fig.7.1 at 500 µm.

Table 7.2: The maximum and average face-on dust opacity, $\max(\tau_{\rm B}^{\rm f})$ and $\langle\tau_{\rm B,\,area}^{\rm f}\rangle$, of the galaxy sample derived using the diffuse (column under 'd') and clumpy (columns under 'c') models. $f^{\rm c}$ is the fraction of total dust mass in the clumpy component. The values are calculated within the truncation radius of the respective galaxy. (1) Inman et al. (2023); (2) Pricopi et al. (2025); (3) Rushton et al. (2022).

Galaxy	$f^{\rm c}$		$\max(\tau_{\rm B}^{\rm f})$		$\langle\tau_{\rm B,\,area}^{\rm f}\rangle$	
	d	c	d	c	d	c
M33	0	0.5	1.3 ± 0.1	1.0 ± 0.1	0.4 ± 0.1	0.2 ± 0.1
M51	0	0.6	5.3 ± 0.3[1]	2.9 ± 0.2	0.5 ± 0.1	0.2 ± 0.1
M101	0	0.4	2.4 ± 0.2[2]	1.9 ± 0.2	0.3 ± 0.1	0.2 ± 0.1
NGC 628	0	0.5	1.7 ± 0.2[3]	0.8 ± 0.1	0.4 ± 0.1	0.3 ± 0.1
NGC 891	0	0.5	4.4 ± 0.3	1.6 ± 0.1	1.0 ± 0.1	0.4 ± 0.1
NGC 3521	0	0.5	2.8 ± 0.2	1.5 ± 0.1	0.5 ± 0.1	0.3 ± 0.1
NGC 3938	0	0.5	1.6 ± 0.1[2]	0.9 ± 0.1	0.7 ± 0.1	0.3 ± 0.1
NGC 5907	0	0.5	1.4 ± 0.1	0.9 ± 0.1	0.5 ± 0.1	0.3 ± 0.1

7.2.1 Dust Opacity

The inclusion of the clumpy component produced, as expected, a solution with less dust opacity than in the pure diffuse model. This can be seen in the values of the maximum dust opacity, $\max(\tau_{\rm B}^{\rm f})$ listed in Table 7.2 for the diffuse and clumpy models, and also in Fig. 7.3, where $\max(\tau_{\rm B}^{\rm f})$-diffuse is plotted against $\max(\tau_{\rm B}^{\rm f})$-clumpy. The global $\tau_{\rm B}^{\rm f}$ is calculated as the sum of $\tau_{\rm B}^{\rm f}$ from the different morphological components at each radial position. Although at any radial position one morphological component dominates, there is still some partial overlap between components, and therefore the need to define a global $\tau_{\rm B}^{\rm f}$. For this galaxy sample $\max(\tau_{\rm B}^{\rm f})$ is at the inner radius of the inner disc for M33, M51 and NGC 891 (see Table 7.3 for the $\max(\tau_{\rm B}^{\rm f})$ of the individual morphological components). For NGC 628 and NGC 3521

the maximum opacity occurs at the inner radius of the main disc, while for M101 the situation is more complex, with the radius being different in the diffuse and clumpy models.

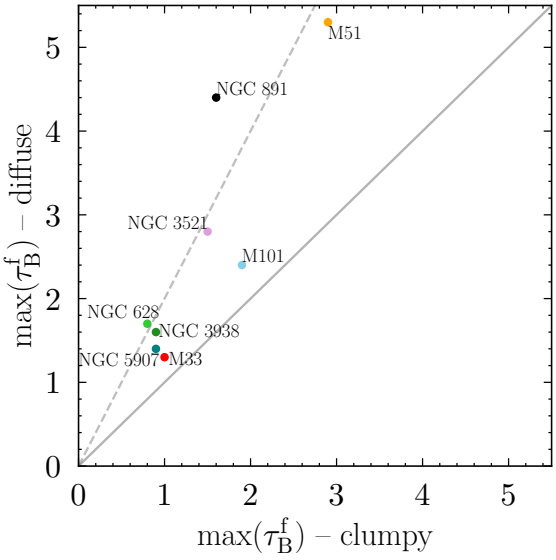

Figure 7.3: Comparison between the maximum optical depths, $\max(\tau_B^f)$ derived with the diffuse (y-axis) and clumpy (x-axis) models. The lines $y = x$ and $y = 2x$ are plotted with the grey-solid and grey-dashed lines, respectively.

The decrease in $\max(\tau_B^f)$ between the diffuse and clumpy models ranges by factors of 1.3 to 2.8 (see again Table 7.2 and Fig. 7.3). NGC 891 exhibits the largest difference, by a factor of 2.8, while M33 and M101 display the smallest differences, each by a factor of 1.3. Naively one would expect that these factors to follow the $\frac{1}{1-f^c}$ ratio. For example for solutions with $f^c = 0.5$ $\left(\frac{1}{1-f^c} = 2\right)$ the decrease in dust opacity between the diffuse and the clumpy model would then follow the $y = 2x$ line, as displayed in Fig. 7.3. However the values seem to fluctuate around the $y = 2x$ line, and are usually between $y = x$ and $y = 2x$ line, due to the modulating effect of the luminosity sources heating the dust and the geometric effects. This can be explained with reference to the optimisation routine described in § 3.3, particularly that the dust opacity is constrained from the 500 µm data. In the clumpy model,

Table 7.3: Maximum optical depth as seen from face-on in the B-band for each morphological component in the galaxy sample for the diffuse and clumpy models. The generic morphological components: inner, main, and outer discs are denoted by the subscripts 'i', 'm', and 'o' respectively. Values under 'd' and 'c' correspond to the diffuse and clumpy models respectively.

Galaxy	$\max\left(\tau^{\mathrm{f}}_{\mathrm{B,i}}\right)$		$\max\left(\tau^{\mathrm{f}}_{\mathrm{B,m}}\right)$		$\max\left(\tau^{\mathrm{f}}_{\mathrm{B,o}}\right)$	
	d	c	d	c	d	c
M33	1.3 ± 0.1	1.0 ± 0.1	0.9 ± 0.1	0.5 ± 0.1	0.4 ± 0.1	0.1 ± 0.1
M51	5.3 ± 0.3	2.9 ± 0.2	2.6 ± 0.1	1.0 ± 0.1	1.3 ± 0.1	0.3 ± 0.1
M101	1.7 ± 0.2	1.6 ± 0.2	1.9 ± 0.1	1.0 ± 0.1	-	-
NGC 628	0.8 ± 0.1	0.3 ± 0.1	1.5 ± 0.1	0.8 ± 0.1	-	-
NGC 891	4.4 ± 0.3	1.6 ± 0.1	3.3 ± 0.2	1.3 ± 0.1	-	-
NGC 3521	-	-	2.8 ± 0.2	1.5 ± 0.1	0.8 ± 0.1	0.4 ± 0.1
NGC 3938	-	-	1.6 ± 0.1	0.9 ± 0.1	-	-
NGC 5907	-	-	1.4 ± 0.1	0.9 ± 0.1	-	-

the dust opacity needed to fit the submm data is lower, due to the additional clumpy component contributing to this emission. A lower dust opacity means that the dust attenuation in the UV will be lower, resulting in a solution with lower UV luminosity, and thus with lower SFR. In the iterative optimisation routine, this will produce a slightly lower amplitude for the dust emission SED, including a small reduction in the 500 μm predicted emission. As a brief aside, it is noted that the 500 μm is deep in the Rayleigh-Jeans side of the dust emission, thus mainly tracing dust column density. However, it is still not deep enough to have zero contribution from the heating sources. It is this very small contribution that is discussed here. To compensate for this small effect, the dust opacity would need to be increased to offset the reduction resulting from the lower SFR. So the overall effect is a decrease

in the dust opacity, but by a smaller factor than the $\frac{1}{1-f^c}$ ratio. The geometric effects also play a role. A lower dust opacity may alter the derived scale-length of the young stellar disc (see Table 7.8 and Fig. 7.4), which, in turn, will alter the derived SFR, producing further effects in the derived dust opacity. Furthermore, in some cases the diffuse model underestimated the submm emission, yielding poorer fits than the clumpy model (see Fig. 7.2).

The clumpy solution indicates that, with respect to the maximum dust opacity (occurring in the central regions at the inner radius of the inner disc or main disc), NGC 5907, NGC 3938, NGC 628 and M33 are optically thin, with $\tau_{\rm B}^{\rm f} < 1$, NGC 3521 and NGC 891 are slightly optically thick, while M101 and M51 are optically thick. By contrast, the diffuse model predicted that all the galaxies in this sample are optically thick in their centre. This makes a big difference in our understanding of dust opacity in nearby galaxies.

Another way to compare the opacity predicted by the two types of models is to inspect the average surface density weighted dust opacity, $\langle \tau_{\rm B,\,area}^{\rm f} \rangle$ (see again Table 7.2). As with the $\max(\tau_{\rm B}^{\rm f})$, the clumpy models have lower $\langle \tau_{\rm B,\,area}^{\rm f} \rangle$ than the diffuse models, with factors ranging between 2.5 (in M51 and NGC 891) and 1.3 (in NGC 628). Interestingly, the galaxy with the lowest difference in average dust opacity between the diffuse and clumpy model, NGC 628, is the galaxy with the second highest difference in the maximum dust opacity. This is mainly due to the morphological/geometrical structure of NGC 628. On the one hand the galaxy has a very small inner disc, with rapidly varying surface brightness at the position of the maximum opacity, with geometric parameters rather difficult to derive in the models (diffuse/clumpy). On the other hand, on large scales the galaxy exhibits a relatively smooth variation in azimuthally averaged surface brightness, which would make the overall average opacity less dependent on fluctuations in the derived geometric parameters.

Table 7.4: The average surface density weighted dust opacity, $\langle \tau^{\rm f}_{\rm B,\,area} \rangle$ for each morphological component in the galaxy sample for the diffuse (column under 'd') and clumpy (column under 'c') models. The generic morphological components: inner, main, and outer discs are denoted by the subscripts 'i', 'm', and 'o' respectively.

Galaxy	$\langle \tau^{\rm f}_{\rm B,\,area,\,i} \rangle$		$\langle \tau^{\rm f}_{\rm B,\,area,\,m} \rangle$		$\langle \tau^{\rm f}_{\rm B,\,area,\,o} \rangle$	
	d	c	d	c	d	c
M33	0.2 ± 0.1	0.2 ± 0.1	0.6 ± 0.1	0.3 ± 0.1	0.1 ± 0.1	0.1 ± 0.1
M51	4.5 ± 0.3	2.5 ± 0.1	1.8 ± 0.1	0.7 ± 0.1	0.3 ± 0.1	0.1 ± 0.1
M101	0.3 ± 0.1	0.2 ± 0.1	0.3 ± 0.1	0.2 ± 0.1	-	-
NGC 628	0.1 ± 0.1	0.03 ± 0.1	0.4 ± 0.1	0.3 ± 0.1	-	-
NGC 891	2.2 ± 0.1	0.8 ± 0.1	0.9 ± 0.1	0.4 ± 0.1	-	-
NGC 3521	-	-	1.6 ± 0.1	0.9 ± 0.1	0.4 ± 0.1	0.2 ± 0.1
NGC 3938	-	-	0.7 ± 0.1	0.3 ± 0.1	-	-
NGC 5907	-	-	0.5 ± 0.1	0.3 ± 0.1	-	-

The clumpy model predicts that on average, disc galaxies are optically thin when seen face-on. Based on $\langle \tau^{\rm f}_{\rm B,\,area} \rangle$, NGC 891 has the highest opacity $\langle \tau^{\rm f}_{\rm B,\,area} \rangle = 0.4$, followed by NGC 3938 with $\langle \tau^{\rm f}_{\rm B,\,area} \rangle = 0.3$. However M51 has the highest maximum opacity in the inner region $\max(\tau^{\rm f}_{\rm B}) = 2.9$, followed by M101 with $\max(\tau^{\rm f}_{\rm B}) = 1.6$. Thus, galaxies with the highest opacity in their inner regions do not necessarily have the largest average opacity. This can be partially explained by the extent of their outer discs and the truncation radius. Both M101 and M51 possess extended, faint outer discs that may bias the area weighted average optical depth toward lower values. M101, the largest galaxy in this sample, has a truncation radius of $R_{\rm t} = 30\,{\rm kpc}$, and therefore has the largest surface area. M51 is relatively centrally dense, with a faint outer disc extending out to 20 kpc. When only the area within the truncation radius of the main disc of M51 ($R_{\rm t} = 7\,{\rm kpc}$) is considered, the area

weighted average optical depth increases to $\langle \tau^{\rm f}_{\rm B,\,area} \rangle = 0.8$.

The various morphological components of the galaxies in the sample show the same decrease in dust opacity between the diffuse and the clumpy models, both in $\max(\tau^{\rm f}_{\rm B})$ (Table 7.3) and in $\langle \tau^{\rm f}_{\rm B,\,area} \rangle$ (Table 7.4), but with different degrees of variation. The smallest variation in $\max(\tau^{\rm f}_{\rm B})$ is in the inner disc of M33, by a factor of 1.3, coinciding with the minimum variation in the global dust opacity. The largest variation in $\max(\tau^{\rm f}_{\rm B})$ is in the outer disc of M51, by a factor of 4. This latter value is largely due to noise in fitting. As discussed in Inman et al. (2023), due to the significant influence of its companion M51b, the axisymmetric approximation becomes poor. For this reason, the authors prioritised the fit at shorter radii. In the clumpy model, no such bias was used in the optimisation procedure, which resulted in a significantly longer scale length in the outer disc (Table I.3).

With respect to the average dust opacity, it is noted that in the clumpy models the outer discs have, as expected, very low opacity, of around $\langle \tau^{\rm f}_{\rm B,\,area} \rangle \sim 0.1$.

7.2.2 Dust Mass

As the defining feature of the clumpy model is the redistribution of a portion of the dust mass into quiescent clumps, one would expect the total dust mass derived from the clumpy and diffuse models to be similar. Indeed, the clumpy models yield a modest average reduction of approximately 5% in total dust mass compared to their diffuse counterparts. However, not all galaxies experience a decreased dust mass, some galaxies show a slight increase in dust mass under the clumpy model. Overall, the dust masses derived from both models agree within their respective uncertainties, suggesting that the observed differences are likely attributable to noise introduced during the fitting process rather than reflecting a systematic shift. The dust masses derived for morphological component for each galaxy is listed in Table J.1.

7.2.3 SFR

As already inferred in Section 7.2.1, the clumpy model predicts smaller SFRs than the diffuse model. Inspection of the tabulated values from Table 7.5 shows a reduction in SFR by factors ranging between 1.2 to 2.0. The decrease directly follows from the lower UV attenuation predicted by the clumpy models. The decreasing factors do not seem to correlate with inclination, which is reassuring, as any such correlation could potentially indicate a systematic bias resulting from the line of sight optical depth. The decreasing factors also do not correlate with the face-on dust opacity of the galaxy. This means that the variation in SFR derived from the diffuse and clumpy models only depends on the detailed structure and morphology of the galaxy under study. The largest variation was found for NGC 5907 (a factor of 2.0) and the minimum variation for NGC 3938 (a factor of 1.2).

Table 7.5: Comparison of global properties of the diffuse ('d') and clumpy ('c') models of the galaxy sample, including SFR, specific star formation rate (sSFR), fraction of stellar light reradiated by dust $f^{\rm abs}$, and the percentage of the dust heating powered by the young stellar disc, $F^{\rm dust}_{\rm young}$.

Galaxy	SFR ($M_\odot\,yr^{-1}$)		sSFR ($\times10^{-11}$ yr^{-1})		$f^{\rm abs}$		$F^{\rm dust}_{\rm young}$ (%)	
	d	c	d	c	d	c	d	c
M33	0.48 ± 0.04	0.30 ± 0.02	7.35 ± 0.66	7.08 ± 0.64	0.33	0.35	80	69
M51	4.1 ± 0.4	2.9 ± 0.2	4.36 ± 0.38	3.30 ± 0.18	0.46	0.63	61	45
M101	3.2 ± 0.2	2.5 ± 0.2	6.23 ± 0.55	4.54 ± 0.40	0.33	0.39	71	62
NGC 628	2.0 ± 0.2	1.7 ± 0.1	9.52 ± 0.85	8.77 ± 0.78	0.38	0.51	67	62
NGC 891	7.2 ± 0.6	4.6 ± 0.4	6.06 ± 0.53	6.04 ± 0.54	0.37	0.48	66	72
NGC 3521	3.3 ± 0.2	1.7 ± 0.1	3.49 ± 0.31	1.99 ± 0.18	0.33	0.25	58	37
NGC 3938	2.2 ± 0.1	1.8 ± 0.1	5.13 ± 0.46	3.84 ± 0.34	0.34	0.40	64	56
NGC 5907	5.1 ± 0.5	2.5 ± 0.2	4.61 ± 0.41	2.44 ± 0.22	0.25	0.29	70	62

The morphological components of the galaxy sample overall follow the same trend of decreasing SFR between the diffuse and the clumpy model, as seen in Tables 7.6 and 7.7. As expected, the closest variation to that shown in the global SFR is in the main disc (see Table 7.7), which usually dominates the bolometric output of a galaxy. The largest departure from the global properties is in the inner disc (see Table 7.6), which exhibits a much larger spread in the decreasing factors, from 1.2 in M33 to 4.8 in M101. It is clear that the inner discs, with their smaller sizes and rapid variation in surface brightness, are more prone to large differences in the fitting parameters. In addition, the inner discs lie in the regions with either maximum dust opacity, or in regions with a linear decrease in dust opacity. This produces complex dust attenuation in the inner regions, with values strongly dependent on the type of model (diffuse or clumpy).

Table 7.6: SFR for the nuclear and inner morphological components in the galaxy sample. These are denoted by the subscript 'n' and 'i' respectively. Values under 'd' and 'c' correspond to the diffuse and clumpy models respectively.

Galaxy	SFR_n ($M_\odot\,yr^{-1}$)		SFR_i ($M_\odot\,yr^{-1}$)	
	d	c	d	c
M33	$(1.0 \pm 0.1) \times 10^{-3}$	$(9.1 \pm 0.2) \times 10^{-4}$	$(1.70 \pm 0.06) \times 10^{-2}$	$(1.40 \pm 0.08) \times 10^{-2}$
M51	-	-	1.4 ± 0.2	0.48 ± 0.07
M101	$(6.0 \pm 0.3) \times 10^{-2}$	$(3.2 \pm 0.2) \times 10^{-2}$	$(2.9 \pm 0.2) \times 10^{-2}$	$(6.0 \pm 0.5) \times 10^{-3}$
NGC 628	-	-	$(4.0 \pm 0.4) \times 10^{-2}$	$(3.0 \pm 0.3) \times 10^{-2}$
NGC 891	-	-	0.94 ± 0.08	0.26 ± 0.03
NGC 3521	-	-	$(2.7 \pm 0.2) \times 10^{-2}$	$(8.0 \pm 0.8) \times 10^{-3}$
NGC 3938	-	-	-	-
NGC 5907	-	-	-	-

Table 7.7: Continuation of Table 7.6. SFR for the main and outer morphological components in the galaxy sample. These are denoted by the subscript 'm' and 'o' respectively. Values under 'd' and 'c' correspond to the diffuse and clumpy models respectively.

Galaxy	SFR_m ($M_\odot\,yr^{-1}$)		SFR_o ($M_\odot\,yr^{-1}$)	
	d	c	d	c
M33	0.45 ± 0.04	0.27 ± 0.02	$(1.8 \pm 0.2) \times 10^{-2}$	$(1.2 \pm 0.1) \times 10^{-2}$
M51	2.73 ± 0.20	1.75 ± 0.13	0.57 ± 0.05	0.64 ± 0.06
M101	3.09 ± 0.23	2.43 ± 0.18	-	-
NGC 628	1.96 ± 0.15	1.63 ± 0.12	-	-
NGC 891	6.31 ± 0.47	4.37 ± 0.33	-	-
NGC 3521	2.49 ± 0.19	1.30 ± 0.10	0.82 ± 0.07	0.37 ± 0.03
NGC 3938	2.20 ± 0.16	1.73 ± 0.13	-	-
NGC 5907	5.63 ± 0.42	2.52 ± 0.19	-	-

7.2.4 sSFR

The specific star-formation rate, sSFR, derived with the clumpy models are typically smaller by 1.01 to 1.89 times than those from the diffuse models (see Table 7.5). This trend arises naturally from the definition sSFR = SFR/$M_\star$, where $M_\star$ is the stellar mass. As previously discussed, the clumpy model produces lower SFRs due to the relatively lower intrinsic UV luminosities. Stellar masses ($M_\star$) are derived from the intrinsic fluxes at 3.6 µm and 4.5 µm using the calibration of Eskew, Zaritsky & Meidt (2012). Because the NIR wavelengths are less affected by dust attenuation, the reduction in $M_\star$ between models is relatively modest compared to the decrease in the UV-derived SFR, leading to an overall decrease in sSFR. Although smaller, the sSFRs derived with the clumpy models still suggest these galaxies are moderately star-forming.

7.2.5 The Fraction of Stellar Light Absorbed and Re-Radiated by Dust

The fraction of the stellar light absorbed and re-radiated by dust, $f^{\rm abs}$ is listed in Table 7.5. This metric provides insight into the efficiency with which dust processes stellar radiation, and is influenced by the dust's microscopic properties, composition, and spatial distribution relative to the distribution of stars. $f^{\rm abs}$ derived from the clumpy models tends to be higher by factors of 1.06 to 1.37, compared to the diffuse models. NGC 3521 is exceptional to this trend with $f^{\rm abs}$ decreasing to 0.76 times that of the diffuse model.

7.2.6 The Contribution of Different Stellar Populations to Dust Heating

The contribution of different stellar populations to dust heating is a very important property of star-forming galaxies, although still a matter of debate in the literature. This section examines the fraction of the energy absorbed by dust coming from young stars, denoted as $F_{\rm young}^{\rm dust}$, under the assumption that the contribution of the old stellar populations represent the $1 - F_{\rm young}^{\rm dust}$. These values are presented in column five of Table 7.5. Across the sample, the clumpy models consistently yield lower values of $F_{\rm young}^{\rm dust}$, indicating a reduced contribution from the young stars to the total dust heating. This reduction arises from the lower efficiency with which UV photons are absorbed in the clumpy dust configuration. The clumpy models are characterised by a flatter extinction curve (Fig. 4.5) whereby UV radiation, primarily emitted by young stars, is less attenuated than in the diffuse models. While the reduction in attenuation is significant in the UV, it becomes negligible in the optical and NIR, hence the contribution of older stars to dust heating remains largely unchanged.

7.2.7 Scale Lengths

As already discussed and explained in § 5.4.1 for NGC 891, the scale length of the stellar discs are usually longer in the clumpy model than in the diffuse model. This can be seen in the top and middle panel of Fig. 7.4, where the x- and y-axis display the clumpy and diffuse derived values for the main disc morphological component. It is clear that the points all lie either on the $y = x$ line (a few) or below it (most of them), with various degree of departure from it.

For the scale length of the dust there is no trend (see bottom panel of Fig. 7.4), with galaxies both above and below the equality line. Table 7.8 lists the scale lengths of all the disc components of the galaxy sample: inner discs, main discs and outer

discs, derived with the diffuse and clumpy models.

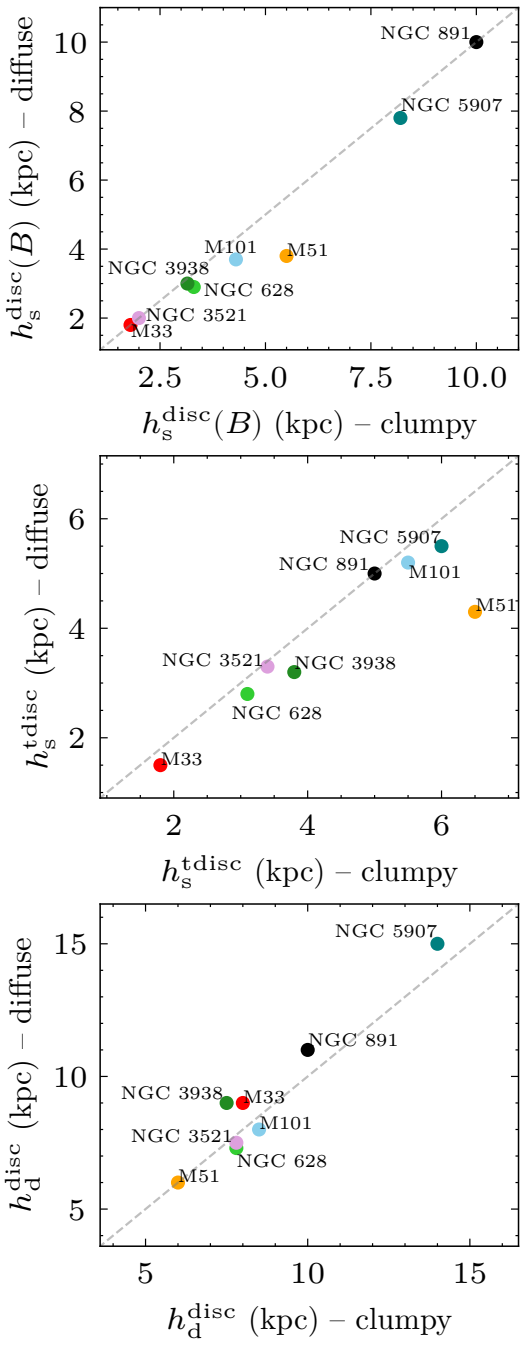

Figure 7.4: Comparison between the scale lengths of the stellar disc (in the B-band) $h_s^{disc}(B)$, thin stellar disc h_s^{tdisc}, and dust disc h_d^{disc} derived with the diffuse and clumpy models. In all cases the scale lengths refer to the main disc morphological component. The x- and y-coordinates display the clumpy and diffuse derived values, respectively. The line $y = x$ is plotted with the grey-dashed line to help visualise any trends.

Table 7.8: Scale lengths of all disc components of the galaxy sample. Where applicable, the nuclear, inner, main, and outer discs are denoted with 'n', 'i', 'm', and 'o' respectively. Values under 'd' and 'c' correspond to the diffuse and clumpy models respectively. All values are given in kpc.

Galaxy	morphological component	Parameter (kpc)					
		$h_{\rm s}^{\rm tdisc}$		$h_{\rm s}^{\rm disc}(B)$		$h_{\rm d}^{\rm disc}$	
		d	c	d	c	d	c
M33	n	0.02	0.02	-	-	-	-
	i	0.10	0.13	0.05	0.05	0.15	0.15
	m	1.5	1.8	1.8	1.8	9.0	8.0
	o	0.6	0.65	1.0	1.0	1.0	1.3
M51	i	0.6	0.55	0.74	0.72	5	4.7
	m	4.3	6.5	3.8	5.5	6.0	6.0
	o	1.45	1.80	2.0	2.4	3.6	4.5
M101	n	0.06	0.08	-	-	-	-
	i	0.4	0.5	0.4	0.5	0.90	0.75
	m	5.2	5.5	3.7	4.3	8.0	8.5
NGC 628	i	0.2	0.15	-	-	-	-
	m	2.8	3.1	2.9	3.3	7.3	7.8
NGC 891	i	3.0	3.0	-	-	3.0	3.0
	m	5.0	5.0	10	10	10	10
NGC 3521	i	0.5	0.5	-	-	-	-
	m	3.3	3.4	2.0	2.0	7.5	7.8
	o	2.3	2.8	4.1	4.1	7.5	7.0
NGC 3938	m	3.2	3.8	3.00	3.15	9.0	7.5
NGC 5907	m	5.5	6.0	7.8	8.2	15.0	14.0

7.3 Spatial Variation of Key Properties in the Clumpy Model

As shown in this section, the clumpy model solves the long standing energy balance problem in edge-on galaxies and provides consistent solutions to galaxies of any orientation. It is therefore adopted as the standard model. Because of this it is important to analyse the statistical trends of this galaxy sample using the new model.

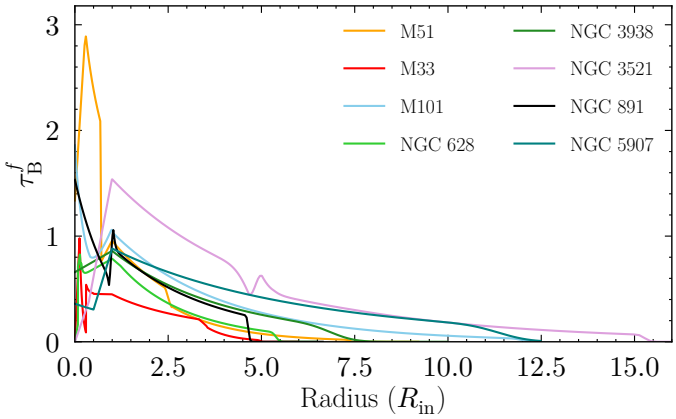

Figure 7.5: The radial variation of τ_B^f for each galaxy in the sample as a function of radius in units of the inner radius of the main dust disc.

Since the defining characteristic of the clumpy model is lower dust opacity, it is insightful to study the radial trends in dust opacity. Fig. 7.5 shows the τ_B^f versus radial distance (in units of their inner radius) for all the galaxies in the sample. The plot shows that overall most of the galaxies are optically thin when viewed face-on, throughout their discs. The inner regions of M51 and NGC 3521 are definitively optically thick. The figure also shows rather transparent extended outer discs.

Fig. 7.6 shows the radial variation of SFR surface density (Σ_{SFR}), specific star-formation rate (sSFR), and the stellar mass surface density ($\Sigma_{M_\star}$). To enable better comparison between galaxies, each plot is normalised to the inner radius of its main

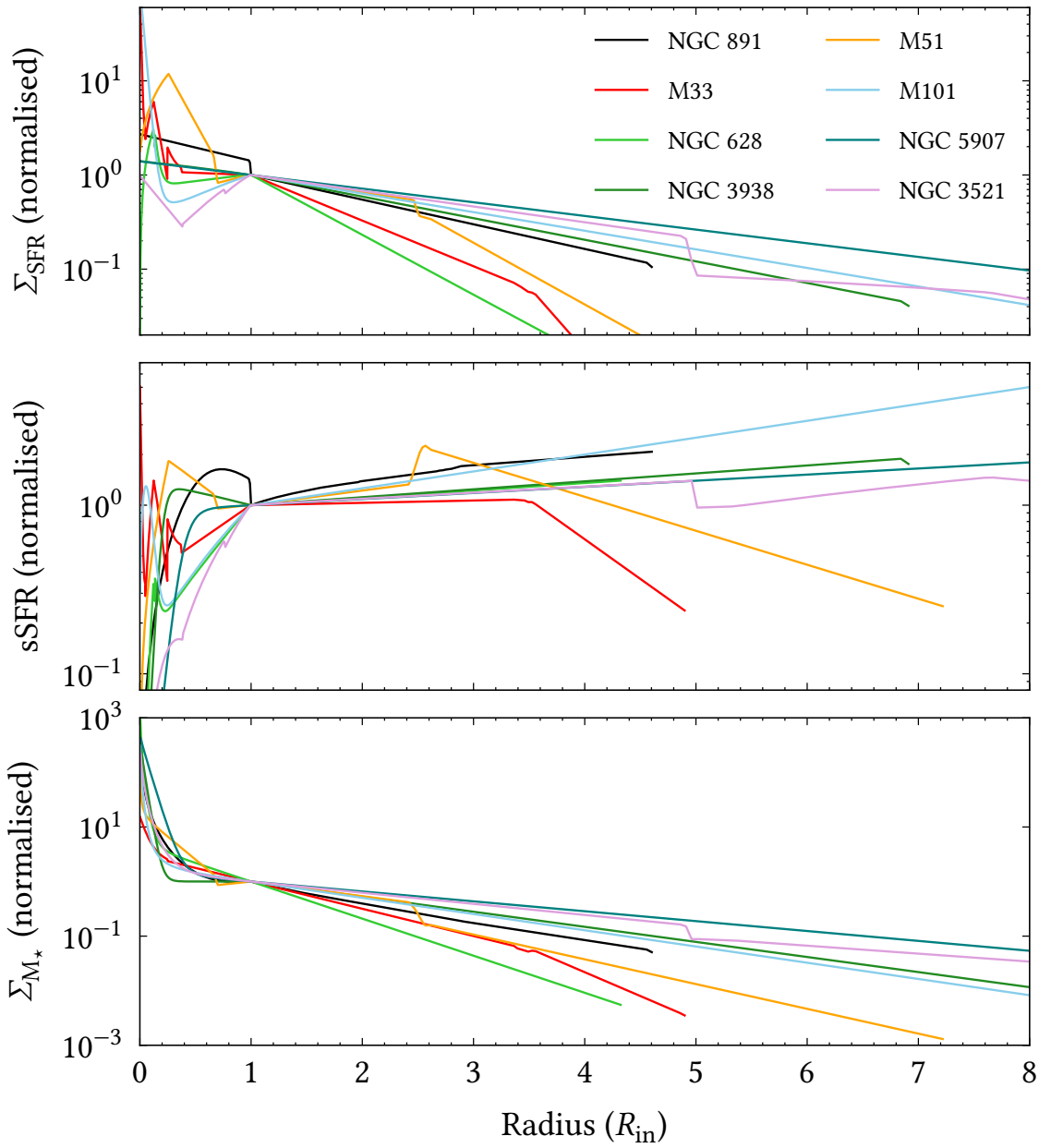

Figure 7.6: Radial profiles of surface densities (face-on) for key stellar parameters derived for the galaxy sample. The top panel shows the surface density of star formation $\Sigma_{\rm SFR}$. The middle panel shows the specific SFR (sSFR). The bottom panel shows the surface density of stellar mass $\Sigma_{\rm M_\star}$. Each quantity for each galaxy has been normalised at the inner radius of the main dust disc.

dust disc, and the radius is given in units of the inner radius. The SFR surface densities show an overall exponential decline over their main discs, with NGC 5907 exhibiting the longest scale length, and NGC 628 the shortest. $\Sigma_{M_\star}$ is relatively consistent within this galaxy sample: a sharp decline from the centre until the limit of the bulge is reached, after which $\Sigma_{M_\star}$ declines exponentially. Again, NGC 628 shows the shortest scale length, and NGC 5907 the longest.

The sSFR across the sample shows similar behaviour beyond the inner radius; a gradual exponential increase with radius. This is expected for late-type spiral galaxies under the inside-out growth scenario, where the main and outer discs are actively forming stars. M101 and NGC 891 show the greatest rate of increase with radius. While the sSFR for NGC 891 is increasing only modestly, and appears to begin to plateau at larger radii, M101 exhibits a consistently increasing sSFR. This enhanced star formation rate could be explained by interactions with its environment, particularly with NGC 5474 (Mihos et al., 2013; Linden & Mihos, 2022). The outer discs of M51 and M33 exhibit a marked decline in sSFR. TP20 note that the outer disc of M33 may be influenced by environmental effects being a satellite in the Local Group. Gas could be removed from the outer disc via ram-pressure stripping, thereby quenching star formation. Similarly, M51 is a heavily interacting with its companion galaxy, M51b, which significantly influences the star formation in its outer disc.

Fig. 7.7 shows the radial variation of $F^{\rm dust}_{\rm young}$ and $F^{\rm dust}_{\rm old}$ for the clumpy models across the galaxy sample. In all cases, the energy absorbed near the galaxy centres is dominated by the bulge. The only exception is M33, which does not have a bulge but instead hosts a nuclear thin disc comprised of young stars. A consistent trend is observed: the contribution from young stars increases with radius until the influence of the bulge diminishes, after which $F^{\rm dust}_{\rm young}$ either plateaus or continues to gradually increase before declining near the edge of the galaxy. M51 largely follows

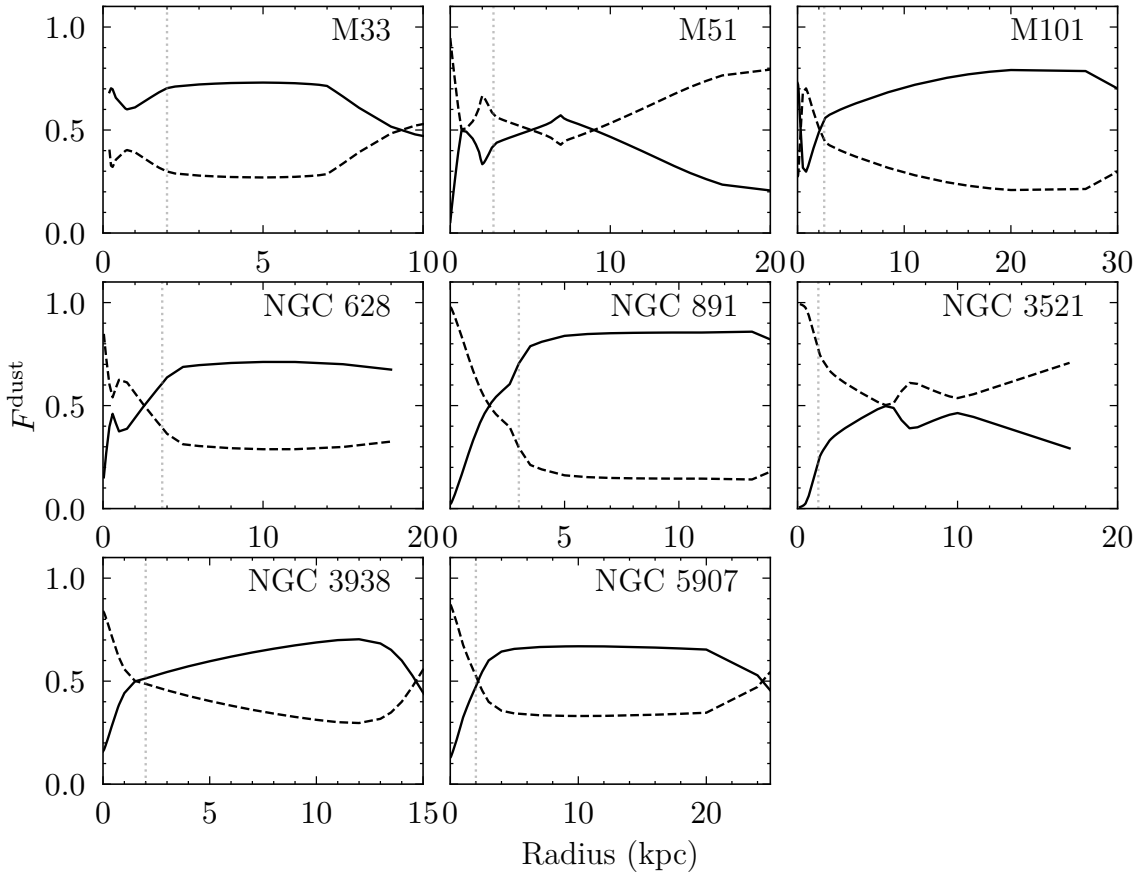

Figure 7.7: Radial profiles of the total energy absorbed by the young ($F^{\rm dust}_{\rm young}$, solid line) and old ($F^{\rm dust}_{\rm old}$, dashed line) stellar populations. The inner radius of the main dust disc of each galaxy is plotted with the grey dotted lines.

this behaviour within $R \approx 7\,\mathrm{kpc}$, beyond which it abruptly reverses trend exhibiting a decreasing $F^{\rm dust}_{\rm young}$. As discussed by Inman et al. (2023), the spiral structure of M51 is well preserved up to this radius, beyond which interactions with its lenticular companion, M51b, become significant. These interactions likely compromise the reliability of the model beyond this point.

7.4 Trends and Variability in the Galaxy Sample

A total of eight galaxies have now been modelled using the RT codes of PT11 updated with the clumpy formalism. From this small sample, trends in various properties begin to emerge. For example, each galaxy was successfully modelled with a Milky Way (MW) type dust whose properties are described in Weingartner & Draine (2001), without needing to invoke different grain properties. However, in previous work using the diffuse model (Inman et al., 2023) it was found that in the case of M51, allowing for varying dust properties provided better fits in the PAH region and a more realistic UV intrinsic stellar SED. In that work the derived attenuation curve suggested the need for a dust model with a reduced 2200 Å bump in the inner disc, which was modelled with a Large Magellanic Cloud type dust (Weingartner & Draine, 2001).

In this work it was found that the inner disc of M51 was much better fit using the clumpy model with a MW type dust, demonstrating possible degeneracies between the microscopic and macroscopic dust properties. Since the clumpy model provides a consistent approach for all the galaxies in the sample, it is concluded that a MW type dust also provides a consistent solution for all modelled galaxies within the framework of the clumpy model.

In addition, no evidence is found of a 'submm excess' (Bot et al., 2010; Rémy-Ruyer et al., 2013; Hermelo et al., 2016; Williams et al., 2019), as the submm emission is well fit across the galaxy sample, without need of modifying the dust grain emissivity. This can be attributed to the fitting of the detailed geometry, informed by the panchromatic dataset.

It is found that a $f^{c} = 0.5 \pm 0.1$ is able to adequately reproduce the panchromatic data. Six of the eight galaxies in this sample were best fit with a $f^{c} = 0.5$, while M101 and M51 were best fit with a $f^{c} = 0.4$ and $f^{c} = 0.6$ respectively.

Chapter 8

Summary and Conclusions

The goal of this work was to solve the so-called energy balance problem between direct stellar light and dust emission (Popescu et al., 2000; Dasyra et al., 2005; Bianchi, 2008; Baes et al., 2010; Popescu et al., 2011; Saftly et al., 2015; De Geyter et al., 2015; Mosenkov et al., 2018). This problem was encountered when modelling the UV/optical/FIR/submm SEDs of edge-on spiral galaxies with RT models, and was attributed to the inability of these models to account for both the appearance of the dust lanes in edge-on galaxies as well as for the observed submm dust emission. In general, it was found that the solution needed to fit the optical/NIR images produced an underestimation of the submm emission by factors of $3-5$, while solutions constrained to fit the submm emission predicted too prominent dust lanes. On the other hand no energy balance problem was found when modelling face-on galaxies (De Looze et al., 2014; Viaene et al., 2017; Verstocken et al., 2020; Nersesian et al., 2020a,b; Inman et al., 2023; Pricopi et al., 2025).

In order to solve this long standing problem and find a consistent solution for both face-on and edge-on galaxies, this work introduced quiescent clumps in the RT modelling, and a novel approach in the description of the clumpy ISM. This approach

treats the quiescent dust clouds (with no internal stellar sources) heated by the diffuse interstellar radiation fields as 'pseudo-dust grains' with equivalent optical constants given by the attenuation properties of the clouds. This introduces a sub-grid approach in the RT models, allowing the parsec and subparsec scales to be incorporated into the large-scale calculations of the galaxy discs (kiloparsec scales).

RT calculations of a single dust cloud illuminated externally by stellar radiation fields were done to quantify the amount of absorption and scattering produced by the clump. From these, the absorption and scattering efficiencies of the cloud, $Q_{\rm abs}$ and $Q_{\rm sca}$, as well as the corresponding cross-sections, $C_{\rm abs}$ and $C_{\rm sca}$, were calculated. The temperature of the dust within the cloud was also calculated, enabling the derivation of the dust emission SEDs of the clouds. Since the calculation of the dust emission SED depends on the intensity and colour of the radiation fields (RFs) heating the dust in which the clump is embedded, SEDs were calculated for clumps exposed to RFs of different strength and colour, and from this, a corresponding library of dust emission SEDs for the clump was produced. In all these calculations the same RT codes and techniques were utilised as for the large-scale galaxy calculations, but for the geometry of the clump. Specifically, the RT codes from PT11 were used. The results were also checked using the RT code DART-Ray (Natale et al., 2014, 2015, 2017). Both codes employ a ray-tracing algorithm accounting for both the absorption and anisotropic scattering of stellar light by dust grains of various sizes and chemical composition. The dust model used is comprised of astronomical silicates and carbonaceous grains in form of graphites and PAH molecules, with a grain size distribution from Weingartner & Draine (2001), and optical constants from Draine & Lee (1984) and Draine & Li (2007).

In the present model, the clumps have a volume emissivity described by spherically symmetric King profile (Lane, 1870; Emden, 1907; King, 1962), a core radius $r_{\rm c} = 1\,{\rm pc}$, and a truncation radius $r_{\rm t} = 1\,{\rm pc}$, with the dust opacity through the

clump (from the centre to the truncation radius) of $\tau_{\rm B}^{\rm c,s} = 1$. These clumps describe the cirrus-like clouds observed in the diffuse ISM, being optically thin in the optical range, but becoming progressively optically thick in the UV. Clumps that are optically thick in the optical range have also been calculated, but were not found to provide adequate solutions to the galaxy models, within the framework of the existing dust grain properties.

The derivation of the extinction and emission properties of the clump enabled the virtualisation of the macroscopic dust cloud into a microscopic *pseudo-grain*, that was supplemented into the existing dust grain mixture of graphite, silicate grains, and PAH molecules. This modified dust model was found to be characterised by a flatter extinction curve. Thus a new parameter was added to the RT models of galaxies—the fraction of total dust mass in clumps $f^{\rm c}$.

The new formalism was tested and applied to the prototype edge-on galaxy NGC 891, for which the energy balance problem was first detected (Popescu et al., 2000). The clumpy model with $f^{\rm c} = 0.5$ achieves better fits to the data than the pure diffuse model, and most critically reproduces the dust lane seen in the J and $K_{\rm s}$ bands, thus solving the energy balance problem for this galaxy.

The new formalism was then applied to a small sample of galaxies of various inclinations, to test the general applicability of the model. The sample was chosen to include the face-on galaxies already modelled by us with the pure diffuse model, M33 TP20, NGC 628 (Rushton et al., 2022), M51 (Inman et al., 2023), M101 and NGC 3938 (Pricopi et al., 2025). In addition the sample includes the intermediate-inclination galaxy NGC 3521. The edge-on galaxy NGC 5907 was also included and showed some peculiar behaviour in previous RT modelling (Mosenkov et al., 2018), where the optical/NIR images could not be adequately reproduced by the models, even without the incorporation of constraints from the submm wavelengths. It was found that the clumpy model successfully accounted for the panchromatic images

of all galaxies in the sample, except for NGC 5907, for which some peculiarity in the optical images still remain, indicating a more complex large scale geometry than explored with these models.

The results of this analysis indicate that the clumpy models are characterised by a reduction in attenuation with respect to the pure diffuse models, particularly at shorter wavelengths in the UV. As a result the clumpy models predict a 21–64 % reduction in maximum face-on optical depth in the B-band ($\tau_{\rm B}^{\rm f}$) when compared to their purely diffuse counterparts. This is primarily due to the allocation of a portion of the dust mass away from the diffuse component, but also in part due to the differences in modelling that arises from using a modified dust model. The reduced optical depth is significant as only two of the eight galaxies modelled with the clumpy model yield solutions with an optically thick centre (M101 and M51), with a further two galaxies (NGC 891 and NGC 3521) being moderately optically thick. The remaining four galaxies are optically thin with $\tau_{\rm B}^{\rm f} \leq 1$. In contrast, the diffuse models predict that all the galaxies are optically thick, or moderately optically thick in their centres. As a consequence to the reduced attenuation, the clumpy models predict values of SFR 15–51 % lower than their purely diffuse counterparts. Because dust attenuation does not strongly affect the NIR bands, the stellar masses determined using the 3.6 µm and 4.5 µm fluxes described by Eskew, Zaritsky & Meidt (2012) are relatively unchanged between the clumpy and diffuse models. This, in conjunction with a reduced SFR, implies that the clumpy model systematically derives smaller sSFR when compared to the pure diffuse counterpart.

To conclude, in addition to solving the energy balance problem, this study also gives an answer to the long standing debate of whether spiral galaxies are optically thin or thick. In their fundamental paper 'Are spiral galaxies optically thin or thick?' Xilouris et al. (1999) gave the following answer to the question:

"The face-on central optical depth is less than one in all optical bands, indicating

that typical spiral galaxies like the ones that we have modelled would be completely transparent if they were to be seen face-on." The conclusion was reached from the RT analysis of the optical/NIR images of spiral galaxies. The inclusion of the dust emission in the overall RT modelling complicated the situation and changed the answer in favour of galaxies being optically thick in their centre (Popescu et al., 2000, 2011). However, the energy balance problem in edge-on galaxies indicated that the definitive solution was yet to be found. The incorporation of the quiescent clumps into the model returns the answer to the original one provided by Xilouris et al. (1999), albeit with the backup of the panchromatic dimension. Indeed, in this work it was found that spiral galaxies are overall optically thin when viewed face-on, although some are still optically thick in their centre.

In future studies it would be essential to model the Milky Way with the new clumpy models, and provide a revised solution to that provided by Natale et al. (2022). It would also be of critical importance to produce new libraries of model SEDs, to extend the ones already derived with the diffuse models (Popescu et al., 2011), and apply them to large statistical samples, for the characterisation of the intrinsic properties of galaxy populations.

Bibliography

Allaert F. et al., 2015, A&A, 582, A18

Allen R. J., Baldwin J. E., Sancisi R., 1978, A&A, 62, 397

Aniano G. et al., 2020, ApJ, 889, 150

Baes M. et al., 2010, A&A, 518, L39

Bianchi S., 2008, A&A, 490, 461

Bianchi S., Davies J. I., Alton P. B., 2000, A&A, 359, 65

Bianchi S., Xilouris E. M., 2011, A&A, 531, L11

Bohlin R. C., Savage B. D., Drake J. F., 1978, ApJ, 224, 132

Bot C., Ysard N., Paradis D., Bernard J. P., Lagache G., Israel F. P., Wall W. F., 2010, A&A, 523, A20

Briggs F. H., 1982, ApJ, 259, 544

Briggs F. H., Wolfe A. M., Krumm N., Salpeter E. E., 1980, ApJ, 238, 510

Calzetti D., 2001, PASP, 113, 1449

Carniani S. et al., 2024, Nature, 633, 318

Ciotti L., Bertin G., 1999, A&A, 352, 447

Conroy C., 2013, ARA&A, 51, 393

Corbelli E., 2003, MNRAS, 342, 199

Dasyra K. M., Xilouris E. M., Misiriotis A., Kylafis N. D., 2005, A&A, 437, 447

de Blok W. J. G., Walter F., Brinks E., Trachternach C., Oh S. H., Kennicutt, Jr. R. C., 2008, AJ, 136, 2648

De Geyter G. et al., 2015, MNRAS, 451, 1728

De Looze I. et al., 2014, A&A, 571, A69

de Vaucouleurs G., 1991, Science, 254, 1667

Disney M., Davies J., Phillipps S., 1989, MNRAS, 239, 939

Dobbs C. L., Theis C., Pringle J. E., Bate M. R., 2010, MNRAS, 403, 625

Draine B. T., 1978, ApJS, 36, 595

Draine B. T., 2003, ARA&A, 41, 241

Draine B. T., Lee H. M., 1984, ApJ, 285, 89

Draine B. T., Li A., 2007, ApJ, 657, 810

Durrell P. R., Mihos J. C., Feldmeier J. J., Jacoby G. H., Ciardullo R., 2003, ApJ, 582, 170

Dwek E., Werner M. W., 1981, ApJ, 248, 138

Emden R., 1907, Gaskugeln. B.G. Teubner

Erwin P., 2015, ApJ, 799, 226

Eskew M., Zaritsky D., Meidt S., 2012, AJ, 143, 139

Fazio G. G. et al., 2004, ApJS, 154, 10

Ferguson A. M. N., Wyse R. F. G., Gallagher J. S., Hunter D. A., 1998, ApJ, 506, L19

Fitzpatrick E. L., 1999, PASP, 111, 63

Galliano F., Galametz M., Jones A. P., 2018, ARA&A, 56, 673

Garcia-Burillo S., Guelin M., Cernicharo J., Dahlem M., 1992, A&A, 266, 21

Gould R. J., Gold T., Salpeter E. E., 1963, ApJ, 138, 408

Gould R. J., Salpeter E. E., 1963, ApJ, 138, 393

Greenberg J. M., 1963, ARA&A, 1, 267

Griffin M. J. et al., 2010, A&A, 518, L3

Henyey L. G., Greenstein J. L., 1941, ApJ, 93, 70

Hermelo I. et al., 2016, A&a, 590, A56

Hernández-Aguayo C. et al., 2023, MNRAS, 524, 2556

Herschel W., 1785, Philosophical Transactions of the Royal Society of London Series I, 75, 213

Hodges-Kluck E. J., Bregman J. N., 2013, ApJ, 762, 12

Hodges-Kluck E. J., Bregman J. N., Li J.-t., 2018, ApJ, 866, 126

Hollenbach D., Salpeter E. E., 1971, ApJ, 163, 155

Hoopes C. G., Walterbos R. A. M., Rand R. J., 1999, ApJ, 522, 669

Hummel E., Dahlem M., van der Hulst J. M., Sukumar S., 1991, A&A, 246, 10

Inman C. J., Popescu C. C., Rushton M. T., Murphy D., 2023, MNRAS, 526, 118

Jarrett T. H., Chester T., Cutri R., Schneider S. E., Huchra J. P., 2003, AJ, 125, 525

Jo Y.-S., Seon K.-i., Shinn J.-H., Yang Y., Lee D., Min K.-W., 2018, ApJ, 862, 25

Jones A. P., Köhler M., Ysard N., Bocchio M., Verstraete L., 2017, A&A, 602, A46

Jones F. C., 1968, Physical Review, 167, 1159

Juvela M., Padoan P., Jimenez R., 2003, ApJ, 591, 258

Katsioli S. et al., 2023, A&A, 679, A7

Kennicutt, Jr. R. C., 1998, ApJ, 498, 541

Kessler M. F. et al., 1996, A&A, 315, L27

King I., 1962, AJ, 67, 471

Kylafis N., Xilouris E., 2005, in AIP CONFERENCE PROCEEDINGS, Vol. 761, Spectral Energy Distributions of Gas-Rich Galaxies: Confronting Models with Data, Popescu, CC and Tuffs, RJ, ed., pp. 3–16, International Workshop on Spectral Energy Distributions of Gas-Rich Galaxies, Max Planck Inst, Nucl Phys, Heidelberg, GERMANY, OCT 04-08, 2004

Kylafis N. D., Bahcall J. N., 1987, ApJ, 317, 637

Laine S. et al., 2016, AJ, 152, 72

Lane H. J., 1870, American Journal of Science, 50, 57

Lelièvre M., Roy J.-R., 2000, AJ, 120, 1306

Lemke D. et al., 1996, A&A, 315, L64

Leroy A. K. et al., 2011, ApJ, 737, 12

Leroy A. K. et al., 2019, ApJS, 244, 24

Leroy A. K., Walter F., Brinks E., Bigiel F., de Blok W. J. G., Madore B., Thornley M. D., 2008, AJ, 136, 2782

Linden S. T., Mihos J. C., 2022, ApJ, 933, L33

Martínez-Delgado D., Peñarrubia J., Gabany R. J., Trujillo I., Majewski S. R., Pohlen M., 2008, ApJ, 689, 184

Mathis J. S., 1990, AAR&A, 28, 37

Mihos J. C., Harding P., Spengler C. E., Rudick C. S., Feldmeier J. J., 2013, ApJ, 762, 82

Misiriotis A., Popescu C. C., Tuffs R., Kylafis N. D., 2001, A&A, 372, 775

Montier L. A., Giard M., 2004, A&A, 417, 401

Mosenkov A. V. et al., 2018, A&A, 616, A120

Mosenkov A. V. et al., 2016, A&A, 592, A71

Müller O., Vudragović A., Bílek M., 2019, A&A, 632, L13

Natale G., Popescu C. C., Rushton M., Yang R., Thirlwall J. J., Pricopi D., 2022, MNRAS, 509, 2339

Natale G. et al., 2017, A&A, 607, A125

Natale G., Popescu C. C., Tuffs R. J., Debattista V. P., Fischera J., Grootes M. W., 2015, MNRAS, 449, 243

Natale G., Popescu C. C., Tuffs R. J., Semionov D., 2014, MNRAS, 438, 3137

Nersesian A. et al., 2020a, A&A, 637, A25

Nersesian A. et al., 2020b, A&A, 643, A90

Oosterloo T., Fraternali F., Sancisi R., 2007, AJ, 134, 1019

Persic M., Rephaeli Y., 2007, A&A, 463, 481

Pilbratt G. L. et al., 2010, A&A, 518, L1

Pildis R. A., Bregman J. N., Schombert J. M., 1994, ApJ, 423, 190

Pilyugin L. S., Tautvaišienė G., Lara-López M. A., 2023, A&A, 676, A57

Poglitsch A. et al., 2010, A&A, 518, L2

Pointecouteau E., da Silva A., Catalano A., Montier L., Lanoux J., Roncarelli M., Giard M., 2009, Advances in Space Research, 44, 440

Popescu C. C., Misiriotis A., Kylafis N. D., Tuffs R. J., Fischera J., 2000, A&A, 362, 138

Popescu C. C., Tuffs R. J., 2003, A&A, 410, L21

Popescu C. C., Tuffs R. J., 2010, in American Institute of Physics Conference Series, Vol. 1240, Hunting for the Dark: the Hidden Side of Galaxy Formation, Debattista V. P., Popescu C. C., eds., pp. 35–46

Popescu C. C., Tuffs R. J., 2013, MNRAS, 436, 1302

Popescu C. C., Tuffs R. J., Dopita M. A., Fischera J., Kylafis N. D., Madore B. F., 2011, A&A, 527, A109

Popescu C. C., Tuffs R. J., Kylafis N. D., Madore B. F., 2004, A&A, 414, 45

Popescu C. C., Yang R., Tuffs R. J., Natale G., Rushton M., Aharonian F., 2017, MNRAS, 470, 2539

Pricopi D., Popescu C. C., Rushton M. T., Murphy D., Inman C. J., Toma R., 2025, MNRAS, 537, 56

Radburn-Smith D. J. et al., 2011, ApJs, 195, 18

Rahmani S., Lianou S., Barmby P., 2016, MNRAS, 456, 4128

Rand R. J., 1996, ApJ, 462, 712

Rees M. J., Ostriker J. P., 1977, MNRAS, 179, 541

Rémy-Ruyer et al., 2013, A&A, 557, A95

Rieke G. H. et al., 2004, ApJS, 154, 25

Rosolowsky E., Simon J. D., 2008, ApJ, 675, 1213

Rushton M. T., Popescu C. C., Inman C. J., Natale G., Pricopi D., 2022, MNRAS, 514, 113

Saftly W., Baes M., De Geyter G., Camps P., Renaud F., Guedes J., De Looze I., 2015, A&A, 576, A31

Salo H., Laurikainen E., 2000, MNRAS, 319, 377

Sancisi R., 1976, A&A, 53, 159

Sandage A., 1961, The Hubble Atlas of Galaxies. Carnegie Institution of Washington

Sauvage M., Tuffs R. J., Popescu C. C., 2005, SSR, 119, 313

Savage B. D., Mathis J. S., 1979, ARA&A, 17, 73

Sawala T., Teeriaho M., Johansson P. H., 2023, MNRAS, 521, 4863

Schaye J. et al., 2023, MNRAS, 526, 4978

Scoville N. Z., Thakkar D., Carlstrom J. E., Sargent A. I., 1993, ApJ, 404, L59

Seon K.-i., Witt A. N., Shinn J.-h., Kim I.-j., 2014, ApJ, 785, L18

Sérsic J. L., 1963, Boletin de la Asociacion Argentina de Astronomia La Plata Argentina, 6, 41

Sersic J. L., 1968, Atlas de Galaxias Australes

Shang Z. et al., 1998, ApJ, 504, L23

Shinn J.-H., Seon K.-I., 2015, ApJ, 815, 133

Skrutskie M. F. et al., 2006, AJ, 131, 1163

Springel V. et al., 2005, Nature, 435, 629

Steinacker J., Baes M., Gordon K. D., 2013, ARA&A, 51, 63

Swaters R. A., Sancisi R., van der Hulst J. M., 1997, ApJ, 491, 140

Temple R. F., Raychaudhury S., Stevens I. R., 2005, MNRAS, 362, 581

Thirlwall J. J., Popescu C. C., Tuffs R. J., Natale G., Norris M., Rushton M., Grootes M., Carroll B., 2020, MNRAS, 495, 835

Tielens A. G. G. M., Tokunaga A. T., Geballe T. R., Baas F., 1991, ApJ, 381, 181

Tikhonov N. A., Galazutdinova O. A., 2005, Astrophysics, 48, 221

Toomre A., Toomre J., 1972, ApJ, 178, 623

Trumpler R. J., 1930, PASP, 42, 214

van der Kruit P. C., 1984, A&A, 140, 470

van der Kruit P. C., Searle L., 1981, A&A, 95, 105

van Dokkum P. et al., 2019, ApJ, 883, L32

Városi F., Dwek E., 1999, ApJ, 523, 265

Verstappen J. et al., 2013, A&A, 556, A54

Verstocken S. et al., 2020, A&A, 637, A24

Viaene S. et al., 2017, A&A, 599, A64

Viaene S. et al., 2014, A&A, 567, A71

Walter F., Brinks E., de Blok W. J. G., Bigiel F., Kennicutt, Robert C. J., Thornley M. D., Leroy A., 2008, AJ, 136, 2563

Weingartner J. C., Draine B. T., 2001, ApJ, 548, 296

White S. D. M., Rees M. J., 1978, MNRAS, 183, 341

Wiegert T. et al., 2015, AJ, 150, 81

Williams T. G., Baes M., De Looze I., Relaño M., Smith M. W. L., Verstocken S., Viaene S., 2019, MNRAS, 487, 2753

Williams T. G. et al., 2024, The Astrophysical Journal Supplement Series, 273, 13

Witt A. N., Gordon K. D., 1996, ApJ, 463, 681

Xilouris E. M., Alton P. B., Davies J. I., Kylafis N. D., Papamastorakis J., Trewhella M., 1998, A&A, 331, 894

Xilouris E. M., Byun Y. I., Kylafis N. D., Paleologou E. V., Papamastorakis J., 1999, A&A, 344, 868

Xilouris E. M., Kylafis N. D., Papamastorakis J., Paleologou E. V., Haerendel G., 1997, A&A, 325, 135

Yoon J. H. et al., 2021, MNRAS, 502, 969

York D. G. et al., 2000, AJ, 120, 1579

Zheng Z. et al., 1999, AJ, 117, 2757

Appendix A

Calculating the Luminosity of Light Incident on the Surface of a Clump

For the configuration used to determine the absorption efficiency of the clump, the following formalism was used to determine $L_{\mathrm{inc}}(\lambda, r_{\mathrm{t}})$, the luminosity incident on the clump, that is, the power the clump receives at its surface.

Given the luminosity of the illuminating shell L_{s}, one can then consider some luminosity element of the shell $\mathrm{d}L_{\mathrm{s}}$ that illuminates the clump. The related flux element is

$$\mathrm{d}F_{\mathrm{s}} = \frac{\mathrm{d}L_{\mathrm{s}}}{4\pi d^2}$$

where d is the distance from the surface of the clump to the midpoint of the shell.

The geometric cross-section of the clump is $A = \pi r_{\mathrm{t}}^2$, giving:

$$\begin{aligned}\mathrm{d}L_{\mathrm{inc}} &= \pi r_{\mathrm{t}}^2 \, \mathrm{d}F_{\mathrm{s}} \\ &= \pi r_{\mathrm{t}}^2 \frac{\mathrm{d}L_{\mathrm{s}}}{4\pi d^2}.\end{aligned}$$

As this is true for each element $\mathrm{d}L_\mathrm{s}$ on the shell of emissivity, one can simply integrate over the shell to get the total luminosity incident on the clump:

$$\begin{aligned} \int \mathrm{d}L_\mathrm{inc} &= \pi r_\mathrm{t}^2 \frac{1}{4\pi d^2} \int \mathrm{d}L_\mathrm{s} \\ \Rightarrow L_\mathrm{inc} &= \frac{r_\mathrm{t}^2}{4d^2} L_\mathrm{s}. \end{aligned} \tag{A.1}$$

Appendix B

Optical Cross-Sections by Mass of the Dust in the Diffuse Component

For the diffuse component, the absorption efficiencies $Q^{\rm d}_{\rm abs}$ and scattering efficiencies $Q^{\rm d}_{\rm sca}$ for the grains of composition $i = \{\mathrm{Si}, \mathrm{Gra}, \mathrm{PAH}^0, \mathrm{PAH}^+\}$ are tabulated by Weingartner & Draine (2001). Integrating over the grain size distribution n_i gives the total mass of grains of composition i:

$$\mu_{\mathrm{d},i} = \int_{a_{\min}}^{a_{\max}} \frac{4\pi a^3}{3} n_i(a) \rho_{g,i} \, \mathrm{d}a, \tag{B.1}$$

where $\mu_{\mathrm{d},i}$ is the total mass of grains of composition i per unit hydrogen in units $[\mathrm{g\,H^{-1}}]$, $n_i(a)$ is the number density of grains with size a in units $[\mathrm{H^{-1}}]$, $\rho_{g,i}$ is the volume density by mass of grains of composition i in units $[\mathrm{g\,cm^{-3}}]$, a is the radius of the grain in units [cm] and $a_{\min}$ and $a_{\max}$ are the minimum and maximum grain size respectively. Summing over grain composition i gives the total mass of grains

in units $[\mathrm{g\,H^{-1}}]$:

$$\mu_{\mathrm{d}} = \sum_i \mu_{\mathrm{d},i}. \tag{B.2}$$

The absorption coefficient $\kappa^{\mathrm{d}}_{\mathrm{abs}}$ for grain composition i is calculated as:

$$\kappa^{\mathrm{d}}_{\mathrm{abs},i}(\lambda, a) = \int_{a_{\mathrm{min}}}^{a_{\mathrm{max}}} \pi a^2 n_i(a) Q^{\mathrm{d}}_{\mathrm{abs},i}(\lambda, a)\,\mathrm{d}a \tag{B.3}$$

where $\kappa^{\mathrm{d}}_{\mathrm{abs},i}$ is the absorption coefficient of grains of composition i in units $[\mathrm{cm^2\,H^{-1}}]$ and $Q^{\mathrm{d}}_{\mathrm{abs},i}(\lambda, a)$ is absorption efficiency of grains of composition i. Summing over grain composition i gives the total absorption coefficient in units $[\mathrm{cm^2\,H^{-1}}]$:

$$\kappa^{\mathrm{d}}_{\mathrm{abs}}(\lambda) = \sum_i \kappa^{\mathrm{d}}_{\mathrm{abs},i}(\lambda). \tag{B.4}$$

Dividing Equation B.4 by Equation B.2 gives the absorption cross section $C^{\mathrm{d}}_{\mathrm{abs}}(\lambda)$:

$$C^{\mathrm{d}}_{\mathrm{abs}}(\lambda) = \frac{\kappa^{\mathrm{d}}_{\mathrm{abs}}(\lambda)}{\mu_{\mathrm{d}}} \tag{B.5}$$

in units of $[\mathrm{cm^2\,g^{-1}}]$ which can be converted into units $[\mathrm{pc^2\,M_\odot^{-1}}]$. Similarly, the scattering cross section is calculated by

$$C^{\mathrm{d}}_{\mathrm{sca}}(\lambda) = \frac{\kappa^{\mathrm{d}}_{\mathrm{sca}}(\lambda)}{\mu_{\mathrm{d}}}, \tag{B.6}$$

where $\kappa^{\mathrm{d}}_{\mathrm{sca}}$ is calculated similarly to $\kappa^{\mathrm{d}}_{\mathrm{abs}}$. The extinction cross section $C_{\mathrm{ext}}(\lambda)$ is the sum of the absorption cross section and the scattering cross section:

$$C^{\mathrm{d}}_{\mathrm{ext}}(\lambda) = C^{\mathrm{d}}_{\mathrm{abs}}(\lambda) + C^{\mathrm{d}}_{\mathrm{sca}}(\lambda). \tag{B.7}$$

Appendix C

Dust Mass and Stellar Luminosity

The spatial integration of the stellar volume emissivity and the dust density distribution described by Equations 3.1 and 3.2 up to the truncation radius $R_{\mathrm{t},j}$ and truncation height z_{t}, where $z_{\mathrm{t}} \gg z_j$ is given by

$$I = 4\pi A_{0,j}\, z_j\, T_{z,j} \cdot \begin{cases} h_j^2\, T_{R,j} & \text{if } R_{\mathrm{in},j} = 0 \\ \left(\frac{1}{3} \Big[\left(1 + \frac{\chi_j}{2}\right) R_{\mathrm{in},j}^2 - (1-\chi_j) \frac{R_{\mathrm{tin},j}^3}{R_{\mathrm{in},j}} - \frac{3}{2} \chi_j R_{\mathrm{tin},j}^2 \Big] \exp\left(-\frac{R_{\mathrm{in},j}}{h_j}\right) + h_j^2\, T_{R,j} \right) & \text{if } R_{\mathrm{in},j} > 0 \end{cases} \tag{C.1}$$

$$T_{R,j} = \exp\left(-\frac{R_{\mathrm{in},j}}{h_j}\right) - \exp\left(-\frac{R_{\mathrm{t},j}}{h_j}\right) + \frac{R_{\mathrm{in},j}}{h_j} \exp\left(-\frac{R_{\mathrm{in},j}}{h_j}\right) - \frac{R_{\mathrm{t},j}}{h_j} \exp\left(-\frac{R_{\mathrm{t},j}}{h_j}\right) \tag{C.2}$$

$$T_{z,j} = 1 - \exp\left(-\frac{z_{\mathrm{t}}}{z_j}\right). \tag{C.3}$$

Depending on what A_0 represents the above equations can be used to calculate the integrated luminosity of the stellar disc and the dust mass. When considering a stellar component, A_0 represents the central volume luminosity density L_0 and $j =$'s'. Thus Equation C.1, C.2, C.3 are used to calculate the integrated luminosity

of the stellar disc:

$$L = I\left(L_0, h_\mathrm{s}, z_\mathrm{s}\right) \tag{C.4}$$

where h_s and z_s are the scale length and height stellar disc respectively.

Alternatively, for a dust component, A_0 can take on the value of the central volume density of dust, ρ_0, given by

$$\begin{aligned} \rho_0 &= \frac{\tau_\mathrm{B}^\mathrm{d}}{2\kappa_\mathrm{B} z_\mathrm{d}} \\ &= \frac{\tau_\mathrm{B}^\mathrm{f}\left(R_\mathrm{in,d}\right)\exp\left(\frac{R_\mathrm{in,d}}{h_\mathrm{d}}\right)}{2\kappa_B z_\mathrm{d}} \end{aligned} \tag{C.5}$$

where $\tau_\mathrm{B}^\mathrm{f}$ is the face-on optical depth in the B-band, κ_B is the mass extinction coefficient in the B-band and $j =$ 'd'. Thus Equations C.1, C.2, C.3 give the dust mass

$$M_\mathrm{d} = I\left(\rho_\mathrm{c}, h_\mathrm{d}, z_\mathrm{d}\right) \tag{C.6}$$

where h_d and z_d are the scale length and height of the dust disc respectively.

Appendix D

The Calibration of the Dust Emission SEDs of the Pseudo-Grain Component

The dust emission SED of a single clump, heated by a given radiation field is defined as $F_{\lambda}^{\mathrm{c,s}}$. Since the average dust density in the clump, $\rho^{\mathrm{c,av}}$ (defined in Equation 4.12), and the dust density of the diffuse dust (e.g., at the central position ρ_0^{d}) are known, the dust emission SED of the clumps corresponding to the same dust mass as in the diffuse component can be derived.

The scaling factor for the central position η_{cd} is:

$$\eta_{\mathrm{cd}} = \frac{\rho_0^{\mathrm{d}}}{\rho^{\mathrm{c,av}}} \tag{D.1}$$

and the dust emission SED corresponding to clumps of the same mass as in the diffuse component is

$$F_{\lambda}^{\mathrm{c}} = \eta_{\mathrm{cd}} F_{\lambda}^{\mathrm{c,s}} \tag{D.2}$$

where $F_\lambda^{\rm c}$ is the clump emission SED scaled to the dust density in the disc. This form assumes that the total dust mass will be equally shared between the diffuse and clumpy components. Letting the fraction of mass in clumps (Equation 4.23) be a free parameter, Equation D.2 becomes

$$F_\lambda^{\rm c} = \eta_{\rm cd} F_\lambda^{\rm c,s} \frac{f_{\rm c}}{1 - f_{\rm c}}. \tag{D.3}$$

Generalised to any position in a galaxy, $\rho^{\rm d} = \rho_0^{\rm d} \cdot n^{\rm d}(R, z)$ where $n^{\rm d}$ is the dust density distribution normalised to the centre, the scaling factor becomes a function of R and z,

$$\eta_{\rm cd}(R, z) = \frac{\rho^{\rm d}(R, z)}{\rho^{\rm c,av}}. \tag{D.4}$$

Finally, the dust emission SED of dust associated with clumps at any position in a galaxy is given as:

$$F_\lambda^{\rm c}(R, z) = \eta_{\rm cd}(R, z) F_\lambda^{\rm c,s} \frac{f_{\rm c}}{1 - f_{\rm c}}. \tag{D.5}$$

D.1 Double Interpolation of Clump SEDs in RT Calculations

As it is unfeasible to explicitly calculate the clump SEDs based on the radiation fields of each position for each galaxy in the sample, a library of clumpy dust emission templates as heated by radiation fields of various colours and intensity is utilised. To get an even closer match for any given radiation field in a galaxy, a double interpolation technique is applied. For a given position in the galaxy the strength of the radiation fields can be determined using Equations 4.21–4.22, giving $UV_{\rm RF}^{\rm g}$ and $OPT_{\rm RF}^{\rm g}$. Likely, these will not have been exactly calculated in the library so the sampled values of $UV_{\rm RF}$ and $OPT_{\rm RF}$ that are immediately larger and smaller than the real values are selected. Thus, for each $UV_{\rm RF}^{\rm g}$ and $OPT_{\rm RF}^{\rm g}$ of the galaxy there are

two values UV_1, UV_2 and OPT_1, OPT_2 respectively, such that $UV_1 < UV_{\rm RF}^{\rm g} < UV_2$ and $OPT_1 < OPT_{\rm RF}^{\rm g} < OPT_2$.

There are four clump SEDs corresponding to these four combinations, F_{UV_1,OPT_1}, F_{UV_2,OPT_1}, F_{UV_1,OPT_2}, and F_{UV_2,OPT_2}. Three interpolations are then performed. First, $OPT = OPT_1$ is fixed, and an interpolation is performed between F_{UV_1,OPT_1} and F_{UV_2,OPT_1} to give $F_{UV^{\rm g},OPT_1}$. Secondly, $OPT = OPT_2$ is fixed, and an interpolation is performed between F_{UV_1,OPT_2} and F_{UV_2,OPT_2} to give $F_{UV^{\rm g},OPT_2}$. Finally, an interpolation is performed between $F_{UV^{\rm g},OPT_1}$ and $F_{UV^{\rm g},OPT_2}$ to get $F_{UV^{\rm g},OPT^{\rm g}}$, the final clump emission SED for the given radiation fields.

Appendix E

NGC 891 Fits to the Surface Brightness Profiles and Maps

In this appendix, the fits to the surface brightness profiles and maps of NGC 891 are presented for all wavelengths where data were used.

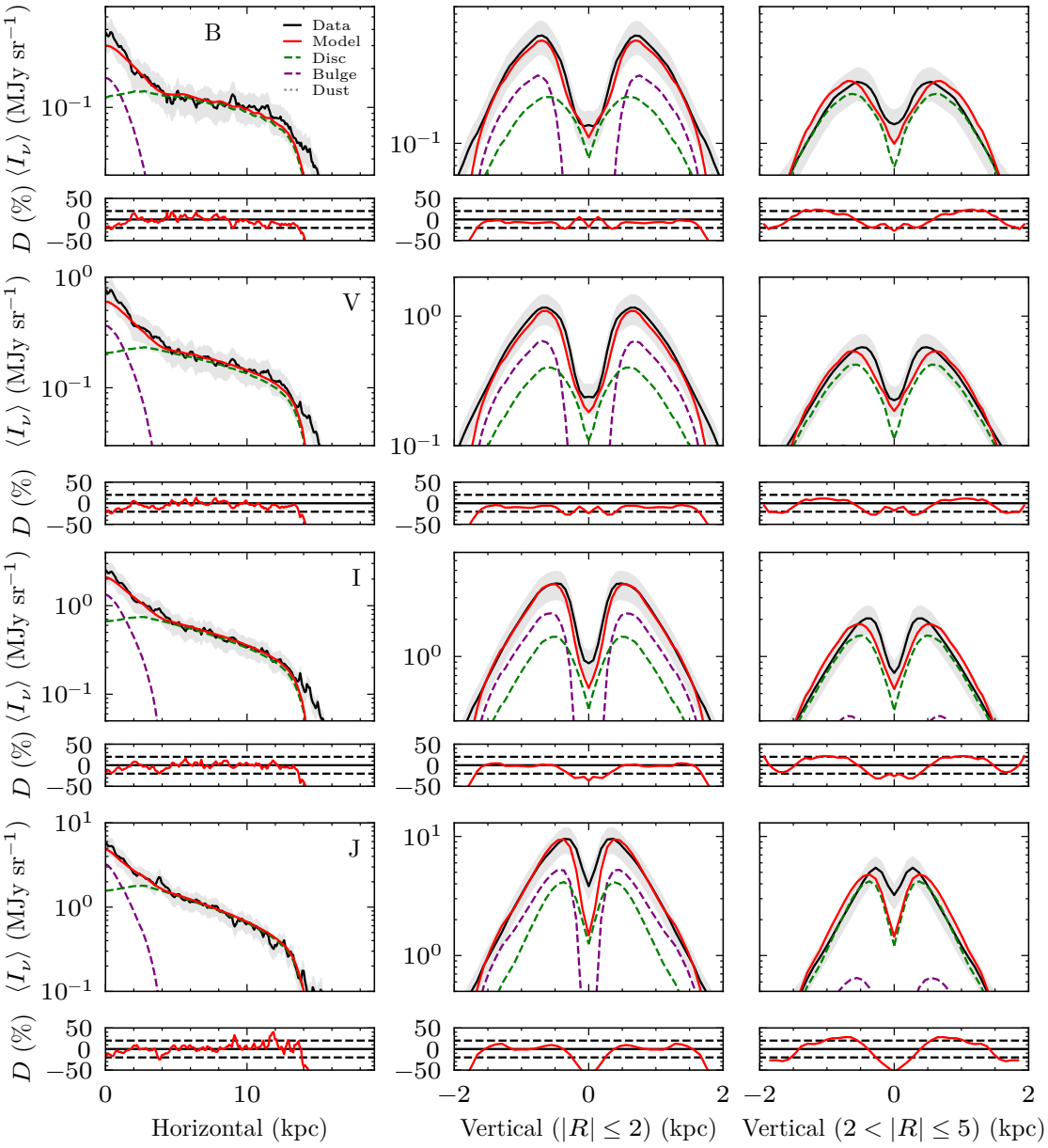

Figure E.1: NGC 891: Averaged horizontal SB profiles (mirrored about the central vertical axis)(LH panel) and averaged vertical SB profiles (middle and RH panel) of the pure diffuse model at the optical wavelengths. The observed SB profiles are plotted with solid black line with the shaded banding indicating the uncertainty. The solid red line indicates the model total, with the individual component contributions plotted with the dashed and dotted lines. The percent differences between the model total and the observed profiles, $D\,[\%]$, are plotted in the panels below each profile, with the dashed horizontal lines indicating $\pm\,20\,\%$ deviation.

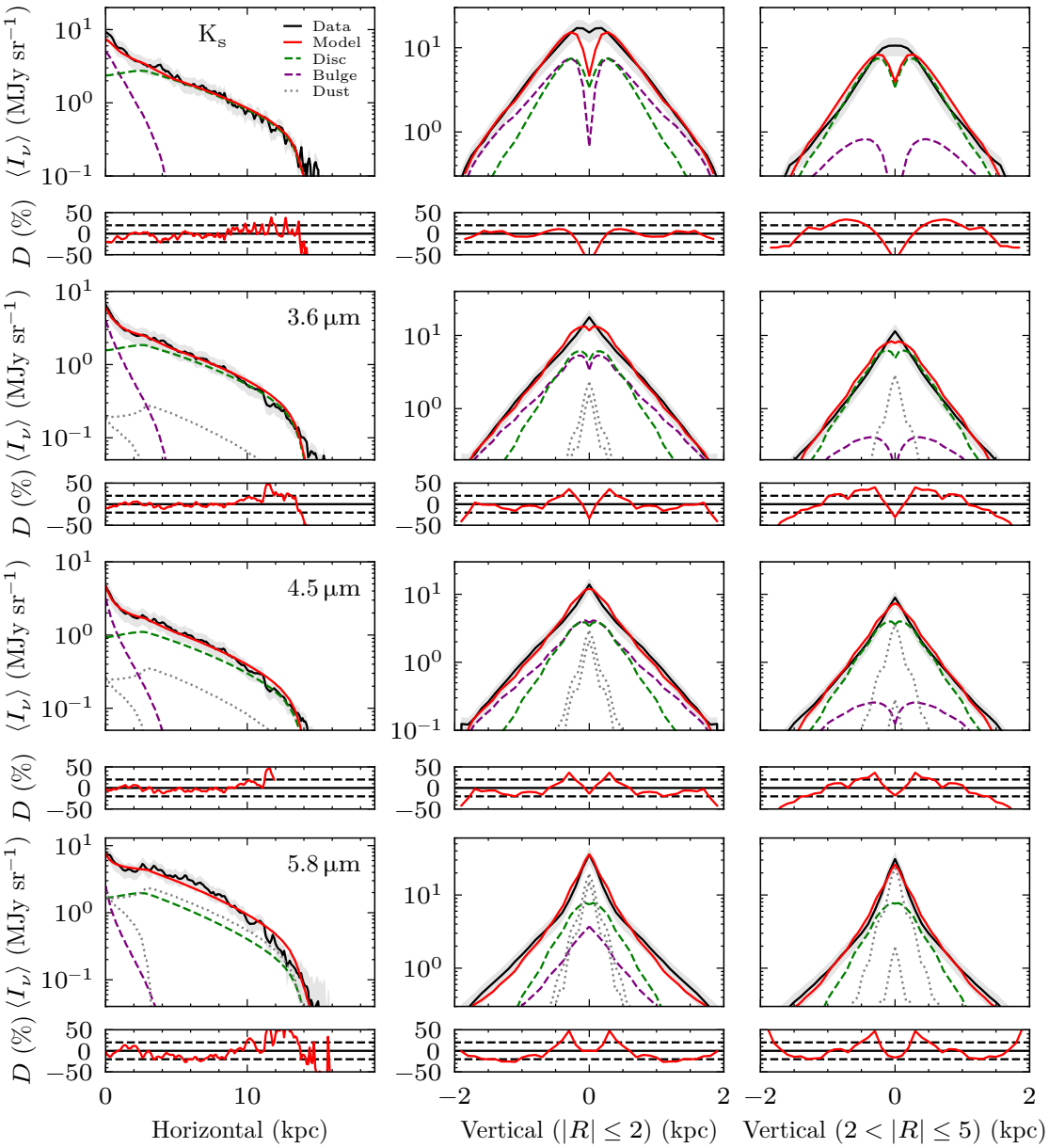

Figure E.2: NGC 891: Same as Fig. E.1 for the diffuse model at NIR wavelengths.

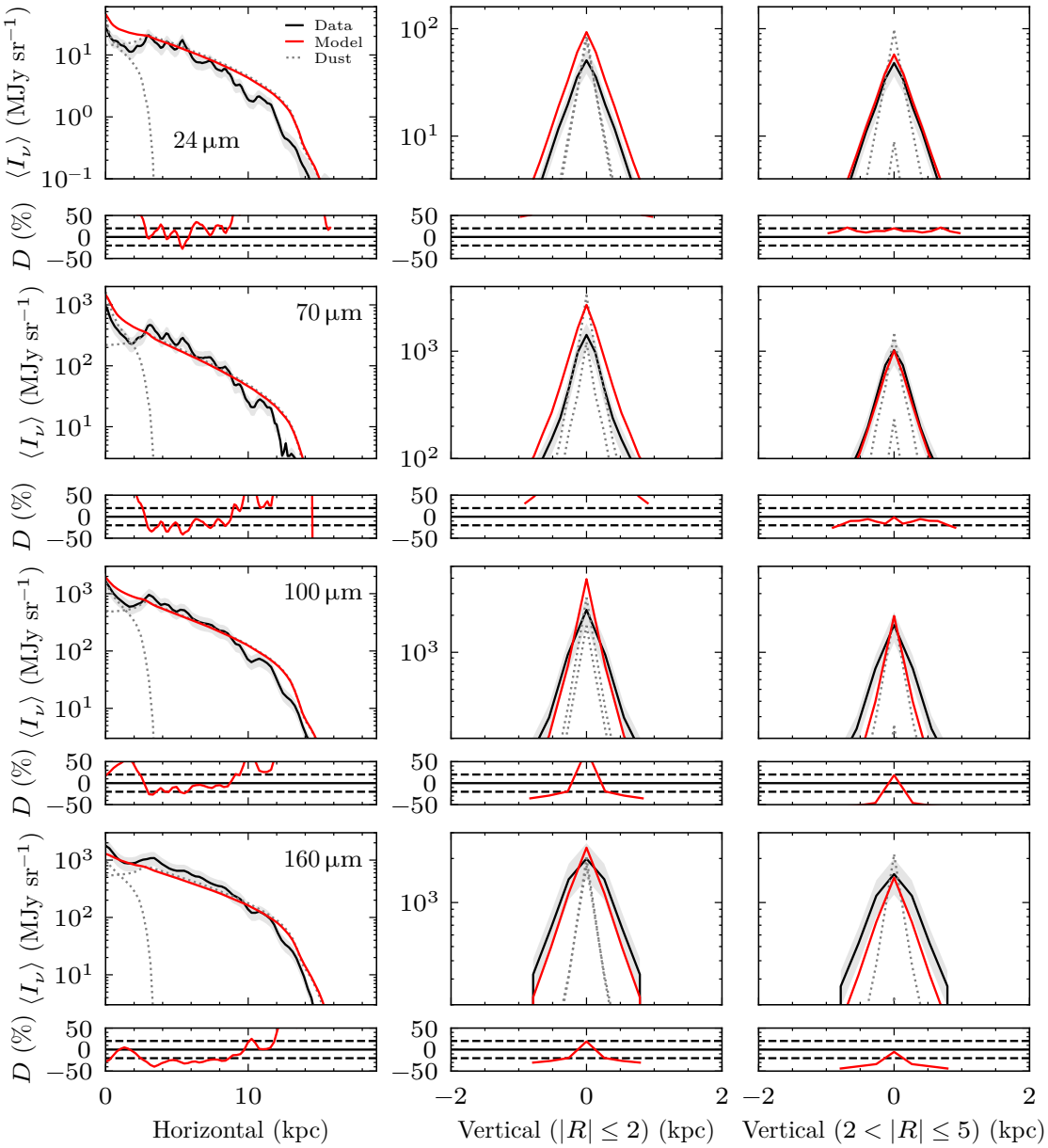

Figure E.3: NGC 891: Same as Fig. E.1 for the diffuse model at MIR/FIR wavelengths.

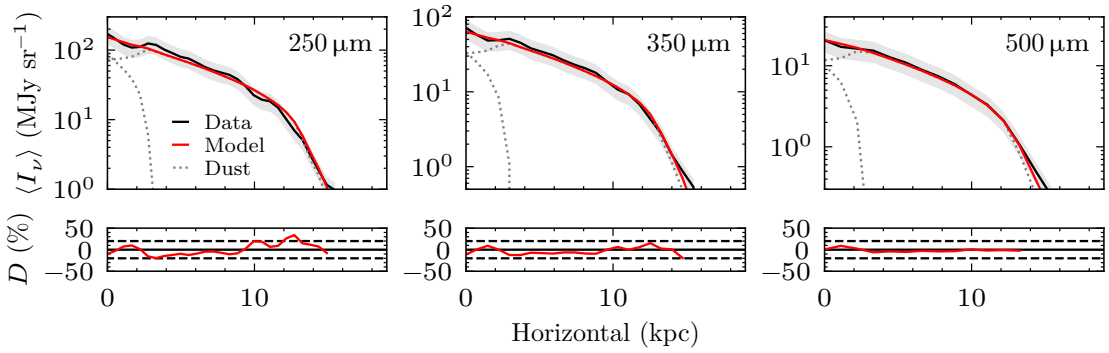

Figure E.4: NGC 891: Averaged horizontal SB profiles (mirrored about the central vertical axis) of the pure diffuse model at wavelengths in the FIR/submm. The observed SB profiles are plotted with the solid black line with the shaded banding indicating the uncertainty. The solid red line indicates the model total, with the individual component contributions plotted with the dashed and dotted lines. The percent differences between the model total and the observed profiles, $D\,[\%]$, are plotted in the panels below each profile, with the dashed horizontal lines indicating $\pm\,20\,\%$ deviation.

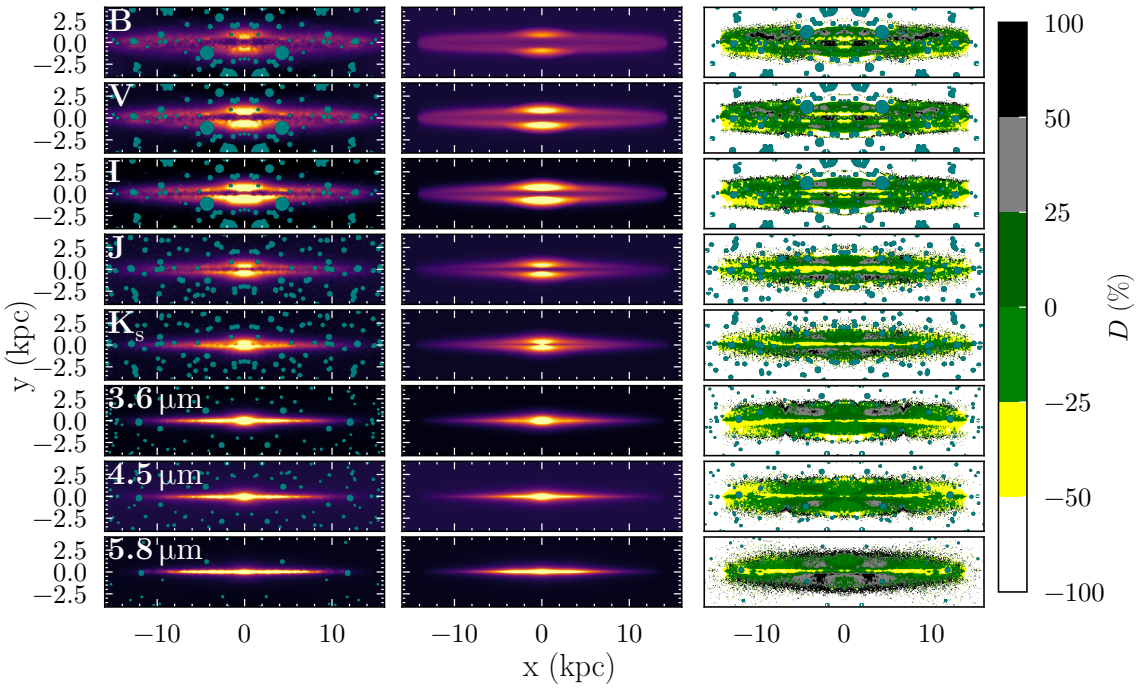

Figure E.5: NGC 891: Fits of the pure diffuse model to the surface brightness maps. Left: surface brightness maps of NGC 891, mirrored about their vertical central axis. Middle: surface brightness maps of the corresponding diffuse model images. Right: residuals between the data and model images calculated as $D = (M - O)/O$. Masked foreground stars are marked in teal.

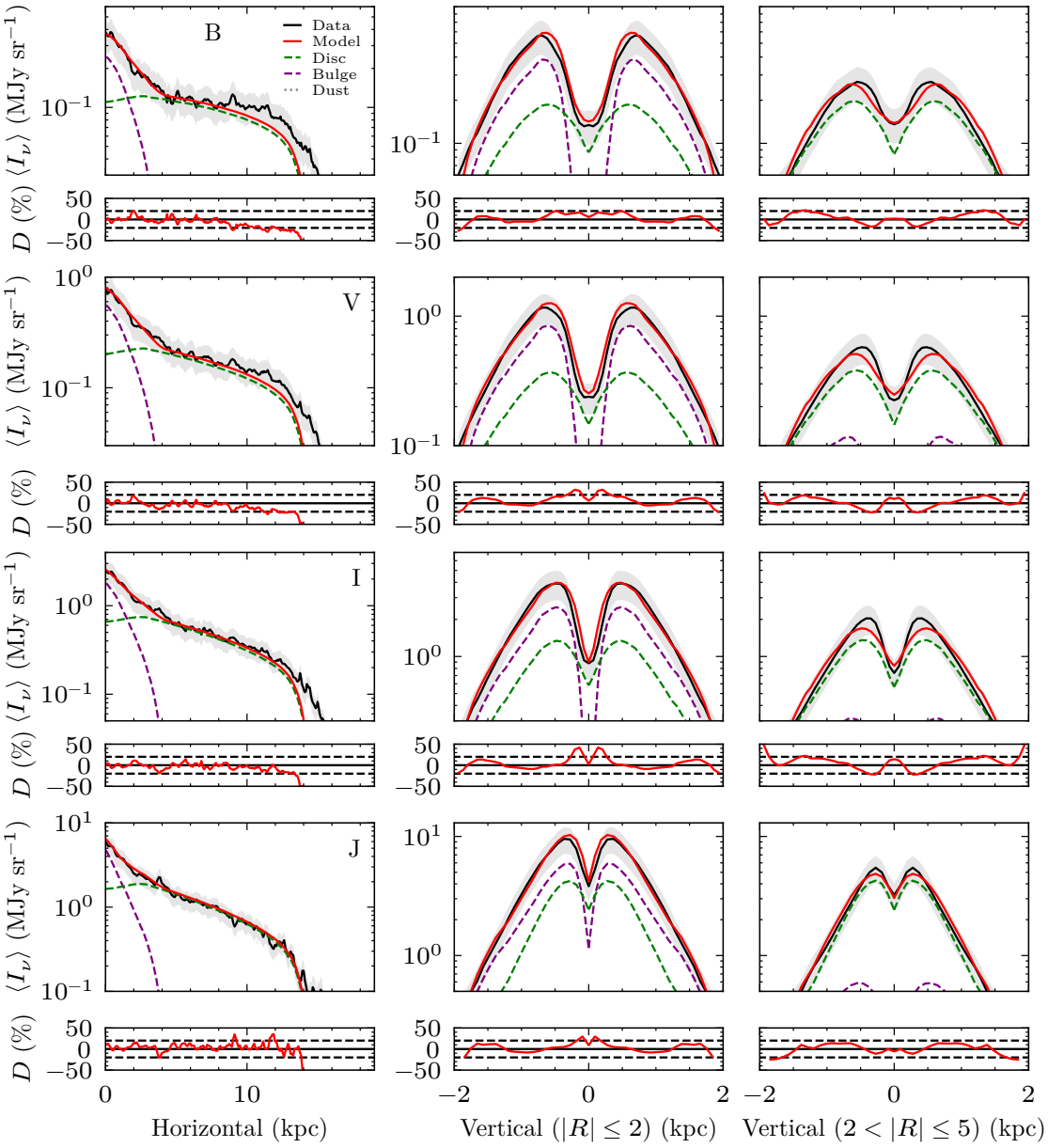

Figure E.6: NGC 891: Averaged horizontal SB profiles (mirrored about the central vertical axis) (LH panel) and averaged vertical SB profiles (middle and RH panels) of the clumpy model at the optical wavelengths. The observed SB profiles are plotted with solid black line with the shaded banding indicating the uncertainty. The solid red line indicates the model total, with the individual component contributions plotted with the dashed and dotted lines. The percent differences between the model total and the observed profiles, $D\,[\%]$, are plotted in the panels below each profile, with the dashed horizontal lines indicating $\pm\,20\,\%$ deviation.

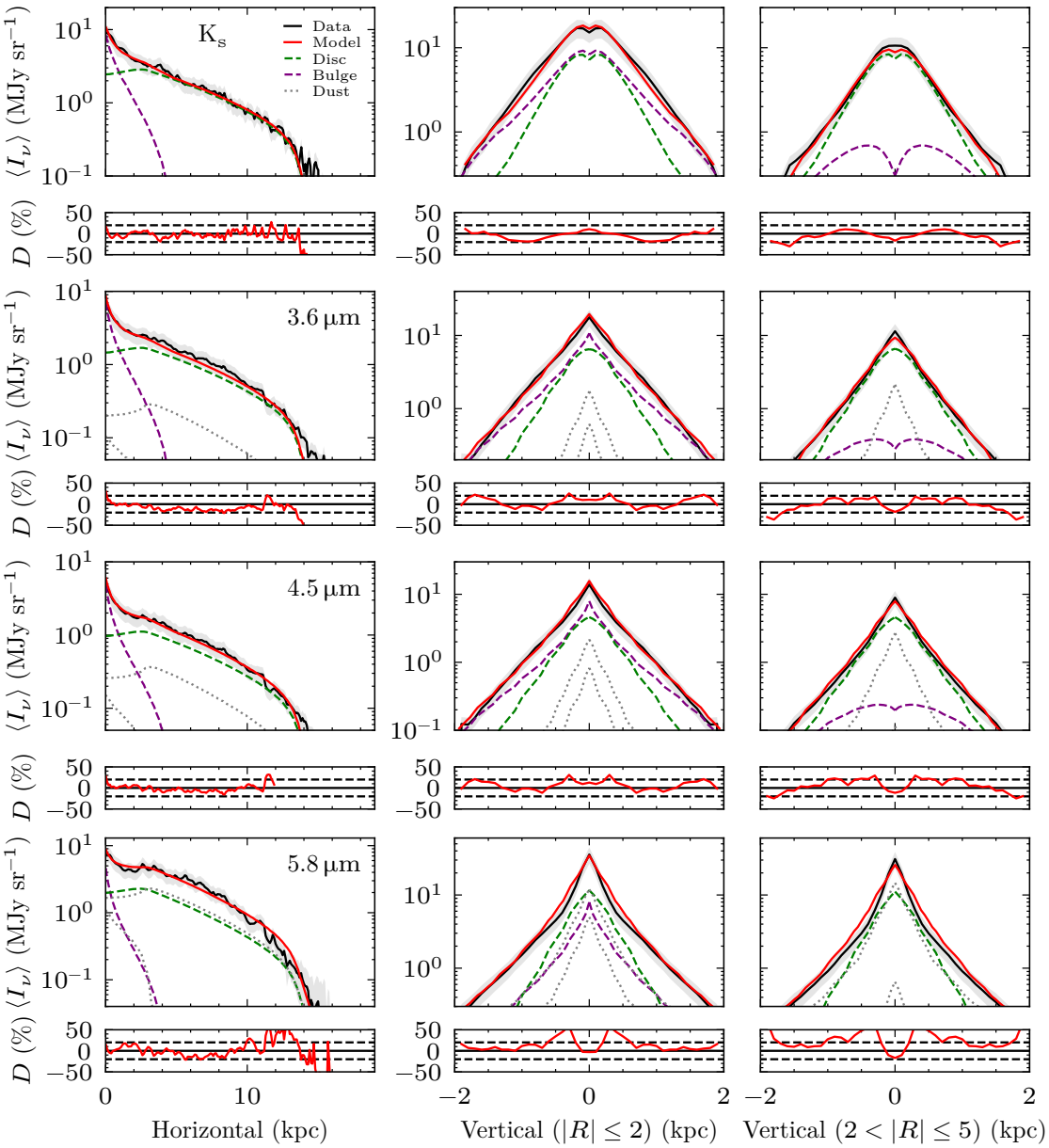

Figure E.7: NGC 891: Same as Fig. E.6 for the clumpy model at NIR wavelengths.

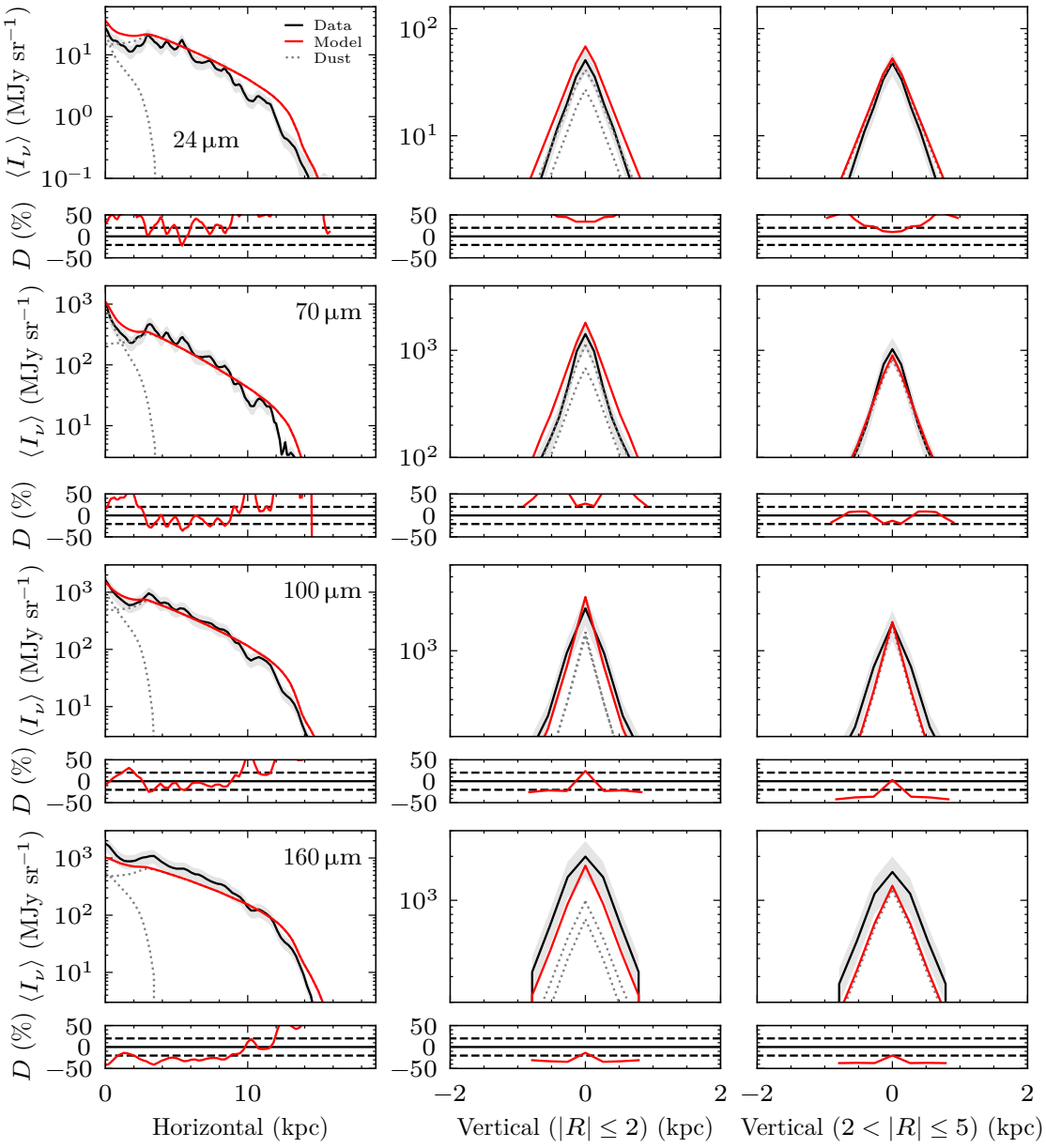

Figure E.8: NGC 891: Same as Fig. E.6 for the clumpy model at MIR/FIR wavelengths.

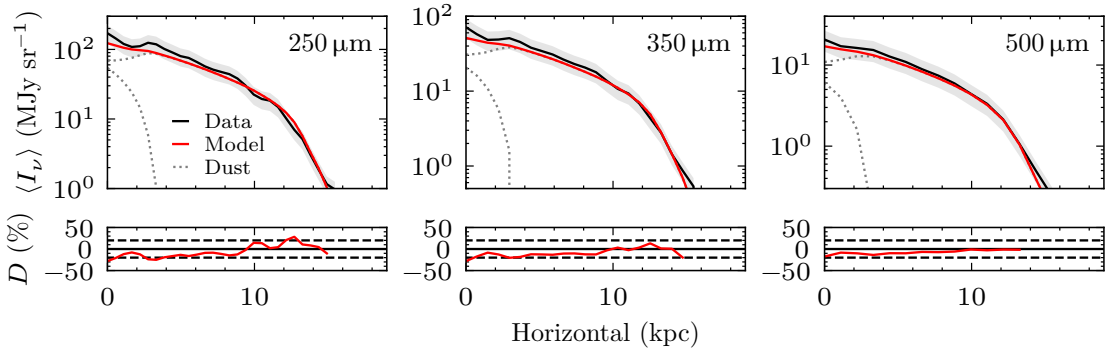

Figure E.9: NGC 891: Averaged horizontal SB profiles (mirrored about the vertical axis) of the clumpy model at wavelengths in the FIR/submm. The observed SB profiles are plotted with the solid black line with the shaded banding indicating the uncertainty. The solid red line indicates the model total, with the individual component contributions plotted with the dashed and dotted lines. The percent differences between the model total and the observed profiles, $D\,[\%]$, are plotted in the panels below each profile, with the dashed horizontal lines indicating $\pm\,20\,\%$ deviation.

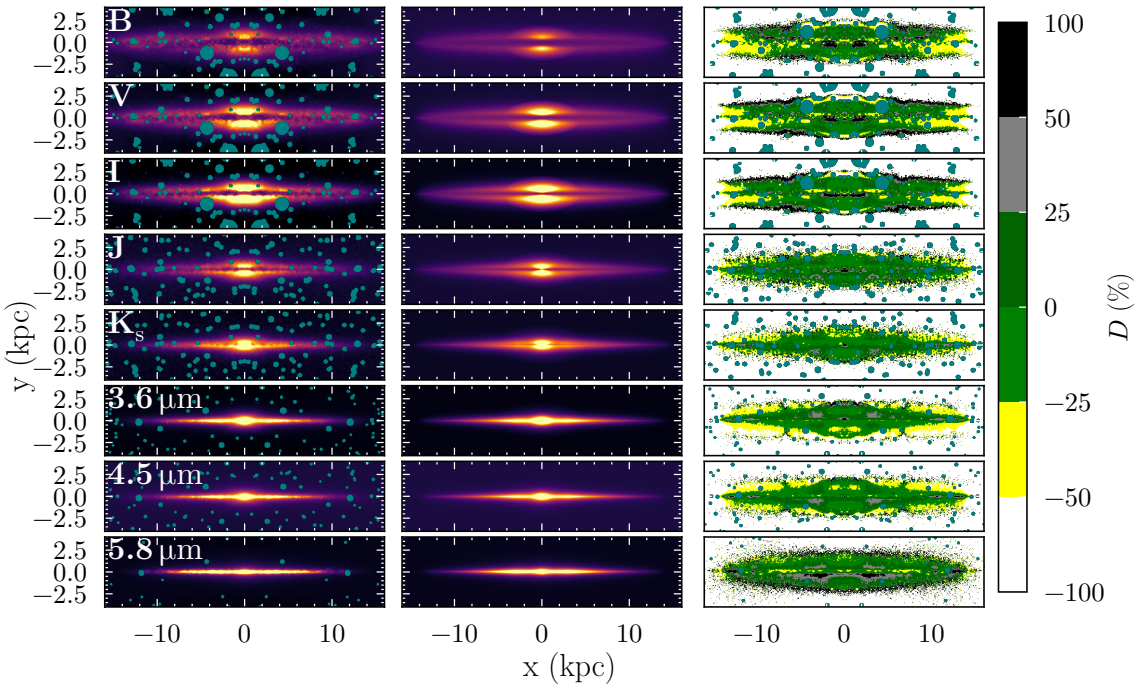

Figure E.10: NGC 891: Fits of the clumpy model to the surface brightness maps. Left: surface brightness maps of NGC 891, mirrored about their vertical central axis. Middle: surface brightness maps of the corresponding diffuse model images. Right: residuals between the data and model images calculated as $D = (M - O)/O$. Masked foreground stars are marked in teal.

Appendix F

NGC 5907 Fits to the Surface Brightness Profiles and Maps

In this appendix, the fits to the surface brightness profiles and maps of NGC 5907 are presented for all wavelengths where data were used.

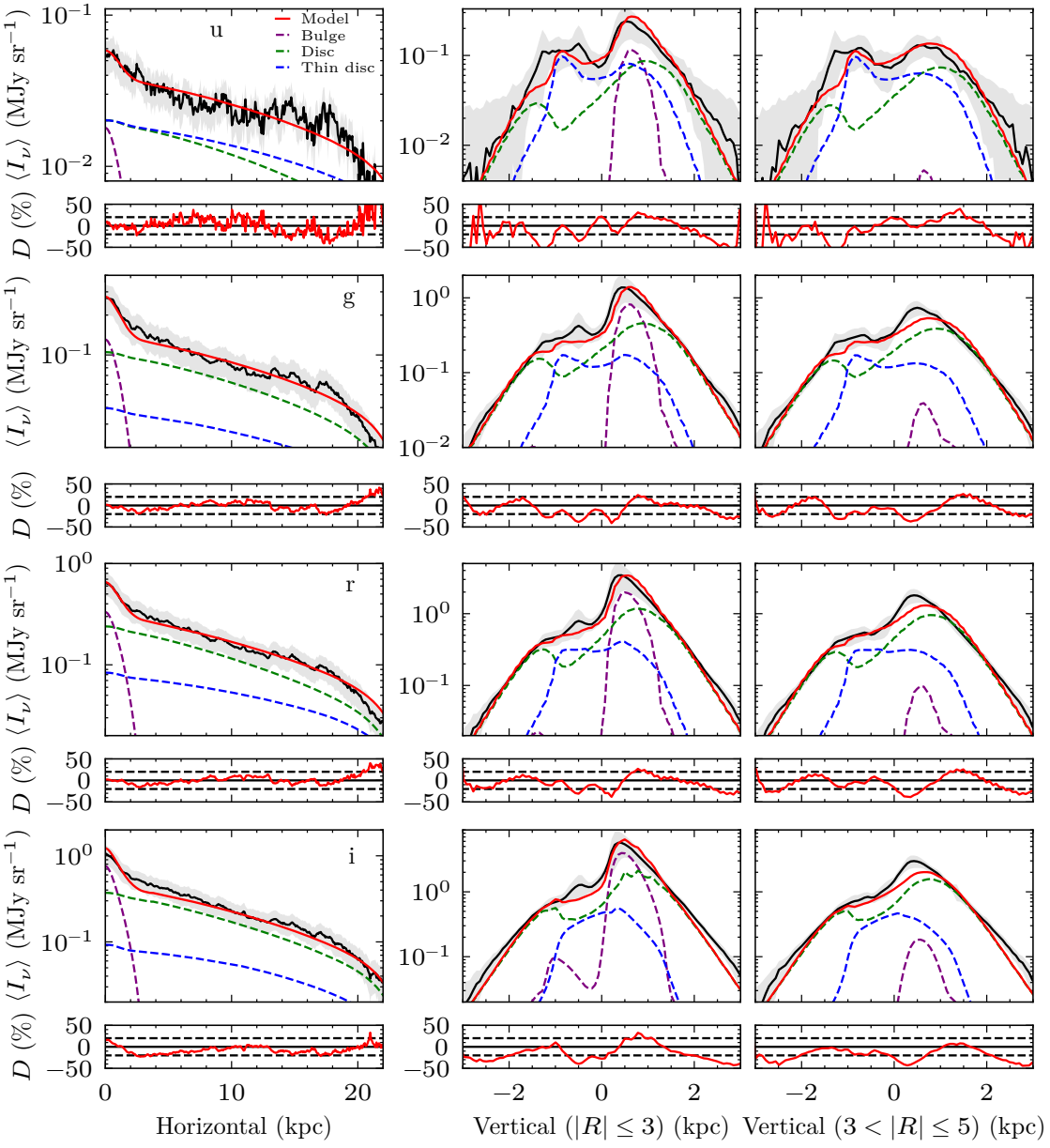

Figure F.1: NGC 5907: Averaged horizontal SB profiles (mirrored about the central vertical axis)(LH panel) and averaged vertical SB profiles (middle and RH panel) of the pure diffuse model at the optical wavelengths The observed SB profiles are plotted with solid black line with the shaded banding indicating the uncertainty. The solid red line indicates the model total, with the individual component contributions plotted with the dashed and dotted lines. The percent differences between the model total and the observed profiles, $D\,[\%]$, are plotted in the panels below each profile, with the dashed horizontal lines indicating $\pm\,20\,\%$ deviation.

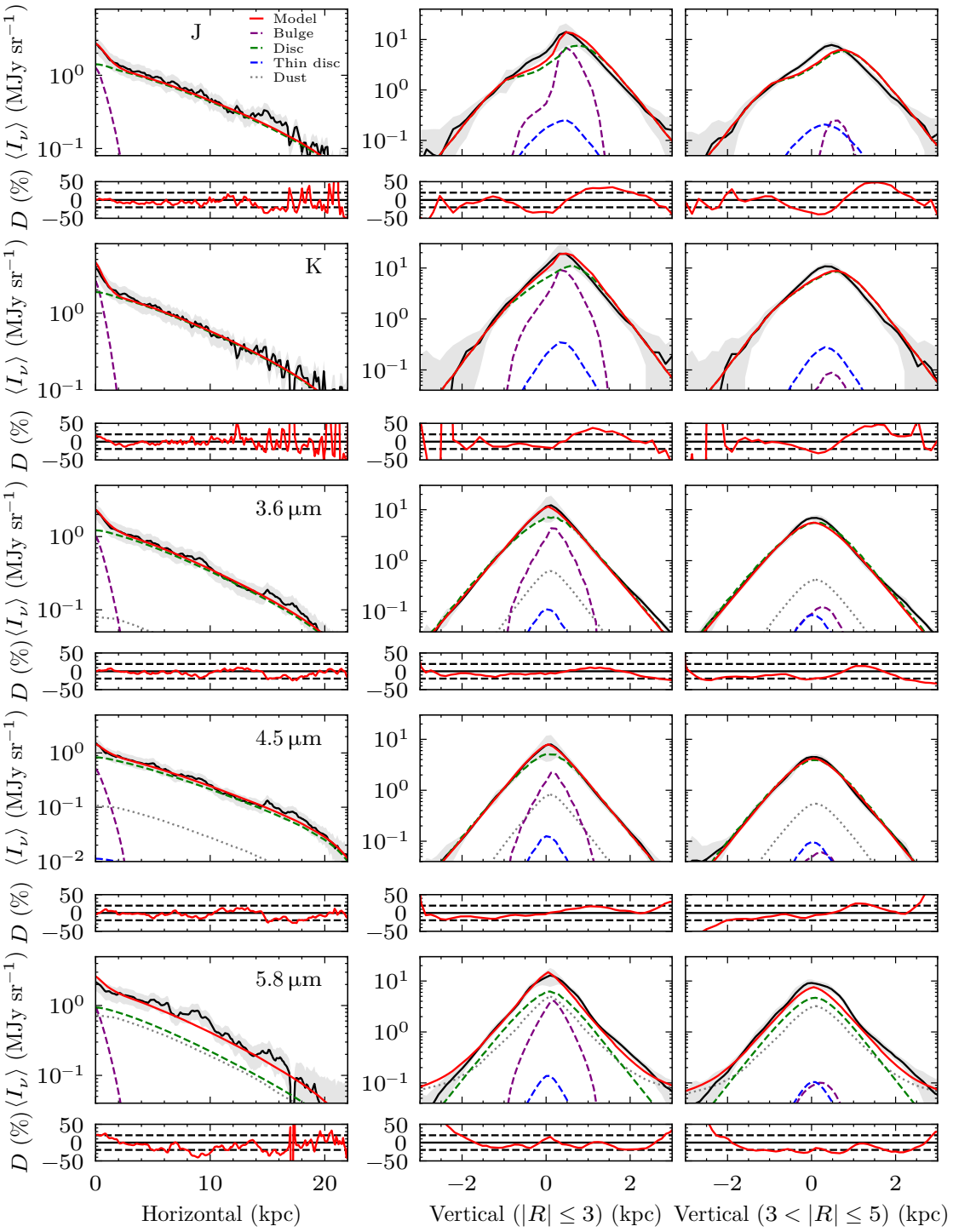

Figure F.2: NGC 5907: Same as Fig. F.1 for the pure diffuse model at the NIR wavelengths.

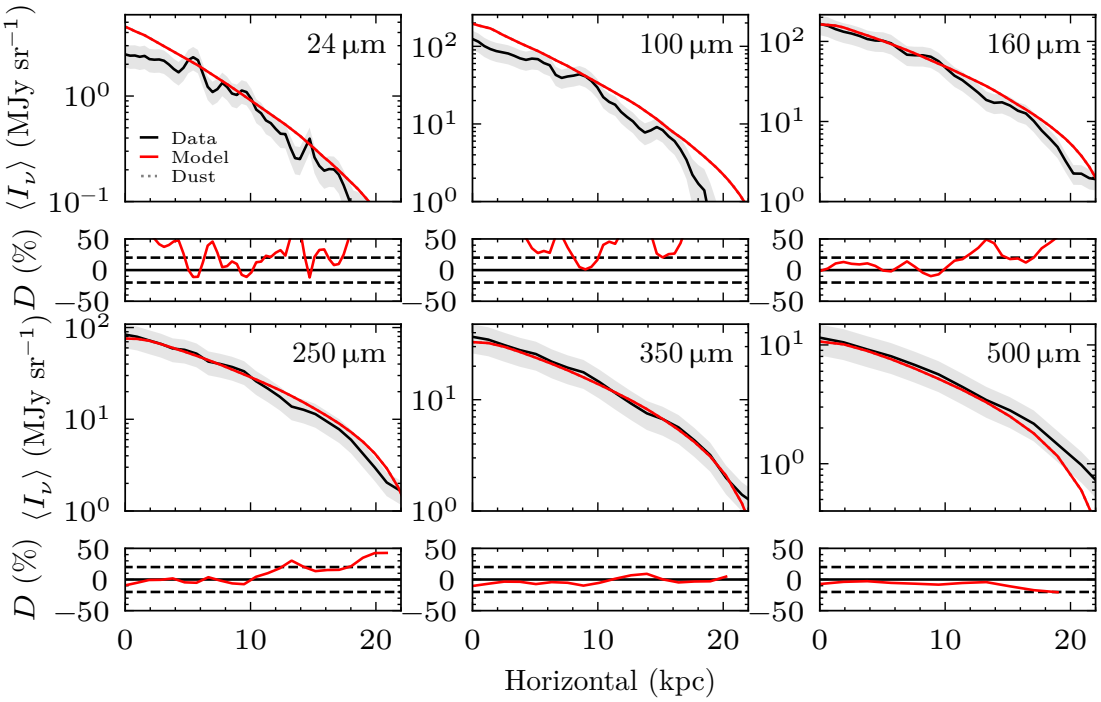

Figure F.3: NGC 5907: Averaged horizontal SB profiles (mirrored about the central vertical axis) of the pure diffuse model at wavelengths in the FIR/submm. The observed SB profiles are plotted with the solid black line with the shaded banding indicating the uncertainty. The solid red line indicates the model total, with the individual component contributions plotted with the dashed and dotted lines. The percent differences between the model total and the observed profiles, $D\,[\%]$, are plotted in the panels below each profile, with the dashed horizontal lines indicating $\pm\,20\,\%$ deviation.

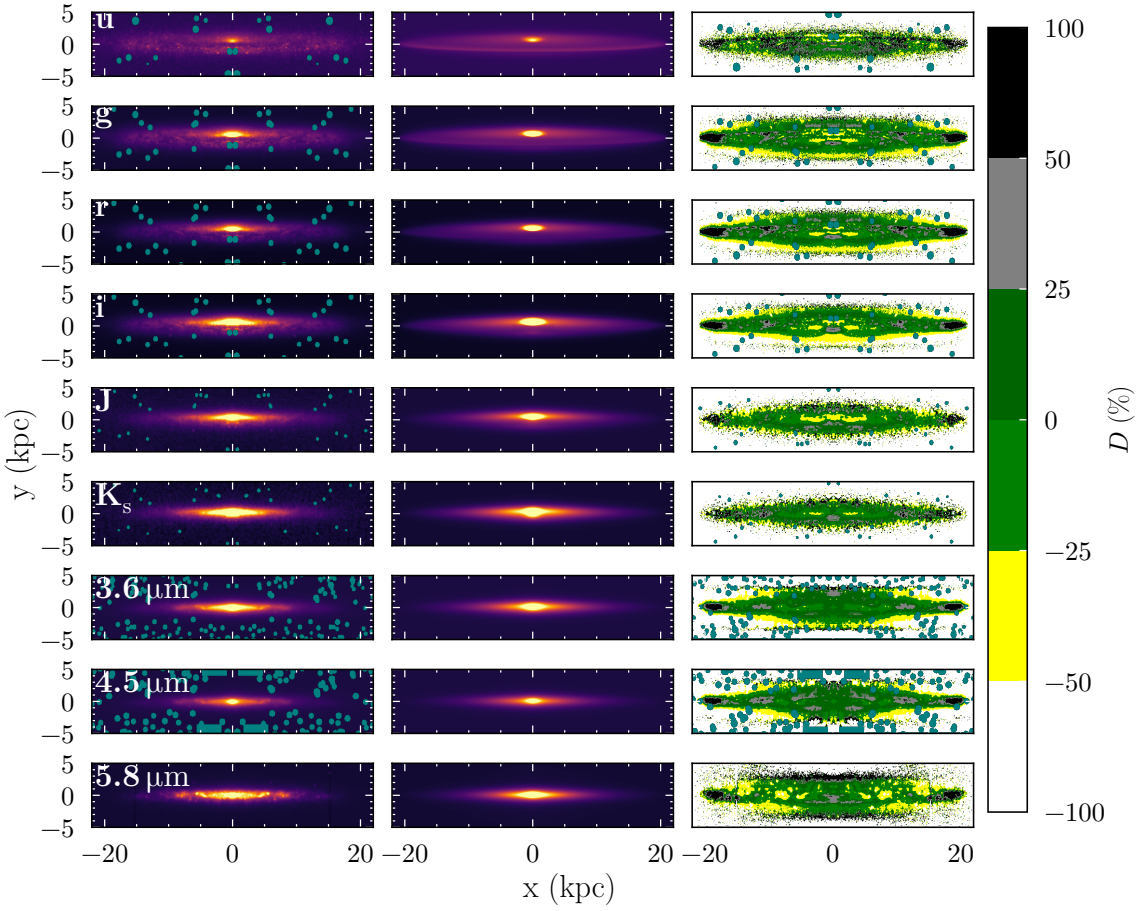

Figure F.4: NGC 5907: Fits of the pure diffuse model to the surface brightness maps. Left: surface brightness maps of NGC 5907, mirrored about their vertical central axis. Middle: surface brightness maps of the corresponding diffuse model images. Right: residuals between the data and model images calculated as $D = (M - O)/O$. Masked foreground stars are marked in teal.

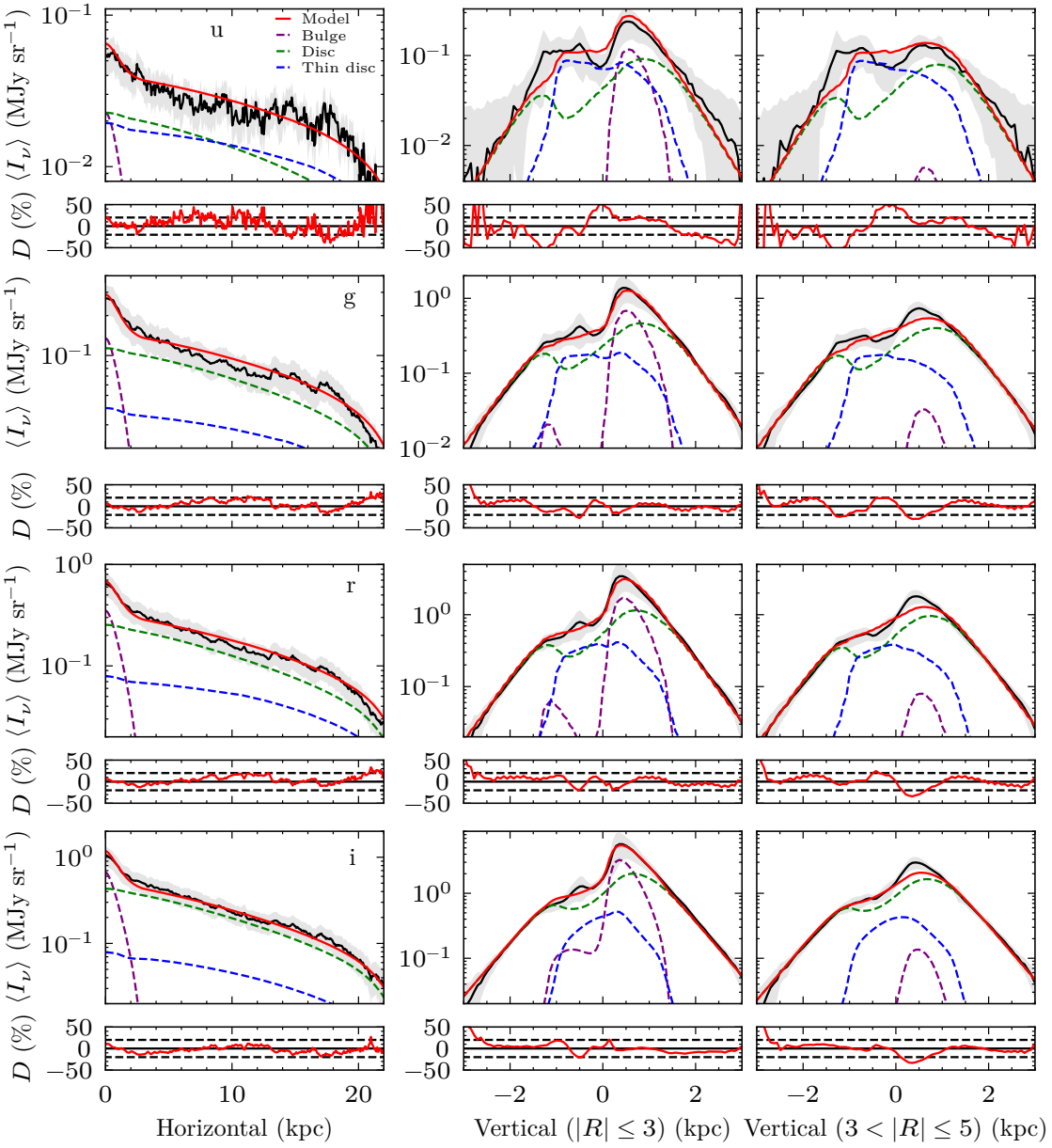

Figure F.5: NGC 5907: Averaged horizontal SB profiles (mirrored about the central vertical axis)(LH panel) and averaged vertical SB profiles (middle and RH panel) of the clumpy model at the optical wavelengths The observed SB profiles are plotted with solid black line with the shaded banding indicating the uncertainty. The solid red line indicates the model total, with the individual component contributions plotted with the dashed and dotted lines. The percent differences between the model total and the observed profiles, $D\,[\%]$, are plotted in the panels below each profile, with the dashed horizontal lines indicating $\pm\,20\,\%$ deviation.

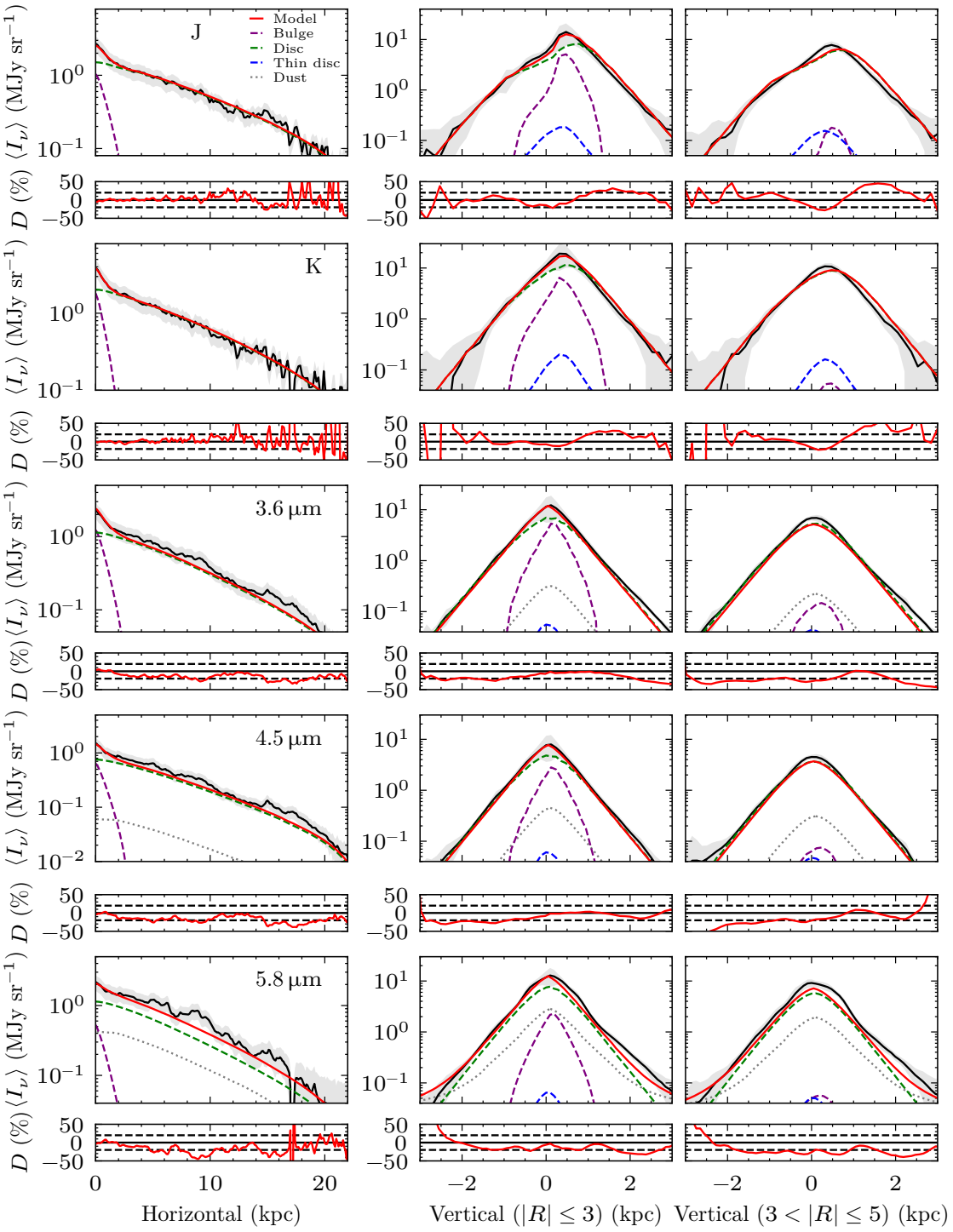

Figure F.6: NGC 5907: Same as Fig. F.5 for the clumpy model at the NIR wavelengths.

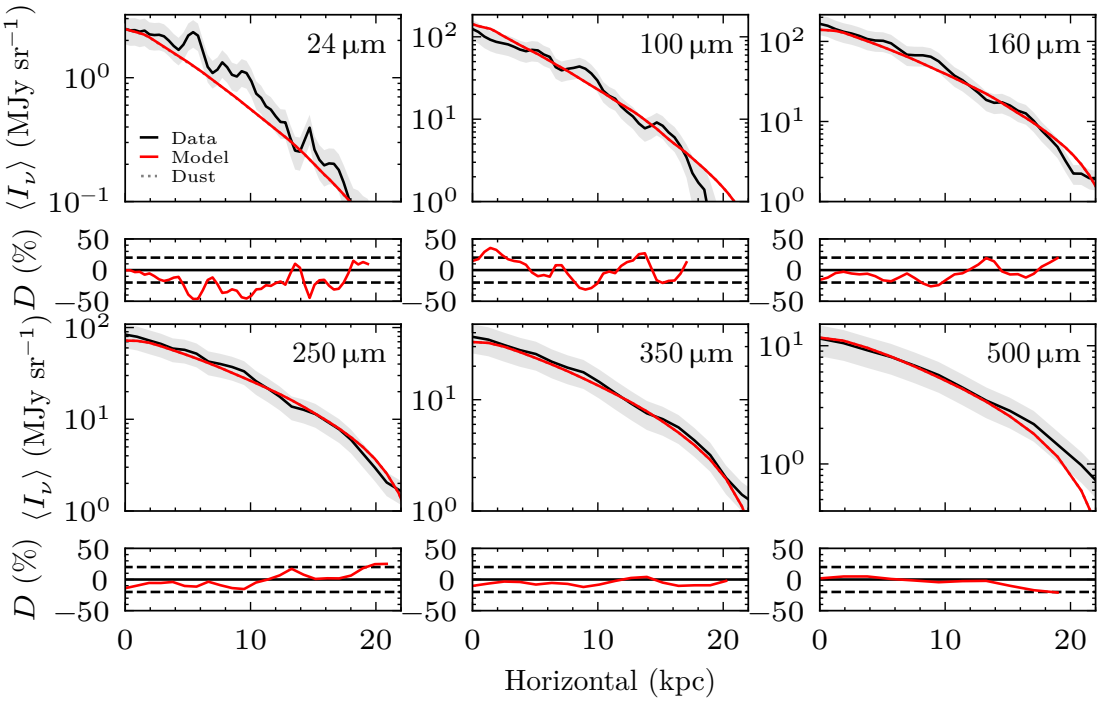

Figure F.7: NGC 5907: Averaged horizontal SB profiles (mirrored about their central vertical centre) of the clumpy model at wavelengths in the FIR/submm. The observed SB profiles are plotted with the solid black line with the shaded banding indicating the uncertainty. The solid red line indicates the model total, with the individual component contributions plotted with the dashed and dotted lines. The percent differences between the model total and the observed profiles, $D\,[\%]$, are plotted in the panels below each profile, with the dashed horizontal lines indicating $\pm\,20\,\%$ deviation.

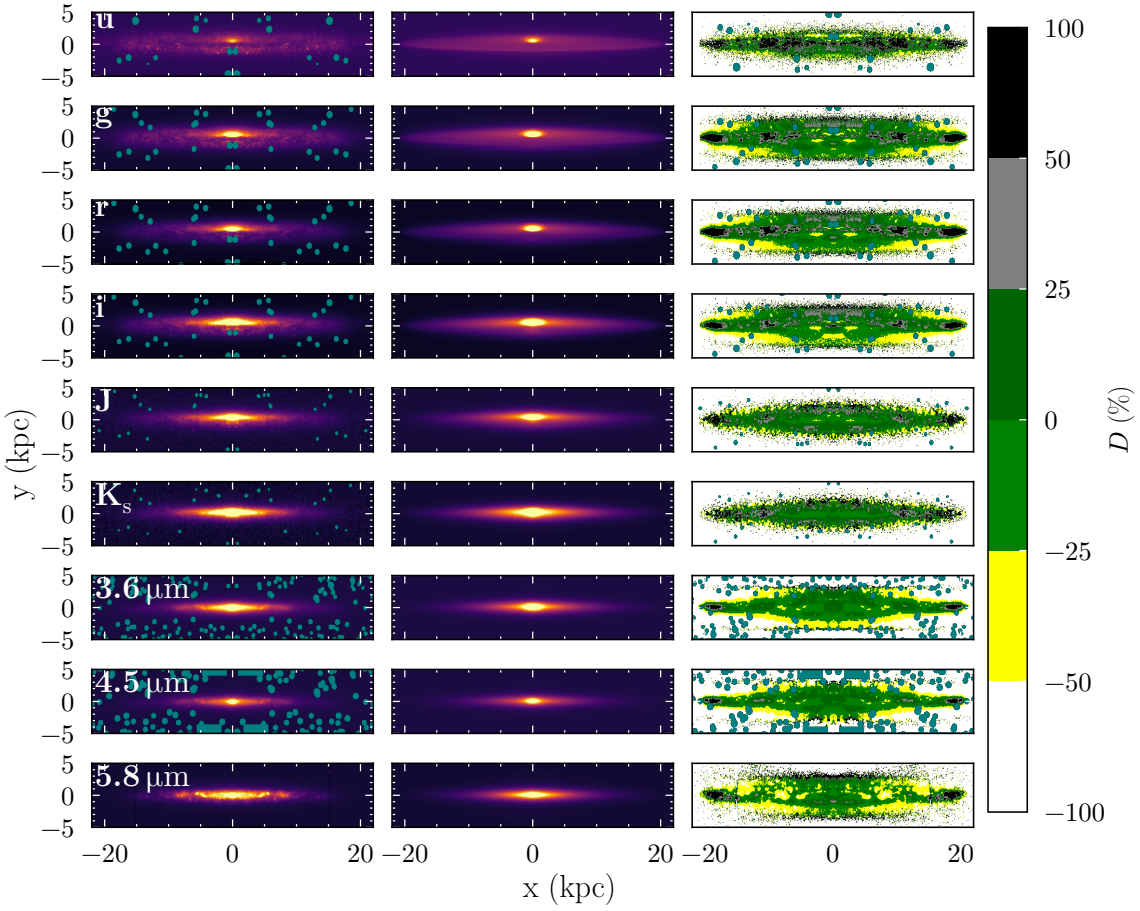

Figure F.8: NGC 5907: Fits of the clumpy model to the surface brightness maps. Left: surface brightness maps of NGC 5907, mirrored about their vertical central axis. Middle: surface brightness maps of the corresponding diffuse model images. Right: residuals between the data and model images calculated as $D = (M - O)/O$. Masked foreground stars are marked in teal.

Appendix G

Surface Brightness Profile Fits for the Clumpy Model

This appendix contains all the fits to the surface brightness profiles used in constraining the clumpy models for the face-on and intermediate inclination galaxies in the sample.

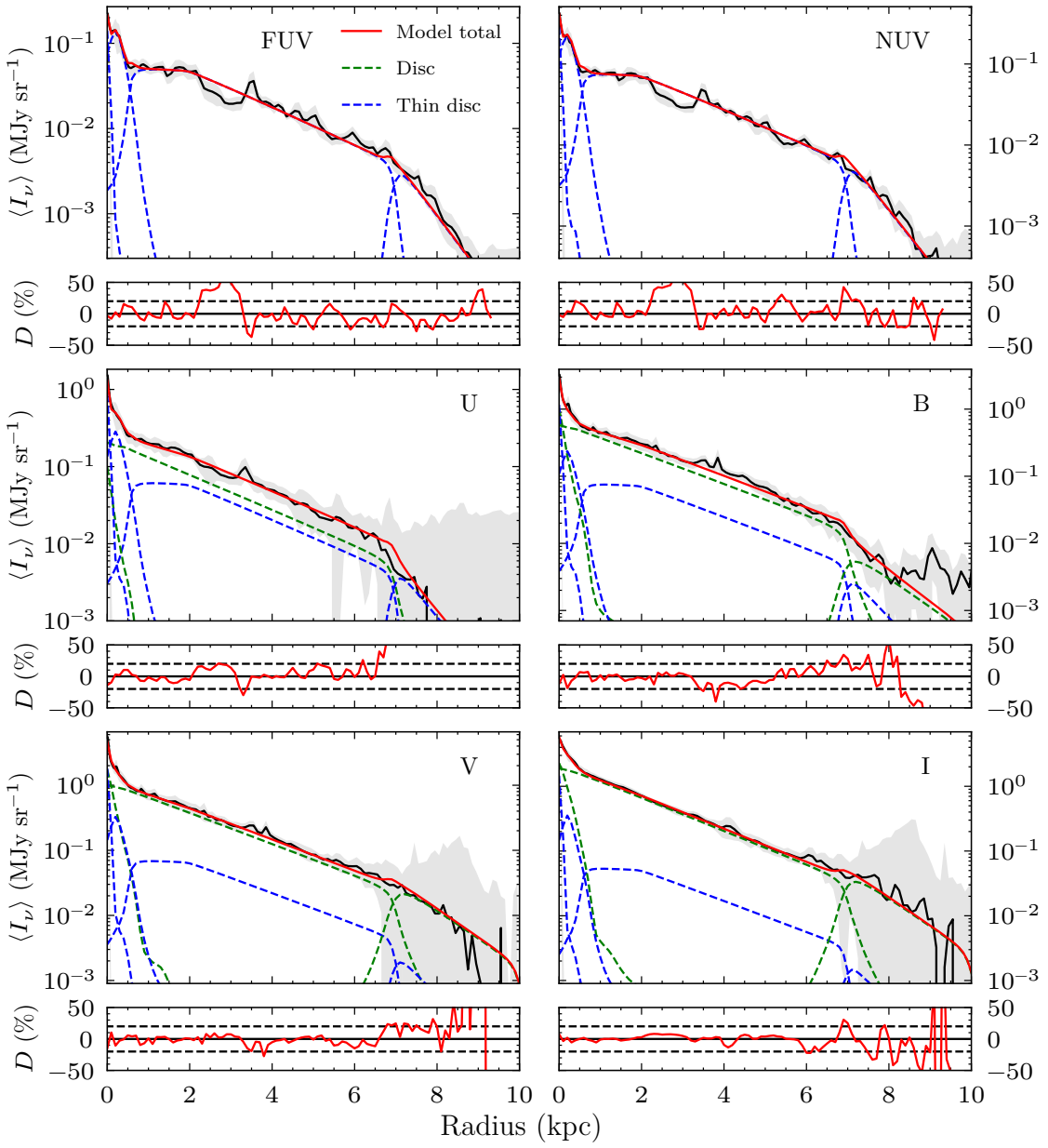

Figure G.1: M33: fits to the azimuthally averaged surface brightness profiles of the best fitting clumpy model in the UV and optical. The data is plotted with the solid black line and the corresponding uncertainties are shown by the grey shaded regions. The model total is plotted with the red solid line, and the individual model components are plotted with the dashed coloured lines. The smaller panels beneath each plot show the per cent residuals with the red solid line. The dashed lines represent the $\pm 20\%$ residuals.

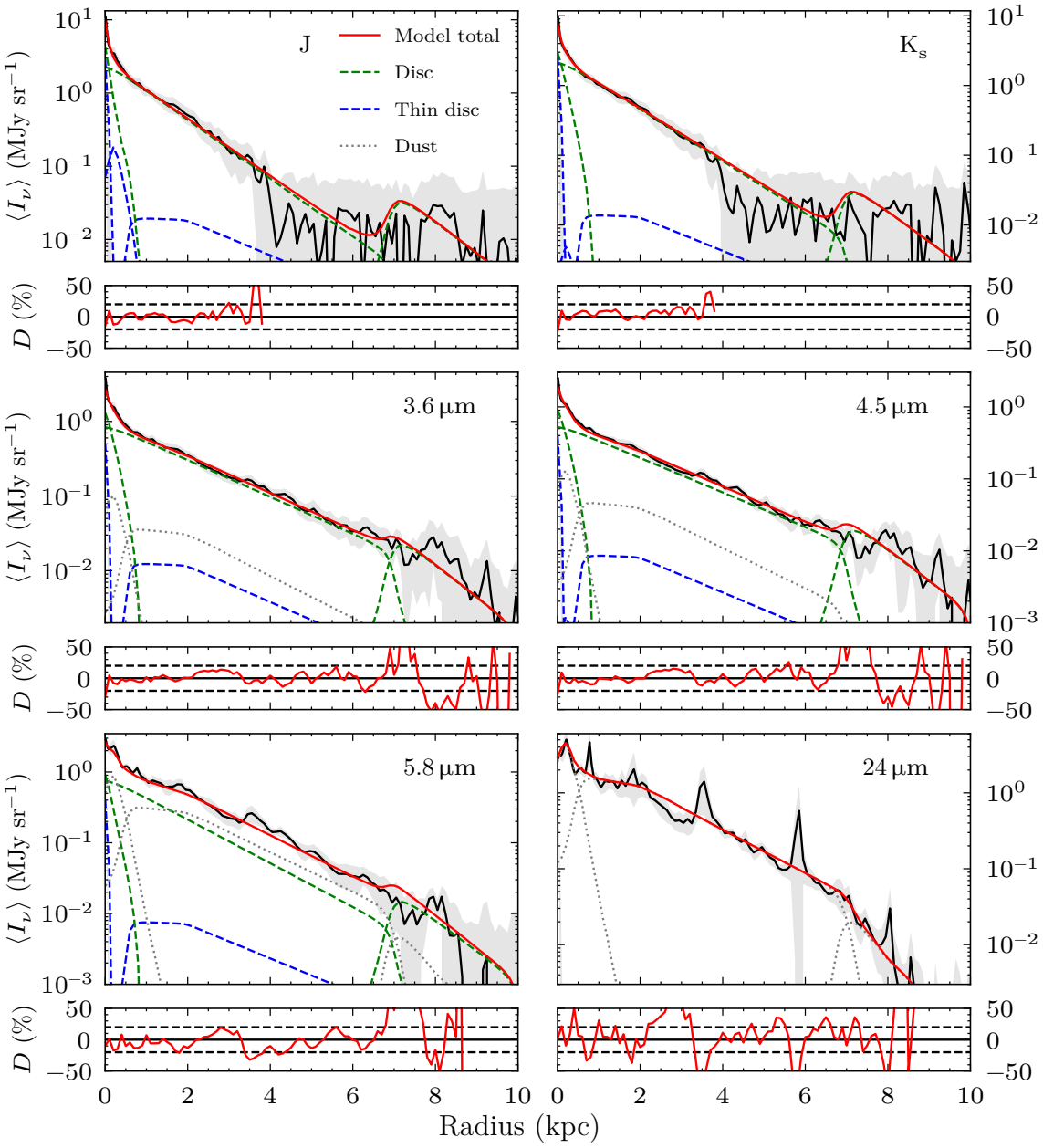

Figure G.2: M33: Same as Fig. G.1 for the NIR and MIR bands. The dust emission is plotted with the dotted lines.

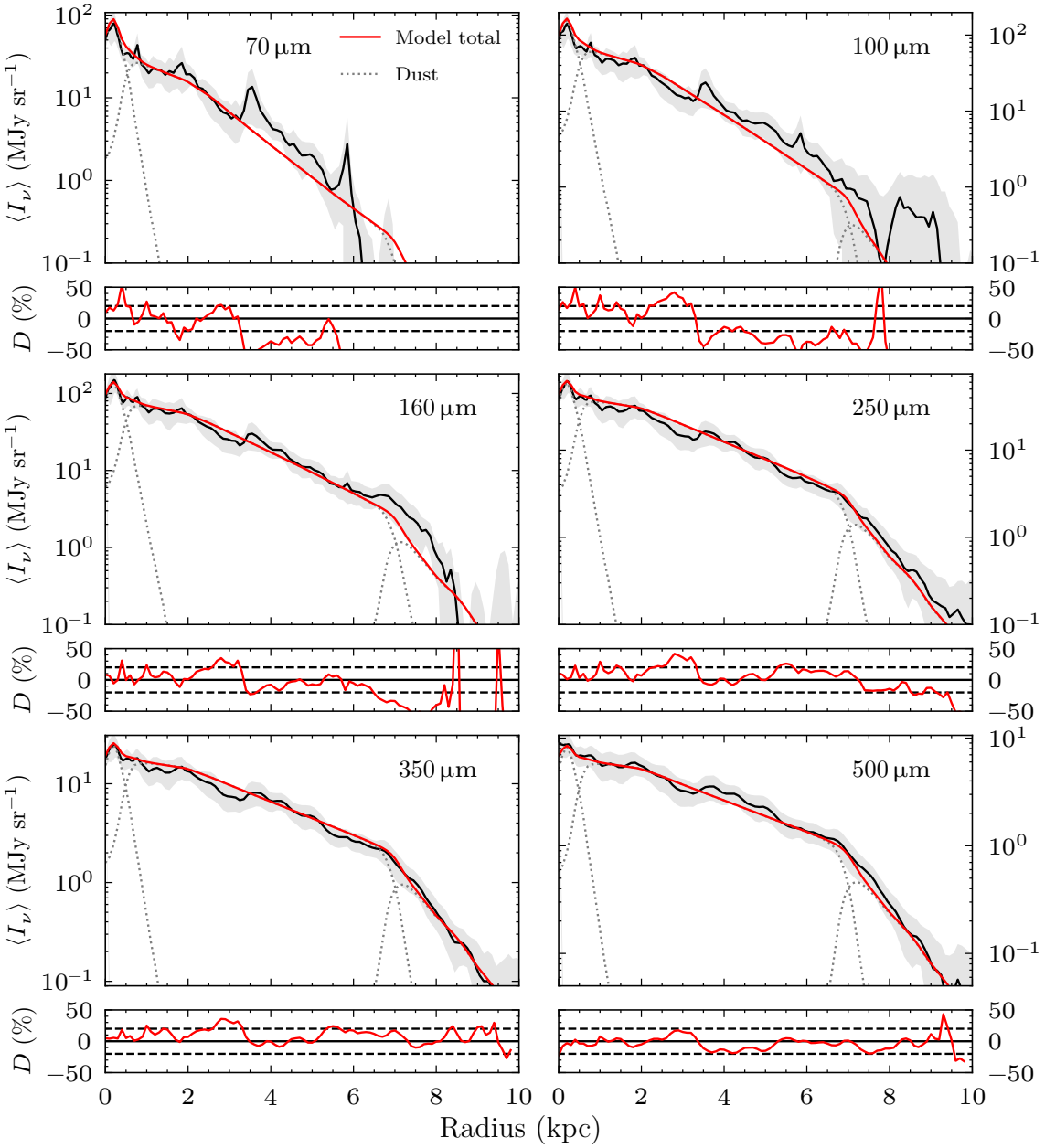

Figure G.3: M33: Same as Fig. G.2 for the FIR and sub millimetre bands.

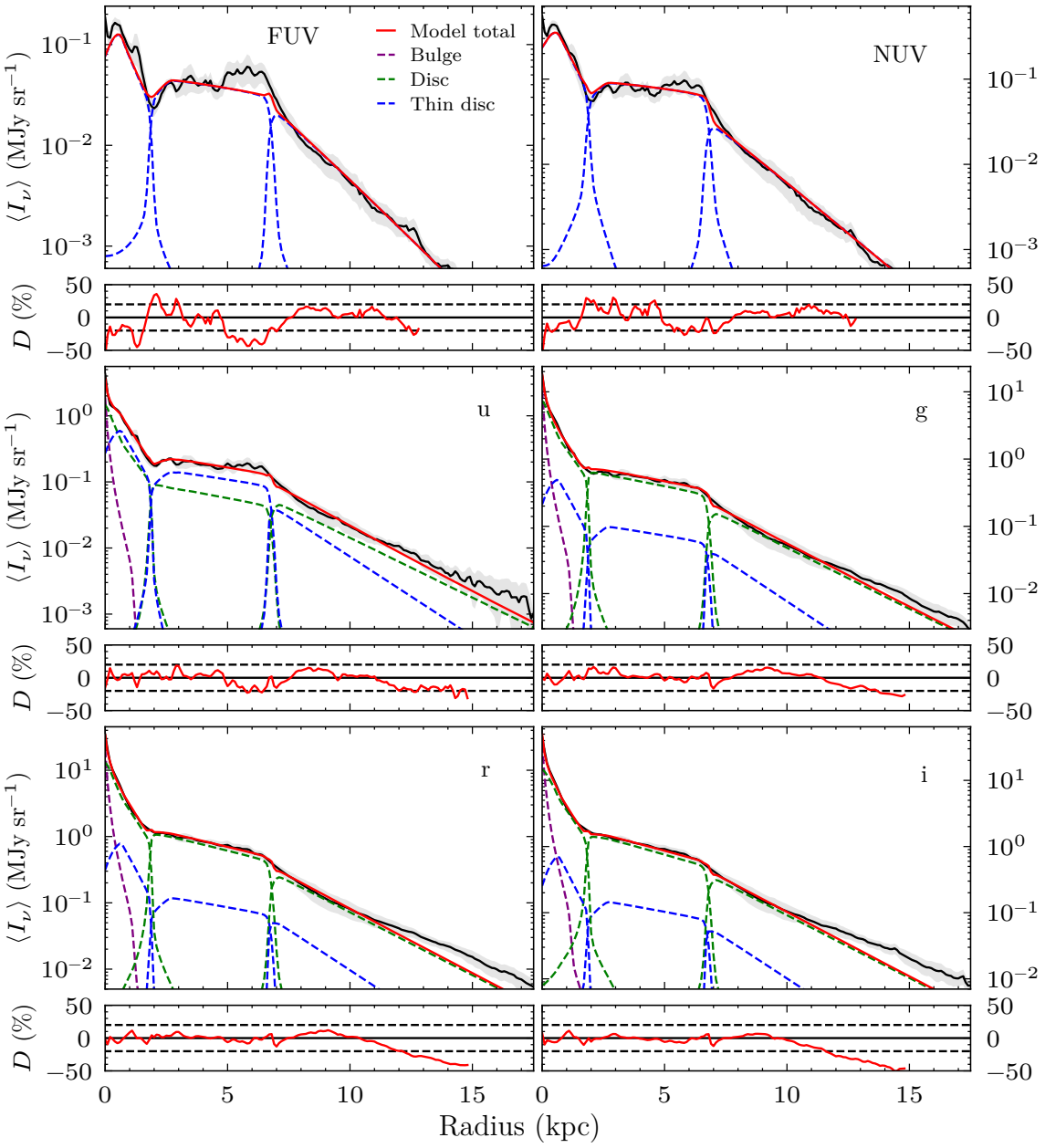

Figure G.4: M51: Same as Fig. G.1 for the clumpy model of M51.

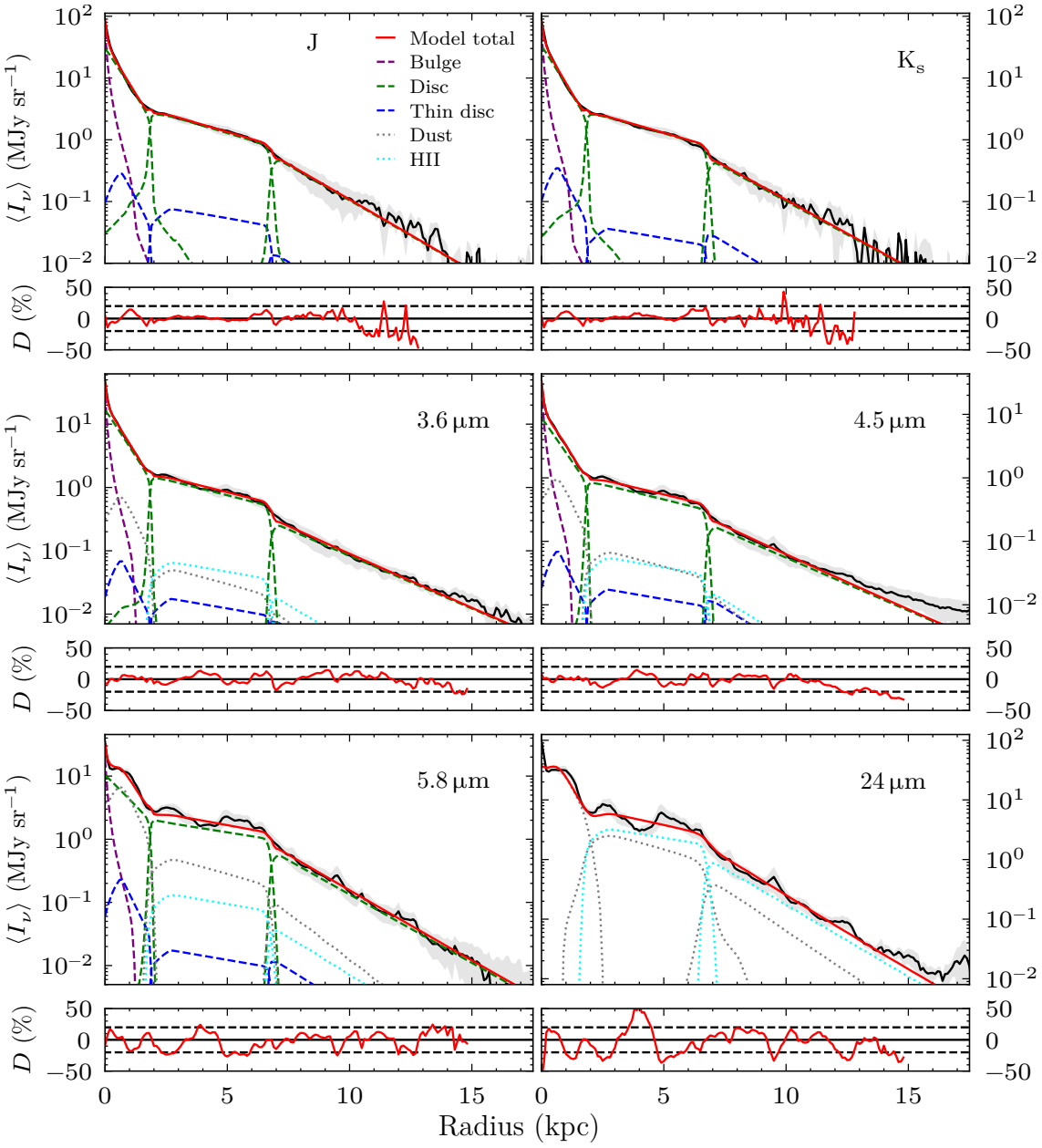

Figure G.5: M51: Same as Fig. G.4 for the NIR and MIR bands. The dust emission is plotted with the dotted lines.

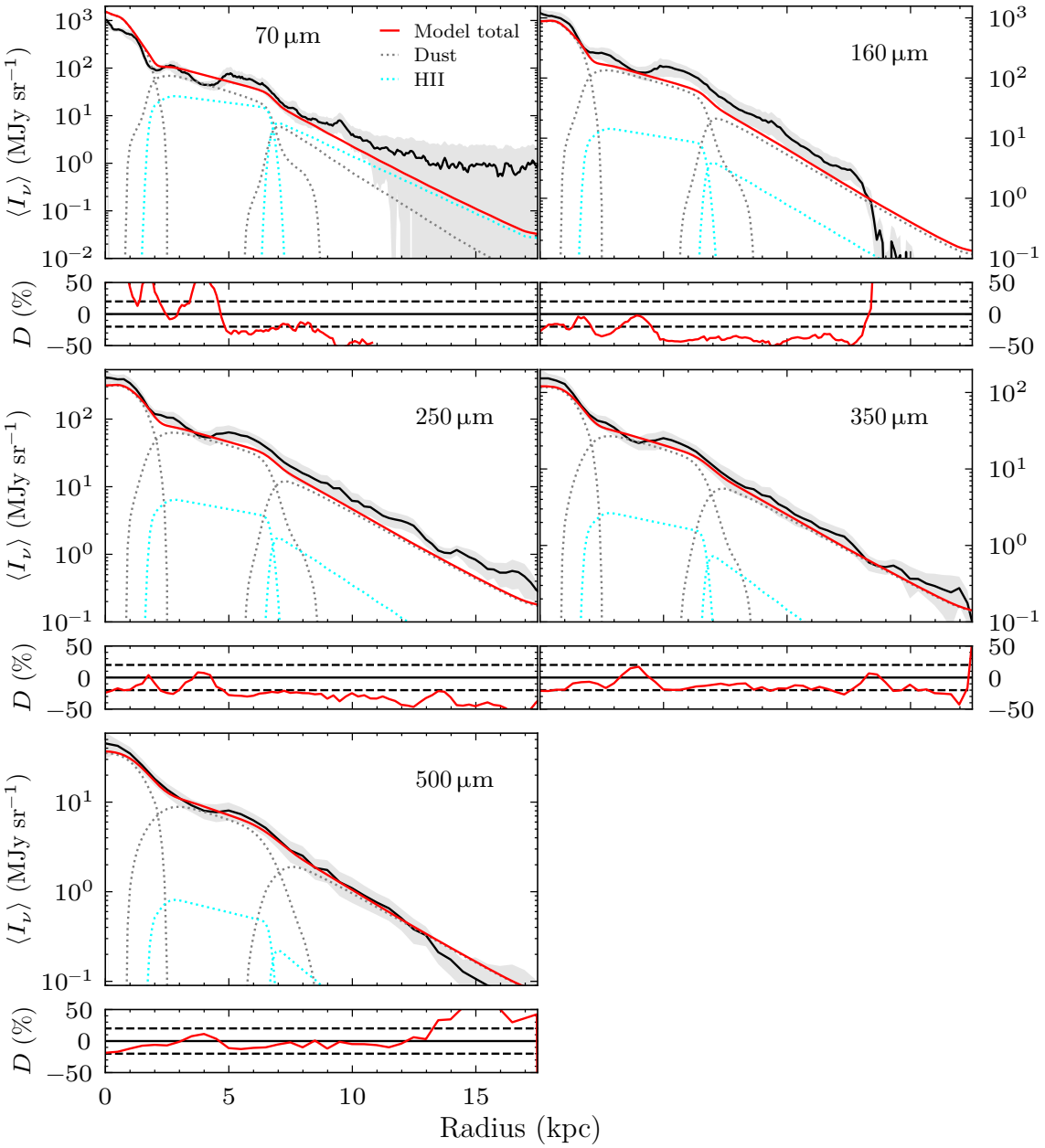

Figure G.6: M51: Same as Fig. G.5 for the FIR and sub millimetre bands.

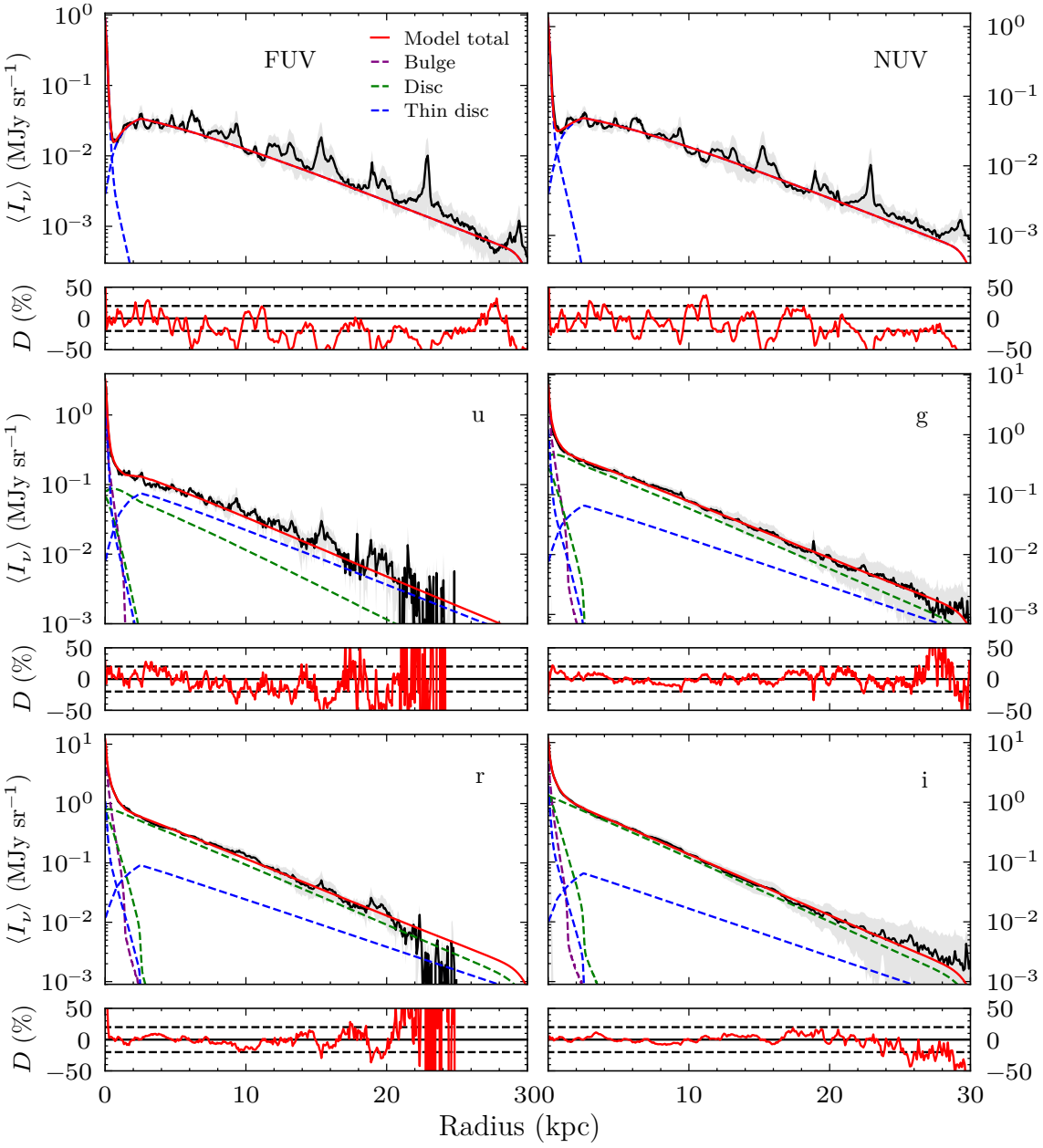

Figure G.7: M101: Same as Fig. G.1 for the clumpy model of M101.

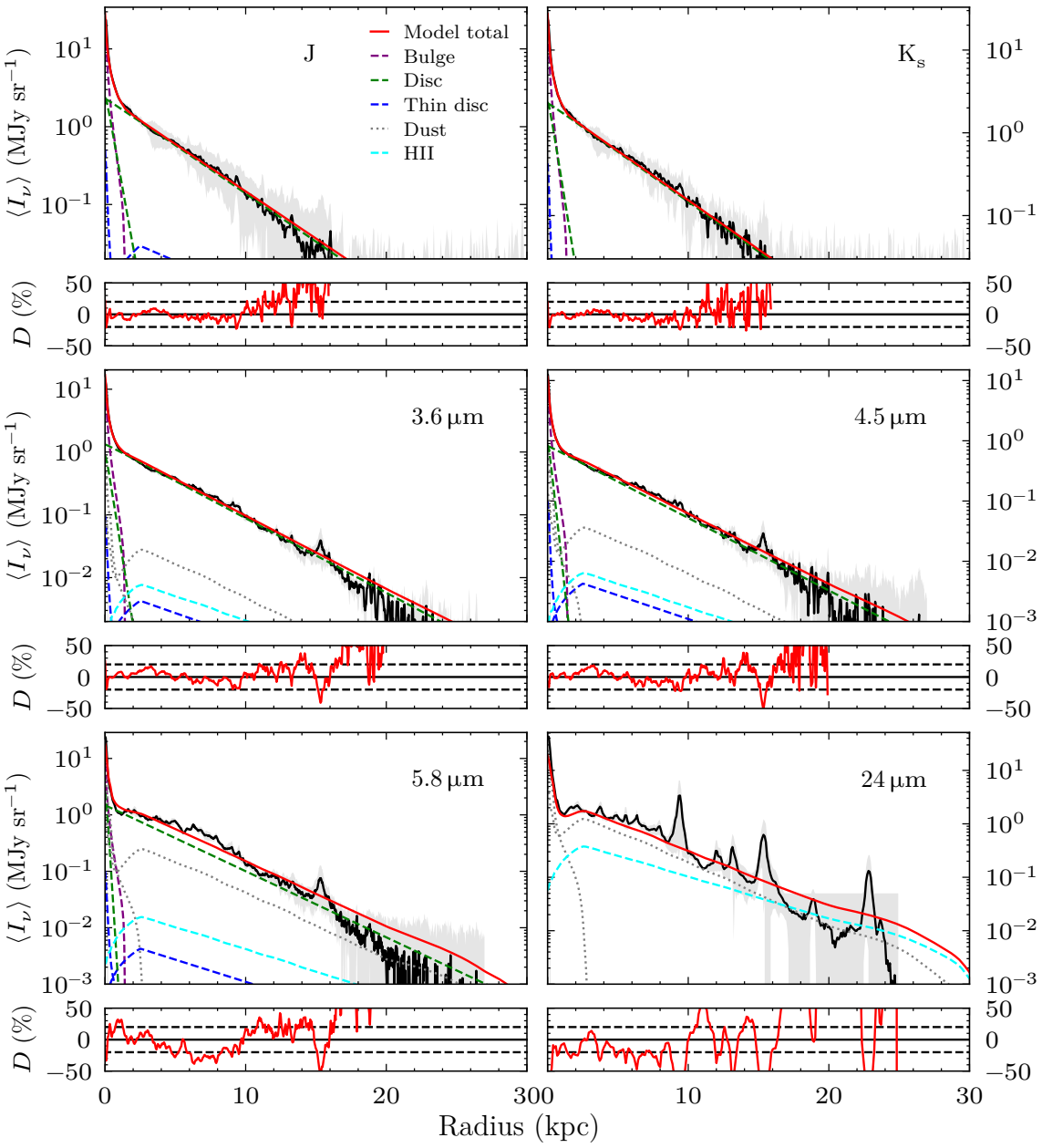

Figure G.8: M101: Same as Fig. G.7 for the NIR and MIR bands. The dust emission is plotted with the dotted lines.

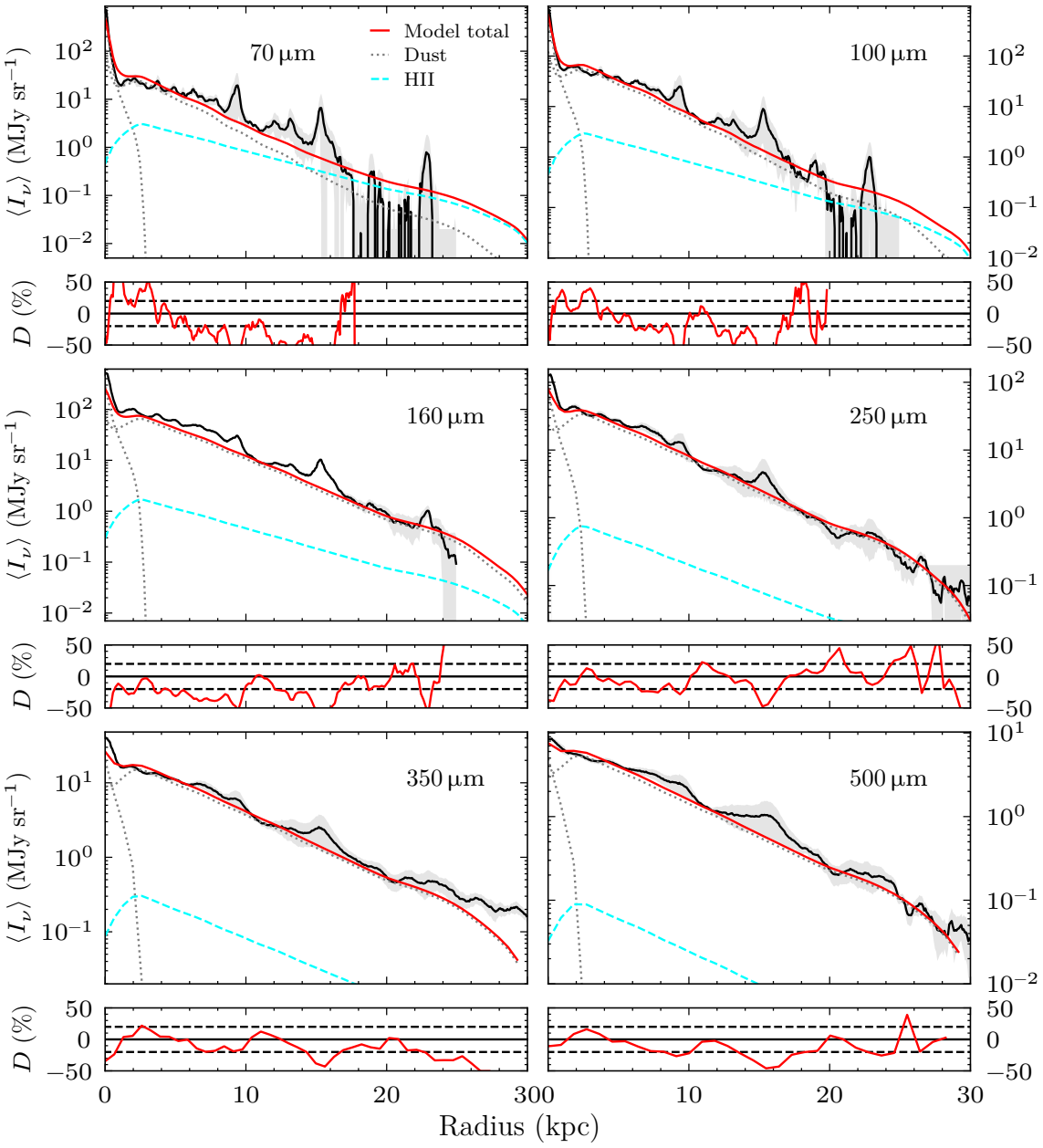

Figure G.9: M101: Same as Fig. G.8 for the FIR and sub millimetre bands.

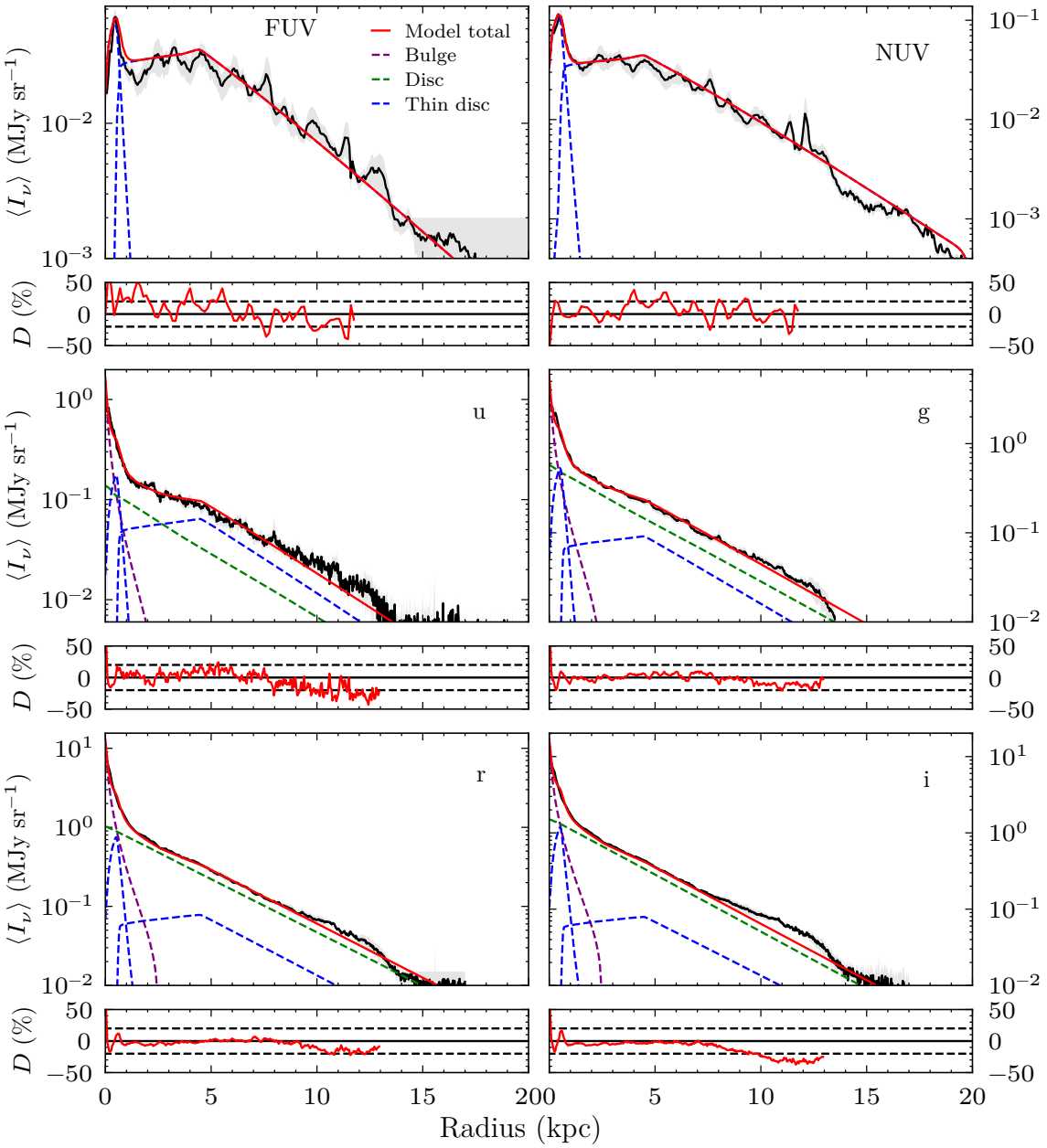

Figure G.10: NGC 628: Same as Fig. G.1 for the clumpy model of NGC 628.

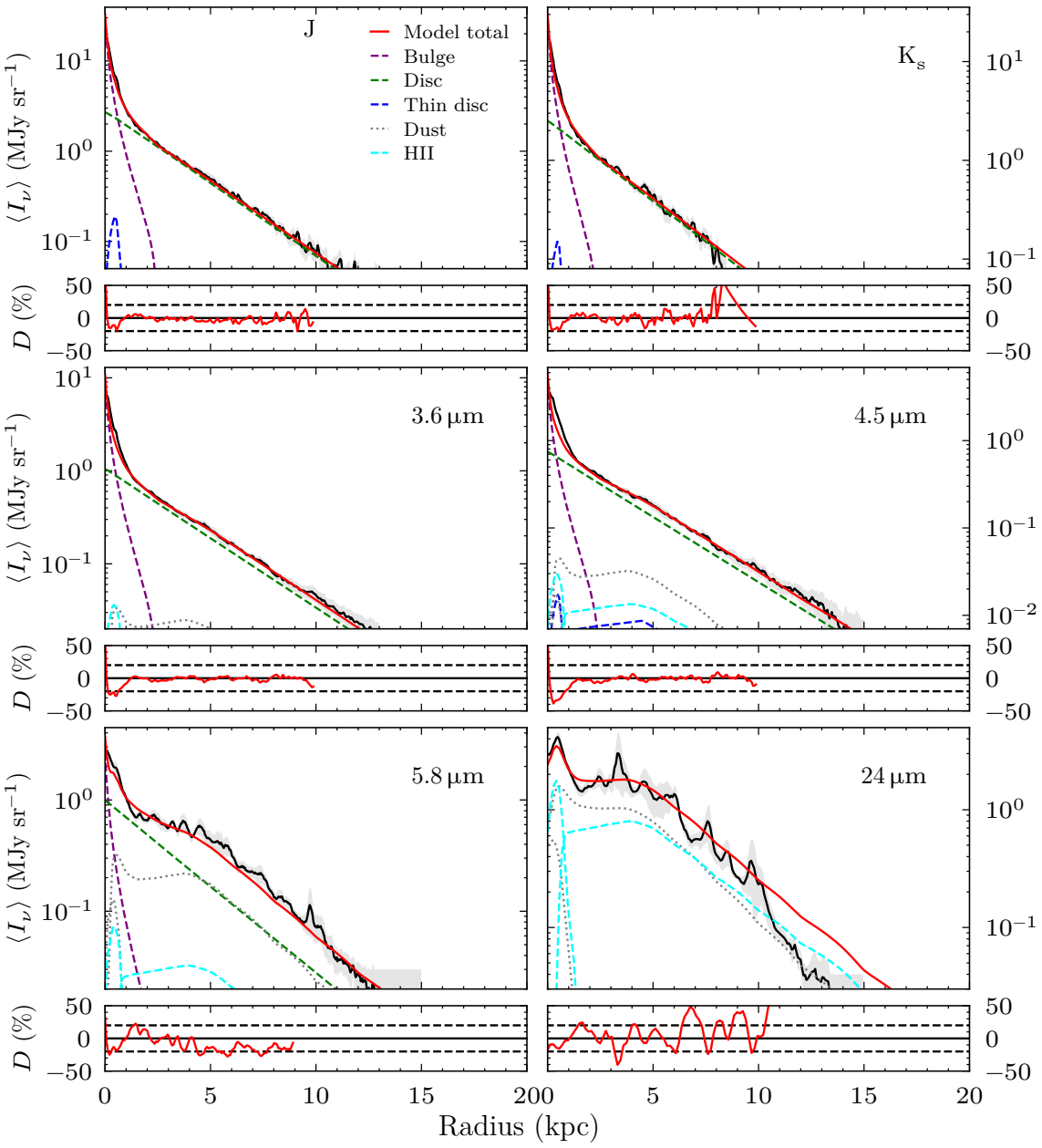

Figure G.11: NGC 628: Same as Fig. G.10 for the NIR and MIR bands. The dust emission is plotted with the dotted lines.

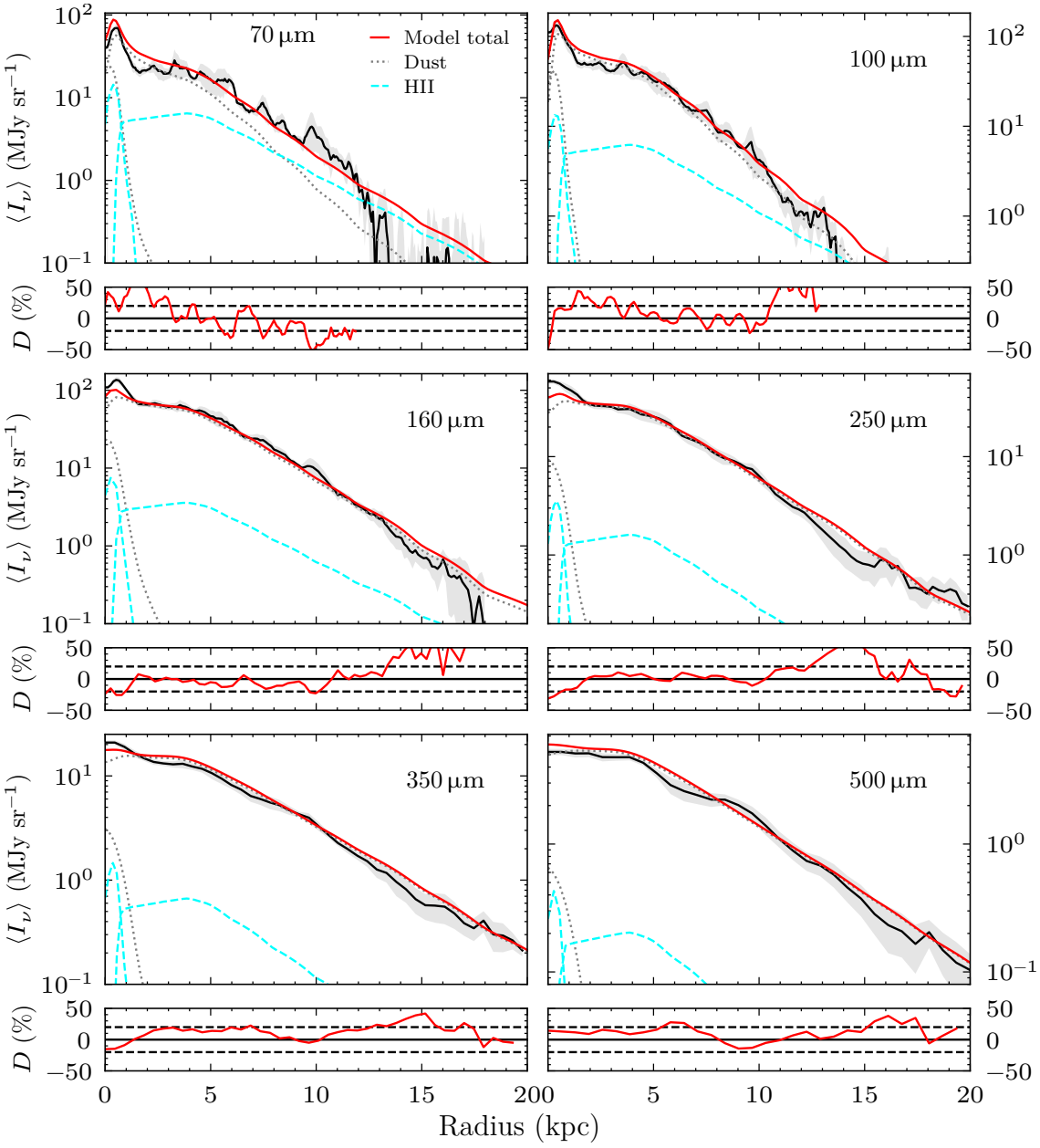

Figure G.12: NGC 628: Same as Fig. G.11 for the FIR and sub millimetre bands.

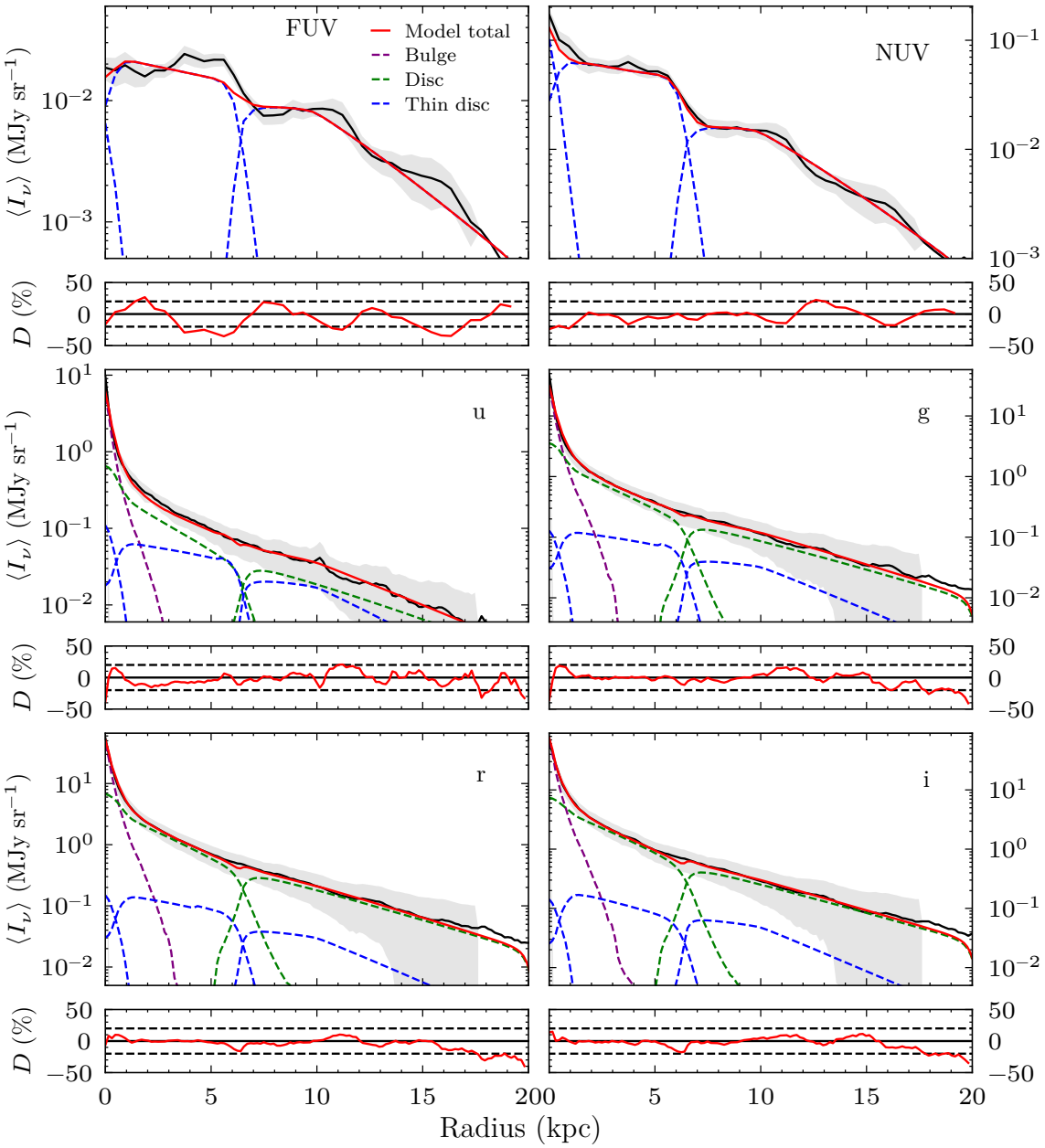

Figure G.13: NGC 3521: Same as Fig. G.1 for the clumpy model of NGC 3521.

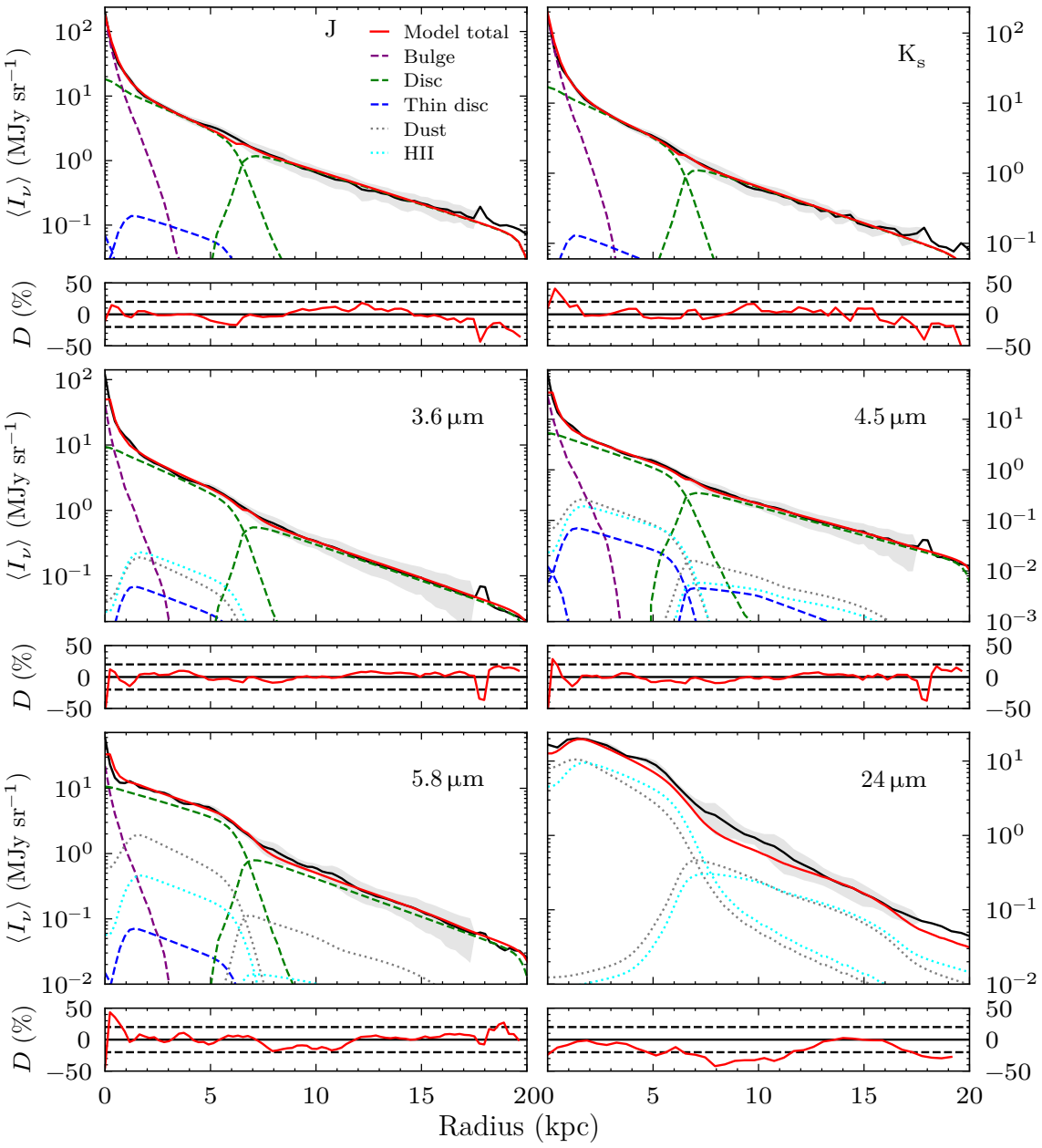

Figure G.14: NGC 3521: Same as Fig. G.13 for the NIR and MIR bands. The dust emission is plotted with the dotted lines.

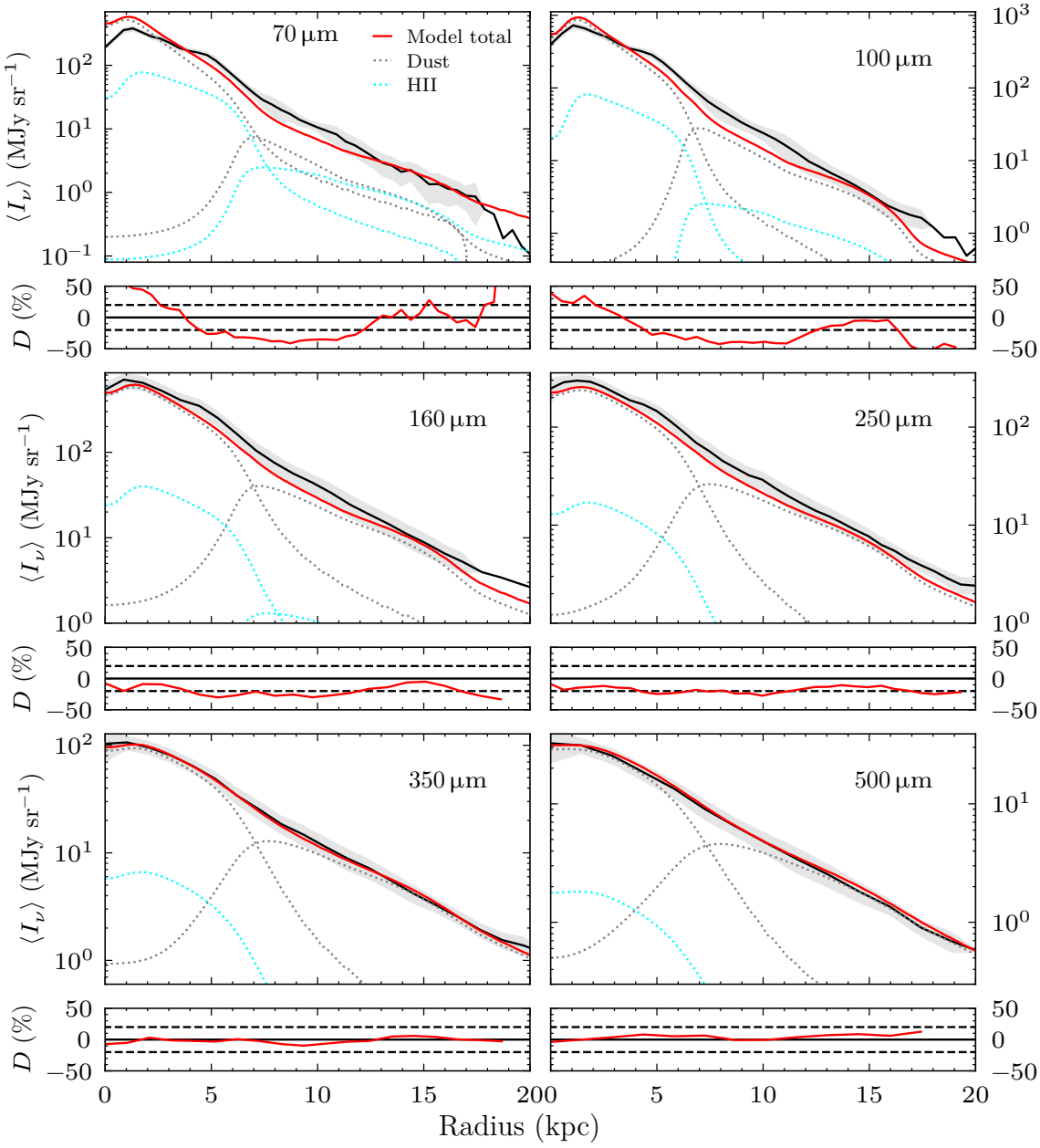

Figure G.15: NGC 3521: Same as Fig. G.14 for the FIR and sub millimetre bands.

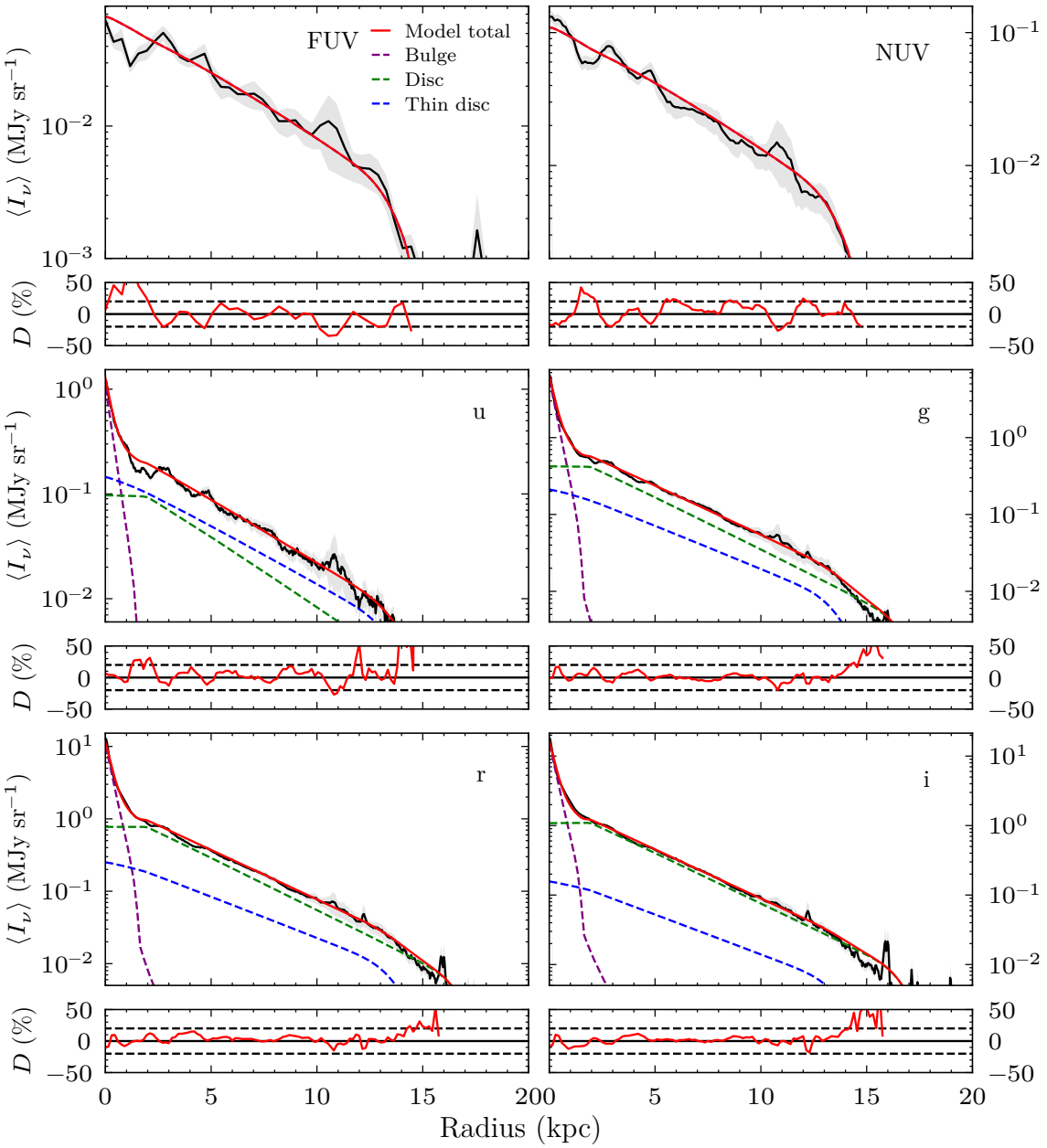

Figure G.16: NGC 3938: Same as Fig. G.1 for the clumpy model of NGC 3938.

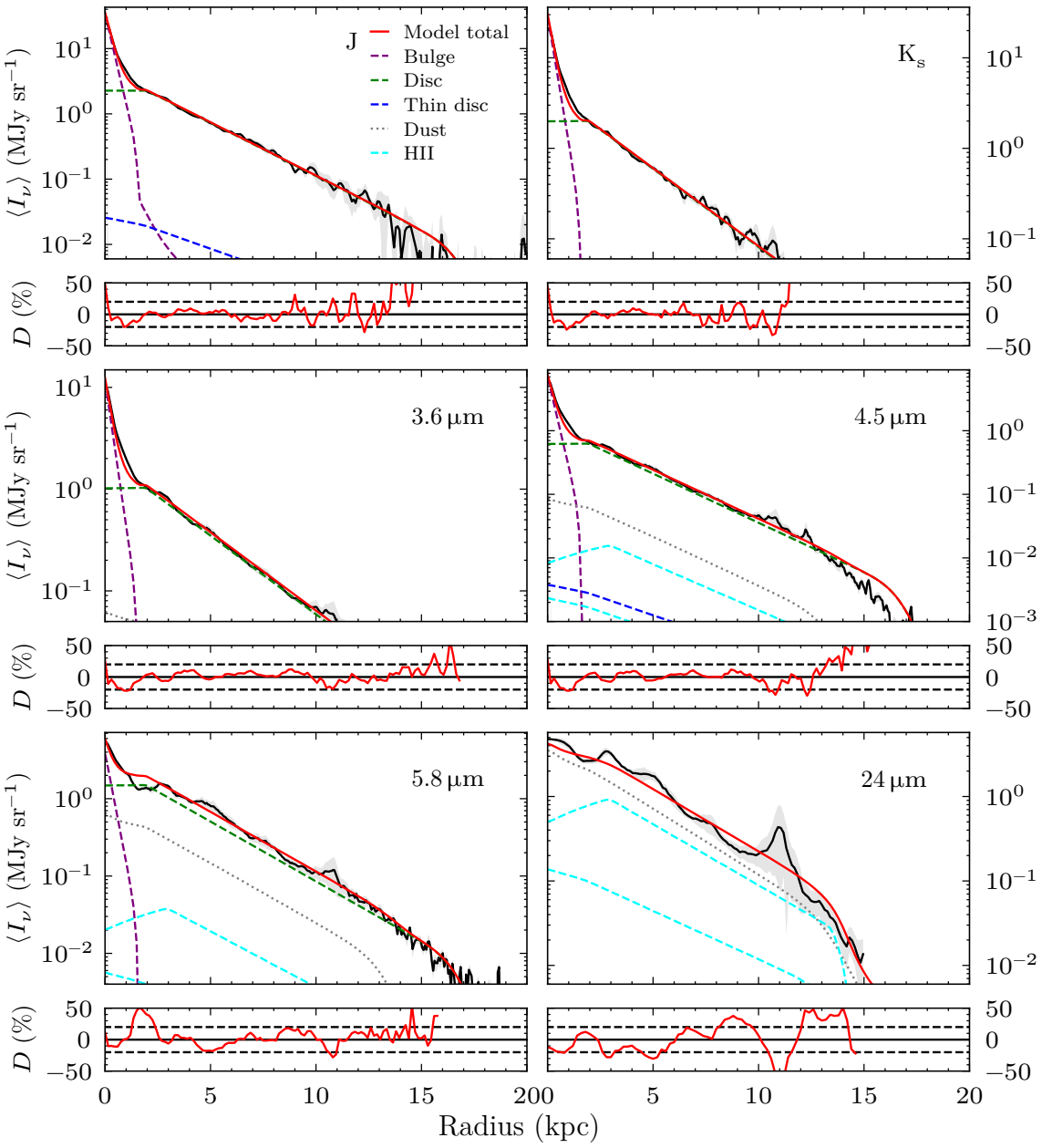

Figure G.17: NGC 3938: Same as Fig. G.16 for the NIR and MIR bands. The dust emission is plotted with the dotted lines.

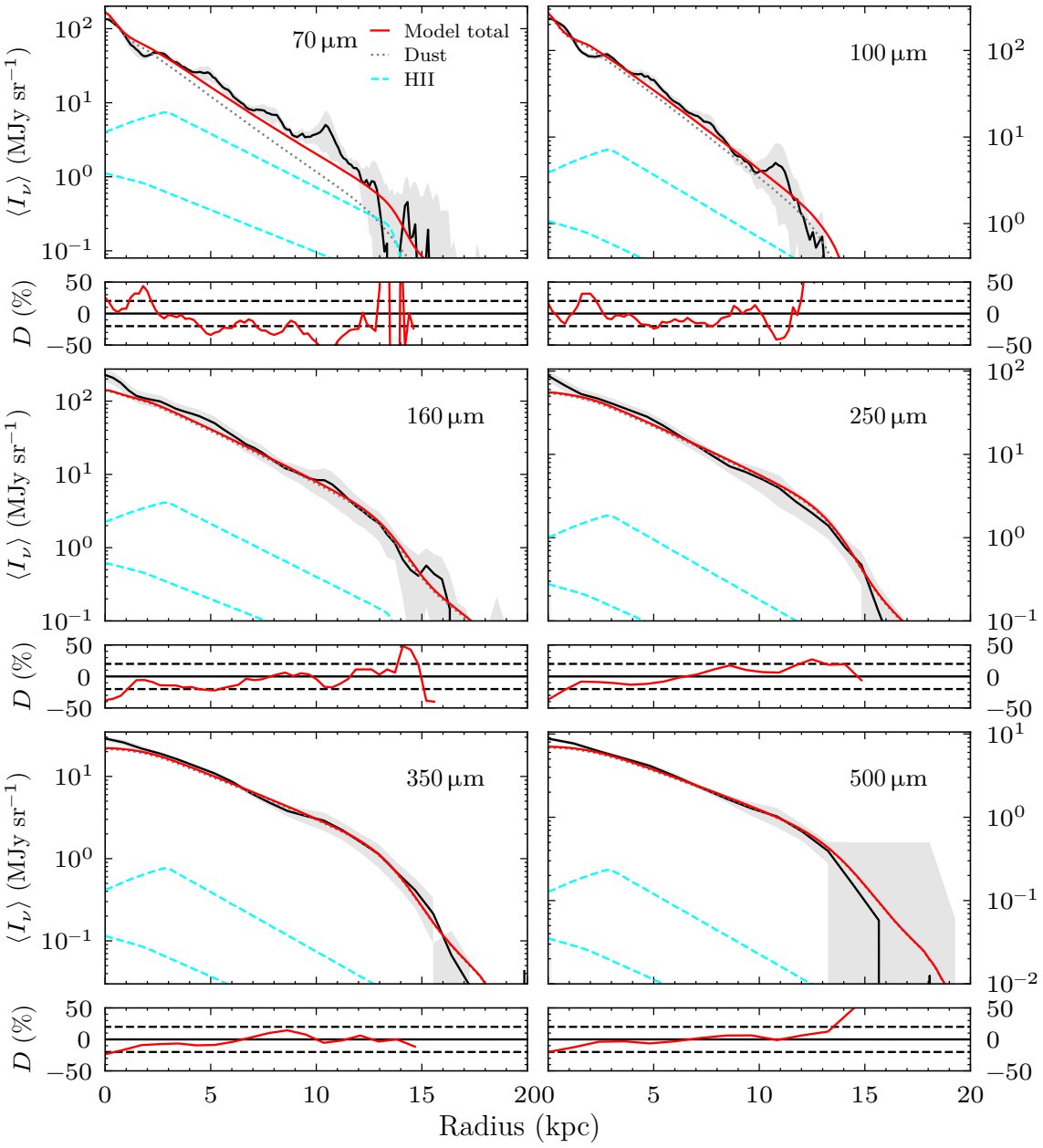

Figure G.18: NGC 3938: Same as Fig. G.17 for the FIR and sub millimetre bands.

Appendix H

SEDs for the Clumpy Model

This appendix contains all the spatially integrated SEDs of the clumpy models for the face-on and intermediate inclination galaxies in the sample.

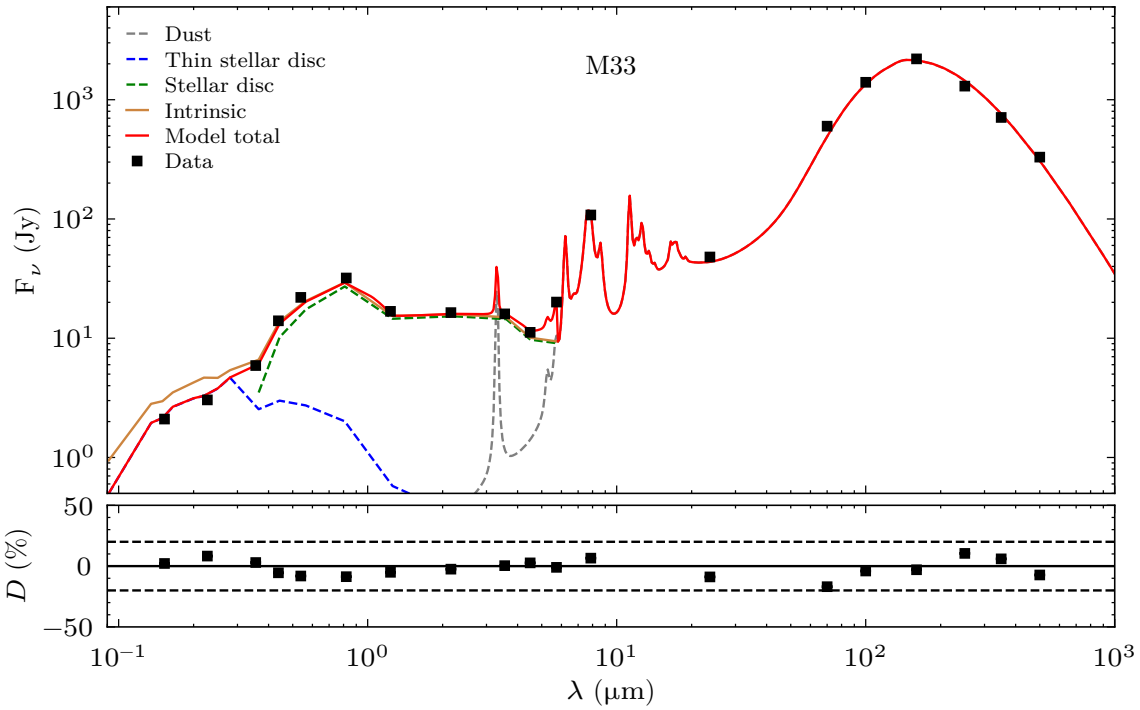

Figure H.1: M33: The spatially integrated model SED of the clumpy model plotted with the observed data (black squares) and the associated uncertainties (which are mainly contained in the black squares). Contributions from each of the galaxy components (dashed lines) and the intrinsic stellar SED (solid brown line) are also shown. The lower panel shows the per cent difference between the model SED and the observed data. To guide the eye dashed lines are plotted to show ±20 % deviation.

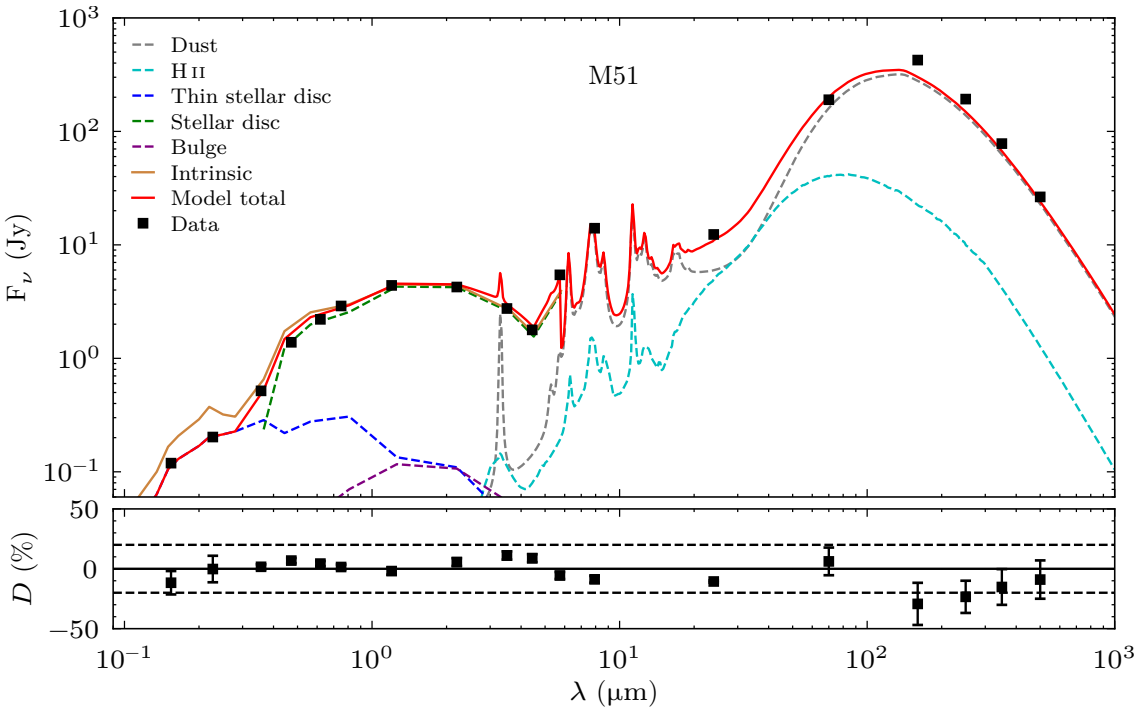

Figure H.2: Same as Fig. H.1 for the clumpy model of M51.

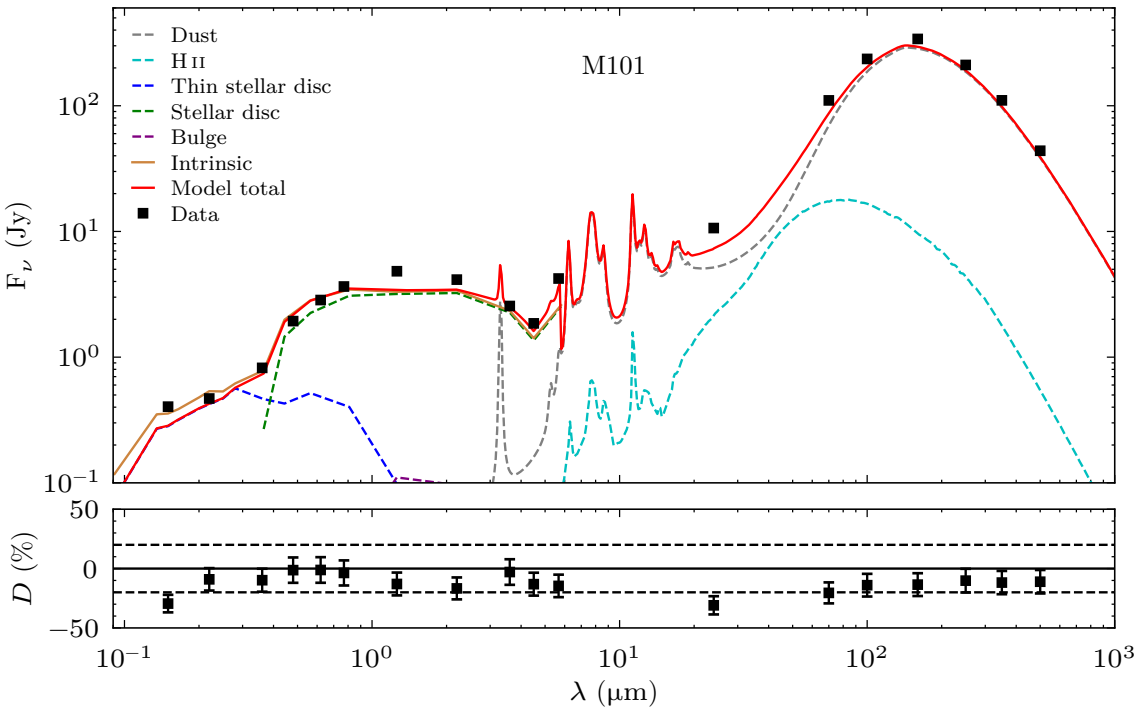

Figure H.3: Same as Fig. H.1 for the clumpy model of M101.

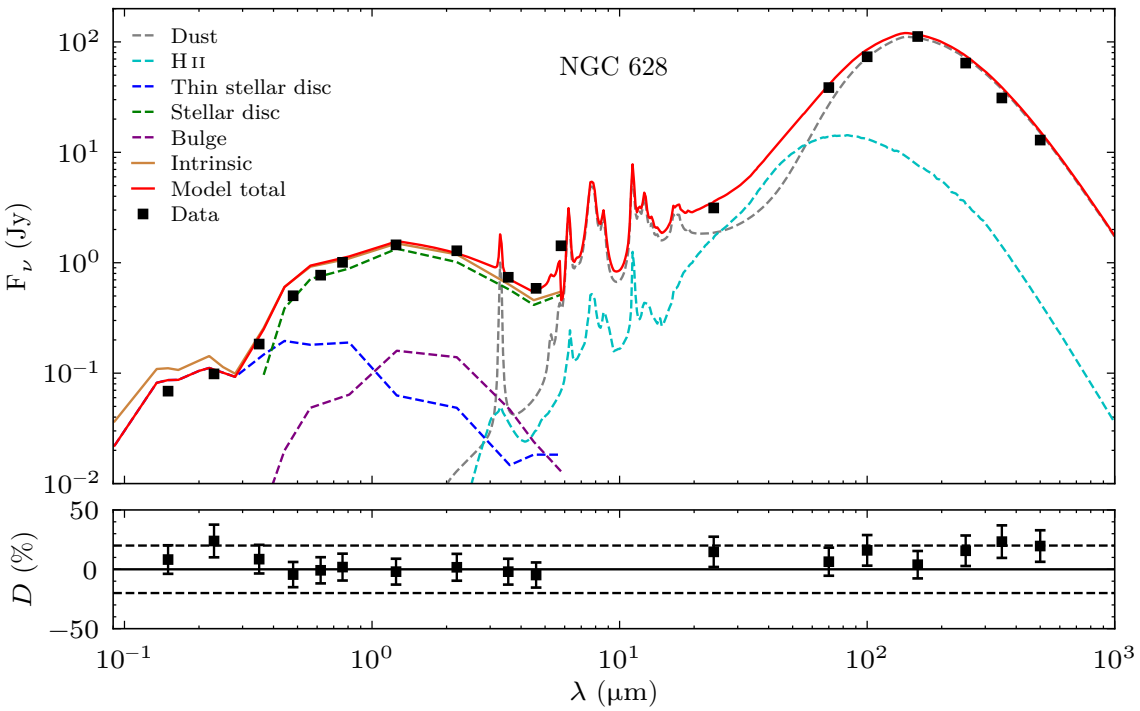

Figure H.4: Same as Fig. H.1 for the clumpy model of NGC 628.

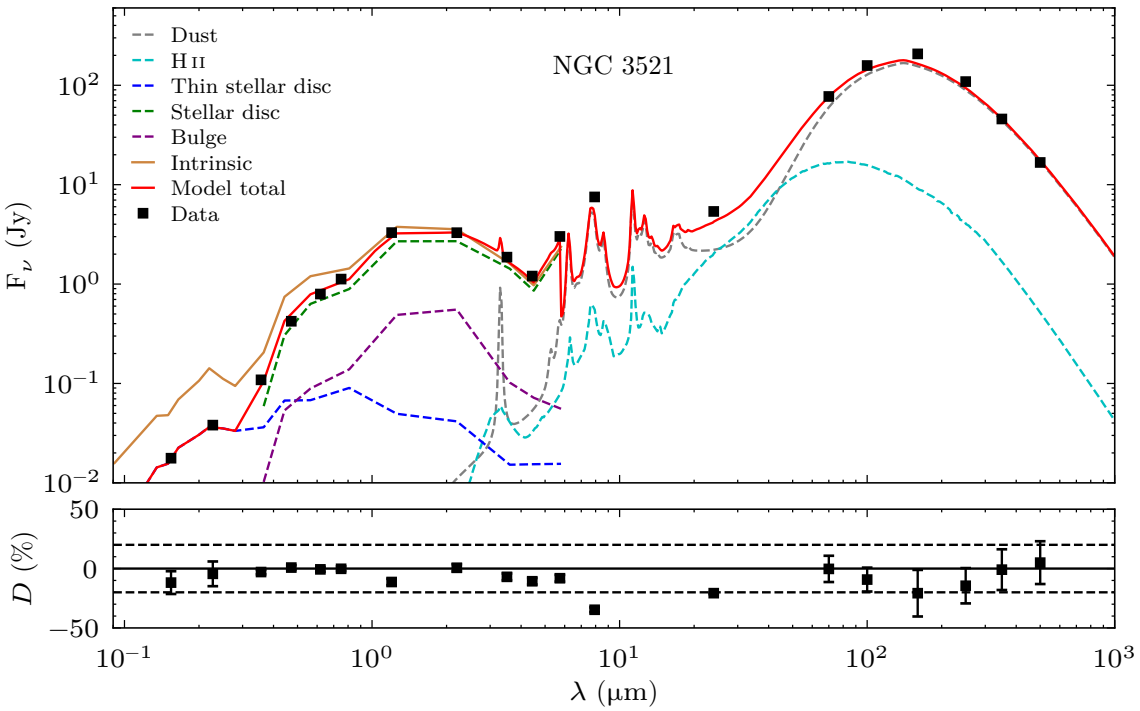

Figure H.5: Same as Fig. H.1 for the clumpy model of NGC 3521.

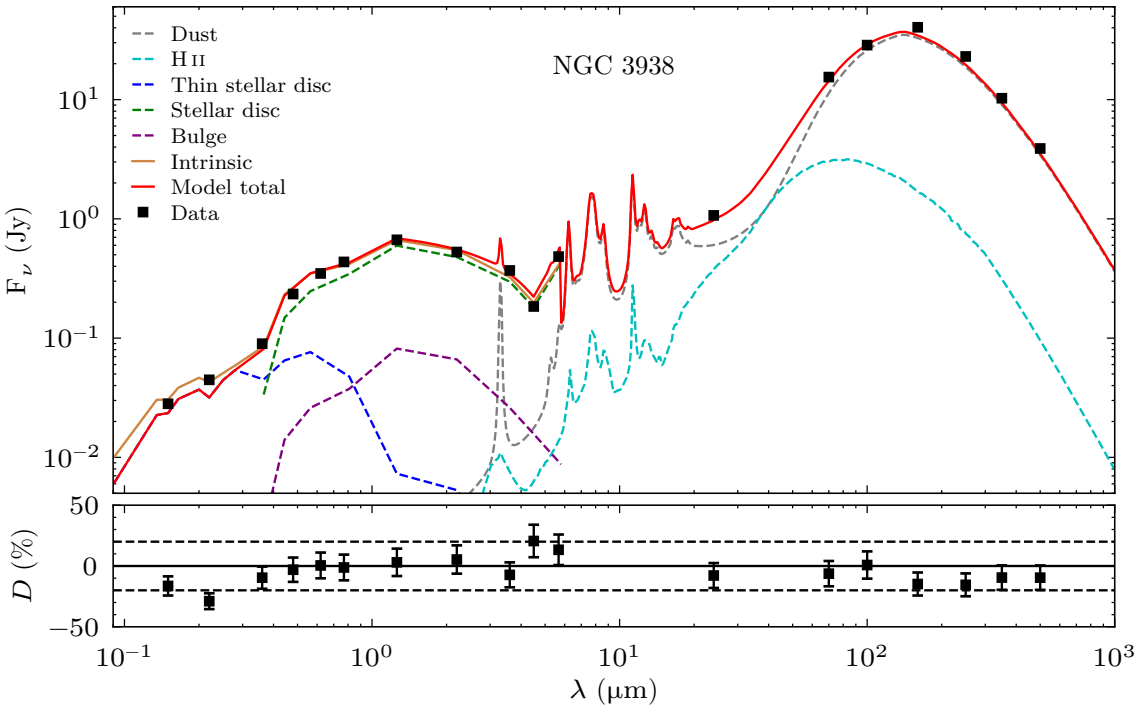

Figure H.6: Same as Fig. H.1 for the clumpy model of NGC 3938.

Appendix I

Geometrical Parameters Derived for the Clump Model

This appendix contains tables comparing the geometrical parameters constrained for diffuse and clumpy models of the galaxy sample.

Table I.1: The free geometrical parameters of the best fitting diffuse (middle column), and clumpy models (right column) of M33, denoted with 'd' and 'c' respectively. The superscripts 'n', 'i', 'm' and 'o' found in the notation for the different parameters denote the nuclear, inner, main, and outer discs, respectively.

Parameter	d	c
$h_{\rm s}^{\rm tdisc-(n,i,m,o)}$	(0.02, 0.10, 1.50, 0.60)	(0.02, 0.13, 1.80, 0.65)
$h_{\rm s}^{\rm disc-(i,m,o)}(B)$	(0.05, 1.80, 1.00)	(0.05, 1.80, 1.00)
$h_{\rm d}^{\rm disc-(i,m,o)}$	(0.15, 9.00, 1.00)	(0.15, 8.00, 1.30)
$\chi_{\rm s}^{\rm tdisc-(n,i,m,o)}$	(1.00, 0.00, 0.75, -20.00)	(1.00, -0.80, 1.10, -20.00)
$\chi_{\rm s}^{\rm disc-(i,m,o)}$	(1.00, 1.00, -20.00)	(1.00, 1.00, -20.00)
$\chi_{\rm d}^{\rm disc-(i,m,o)}$	(0.00, 0.75, -20.00)	(-1.10, 1.00, -20.00)

Table I.2: The geometrical parameters fixed from data and theoretical considerations of M33. The values are the same between the diffuse and clumpy models. The superscripts 'n', 'i', 'm' and 'o' found in the notation for the different parameters denote the nuclear, inner, main, and outer discs, respectively.

Parameter	value
$R_{\rm in,s}^{\rm tdisc-(n,i,m,o)}$	(0.00, 0.25, 2.00, 7.10)
$R_{\rm in,s}^{\rm disc-(i,m,o)}$	(0.00, 0.00, 7.10)
$R_{\rm in,d}^{\rm disc-(i,m,o)}$	(0.25, 2.00, 7.10)
$R_{\rm tin,s}^{\rm tdisc-(n,i,m,o)}$	(0.00, 0.00, 0.60, 6.76)
$R_{\rm tin,s}^{\rm disc-(i,m,o)}$	(0.00, 0.00, 6.76)
$R_{\rm tin,d}^{\rm disc-(i,m,o)}$	(0.00, 0.60, 6.76)
$R_{\rm t,s}^{\rm tdisc-(n,i,m,o)}$	(0.10, 0.75, 7.00, 10.00)
$R_{\rm t,s}^{\rm disc-(i,m,o)}$	(0.50, 7.00, 10.00)
$R_{\rm t,d}^{\rm disc-(i,m,o)}$	(1.00, 7.00, 10.00)
$z_{\rm s}^{\rm tdisc-(n,i,m,o)}$	(0.09, 0.09, 0.09, 0.09)
$z_{\rm s}^{\rm disc-(i,m,o)}$	(0.19, 0.19, 0.19)
$z_{\rm d}^{\rm disc-(i,m,o)}$	(0.16, 0.16, 0.16)

Table I.3: Same as Table I.1 for M51.

Parameter	d	c
$h_{\rm s}^{\rm tdisc-(i,m,o)}$	(0.60, 4.30, 1.45)	(0.55, 6.50, 1.80)
$h_{\rm s}^{\rm disc-(i,m,o)}(B)$	(0.74, 3.80, 2.00)	(0.72, 5.50, 2.40)
$h_{\rm d}^{\rm disc-(i,m,o)}$	(5.00, 6.00, 3.60)	(4.70, 6.00, 4.50)
$\chi_{\rm s}^{\rm tdisc-(i,m,o)}$	(0.10, -0.70, 2.00)	(0.15, -0.60, 2.00)
$\chi_{\rm s}^{\rm disc-(i,m,o)}$	(0.00, 1.50, -5.00)	(0.00, 1.50, -5.00)
$\chi_{\rm d}^{\rm disc-(i,m,o)}$	(0.45, 1.00, -1.00)	(0.50, 0.75, -1.00)
$R_{\rm e}$	0.35	0.40
$\frac{b}{a}$	1.00	1.00

Table I.4: Same as Table I.2 for M51.

Parameter	value
$R_{\rm in,s}^{\rm tdisc-(i,m,o)}$	(0.70, 2.70, 7.10)
$R_{\rm in,s}^{\rm disc-(i,m,o)}$	(0.00, 2.70, 7.10)
$R_{\rm in,d}^{\rm disc-(i,m,o)}$	(0.80, 2.70, 7.10)
$R_{\rm tin,s}^{\rm tdisc-(i,m,o)}$	(0.00, 1.86, 6.70)
$R_{\rm tin,s}^{\rm disc-(i,m,o)}$	(0.00, 1.86, 6.76)
$R_{\rm tin,d}^{\rm disc-(i,m,o)}$	(0.00, 1.86, 6.70)
$R_{\rm t,s}^{\rm tdisc-(i,m,o)}$	(1.90, 6.80, 20.00)
$R_{\rm t,s}^{\rm disc-(i,m,o)}$	(1.90, 6.80, 20.00)
$R_{\rm t,d}^{\rm disc-(i,m,o)}$	(1.90, 6.80, 20.00)
$z_{\rm s}^{\rm tdisc-(i,m,o)}$	(0.09, 0.09, 0.09)
$z_{\rm s}^{\rm disc-(i,m,o)}$	(0.19, 0.19, 0.19)
$z_{\rm d}^{\rm disc-(i,m,o)}$	(0.16, 0.16, 0.16)
$n_{\rm s}$	4.0

Table I.5: Same as Table I.1 for M101.

Parameter	d	c
$h_{\rm s}^{\rm tdisc-(n,i,m)}$	(0.06, 0.40, 5.20)	(0.08, 0.50, 5.50)
$h_{\rm s}^{\rm disc-(i,m)}(B)$	(0.40, 3.70)	(0.50, 4.30)
$h_{\rm d}^{\rm disc-(i,m)}$	(0.90, 8.00)	(0.75, 8.50)
$\chi_{\rm s}^{\rm tdisc-(n,i,m)}$	(0.00, 1.60, 0.10)	(0.00, 1.60, 0.10)
$\chi_{\rm s}^{\rm disc-(i,m)}$	(0.00, 0.10)	(0.00, 0.10)
$\chi_{\rm d}^{\rm disc-(i,m)}$	(0.00, 0.40)	(0.00, 0.40)
$R_{\rm e}$	0.46	0.46
$\frac{b}{a}$	0.60	0.60

Table I.6: Same as Table I.2 for M101.

Parameter	Value
$R_{\rm in,s}^{\rm tdisc-(n,i,m)}$	(0.00, 0.00, 2.50)
$R_{\rm in,s}^{\rm disc-(i,m)}$	(0.00, 0.00)
$R_{\rm in,d}^{\rm disc-(i,m)}$	(0.00, 2.50)
$R_{\rm tin,s}^{\rm tdisc-(n,i,m)}$	(0.00, 0.00, 0.00)
$R_{\rm tin,s}^{\rm disc-(i,m)}$	(0.00, 0.00)
$R_{\rm tin,d}^{\rm disc-(i,m)}$	(0.00, 0.00)
$R_{\rm t,s}^{\rm tdisc-(n,i,m)}$	(1.00, 2.50, 30.00)
$R_{\rm t,s}^{\rm disc-(i,m)}$	(2.50, 30.00)
$R_{\rm t,d}^{\rm disc-(i,m)}$	(2.50, 30.00)
$z_{\rm s}^{\rm tdisc-(n,i,m)}$	(0.09, 0.09, 0.09)
$z_{\rm s}^{\rm disc-(i,m)}$	(0.40, 0.40)
$z_{\rm d}^{\rm disc-(i,m)}$	(0.27, 0.27)
$n_{\rm s}$	2.0

Table I.7: Same as Table I.1 for NGC 628.

Parameter	d	c
$h_{\rm s}^{\rm tdisc-(i,m)}$	(0.20, 2.80)	(0.15, 3.10)
$h_{\rm s}^{\rm disc-m}(B)$	2.90	3.30
$h_{\rm d}^{\rm disc-m}$	7.30	7.80
$\chi_{\rm s}^{\rm tdisc-(i,m)}$	(0.00, 0.35)	(0.00, 0.70)
$\chi_{\rm s}^{\rm disc-m}$	1.00	1.00
$\chi_{\rm d}^{\rm disc-m}$	0.80	0.75
$R_{\rm e}$	0.82	0.82
$\frac{b}{a}$	0.60	0.60

Table I.8: Same as Table I.2 for NGC 628.

Parameter	Value
$R_{\rm in,s}^{\rm tdisc-(i,m)}$	(0.55, 4.50)
$R_{\rm in,s}^{\rm disc-m}$	0
$R_{\rm in,d}^{\rm disc-m}$	3.70
$R_{\rm tin,s}^{\rm tdisc-(i,m)}$	(0, 0.62)
$R_{\rm tin,s}^{\rm disc-m}$	0
$R_{\rm tin,d}^{\rm disc-m}$	0.30
$R_{\rm t,s}^{\rm tdisc-(i,m)}$	(20.0, 20.0)
$R_{\rm t,s}^{\rm disc-m}$	20.0
$R_{\rm t,d}^{\rm disc-m}$	20.0
$z_{\rm s}^{\rm tdisc-(i,m)}$	(0.09, 0.09)
$z_{\rm s}^{\rm disc-m}$	0.22
$z_{\rm d}^{\rm disc-m}$	0.14
$n_{\rm s}$	2

Table I.9: Same as Table I.1 for NGC 891.

Parameter	d	c
$h_{\rm s}^{\rm tdisc-(i,m)}$	(3.0, 3.0)	(3.0, 5.0)
$h_{\rm s}^{\rm disc-m}(B)$	10.0	10.0
$h_{\rm d}^{\rm disc-(i,m)}$	(3.0, 11.0)	(3.0, 10.0)
$\chi_{\rm s}^{\rm tdisc-(i,m)}$	(0.0, 1.0)	(0.0, 1.0)
$\chi_{\rm s}^{\rm disc-m}$	-1.0	0.0
$\chi_{\rm d}^{\rm disc-(i,m)}$	(0.00, -0.85)	(0.00, -0.90)
$z_{\rm s}^{\rm disc-m}(B)$	0.32	0.50
$z_{\rm d}^{\rm disc-(i,m)}$	(0.28, 0.28)	(0.28, 0.28)
$R_{\rm e}(B)$	1.60	1.44
$\frac{b}{a}(B)$	0.39	0.47

Table I.10: Same as Table I.2 for NGC 891.

Parameter	Value
$R_{\rm in,s}^{\rm tdisc-(i,m)}$	(0.0, 0.0)
$R_{\rm in,s}^{\rm disc-m}$	3.0
$R_{\rm in,d}^{\rm disc-(i,m)}$	(0.0, 3.0)
$R_{\rm tin,s}^{\rm tdisc-(i,m)}$	(0.0, 3.0)
$R_{\rm tin,s}^{\rm disc-m}$	0.0
$R_{\rm tin,d}^{\rm disc-(i,m)}$	(1.0, 3.0)
$R_{\rm t,s}^{\rm tdisc-(i,m)}$	(3.0, 14.0)
$R_{\rm t,s}^{\rm disc-m}$	14.0
$R_{\rm t,d}^{\rm disc-(i,m)}$	(3.0, 14.0)
$z_{\rm s}^{\rm tdisc-(i,m)}$	(0.09, 0.09)
$n_{\rm s}$	4

Table I.11: Same as Table I.1 for NGC 3521.

Parameter	d	c
$h_{\rm s}^{\rm tdisc-(i,m,o)}$	(0.50, 3.30, 2.30)	(0.50, 3.40, 2.80)
$h_{\rm s}^{\rm disc-(m,o)}$	(2.00, 4.10)	(2.00, 4.10)
$h_{\rm d}^{\rm disc-(m,o)}$	(7.50, 7.50)	(7.80, 7.00)
$\chi_{\rm s}^{\rm tdisc-(i,m,o)}$	(0.10, -0.50, 2.50)	(0.10, -0.60, 2.50)
$\chi_{\rm s}^{\rm disc-(m,o)}$	(1.00, 2.00)	(1.00, 2.00)
$\chi_{\rm d}^{\rm disc-(m,o)}$	(-0.10, 1.00)	(0.00, 1.00)
$R_{\rm e}$	0.55	0.60
$\frac{b}{a}$	0.50	0.50

Table I.12: Same as Table I.2 for NGC 3521.

Parameter	d
$R_{\rm in,s}^{\rm tdisc-(i,m,o)}$	(0.00, 1.30, 10.00)
$R_{\rm in,s}^{\rm disc-(m,o)}$	(0.00, 7.00)
$R_{\rm in,d}^{\rm disc-(m,o)}$	(1.30, 7.00)
$R_{\rm tin,s}^{\rm tdisc-(i,m,o)}$	(0.00, 0.50, 6.50)
$R_{\rm tin,s}^{\rm disc-(m,o)}$	(0.00, 6.50)
$R_{\rm tin,d}^{\rm disc-(m,o)}$	(0.00, 6.50)
$R_{\rm t,s}^{\rm tdisc-(i,m,o)}$	(1.00, 6.30, 20.00)
$R_{\rm t,s}^{\rm disc-(m,o)}$	(6.50, 20.00)
$R_{\rm t,d}^{\rm disc-(m,o)}$	(6.30, 20.00)
$z_{\rm s}^{\rm tdisc-(i,m,o)}$	(0.09, 0.09, 0.09)
$z_{\rm s}^{\rm disc-(m,o)}$	(0.19, 0.19)
$z_{\rm d}^{\rm disc-(m,o)}$	(0.16, 0.16)
$n_{\rm s}$	2.0

Table I.13: Same as Table I.1 for NGC 3938.

Parameter	d	c
$h_{\rm s}^{\rm tdisc}$	3.20	3.80
$h_{\rm s}^{\rm disc}(B)$	3.00	3.15
$h_{\rm d}^{\rm disc}$	9.00	7.50
$\chi_{\rm s}^{\rm tdisc}$	1.10	1.40
$\chi_{\rm s}^{\rm disc}$	1.00	1.00
$\chi_{\rm d}^{\rm disc}$	1.00	0.60
$R_{\rm e}$	0.53	0.53
$\frac{b}{a}$	0.94	0.94

Table I.14: Same as Table I.2 for NGC 3938.

Parameter	Value
$R_{\rm in,s}^{\rm tdisc}$	2
$R_{\rm in,s}^{\rm disc}$	2
$R_{\rm in,d}^{\rm disc}$	2
$R_{\rm tin,s}^{\rm tdisc}$	0
$R_{\rm tin,s}^{\rm disc}$	0
$R_{\rm tin,d}^{\rm disc}$	0
$R_{\rm t,s}^{\rm tdisc}$	14
$R_{\rm t,s}^{\rm disc}$	17
$R_{\rm t,d}^{\rm disc}$	14
$z_{\rm s}^{\rm tdisc}$	0.09
$z_{\rm s}^{\rm disc}$	0.19
$z_{\rm d}^{\rm disc}$	0.16
$n_{\rm s}$	1

Table I.15: Same as Table I.1 for NGC 5907.

Parameter	d	c
$h_{\rm s}^{\rm tdisc-m}$	5.50	6.00
$h_{\rm s}^{\rm disc-m}(g)$	7.80	8.20
$h_{\rm d}^{\rm disc-m}$	15.0	14.0
$\chi_{\rm s}^{\rm tdisc-m}$	-0.50	-0.50
$\chi_{\rm s}^{\rm disc-m}$	-2.0	-2.0
$\chi_{\rm d}^{\rm disc-m}$	-1.0	-1.0
$z_{\rm s}^{\rm disc-m}(g)$	0.44	0.52
$z_{\rm d}^{\rm disc-m}$	0.30	0.30
$R_{\rm e}(g)$	1.0	1.0
$\frac{b}{a}(g)$	0.40	0.48

Table I.16: Same as Table I.2 for NGC 5907.

Parameter	Value
$R_{\rm in,s}^{\rm tdisc}$	0
$R_{\rm in,s}^{\rm disc}$	0
$R_{\rm in,d}^{\rm disc}$	2
$R_{\rm tin,s}^{\rm tdisc}$	0
$R_{\rm tin,s}^{\rm disc}$	0
$R_{\rm tin,d}^{\rm disc}$	0
$R_{\rm t,s}^{\rm tdisc}$	23
$R_{\rm t,s}^{\rm disc}$	23
$R_{\rm t,d}^{\rm disc}$	23
$z_{\rm s}^{\rm tdiscm}$	0.09
$n_{\rm s}$	1

Table I.17: Values for the wavelength dependent parameters of the clumpy model for each galaxy.

Galaxy	Parameter	B	V	I	J	K_s	3.6 µm	4.5 µm	5.8 µm
M33	$h_\mathrm{s}^{\mathrm{disc-m}}$	1.80	1.75	1.65	1.05	1.15	1.75	1.80	1.40
	$h_\mathrm{s}^{\mathrm{disc-i}}$	0.05	0.07	0.12	0.05	0.10	0.12	0.13	0.09
	$h_\mathrm{s}^{\mathrm{disc-o}}$	1.00	1.00	1.00	1.00	1.00	1.00	1.00	1.00
M51	$h_\mathrm{s}^{\mathrm{disc-m}}$	5.50	4.60	4.18	3.70	3.80	4.40	4.60	7.00
	$h_\mathrm{s}^{\mathrm{disc-i}}$	0.72	0.68	0.70	0.67	0.66	0.72	0.77	1.10
	$h_\mathrm{s}^{\mathrm{disc-o}}$	2.40	2.30	2.30	1.90	2.00	2.60	2.60	2.00
M101	$h_\mathrm{s}^{\mathrm{disc-m}}$	4.30	4.30	4.10	3.50	3.60	3.65	3.60	3.70
	$h_\mathrm{s}^{\mathrm{disc-i}}$	0.50	0.50	0.50	0.40	0.40	0.30	0.20	0.10
NGC 628	$h_\mathrm{s}^{\mathrm{disc-m}}$	3.30	3.20	2.90	2.68	2.64	2.90	2.90	2.80
NGC 891	$h_\mathrm{s}^{\mathrm{disc-m}}$	10.00	7.00	5.30	4.40	4.00	4.20	4.20	3.60
	z_s	0.50	0.50	0.46	0.36	0.31	0.30	0.31	0.27
	$\frac{b}{a}$	0.47	0.47	0.47	0.47	0.47	0.47	0.47	0.47
	R_e	1.44	1.44	1.44	1.44	1.60	1.60	1.60	1.44
NGC 3521	$h_\mathrm{s}^{\mathrm{disc-m}}$	2.00	2.00	2.20	2.60	2.80	2.80	2.90	4.30
	$h_\mathrm{s}^{\mathrm{disc-o}}$	4.10	4.10	4.30	4.10	4.15	3.90	3.80	3.70
NGC 3938	$h_\mathrm{s}^{\mathrm{disc-m}}$	3.15	3.00	3.00	2.65	2.50	2.80	2.80	2.80
NGC 5907	$h_\mathrm{s}^{\mathrm{disc-m}}$	8.20	6.70	6.30	5.00	5.00	4.80	4.70	4.50
	z_s	0.52	0.50	0.52	0.45	0.43	0.44	0.43	0.42
	$\frac{b}{a}$	0.48	0.48	0.44	0.36	0.50	0.38	0.38	0.38
	R_e	1.00	1.00	1.00	1.00	0.80	1.00	1.00	1.00

Appendix J

Dust Masses of the Galaxy Sample

This appendix contains the integrated dust masses for each galaxy in the sample. Table J.1 shows the dust mass of the inner, main, and outer discs (columns 2–4), and the global dust mass (column 5).

Table J.1: Dust masses derived with the clumpy model for each galaxy. The subscripts 'i', 'm', 'o' indicate the dust mass in the inner, main, outer discs, respectively, and 'tot' indicates the global dust mass

Galaxy	$M_{\rm d,i}$ ($\times 10^5\,{\rm M}_\odot$)	$M_{\rm d,m}$ ($\times 10^7\,{\rm M}_\odot$)	$M_{\rm d,o}$ ($\times 10^7\,{\rm M}_\odot$)	$M_{\rm d,tot}$ ($\times 10^7\,{\rm M}_\odot$)
M33	1.04 ± 0.10	1.11 ± 0.08	0.23 ± 0.021	1.35 ± 0.08
M51	86.6 ± 8.6	2.85 ± 0.19	3.06 ± 0.27	6.78 ± 0.34
M101	8.32 ± 0.82	9.65 ± 0.65	-	9.73 ± 0.65
NGC 628	0.78 ± 0.077	8.06 ± 0.54	-	8.06 ± 0.54
NGC 891	58.1 ± 5.7	6.43 ± 0.43	-	7.01 ± 0.43
NGC 3521	-	2.87 ± 0.19	4.91 ± 0.44	7.78 ± 0.48
NGC 3938	-	4.90 ± 0.33	-	4.90 ± 0.33
NGC 5907	-	12.4 ± 0.83	-	12.4 ± 0.83